



**HAL**  
open science

# Probing the impact of structural defects on spin dependent tunneling using photons

Ufuk Halisdemir

► **To cite this version:**

Ufuk Halisdemir. Probing the impact of structural defects on spin dependent tunneling using photons. Physics [physics]. Université de Strasbourg, 2016. English. NNT : 2016STRAE018 . tel-01468571

**HAL Id: tel-01468571**

**<https://theses.hal.science/tel-01468571>**

Submitted on 15 Feb 2017

**HAL** is a multi-disciplinary open access archive for the deposit and dissemination of scientific research documents, whether they are published or not. The documents may come from teaching and research institutions in France or abroad, or from public or private research centers.

L'archive ouverte pluridisciplinaire **HAL**, est destinée au dépôt et à la diffusion de documents scientifiques de niveau recherche, publiés ou non, émanant des établissements d'enseignement et de recherche français ou étrangers, des laboratoires publics ou privés.



---

**THÈSE DE DOCTORAT**  
pour obtenir le grade de  
Docteur de l'université de Strasbourg  
Discipline/S spécialité: Physique

---

**PROBING THE IMPACT OF STRUCTURAL DEFECTS ON SPIN  
DEPENDENT TUNNELING USING PHOTONS**

---

Université de Strasbourg  
École Doctorale de Physique et Chimie-Physique  
Institut de Physique et Chimie des Matériaux de Strasbourg  
présentée par  
**HALISDEMIR Ufuk**  
soutenue le : 09 Novembre 2016

**Membres du jury:**

**Directeur de thèse**

Dr. BOUKARI Samy                      IPCMS - Université de Strasbourg

**Rapporteurs**

Prof. KOSTER Gertjan                      MESA+ - Université de Twente

PD Dr. THOMAS Andy                      IFW Dresden

**Examineurs**

Dr. BOWEN Martin                      IPCMS - Université de Strasbourg

Prof. TUREK Philippe                      POMAM - Université de Strasbourg

Prof. HEHN Michel                      ILJ - Université de Lorraine



“I must not fear. Fear is the mind-killer. Fear is the little-death that brings total obliteration. I will face my fear. I will permit it to pass over me and through me. And when it has gone past I will turn the inner eye to see its path. Where the fear has gone there will be nothing. Only I will remain.”

Frank Herbert, The Litany Against Fear, *Dune*.



# Contents

Bibliographie

xxvii

<b>I</b>	<b>Theoretical and Experimental background</b>	<b>1</b>
	<b>General Introduction</b>	<b>3</b>
<b>1</b>	<b>Introduction to Spintronic</b>	<b>7</b>
1.1	Phenomenological theory of giant magnetoresistance . . . . .	7
1.1.1	Electrical conductivity of rare earth elements . . . . .	7
1.1.2	Electrical conductivity of ferromagnets . . . . .	9
1.1.3	Giant magnetoresistance . . . . .	10
1.2	Tunneling magnetoresistance in amorphous magnetic tunnel junctions . .	12
1.2.1	Tunneling basics . . . . .	12
1.2.1.1	Quantum tunneling . . . . .	12
1.2.1.2	Bardeen's approach of solid state tunneling . . . . .	13
1.2.1.3	Simmons' formula of tunneling current . . . . .	15
1.2.2	Phenomenological theory of tunneling magnetoresistance . . . . .	16
1.2.2.1	Spin-dependent tunneling . . . . .	16
1.2.2.2	The Jullière model of tunneling magnetoresistance . . . . .	17
1.2.3	Theoretical refinements . . . . .	19
1.2.3.1	Stearns' approach . . . . .	19
1.2.3.2	Importance of interfaces . . . . .	20
1.2.3.3	Slonczewski model . . . . .	20
1.2.4	Summary . . . . .	21
1.3	Tunneling magnetoresistance in crystalline magnetic tunnel junctions . .	22
1.3.1	Theoretical model and formalism . . . . .	22
1.3.1.1	Crystal structure . . . . .	22
1.3.1.2	Formalism . . . . .	24
1.3.2	Electric and magnetic properties . . . . .	25
1.3.3	$k_{\parallel}$ -resolved tunneling current . . . . .	26
1.3.4	Electrical transport for $k_{\parallel} = (0, 0)$ . . . . .	27
1.3.4.1	Effect of lateral symmetry of incident Bloch states . . . . .	27
1.3.4.2	Wave-functions matching at interfaces . . . . .	28
1.3.4.3	Tunneling DOS across the junction . . . . .	30
1.3.5	Electrical transport for $k_{\parallel} \neq (0, 0)$ . . . . .	32
1.3.6	Co and CoFe electrodes . . . . .	33
1.3.7	Experimental confirmation . . . . .	34

1.3.8	Summary . . . . .	35
1.4	From Epitaxial to textured magnetic tunnel junctions . . . . .	35
1.5	Conclusion . . . . .	38
<b>2</b>	<b>Spin dependent tunneling in realistic junctions</b>	<b>41</b>
2.1	Interface considerations . . . . .	42
2.1.1	Tunneling through interface resonant states . . . . .	42
2.1.2	Interface oxidation . . . . .	45
2.1.3	Effect of interface carbon contamination . . . . .	47
2.1.4	Impact of misfit dislocations . . . . .	50
2.1.5	Interface disorder from first principle . . . . .	52
2.2	Effect of bias voltage . . . . .	54
2.2.1	Impact of bias on coherent tunneling . . . . .	55
2.2.1.1	Modification of the potential landscape . . . . .	55
2.2.1.2	Density of states effects . . . . .	57
2.2.2	Bias induced inelastic processes . . . . .	60
2.2.2.1	Inelastic electron tunneling spectroscopy . . . . .	60
2.2.2.2	Zero bias anomaly, phonons and magnons . . . . .	63
2.2.2.3	Quantum well states . . . . .	70
2.2.2.4	Trapping states . . . . .	71
2.2.3	Summary . . . . .	71
2.3	Effect of temperature . . . . .	72
2.3.1	AIO based MTJs . . . . .	72
2.3.2	MgO based MTJs . . . . .	74
2.4	Impact of localized states on spin dependent tunneling . . . . .	75
2.4.1	Impact of localized states: Early models . . . . .	76
2.4.1.1	Resonant tunneling through a single localized state . . . . .	77
2.4.1.2	Hopping via chains of localized states . . . . .	78
2.4.1.3	Resonant tunneling with spin-flip scattering . . . . .	80
2.4.1.4	Impact of localized states induced by boron impurities in CoFeB/MgO/CoFeB MTJs . . . . .	81
2.4.2	Impact of oxygen vacancies in MgO based MTJs from first principles . . . . .	83
2.4.2.1	Electrical properties of MgO containing oxygen vacancies . . . . .	83
2.4.2.2	Impact of oxygen vacancies on spin dependent tunneling in Fe/MgO/Fe MTJs . . . . .	85
2.4.2.3	Systematic study of the effect of oxygen vacancies in Fe/MgO/Fe MTJs . . . . .	86
2.4.2.4	Effect of oxygen vacancies on interlayer exchange coupling in Fe/MgO/Fe MTJs . . . . .	88
2.4.3	Optical activity of oxygen vacancies in MgO . . . . .	91
2.4.3.1	Photoluminescence of point defects . . . . .	92
2.4.3.2	Single oxygen vacancies . . . . .	93
2.4.3.3	Double oxygen vacancies . . . . .	99
2.4.3.4	Coherent tunneling between defects in MgO . . . . .	100

2.5	Conclusion	102
2.6	This thesis scientific motivations	103
2.6.1	Impact of localized states on electrical transport properties	103
2.6.2	An attempt to exploit the effect of localized states as additional functionality in working devices	105
2.6.3	Combining X-ray absorption spectroscopy and electrical measurements	105
<b>3</b>	<b>Experimental techniques</b>	<b>107</b>
3.1	Sample Growth and device fabrication	107
3.1.1	Introduction to sputtering	107
3.1.2	Sample deposition	108
3.1.3	MTJ patterning	108
3.1.3.1	Step I: Pillars definition	110
3.1.3.2	Step II: Lower electrode definition	111
3.1.3.3	Step III: Passivation layer deposition	111
3.1.3.4	Step IV: Electrode deposition	112
3.2	Magnetotransport experiment	114
3.2.1	Setup general description	114
3.2.1.1	Gifford-McMahon cycle	114
3.2.2	Calibration and automation	117
3.2.2.1	Temperature calibration	117
3.2.2.2	Dilation of the cold finger and optical device tracking	118
3.2.2.3	Electrical multiplex transmitter	119
3.2.2.4	Setup automation	120
3.3	Synchrotron Experiments	121
3.3.1	DEIMOS X-ray absorption spectroscopy setup	121
3.3.2	Versatile insert for in situ electrical probing	125
3.3.3	Association of XAS and electrical measurements	125
<b>II</b>	<b>Results and discussion</b>	<b>127</b>
<b>4</b>	<b>Bias and temperature dependence of magnetotransport properties</b>	<b>129</b>
4.1	Optical activity of sputtered MgO thin films	130
4.1.1	Overview of the literature	130
4.1.2	Temperature dependent photoluminescence of sputtered MgO thin films	133
4.1.2.1	Photoluminescence spectra	133
4.1.2.2	Interpretation	134
4.2	Magnetotransport experiments	136
4.2.1	Basic magneto-electric properties	136
4.2.2	Considerations on the device barrier height	138
4.2.3	Bias and temperature dependent measurements	140

4.3	Discussion . . . . .	143
4.3.1	Initial model and limitations . . . . .	143
4.3.1.1	Model . . . . .	143
4.3.1.2	Limitations . . . . .	144
4.3.2	Extended dataset . . . . .	146
4.3.3	Alternative interpretations . . . . .	147
4.4	Conclusion and perspectives . . . . .	149
<b>5</b>	<b>Optical excitation of localized states</b>	<b>151</b>
5.1	Introduction . . . . .	151
5.2	Initial results and models . . . . .	152
5.2.1	Experiment . . . . .	152
5.2.2	Basic magneto-electric properties . . . . .	154
5.2.3	Bias and temperature dependence of optically excited devices . . . . .	155
5.2.3.1	Impact of 3.05 eV p-polarized light on magnetotransport . . . . .	155
5.2.3.2	Impact of varying light's polarization on magnetotransport . . . . .	157
5.3	Discussion . . . . .	158
5.3.1	Model I: Optical addressing . . . . .	159
5.3.2	Model II: Heat . . . . .	160
5.3.3	Estimation of laser-induced heat . . . . .	162
5.3.4	Impact of 0.8 eV photons on magnetotransport properties . . . . .	163
5.4	Conclusion . . . . .	164
<b>6</b>	<b>Synchrotron experiments</b>	<b>167</b>
6.1	Introduction . . . . .	167
6.2	Experiment . . . . .	168
6.2.1	Experimental setup . . . . .	168
6.2.2	X-ray absorption reference spectra . . . . .	169
6.2.3	Synchronized electronic transport measurement . . . . .	170
6.2.4	Noise management . . . . .	171
6.2.5	Principle of concurrent electrical and XAS measurements . . . . .	172
6.2.6	Results and discussion . . . . .	173
6.2.6.1	Combined XAS and magnetotransport measurements . . . . .	173
6.2.6.2	Impact on magnetotransport: Pre-edge region . . . . .	175
6.2.6.3	Impact on magnetotransport: Oxygen K absorption edge . . . . .	176
6.3	Conclusion . . . . .	177
<b>7</b>	<b>Conclusion and perspectives</b>	<b>179</b>
7.1	Bias and temperature dependence of magnetotransport properties . . . . .	179
7.2	Optical excitation of localized states . . . . .	180
7.3	Synchrotron experiments . . . . .	181
	<b>Bibliography</b>	<b>183</b>

# Résumé en Français

## Introduction

L'effet tunnel est un phénomène quantique dans lequel une particule peut franchir une barrière de potentielle qu'elle ne pourrait pas surmonter dans le cadre de la mécanique Newtonienne. C'est un effet basique et spectaculaire (parce que contre-intuitif) décrit par la mécanique quantique, il est notamment utilisé comme un exemple canonique dans la plupart des livres d'introduction à la physique quantique. L'effet tunnel se retrouve dans de nombreux phénomènes naturels et est utilisé dans de nombreuses techniques expérimentales dont la plus connue est le microscope à effet tunnel.

Dans cette thèse, nous nous sommes concentrés sur l'effet tunnel dans une catégorie particulière de dispositifs électroniques, à savoir des jonctions tunnels. Une jonction tunnel est constituée de trois couches, deux électrodes métalliques (M) séparées par une fine couche d'un matériau isolant (I), et peut aussi s'appeler MIM ou M/I/M. Dans ces dispositifs, l'effet tunnel fait référence à la transmission d'électrons d'une électrode à une autre à travers la couche isolante et se nomme *effet tunnel à l'état solide*. Les propriétés électriques des MIMs ainsi que les premiers modèles théoriques qui les décrivent ont été développés il y a plus de 50 ans. Depuis, le domaine a progressé plutôt lentement hormis au cours de deux périodes durant lesquelles il a attiré l'attention de la communauté scientifique et s'est développé très rapidement.

La première période correspond à l'émergence du domaine du transport tunnel polarisé en spin. Dans ce cas, le transport électronique est similaire au transport tunnel dans les structures MIM à l'exception que les électrodes métalliques sont remplacées par des couches ferromagnétiques (FM). Le développement du domaine a été provoqué par l'expérience pionnière de Giaever<sup>7</sup> qui a mesuré les propriétés électriques de structures métal-isolant-superconducteur. Par la suite, la couche métallique a été remplacée par une couche ferromagnétique (FM), et la densité d'état très particulière de la couche superconductrice a été utilisée comme détecteur de spin. Finalement, en 1975, Julliere<sup>1</sup> a remplacé la couche superconductrice par une deuxième couche ferromagnétique et a montré pour la première fois que la résistance d'un tel dispositif dépendait de l'alignement relatif des aimantations des deux électrodes. Il a mesuré pour la première ce qu'on appelle aujourd'hui la magnétorésistance tunnel (abrégée TMR) dans des structures FM/I/FM aussi appelées des *jonctions tunnels magnétiques* (JTM). A cette époque, le transport tunnel polarisé en spin n'a pas attiré l'attention de la communauté scientifique principalement à cause des difficultés expérimentales liées à l'élaboration d'hétérostructures de couches minces, du besoin de températures cryogéniques ainsi que de la faible amplitude de l'effet.

La seconde percée expérimentale qui a définitivement déclenché le développement très rapide du domaine est la découverte de la magnétorésistance géante (GMR) en 1988<sup>8,9</sup>. La GMR se produit dans les triples couches ferromagnétique-métallique-ferromagnétique et

fait référence au changement de résistance du dispositif en fonction que l'aimantation des électrodes pointent dans la même direction ou bien dans des directions opposées. Comme nous l'avons mentionné précédemment, les effets magnétorésistifs ne sont pas limités au dispositif de type GMR, mais peuvent aussi se produire dans les jonctions tunnels magnétiques. Étant donné que la TMR et la GMR ont toutes deux de nombreuses applications potentielles, un effort de recherche très important a été fait afin d'améliorer les performances de ces dispositifs. Après les premières expériences menées par Julliere en 1975, la fabrication de jonctions tunnels magnétiques avec une TMR mesurable à température ambiante a été réalisée en 1995<sup>10,11</sup>. Les phénomènes de TMR et GMR sont déjà utilisés dans de nombreuses applications industrielles<sup>12-14</sup>, mais sont aussi étudiés intensivement pour leurs applications potentielles qui permettraient de réaliser des dispositifs de nouvelles générations qui posséderaient des fonctionnalités avancées<sup>15</sup>.

La compréhension du transport tunnel polarisé en spin a d'abord été limitée par des difficultés théoriques à modéliser les barrières isolantes amorphes. Les progrès réalisés dans le processus de fabrication ainsi que le raffinement des techniques expérimentales ont permis la croissance d'hétérostructure épitaxiales, ces structures cristallines ont permis la comparaison entre modèles théoriques et résultats expérimentaux et ont fortement amélioré notre compréhension du transport polarisé en spin dans les JTM. Les modèles théoriques permettent d'avoir une bonne compréhension du transport polarisé en spin dans les systèmes épitaxiaux, et l'obtention de TMR relativement grande dans le système Fe/MgO/Fe (que nous allons discuter plus en détail plus tard) cristallin semble confirmer ces modèles<sup>16</sup>.

Cependant, il existe encore des divergences entre modèles théoriques et résultats expérimentaux qui ne sont toujours pas expliquées. Par exemple, des calculs *ab-initio* prédisent des valeurs de TMR supérieures à 30 000 %<sup>17</sup> tandis que les valeurs expérimentales atteignent des valeurs de 600 % (1100 %)<sup>18</sup> à température ambiante (basse température). De plus, des zones d'ombres limitent aussi notre compréhension de la dépendance en température en ce qui concerne les propriétés magnétoélectriques. Finalement, un des résultats les plus surprenants concerne la hauteur de barrière JTM à base de MgO. Alors que le gap optique du MgO suggère une hauteur de barrière de 3.9 eV, les valeurs rapportées dans la littérature varient entre 0.4 et 1.1 eV, soit 3 à 10 fois plus petit que ce à quoi on peut s'attendre.

Naturellement, ces divergences peuvent être expliquées en partie par le fait que les calculs théoriques considèrent des structures cristallines parfaites alors que dans la réalité les dispositifs contiennent toujours différents types de défauts structuraux. Cependant, l'importance de l'impact des défauts sur les performances des JTM à base d'oxydes n'est pas autant reconnue que dans le domaine des semi-conducteurs. L'impact des défauts structuraux dans le MgO sur le transport tunnel polarisé en spin est à son balbutiement dans ce système canonique qui est autrement largement étudié.

Dans ce travail, nous nous sommes concentrés sur un type de défaut structural très spécifique, à savoir les lacunes d'oxygène situées dans la couche d'oxyde isolante. Plus particulièrement, cette thèse a pour principal objectif de caractériser l'impact de tels défauts sur le transport tunnel polarisé en spin dans des JTM à base de MgO. Nous nous sommes concentrés sur les lacunes d'oxygènes car il est possible que ce type de défaut donne lieu à des propriétés avancées dans certains dispositifs<sup>2-6</sup>. Par exemple, les états localisés in-

duits par les lacunes d'oxygènes sont suspectés d'être responsables des faibles hauteurs de barrières observées expérimentalement. Néanmoins, les applications qui utilisent le mécanisme de transfert de spin (SST) nécessitent de fortes densités de courant qui peuvent être accommodées, dans les JTM à base de MgO, seulement grâce à ces faibles hauteurs de barrières. Plus qu'un problème purement académique, résoudre cette divergence, en corrélant la nature des défauts structuraux à leur impact sur les propriétés des dispositifs électroniques, peut avoir d'importantes répercussions dans d'autres applications qui utilisent le transfert de spin.

Les objectifs de ce travail peuvent être divisés en deux parties : notre objectif premier est de caractériser l'impact des états localisés induits par les lacunes d'oxygène sur les propriétés magnétoélectriques des jonctions tunnels magnétiques CoFeB/MgO/CoFeB ainsi que d'utiliser l'excitation optique comme degrés de liberté supplémentaire du système afin de caractériser la présence et l'impact de ces défauts. Dans un deuxième temps, nous souhaitons également utiliser les modifications induites par l'excitation optique comme fonctionnalité supplémentaire de ces appareils pour des applications optoélectroniques.

La première partie de cette thèse introduit différentes techniques expérimentales et quelques concepts théoriques afin de mieux aborder l'objet de ce travail, elle est divisée en trois parties. Le premier chapitre introduit d'abord un modèle phénoménologique simple qui permet de comprendre la magnétorésistance tunnel. La seconde partie du chapitre discute plus en détail des propriétés magnétiques et électriques d'hétérostructure Fe/MgO/Fe obtenues par des calculs *ab-initio* plus sophistiqués et discute du phénomène de filtrage de symétrie qui permet d'obtenir de fortes valeurs de TMR dans ce système. Le second chapitre est consacré aux effets intrinsèque et extrinsèque qui limitent les performances de JTM à base de MgO. Nous nous concentrerons d'abord sur les effets d'interfaces et discuterons de quelles façons les états d'interface résonants ainsi que les contaminations et le désordre aux interfaces modifient le transport tunnel. Nous verrons ensuite comment la température et la tension appliquée altère les propriétés des dispositifs. La dernière partie du chapitre est consacrée à l'impact des états localisés. La dernière section est dédiée à une discussion sur l'activité optique induite par les lacunes d'oxygène dans MgO. Le troisième chapitre décrit la croissance des échantillons ainsi que la fabrication des dispositifs par photolithographie UV. Le banc sur lequel les mesures magnétoélectriques ont été effectuées est également présenté. Finalement, le dispositif expérimental de la ligne synchrotron qui a été utilisé dans la dernière partie de cette thèse est brièvement introduit.

La seconde partie du manuscrit est dédiée aux résultats expérimentaux obtenus durant ma thèse, cette partie est divisée en trois chapitres. Dans le chapitre 4, je présente les résultats de nos mesures magnétoélectriques en fonction de la température et de la tension appliquée. Nous discutons d'abord les spectres de photoluminescence mesurés sur nos couches de MgO déposées par pulvérisation cathodique. Nous détaillons ensuite la technique expérimentale que nous avons utilisée afin de déterminer la hauteur de barrière de nos dispositifs. Finalement nous discutons comment nous avons essayé d'identifier l'impact de défauts spécifiques en comparant nos mesures optiques et magnétoélectriques. Dans le chapitre 5, j'analyse notre tentative qui consistait à utiliser le degré de liberté optique comme fonctionnalité supplémentaire de nos jonctions. Dans le dernier chapitre de ce manuscrit, je présente les résultats que nous avons obtenus dans une expérience où nous

avons combiné des mesures d'absorption X et des mesures magnétoélectriques.

## Transport polarisé en spin dans le système Fe/MgO/Fe(001)

Pour comprendre les phénomènes physiques sous-jacents au transport tunnel polarisé en spin dans les dispositifs que nous avons étudié durant ma thèse, il est utile de considérer les résultats de calculs ab-initio sur le système canonique Fe/MgO/Fe(001).

La Figure AI représente la structure cristalline du système cristallin Fe/MgO/Fe(001). Le MgO adopte une structure NaCl tandis que le Fe possède une structure cubique centrée. La couche de MgO(001) croit avec une relation épitaxiale Fe(001)[110]/MgO(001)[100], c'est-à-dire qu'il y a un angle de  $45^\circ$  entre les axes MgO[100] et Fe[100]. Par conséquent, le décalage entre les mailles  $a_{MgO}$  et  $\sqrt{2}a_{Fe}$  est de seulement 3.7%. Des études théoriques et des résultats expérimentaux suggèrent que les atomes d'oxygène du MgO se trouvent

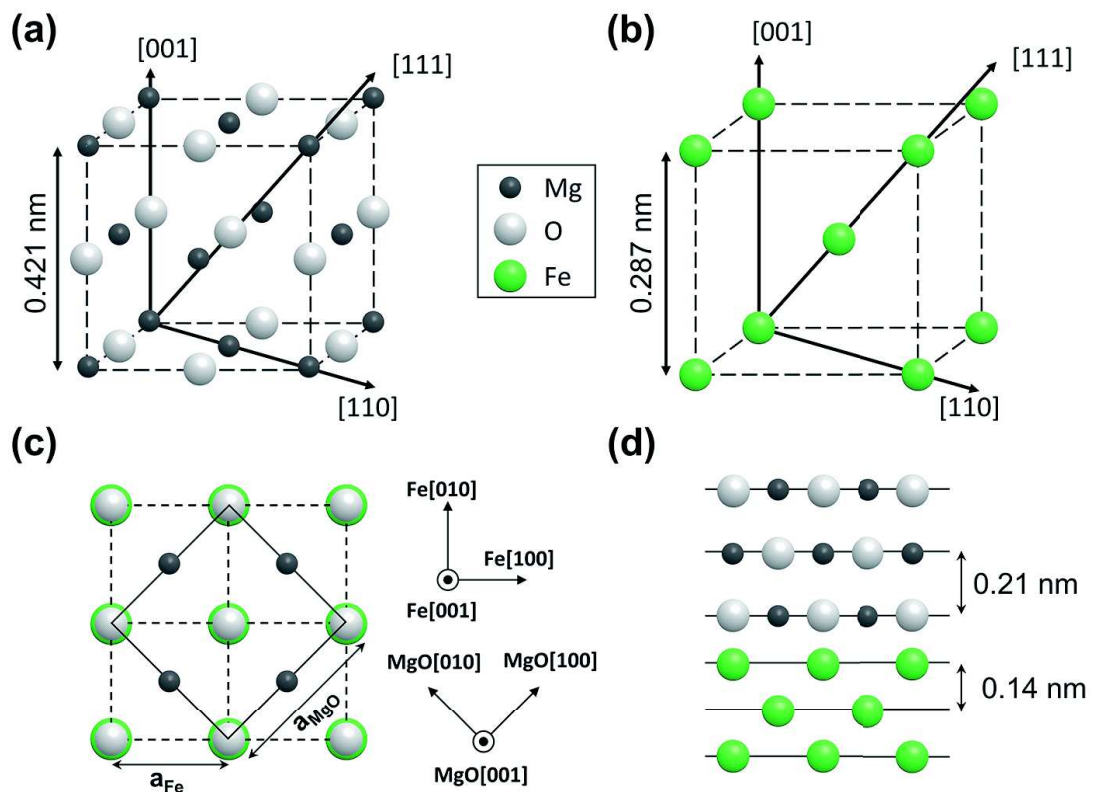


FIGURE AI : Structure de l'interface Fe/MgO (001) : La structure NaCl et cubique centrée du MgO et du fer sont schématisé dans les panneaux (a) et (b) respectivement. Une vue de dessus ainsi qu'un vue en tranche de l'interface Fe/MgO(001) sont représentées dans les panneaux (c) et (d). On constate que la direction MgO[100] est parallèle à la direction Fe[110].

directement au-dessus des atomes de Fe à une distance de 0.20-0.23 nm. Les calculs<sup>44</sup> ont aussi montré que les propriétés magnétique et électrique de Fe et du MgO sont peu modifier aux interfaces.

Comme nous l'avons mentionné en introduction, la difficulté à modéliser les barrières isolantes amorphes a longtemps limité notre compréhension de l'effet tunnel à l'état solide. A contrario, dans les systèmes épitaxiés les atomes sont arrangés de manière ordonnés et la périodicité de la structure cristalline permet d'utiliser des outils de calculs plus sophistiqués. Dans ce cadre, il est notamment possible de classer et décrire les porteurs de charges par des considérations de symétrie. Il a également été montré que la probabilité pour un porteur de charge de traverser la barrière tunnel était maximal dans la direction perpendiculaire au plan des couches minces, cette direction est dénotée  $\Delta$  dans l'espace réciproque, et ce sont donc les électrons présents au niveau de fermi dans cette direction particulière qui vont participer au transport tunnel polarisé en spin.

La figure Figure AII représente la densité d'état polarisé en spin pour les électrons majoritaire (a) et minoritaire (b). Nous pouvons constater que dans le canal majoritaire, les électrons  $\Delta_1$ ,  $\Delta_5$  et  $\Delta_{2'}$  participent au transport tandis que dans le canal minoritaire ce sont les électrons  $\Delta_5$ ,  $\Delta_{2'}$  et  $\Delta_2$ . Les schémas (c) et (d) illustrent les principales différences entre la transmission par effet tunnel à travers des barrières amorphes et épitaxiés. Lorsque la barrière est amorphe (c), les électrons des différentes bandes (qui sont classés par symétries) sont tous transmis avec la même probabilité. Lorsque la barrière est cristalline, les électrons des différentes bandes sont transmis avec une probabilité spécifique, les calculs ont montré que les électrons  $\Delta_1$  (qui possèdent des orbitales des type  $s$ ) sont transmis avec la plus forte probabilité tandis que les électrons de type  $\Delta_5$  (orbitales des type  $p$ ) et  $\Delta_{2'}$

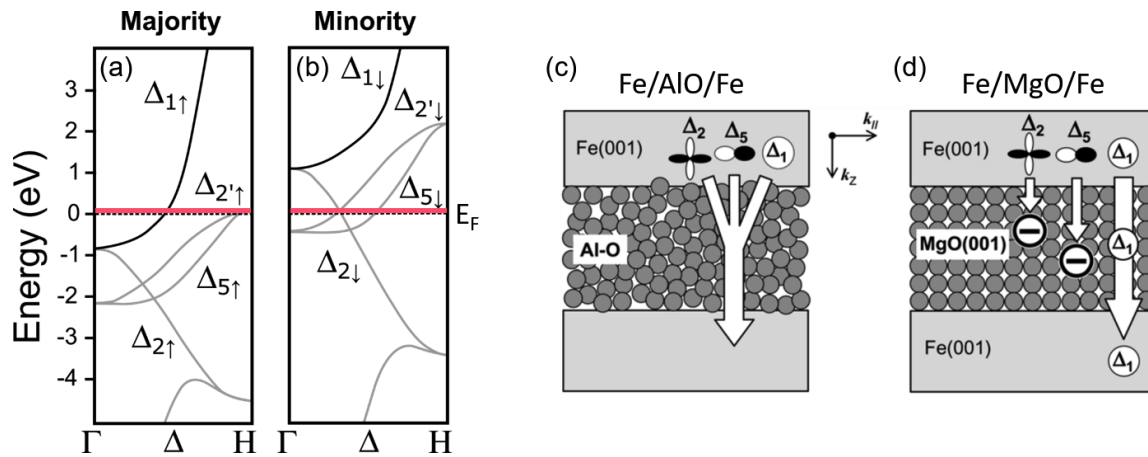


FIGURE AII : **Propriétés électriques des systèmes épitaxiés** : Densité d'état résolue en spin et en symétrie dans la direction  $\Delta$  de l'espace réciproque pour (a) les électrons majoritaire et (b) les électrons minoritaire. Toutes les bandes présentes au niveau de Fermi participe au tunnel courant (c) lorsque la barrière est amorphe, les électrons sont tous transmis avec la même probabilité et (d) lorsque la barrière est cristalline, les porteurs de charges de chaque bande possèdent une probabilité de transmission spécifique.

(orbitales des type  $d$ ) sont transmis avec une probabilité beaucoup plus faible.

Étant donné que les électrons  $\Delta_1$  sont transmis avec le plus de probabilité (ou réciproquement, ces électrons ont le taux de décroissance le plus lent dans MgO), on peut concevoir que les propriétés électriques de ces dispositifs sont donc principalement caractéristiques des états  $\Delta_1$ . Cependant, si on se réfère aux figures [Figure AII a](#) et [b](#), nous pouvons constater que les états  $\Delta_1$  sont totalement polarisés au niveau de Fermi, ils sont présent dans le canal majoritaire seulement. Si nous supposons que le spin est conservé lors d'un événement tunnel (ce qui est généralement vrai à basse température), alors un électron dans l'électrode émettrice ne peut traverser la couche isolante par effet tunnel que si un état avec le même spin et la même symétrie est disponible dans l'électrode receptrice. Par conséquent, le canal de conduction induit par les électrons  $\Delta_1$  n'est ouvert que dans la configuration magnétique parallèle (P) du dispositif, il est fermé dans la configuration antiparallèle (AP). Puisque les électrons  $\Delta_1$  sont les mieux transmis, cela résulte en une conductance beaucoup plus élevée dans la configuration P que dans la configuration AP et cela explique les fortes TMR observées dans les JTM à base de MgO qui est défini comme l'asymétrie de conductance entre les états P et AP :

$$TMR = \frac{G_P - G_{AP}}{G_{AP}} = \frac{R_{AP} - R_P}{R_P} \quad (1)$$

Ce processus est appelé phénomène de filtrage de symétrie.

Dans ce manuscrit, nous nous sommes concentrés sur un système qui diffère légèrement du système canonique Fe/MgO/Fe. Nous avons étudiés des JTM CoFeB/MgO/CoFeB. Toutes les couches sont déposées par pulvérisation cathodique, les électrodes de CoFeB sont initialement amorphes alors que le MgO est texturé dans la direction (001). Une étape supplémentaire de recuit après dépôt est nécessaire afin de cristalliser les interfaces ainsi que les électrodes. Tous les concepts introduits afin d'expliquer le transport tunnel dans les jonctions cristallines peuvent être appliqués à ces jonctions initialement amorphes.

## Motivations

Mon travail a été effectué dans le cadre d'un projet plus large dans le domaine de la Spintronique inorganique qui a pour but de développer des dispositifs de nouvelles générations. Mon travail a principalement porté sur l'impact des lacunes d'oxygènes présentes dans des couches d'oxydes intégrés dans des dispositifs électroniques. En particulier, notre objectif est de caractériser l'effet de tels défauts sur le transport polarisé en spin dans des JTM à base de MgO. Dans un second temps nous souhaitons également utiliser les connaissances acquises lors de la phase initiale du projet afin d'utiliser les propriétés induites par les lacunes d'oxygène comme degrés de liberté supplémentaire de nos jonctions.

Premièrement, il est clair que les oxydes jouent un rôle stratégique d'un point de vue technologique car ils sont déjà utilisés dans de nombreuses applications. Mais ces matériaux jouent également un rôle stratégique pour de futures applications car ils manifestent beaucoup de propriétés intéressantes. Bien que ces matériaux soient considérés comme très importants, l'importance de l'impact des défauts structuraux sur leurs propriétés n'est

pas autant reconnue que dans le domaine des semi-conducteurs. En effet, les défauts, et plus particulièrement les lacunes d'oxygènes jouent un rôle crucial dans la fiabilité et la performance des dispositifs. Dans cette perspective, il est essentiel d'identifier clairement leur impact sur le transport électronique dans les JTM. Le premier objectif de ce travail est non seulement d'identifier l'impact de populations de défauts spécifiques mais aussi de déterminer les processus physiques sous-jacent les changements des propriétés des JTM.

Deuxièmement, nous avons souhaité prendre avantage des propriétés induites par les lacunes d'oxygènes. En effet, il a été rapporté que les lacunes d'oxygènes pouvait potentiellement jouer un rôle central dans deux domaines intéressants, à savoir le domaine des memristors et le domaine des oxydes magnétiques dilués. Le premier domaines fait référence aux dispositifs dont la résistance n'est pas constante mais dépend de l'histoire de la tension appliquée. Le second domaine fait référence aux oxydes dopés avec des cations 3d magnétiques qui présentent un ordres ferromagnétiques à longue distance pour des niveaux très faibles de dopages. Les deux exemples peuvent être expliqués par la présence de lacunes d'oxygènes et suggèrent la présence de ces derniers peut être désirable dans certains cas. L'idée principale idée qui a motivé ce second axe de recherche est de prendre avantage des propriétés optique du MgO induites par les lacunes d'oxygènes et plus particulièrement d'exploiter le couplage qui existe entre les propriétés optiques de l'oxyde et les propriétés électrique des dispositifs.

## Étude de l'impact des lacunes d'oxygènes sur le transport polarisé en spin

Il est bien établit que retirer un atome d'oxygène d'une matrice de MgO crée un puit de potentiel capable de *piéger* des électrons. La charge de ces défauts ponctuels peut varier et par conséquent il existe toute une variété d'états localisés dont l'énergie est située dans le gap de l'isolant du matériau diélectrique. De plus, ces défauts peuvent dans leur état fondamental ou excité et peuvent également interagir entre eux pour créer des lacunes d'oxygène double. Dans cette partie, notre objectif est d'identifier clairement l'impact de populations de défauts spécifique induites pas les lacunes d'oxygène sur les propriétés électrique de JTM CoFeB/MgO/CoFeB.

Pour comprendre l'approche expérimentale que nous avons choisie, nous allons brièvement discuter de la façon dont les lacunes d'oxygènes modifient les propriétés du MgO et du dispositif dans lequel le MgO est intégré.

La [Figure AIII\(a\)](#) représente (de manière simplifiée) comment les lacunes d'oxygène modifient les propriétés du MgO. Comme nous l'avons indiqué précédemment, les lacunes d'oxygènes créent une variété d'états localisés dont l'énergie se trouve dans le gap du MgO. Il est donc possible d'utiliser une excitation optique (d'énergie appropriée) afin d'exciter ces états de leur niveau fondamental vers leur niveau excité. Mesurer le spectre d'absorption du MgO ainsi que les photons émis lors du processus de recombinaison (photoluminescence) permet d'obtenir des informations intéressantes sur la position énergétique de ces états dans le gap.

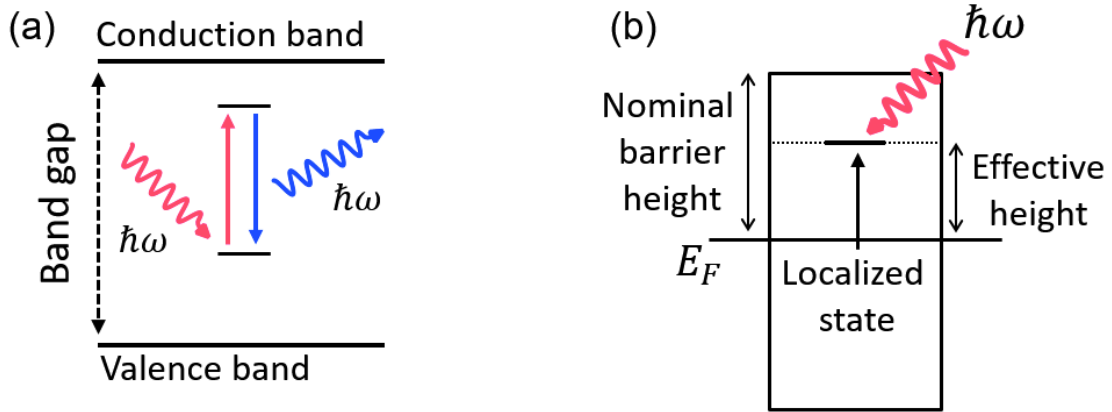


FIGURE AIII : **Impact des lacunes d'oxygènes** : (a) Gap du MgO modifié par la présence d'états localisés induit par une lacune d'oxygène. L'état fondamental ainsi que l'état excité sont représentés. L'excitation optique d'énergie approprié (l'énergie du photon  $\hbar\omega$  doit être égale à la différence d'énergie entre niveau fondamental et excité  $\Delta E$ ) permet d'exciter un électron de l'état fondamental vers l'état excité (rouge), le processus de recombinaison est accompagné par l'émission d'un photon (bleu). (b) Schéma simplifié du paysage de potentiel d'une JTM. La présence d'un état localisé réduit la hauteur de barrière du dispositif électrique au niveau énergétique du défaut.

La Figure AIII(b) représente comment les lacunes d'oxygène modifient les propriétés d'une JTM contenant du MgO. En première approximation, la barrière de potentiel du diélectrique peut être représentée par une simple marche de potentielle. Dans les dispositifs dont la structure cristalline est parfaite, la hauteur de barrière est définie par la distance entre le niveau de Fermi dans l'électrode et la bande de conduction dans l'isolant. Lorsqu'un état localisé est introduit dans le gap, celui-ci réduit la hauteur de barrière effective du dispositif à la position en énergie du défaut. Mesurer la hauteur de barrière du dispositif à l'aide de mesures électriques permet ainsi d'obtenir des informations sur la position en énergie des défauts impliqués dans le transport tunnel.

Afin d'identifier explicitement les différents états localisés dans le transport tunnel de nos jonctions, nous avons adopté la stratégie suivante. Premièrement, nous avons mesurés les spectres de photoluminescence dépendant en température de nos couches de MgO déposés par pulvérisation cathodique. À partir de ces spectres et d'autres résultats rapportés dans la littérature, nous avons établi un paysage de potentiel du MgO modifié par des états localisés. Dans un deuxième temps, nous avons mesurés expérimentalement la dépendance en température des propriétés magnétoélectriques de nos jonctions (et notamment la hauteur de barrière effective), ce qui nous a permis de déterminer la position énergétique des défauts impliqués dans le transport tunnel électriquement. Finalement, nous avons essayé d'identifier les états localisés impliqués dans le transport tunnel en comparant les mesures électriques du paysage de potentiel construit à partir de nos mesures optiques.

L'approche la plus simple pour déterminer la hauteur de barrière effective d'un dispositif

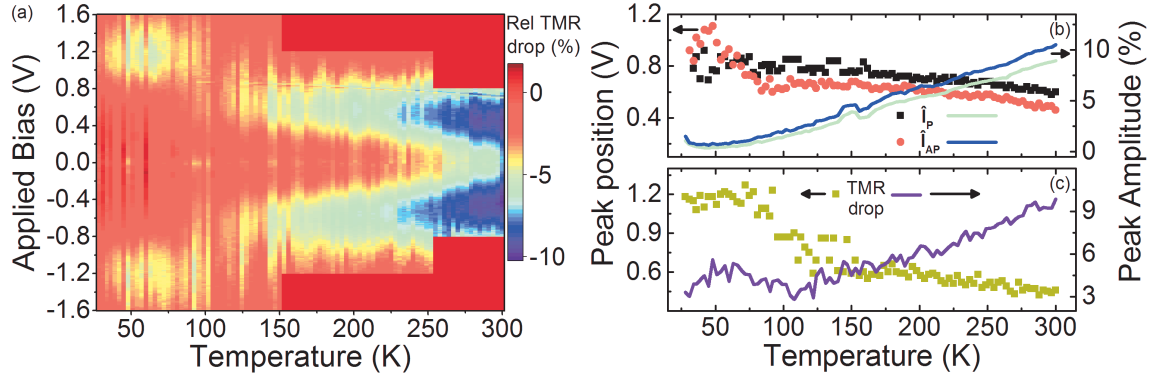


FIGURE AIV : **Propriétés magnétorésistive dans l'espace de paramètre (V,T) :** (a) Carte couleur 2D de la diminution relative de la TMR due à l'excitation thermique, (b) la position du maximum des pic et leur amplitude maximale extraite des  $\hat{I}$  pour les configurations magnétiques parallèle et antiparallèle et (c) la position du maximum des pic et leur amplitude maximale extraite des données représentées dans le panneau (a).

est mesurer le courant en fonction de la tension appliqué (I-V) et d'effectuer un ajustement de courbe avec les formules de Simmons ou de Brinkman. Cependant cette approche est limitée par le fait que ces formules ont été dérivées pour de simples barrières de potentiels (non cristallines) et parfaites (qui ne prennent pas en compte le paysage de potentiel compliqué induit par les états localisés). Afin de contourner ces difficultés, nous avons décidé d'opter pour une approche totalement expérimentale. Nous avons utilisé la technique  $\hat{I}$  (lire I chapeau) initialement introduite par Rottländer *et al.*.

Le principe de fonctionnement est très simple. Il suffit de mesurer des caractéristiques courant-tension (I-V) à différentes température, en général la plus basse ( $T_1$ ) et la plus haute ( $T_2$ ) accessible au système, et de calculer la différence relative entre ces deux courbes avec la formule suivante :

$$\hat{I}(T_1; T_2) = \left( \frac{I(T_2)}{I(T_1)} - 1 \right) \times 100 \quad (2)$$

La courbe qui résulte de ce calcul est caractérisée par deux maxima dont la position énergétique correspond à la hauteur de barrière.

Nous avons étendu la technique initialement introduite par Rottländer *et al.*. Nous avons mesuré les propriétés magnétoélectriques d'une jonction de 25  $\mu\text{m}$  de diamètre pour les configurations magnétiques parallèle et antiparallèle de  $T = 15 \text{ K}$  à  $T = 300 \text{ K}$  par pas de  $\Delta T = 3 \text{ K}$ . Nous avons alors calculé la dépendance en température des différences relatives entre caractéristiques I-V à l'aide de l'Equation (2). Nous avons ensuite tracé le résultat sous la forme de cartes de couleur 2D dans l'espace de paramètres (V,T). Puisque nous avons mesuré les I-V pour les deux configurations magnétiques, il nous a été possible de calculer et d'appliquer le même traitement à la TMR.

La carte couleur 2D pour la TMR est représentée sur la Figure AIV (a). Afin d'obtenir des informations plus quantitative de ces données, nous avons décidé d'extraire la position

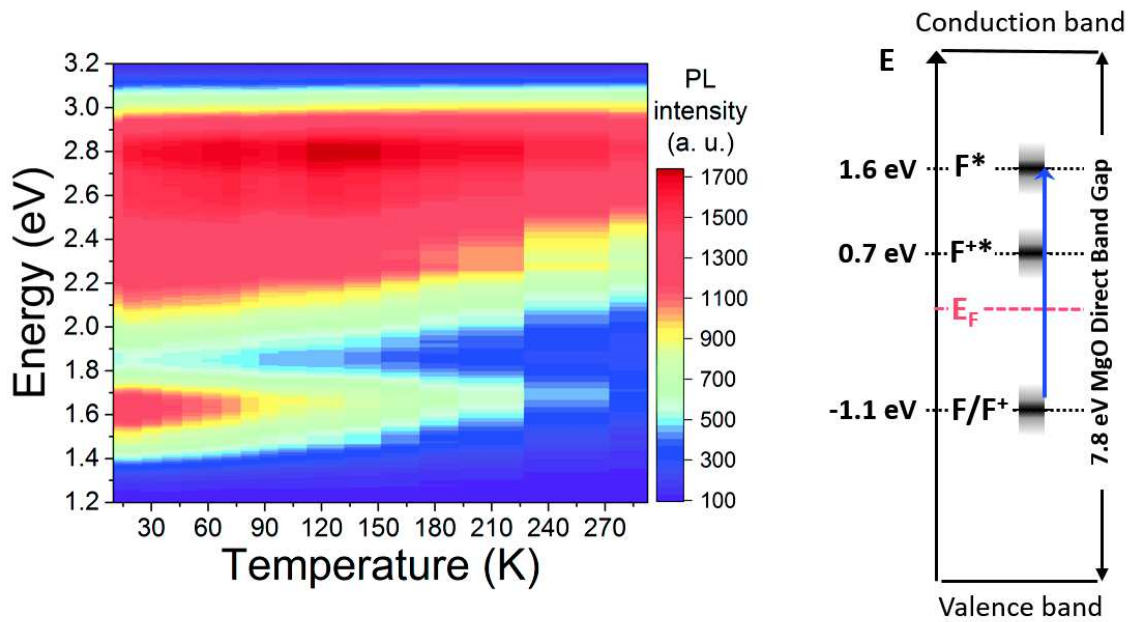


FIGURE AV : **Spectres de photoluminescence** : Dépendance en température des spectres de photoluminescence obtenu en en excitant une couche de MgO avec des photon d'énergie 3.81 eV.

ainsi que l'amplitude du maximum des pic observé. La position du maximum des pic et leur amplitude maximale extraite des  $\hat{I}$  pour (b) les configurations magnétique parallèle et antiparallèle et (c) la TMR. Pour rappel, la position des pics dans les  $\hat{I}$  correspondent à la hauteur de barrière effective des dispositif.

Très brièvement, nous constatons que le TMR décroît à des tensions appliquées bien précise et dans des plages de température bien définies (voir Figure AIV (c)). Premièrement, on distingue l'impact d'un état situé autour de 1.2 eV entre 20 et 100 K. Comme on peut le déduire de la dépendance en température de l'amplitude de ce pic, l'impact de cet état localisé décroît en fonction de la température. Aux alentours de  $T = 100$  K, l'impact d'un pic situé autour de 0.7 eV commence à avoir un impact non négligeable sur les propriétés magnétoélectriques. L'impact de cet état augment en fonction de la température et domine totalement le transport tunnel au-dessus de et 120 K.

Afin d'identifier ces deux états, nous avons comparé nos mesures magnétoélectrique à nos mesures optique. La dépendance en température des spectres de photoluminescence du MgO est représentée sur la Figure AV (a). A l'aide de ces mesures, et d'autres mesures rapportées dans la littérature, nous avons établis un paysage de potentiel modifié par les défauts, celui est représenté sur la Figure AV(b).

**Identification des pics à 1.2 et 0.7 V :** Dans notre interprétation initiale, nous supposons que la position des pics observés dans les courbe  $\hat{I}$  correspond à la hauteur de barrière effective de nos jonctions. Les jeux de données présentés précédemment sont interprétés de la manière suivante.

A basse température, un mécanisme modifie les propriétés magnétoélectriques à 1.2 V.

Lorsque la température augmente, un mécanisme supplémentaire localisé autour de 0.7 V commence à avoir un impact sur le transport tunnel. Dans la plage de température  $15 \text{ K} < T < 100 \text{ K}$ , le mécanisme situé à 0.7 V cause la diminution de la hauteur de barrière, mais dans cette gamme de température c'est toujours le mécanisme situé à 1.2 V qui domine. Cependant, un changement soudain se produit à  $T = 100 \text{ K}$ , température à laquelle le mécanisme à 0.7 V commence à dominer le transport tunnel. Ceci est suggéré par (i) le ralentissement de la position du pic autour de 0.7 V avec l'augmentation simultanée de l'amplitude de l'impact de ce pic et (ii) du changement brusque de la position du pic de 1.2 à 0.7 V.

Dans ce modèle, nous supposons que toutes les modifications résultant de l'excitation thermique sont dues aux lacunes d'oxygène. Si l'on se réfère au paysage de potentiel que nous avons déduit de nos mesures de photoluminescence, nous pouvons identifier les mécanismes situés à 1.2 V et 0.7 V aux états  $F/F^+$  et  $F^{+*}$  situés à  $E - E_F = -1.1 \text{ eV}$  et  $E - E_F = 0.7 \text{ eV}$  respectivement.

A l'aide de ce modèle, nous avons premièrement corrélé les faibles hauteurs de barrière rapportées dans la littérature à la réduction de la hauteur de barrière due à la présence d'états localisés. De plus, l'impact de ces défauts est différent pour l'état P et AP. Ceci peut refléter le caractère électronique des états localisés. Par exemple, il est bien établi que l'état  $F/F^+$  ressemble à une orbitale de type  $s$ , tandis que les électrons de type  $s$  et  $p$  dominent le transport tunnel dans l'état P et AP respectivement. Si les états localisés interagissent plus efficacement avec des électrons de la même symétrie, ceci expliquerait pourquoi l'impact des états  $F/F^+$  et  $F^{+*}$  ne soit pas le même sur le courant dans la configuration P et AP. Finalement, nous discutons également l'impact d'état  $M$ , qui pourrait jouer un rôle crucial. Nous suggérons que ces doubles lacunes d'oxygène réduisent la hauteur de barrière des jonctions mais conservent un transport tunnel cohérent. Certaines limitations de ce modèle sont discutées plus en détail dans le manuscrit.

## Excitation optique d'états localisés induits par les lacunes d'oxygènes

Dans la partie précédente nous avons décrit comment les états localisés induits par des lacunes d'oxygènes modifient les propriétés magnétoélectriques de nos JTM. Dans notre modèle initial, nous avons distingué deux plages de température bien distinctes. Entre  $33 \text{ K} < T < 80 \text{ K}$ , les modifications induites par l'excitation thermique sont maximales à 1.2 V et sont attribuées à l'impact des états fondamentaux  $F/F^+$  situés  $E - E_F = -1.1 \text{ eV}$  sous le niveau de Fermi. En augmentant la température, un nouvel état localisé commence à modifier le courant tunnel et domine totalement les propriétés électriques au-dessus de  $T = 100 \text{ K}$ . Pour résumer brièvement, nous avons supposé que la dépendance en température des propriétés magnéto-résistive est causée par un changement d'occupation depuis les états fondamentaux  $F/F^+$  vers l'état excité  $F^{+*}$ .

Toutes les expériences présentées dans cette partie sont basées sur cette interprétation. Basé sur ce modèle, notre objectif est de modifier le paysage de potentiel du MgO, et dans

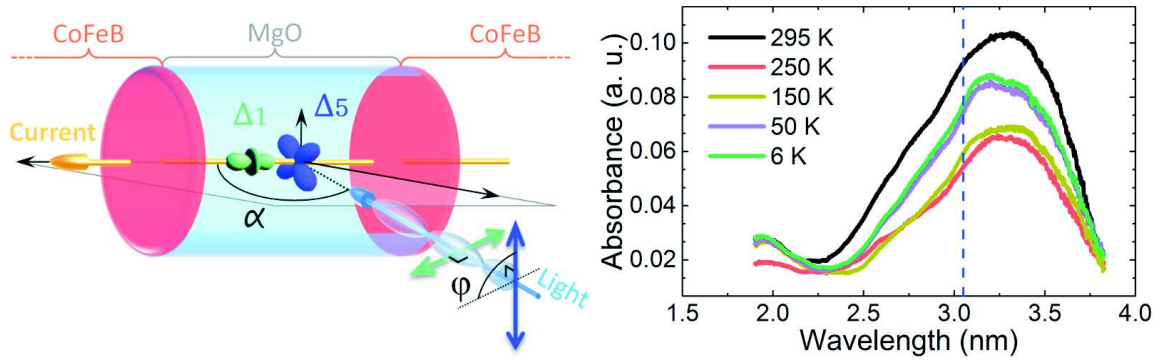


FIGURE AVI : **Géométrie de l'excitation optique** : (a) Un courant tunnel dominé par des états  $\Delta_1$  ou  $\Delta_5$  traverse la barrière de MgO (en bleu transparent). La direction de propagation de photons fait un angle  $\alpha$  par rapport à la normale à la surface de l'échantillon. L'angle entre la direction de propagation du courant  $I$  et le champ électrique de la lumière est dénoté  $\phi$ . (b) Dépendance en énergie de l'absorption optique d'une couche de MgO d'épaisseur 2.5 nm déposée par pulvérisation cathodique.

un sens modifier la hauteur de barrière ressentie par les porteurs de charges, en contrôlant optiquement l'occupation des différentes populations d'état localisé. Contrôler optiquement les propriétés électriques de nos jonctions peut être très intéressant, notamment pour des applications optoélectronique. Afin d'induire ce changement d'occupation entre états localisés, nous avons utilisé des photons dont l'énergie  $\hbar\omega$  correspond à la différence d'énergie  $\Delta E$  entre l'état fondamental et excité d'une population spécifique. Les modifications induites par l'excitation optique sont simultanément sondées par des mesures magnétorésistive dépendante en température et en tension appliquée. Nous nous sommes basés sur nos spectres de photoluminescences afin de choisir l'énergie de photon appropriée.

Notre ligne optique est composée de différentes sources laser, d'un polariseur Glan-Taylor qui permet de définir l'angle absolu de polarisation linéaire, d'une lame de retard demi-onde d'ordre zéro montée sur une rotation motorisée, d'un obturateur ainsi que d'une lentille convergente qui permet de focaliser le rayon laser sur l'échantillon.

La géométrie expérimentale que nous avons adoptée est représentée est schématisé dans la Figure AVI (a). Nous excitation avec des photons linéairement polarisée dont la direction de propagation fait un angle  $\alpha$  par rapport à la normale de la surface de l'échantillon. L'angle azimutal entre la direction de propagation du courant et le champ électrique de la lumière est dénoté  $\phi$ .

**Impact de l'excitation avec de la lumière de 3.05 eV polarisée p** : Nous avons d'abord étudié l'impact d'éclairer nos échantillons avec de la lumière continue de 3.05 eV et polarisée p. Cette énergie correspond au processus d'excitation  $F \rightarrow F^*$ . La Figure AVI (b) trace l'absorption optique d'une couche de MgO d'épaisseur 2.5 nm. Cette courbe confirme que notre couche de MgO déposée par pulvérisation cathodique absorbe bien à l'énergie d'excitation.

Dans ce chapitre, notre approche est très similaire à celle du chapitre précédent. Nous

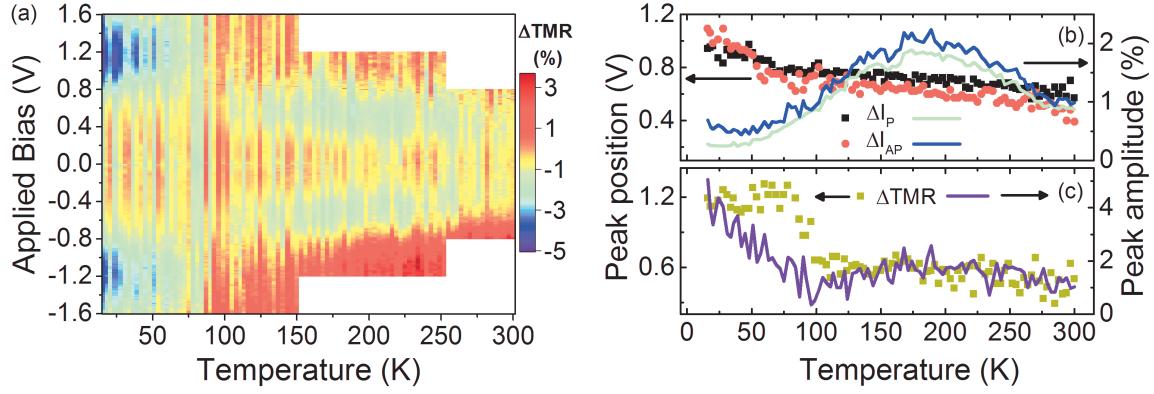


FIGURE AVII : **Impact de l'excitation avec de la lumière de 3.05 eV** : (a) Carte couleur 2D de la diminution relative de la TMR due à l'excitation optique dans l'espace de paramètre (V,T), (b) la position du maximum des pic et leur amplitude maximale extraite des  $\Delta I_\sigma(V, T)$  pour les configurations magnétiques parallèle et antiparallèle et (c) la position du maximum des pic et leur amplitude maximale extraite des données représentées dans le panneau (a).

avons mesuré des caractéristiques IV de 16 K à 300 K avec des pas de  $\Delta T = 3$  K pour les deux états magnétiques P et AP. De plus, à chaque température, nous avons mesuré des I-V pendant que nous excitions optiquement les jonctions avec de la lumière linéairement polarisée.

Afin de sonder l'impact de l'excitation optique sur les propriétés magnétorésistives de nos échantillons, nous avons utilisé l'approche de Rottländer *et al.* que nous avons introduit dans le chapitre précédent. Au lieu de calculer la différence relative entre deux I-V mesurées à des températures différentes, nous avons calculé la différence relative entre des I-V mesurées à la même température avec ou sans excitation optique avec la formule suivante :

$$\Delta I_\sigma(V, T) = \left( \frac{I_{ON}(V, T)}{I_{OFF}(V, T)} - 1 \right) \times 100 \quad (3)$$

ou  $\sigma$  représente l'état magnétique du dispositif (P ou AP) et ou  $I_{ON}$  et  $I_{OFF}$  sont les I-V mesurées avec et sans excitation optique respectivement. En outre, il est possible de calculer la TMR à chaque température et il est ainsi possible d'appliquer la même traitement à la TMR avec la formule suivante :

$$\Delta TMR(V, T) = \left( \frac{TMR_{ON}(V, T)}{TMR_{OFF}(V, T)} - 1 \right) \times 100 \quad (4)$$

ou  $TMR_{ON}$  et  $TMR_{OFF}$  sont les TMR du dispositif avec et sans excitation optique. De la même façon que l'impact de la température,  $\Delta I_\sigma(V, T)$  et  $\Delta TMR(V, T)$  sont caractérisés par des pic dont la position est interprétée comme la position énergétique d'états localisés optiquement actifs.

Nous adoptons la configuration géométrique représentée sur la Figure AVI (a), avec des photons se propageant avec un angle  $\alpha = 45^\circ$  par rapport à la surface de l'échantillon et un angle azimutal  $\phi = 0^\circ$  (lumière polarisée p).

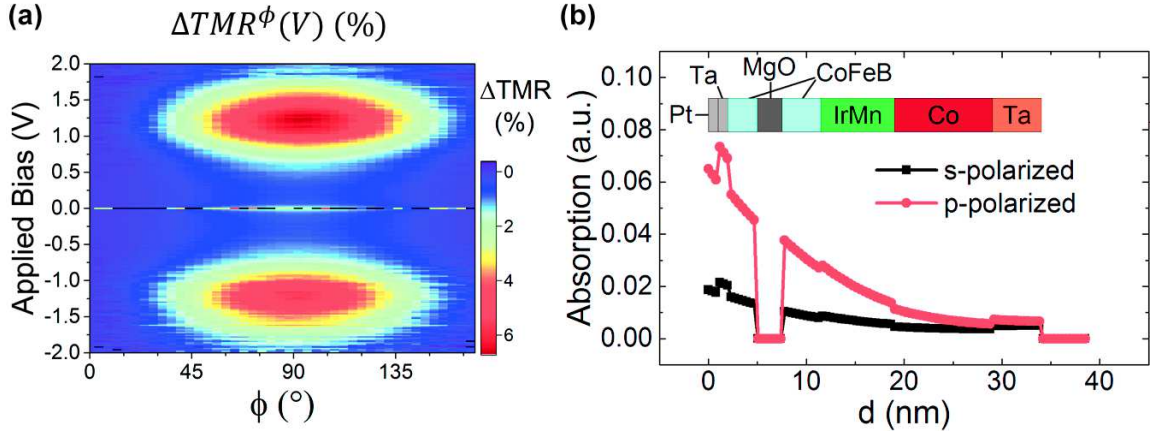


FIGURE AVIII : **Dépendance des propriétés magnétorésistive à l'angle de polarisation linéaire des photons** : (a) Carte couleur 2D de la dépendance de la TMR à l'angle de polarisation de la lumière dans l'espace de paramètre  $(\phi, T)$  et (b) Absorption locale de la lumière polarisée s et p en fonction de la position dans l'hétérostructure.

La Figure AVII trace le résultat obtenu en excitant une jonction avec des photons de 3.05 eV. Comme pour le cas de l'excitation thermique, le panneau (a) trace une carte couleur 2D de la diminution de la TMR due à l'excitation optique. La position du maximum des pics et leur amplitude maximale extraite des  $\Delta I_\sigma(V, T)$  pour (b) les configurations magnétiques parallèle et antiparallèle et (c) la TMR.

Nous notons immédiatement la ressemblance frappante entre ce jeu de données et les données présentés dans le chapitre précédent. Sans entrer dans les détails, nous constatons que les propriétés magnétorésistives sont modifiées aux mêmes énergies (1.2 eV et 0.7 eV) dans les mêmes gammes de température. Une petite différence réside dans l'amplitude de l'effet à forte température. Cette divergence est discutée plus en détail dans le manuscrit, elle est attribuée aux effets de chauffage induits par l'excitation de l'échantillon avec un laser continu.

**Dépendance des propriétés magnétorésistive à l'angle de polarisation linéaire des photons** : Dans un deuxième temps, nous nous sommes intéressés à l'impact de la polarisation de la lumière sur les propriétés magnétorésistives. Nous adoptons la même configuration géométrique que précédemment. Nous fixons la température et faisons varier  $\phi$  de 0° à 180° par pas de  $\Delta\phi = 2^\circ$  et mesurons des caractéristiques I-V pour les deux configurations magnétiques pour chaque angle de polarisation.

Nous adoptons la même stratégie que pour les mesures précédentes. Nous calculons la différence relative entre deux I-V mesurées pour des angles de polarisation des photons différents à l'aide de la formule suivante :

$$\Delta I_\sigma^\phi(V) = \left( \frac{I(\phi, V)}{I(\phi = 0^\circ, V)} - 1 \right) \times 100 \quad (5)$$

où  $\sigma$  représente l'état magnétique du dispositif (P ou AP). Encore une fois, il est possible

d'appliquer le même traitement à la TMR :

$$\Delta TMR^\phi(V) = \left( \frac{TMR(\phi, V)}{TMR(\phi = 0^\circ, V)} - 1 \right) \times 100 \quad (6)$$

La Figure AVIII (a) trace les résultats obtenus pour la TMR sous la forme d'une carte couleur 2D. Nous constatons que varier la polarisation de la lumière de p à s augmente la TMR. De plus cette augmentation est maximale autour de 1.2 eV. Ce résultat plutôt surprenant peu en fait être expliqué par un effet de chauffe triviale : Il est bien établi que la lumière p et s ne sont pas réfléchies, transmises et absorbées avec la même amplitude lorsqu'elles rencontrent une interfaces entre deux milieux qui ne possèdent pas le même indice de réfraction. Cette propriété est illustrée dans la figure Figure AVIII (b), si nous supposons que l'échantillon est chauffé par l'excitation laser, alors la température engendrée par de la lumière p sera plus importante que pour de la lumière polarisée s. Ce point est discuté plus en détail dans le manuscrit.

## Mesures électriques et XAS simultanées

Durant ma thèse, j'ai eu la chance de travailler sur un insert nouvellement installé sur la ligne DEIMOS au synchrotron SOLEIL. Cet insert, nommé V<sup>2</sup>TI pour *versatile variable temperature insert* (ou insert versatile à température variable), permet un accès électrique à des échantillons exposés à des rayons X et offre la possibilité d'effectuer des études dites *operando*. Le principe des études *operando* est d'offrir aux utilisateurs la possibilité d'appliquer un stimulus externe à l'échantillon tout en conservant les possibilités offertes par les rayons X.

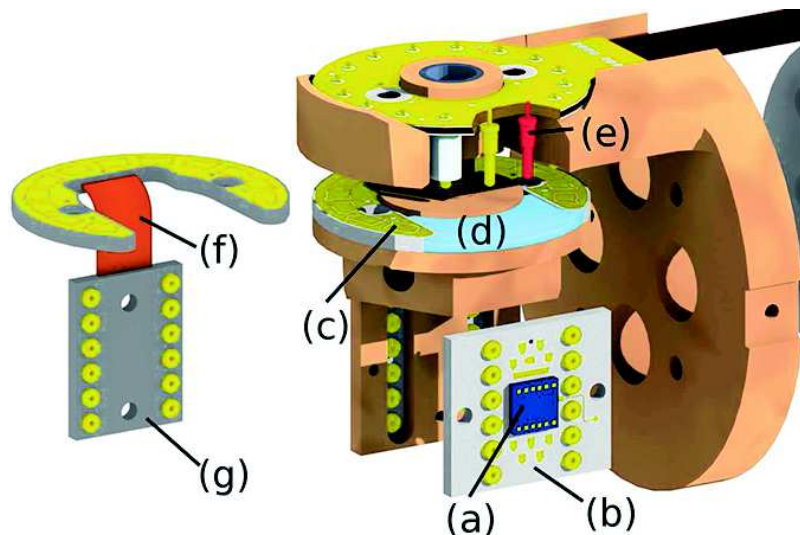


FIGURE AIX : **Insert versatile à température variable** : (a) Coupe en tranche du porte échantillon et (b) une vue d'ensemble. Les différents éléments sont discutés plus en détails dans le manuscrit.

La spectrométrie d'absorption des rayons X (XAS) mesure le coefficient d'absorption (ou une quantité proportionnelle) d'un échantillon en fonction de l'énergie de photon qui excite l'échantillon. Lorsque l'énergie des photons est égale à l'énergie nécessaire pour exciter un électron de cœur vers des états accessibles, l'absorption de l'échantillon augmente très fortement. Parce que ces processus d'absorption sont liés à des électrons de cœur, XAS est une technique chimiquement sélective, c'est-à-dire que l'énergie de photon peut être ajustée afin de ne réagir qu'avec un élément spécifique dans l'échantillon.

D'un autre côté, il est également bien établi que le transport tunnel polarisé en spin est extrêmement sensible à un sous-ensemble d'atomes aux interfaces. De ce fait, on peut considérer que le transport tunnel polarisé en spin possède une sélectivité atomique.

Mesurer les propriétés magnétorésistives d'un dispositif (sélectivité atomique) tout en sondant ses propriétés avec la technique XAS (sélectivité chimique) peut fournir des preuves expérimentales directes de comment exactement un sous ensemble d'atomes influence

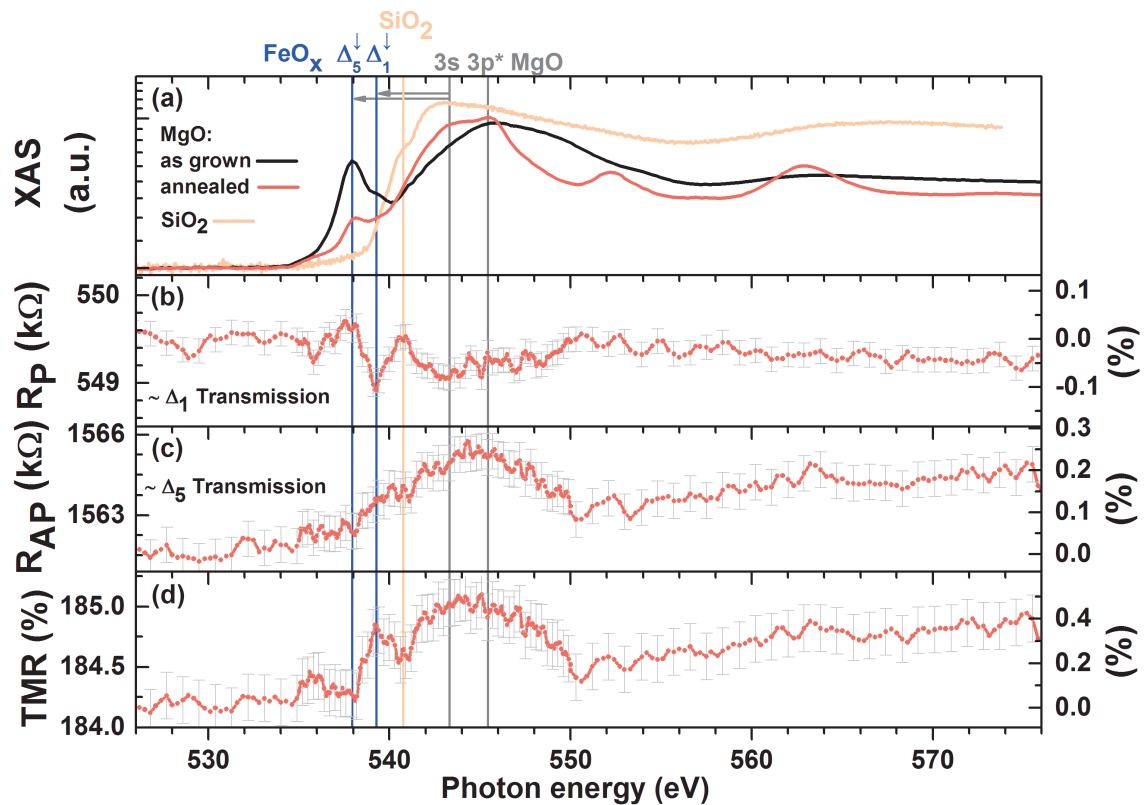


FIGURE AX : Mesures électriques et XAS simultanées : (a) Spectres XAS acquis avec une polarisation linéaire verticale des photons sur les jonctions en MgO recuit et non recuit et encapsulées avec du SiO<sub>2</sub>. On remarque une diminution de l'intensité des pics d'oxyde de Fe lors du recuit. Résistance des jonctions dans les états P (b), AP (c), et TMR (d) en fonction de l'énergie des photons, enregistrée à T = 20K et une faible tension de polarisation V = ±10 mV. L'échelle de droite représente l'écart par rapport à la ligne de base établie au préseuil..

les propriétés du dispositif.

Afin de pouvoir combiner la spectroscopie XAS à des mesures électriques sur des JTM, nous avons interfacé un banc de magnéto-transport mobile sur la ligne DEIMOS. A cause de la complexité de l'architecture de la ligne, nous n'avons pas pu intégrer le banc directement dans le programme de control de la ligne. AU lieu de ça, nous avons programmé la ligne synchrotron afin que celle-ci déclenche le banc mobile lorsque nécessaire. Pour corréler les mesures électriques avec les mesures XAS, nous avons synchronisé les horloges des deux expériences. Les mesures électriques est XAS ont été corrélé en interpolant chaque jeu de données à des points absolus en temps.

Afin de pouvoir combiner la spectroscopie XAS à des mesures électriques sur des JTM, nous avons interfacé un banc de magnéto-transport mobile sur la ligne DEIMOS. A cause de la complexité de l'architecture de la ligne, nous n'avons pas pu intégrer le banc directement dans le programme de control de la ligne. AU lieu de ça, nous avons programmé la ligne synchrotron afin que celle-ci déclenche le banc mobile lorsque nécessaire. Pour corréler les mesures électriques avec les mesures XAS, nous avons synchronisé les horloges des deux expériences. Les mesures électriques est XAS ont été corrélé en interpolant chaque jeu de données à des points absolus en temps.

Nos résultats principaux sont tracés dans la [Figure AX](#). Nous avons d'abord mesuré des spectres XAS de référence au seuil K de l'oxygène sur la structure CoFeB/MgO avant et après recuit (panneau (a)). Nous avons identifié les pics du préseuil à des états d'oxydes à l'interface. Ceux-ci sont atténués lorsque l'échantillon est recuit, ce phénomène a déjà été observé dans d'autres études.

Par la suite, simultanément aux mesures XAS, nous avons mesuré la résistance de notre jonction en fonction de l'énergie des photons d'excitation pour les deux configurations magnétiques. Nous notons deux modifications majeures : une au préseuil que nous attribuons à l'excitation d'oxydes aux interfaces et une au seuil de l'oxygène que nous attribuons à la modification de la couche de MgO.



# Bibliographie

- [R7] Ivar Giaever. Electron tunneling between two superconductors. *Phys. Rev. Lett.*, 5 (10) :464–466, 1960. ISSN 00319007. doi : 10.1103/PhysRevLett.5.464.
- [R8] M. N. Baibich, J. M. Broto, A. Fert, F. Nguyen Van Dau, F. Petroff, P. Eitenne, G. Creuzet, A. Friederich, and J. Chazelas. Giant magnetoresistance of (001)Fe/(001)Cr magnetic superlattices. *Phys. Rev. Lett.*, 61(21) :2472–2475, 1988. ISSN 00319007. doi : 10.1103/PhysRevLett.61.2472.
- [R9] G. Binasch, P. Grünberg, F. Saurenbach, and W. Zinn. Enhanced magnetoresistance in layered magnetic structures with antiferromagnetic interlayer exchange. *Phys. Rev. B*, 39(7) :4828–4830, mar 1989. ISSN 0163-1829. doi : 10.1103/PhysRevB.39.4828. URL <http://journals.aps.org/prb/abstract/10.1103/PhysRevB.39.4828>.
- [R10] J. S. Moodera, Lisa R. Kinder, Tunnel Junctions, Terrilyn M. Wong, and R. Meservey. Large Magnetoresistance at Room Temperature in Ferromagnetic Thin Film Tunnel Junctions. *Phys. Rev. B*, 74(16) :3273–3276, 1995.
- [R11] T. Miyazaki and N. Tezuka. Giant magnetic tunneling effect in Fe/Al<sub>2</sub>O<sub>3</sub>/Fe junction. *J. Magn. Magn. Mater.*, 139(3) :94–97, 1995. ISSN 03048853. doi : 10.1016/0304-8853(95)90001-2.
- [R12] Johan Akerman. Toward a Universal Memory. *Science (80-. )*, 308, 2005.
- [R13] Sining Mao, Yonghua Chen, Feng Liu, Xingfu Chen, Bin Xu, Puling Lu, Mohammed Patwari, Haiwen Xi, Clif Chang, Brad Miller, Dave Menard, Bharat Pant, Jay Loven, Kristin Duxstad, Shaoping Li, Zhengyong Zhang, Alan Johnston, Robert Lamberton, Mark Gubbins, Tom McLaughlin, Jason Gadbois, Juren Ding, Bill Cross, Song Xue, and Pat Ryan. Commercial TMR heads for hard disk drives : Characterization and extendibility at 300 Gbit/in<sup>2</sup>. *IEEE Trans. Magn.*, 42(2) :97–102, 2006. ISSN 00189464. doi : 10.1109/TMAG.2005.861788.
- [R14] Rie Matsumoto, Akio Fukushima, Kay Yakushiji, Satoshi Yakata, Taro Nagahama, Hitoshi Kubota, Toshikazu Katayama, Yoshishige Suzuki, Koji Ando, Shinji Yuasa, Benoit Georges, Vincent Cros, Julie Grollier, and Albert Fert. Spin-torque-induced switching and precession in fully epitaxial Fe/MgO/Fe magnetic tunnel junctions. *Phys. Rev. B - Condens. Matter Mater. Phys.*, 80(17) :1–8, 2009. ISSN 10980121. doi : 10.1103/PhysRevB.80.174405.
- [R15] Patryk Krzysteczko, Jana Münchenberger, Markus Schäfers, Günter Reiss, and Andy Thomas. The memristive magnetic tunnel junction as a nanoscopic synapse-neuron system. *Adv. Mater.*, 24(6) :762–6, feb 2012. ISSN 1521-4095. doi : 10.1002/adma.201103723. URL <http://www.ncbi.nlm.nih.gov/pubmed/22223304>.

## Bibliographie

- [R16] Guo-Xing Miao, Markus Münzenberg, and Jagadeesh S Moodera. Tunneling path toward spintronics. *Reports Prog. Phys.*, 74(3) :036501, mar 2011. ISSN 0034-4885. doi : 10.1088/0034-4885/74/3/036501. URL <http://stacks.iop.org/0034-4885/74/i=3/a=036501?key=crossref.7b39c4c133cc384896c0ba96a48023e6>.
- [R17] X. G. Zhang and W. H. Butler. Large magnetoresistance in bcc Co/MgO/Co and FeCo/MgO/FeCo tunnel junctions. *Phys. Rev. B - Condens. Matter Mater. Phys.*, 70(17) :1–4, 2004. ISSN 01631829. doi : 10.1103/PhysRevB.70.172407.
- [R18] S. Ikeda, J. Hayakawa, Y. Ashizawa, Y. M. Lee, K. Miura, H. Hasegawa, M. Tsunoda, F. Matsukura, and H. Ohno. Tunnel magnetoresistance of 604% at 300 K by suppression of Ta diffusion in CoFeB/MgO/CoFeB pseudo-spin-valves annealed at high temperature. *Appl. Phys. Lett.*, 93(8) :082508, 2008. ISSN 00036951. doi : 10.1063/1.2976435. URL <http://scitation.aip.org/content/aip/journal/apl/93/8/10.1063/1.2976435>.
- [R44] W. Butler, X.-G. Zhang, T. Schulthess, and J. MacLaren. Spin-dependent tunneling conductance of Fe/MgO/Fe sandwiches. *Phys. Rev. B*, 63(5) :054416, jan 2001. ISSN 0163-1829. doi : 10.1103/PhysRevB.63.054416. URL <http://link.aps.org/doi/10.1103/PhysRevB.63.054416>.

# **Part I**

## **Theoretical and Experimental background**



# General Introduction

Quantum tunnelling refers to a quantum mechanical process in which a particle can overcome a potential step that it could not surmount in the classical framework. It is one of the most basic and spectacular (because counterintuitive) effect described by quantum mechanics, and is often used as a canonical example in many introductory books to quantum physics. Quantum tunnelling occurs in many natural phenomenon and is used in many experimental techniques, the best known example being the scanning tunnelling microscope.

In this thesis, we focus on the tunnelling effect in a very specific class of devices, namely tunnel junctions. A tunnel junction is a trilayer composed of two metallic (M) electrodes separated by a thin insulating (I) layer, also denoted MIM or M/I/M. In these devices, tunnelling refers to the transmission of electrons from one electrode to the other through the insulating layer and is sometimes called solid state tunneling. The electrical properties of MIMs and the first theoretical models were first investigated more than 50 years ago. The field of solid state tunneling progressed quite slowly, except for two periods in time during which it attracted a lot of attention and developed very rapidly.

The first period corresponds to the emergence of spin-dependent tunneling (SDT). SDT is similar to tunneling in MIM structures, except that the metallic electrodes are replaced by ferromagnets (FM). The development of SDT was triggered by the pioneering experiments of [Giaever](#)<sup>7</sup>, who measured the electrical properties of metal-insulator-superconductor trilayers. He showed for the first time that the tunnel current was proportional to the density of states (DOS) of one of the electrodes, in this particular case to the quasi-particle DOS of the superconducting layer. The metallic layer was then replaced by a ferromagnetic (FM) layer, and the peculiar DOS of the superconductor was used as a spin detector in order to measure the spin polarization of the FM layer. Eventually, in 1975, [Julliere](#)<sup>1</sup> replaced the superconducting layer by another ferromagnetic layer and showed that the resistance of the device was dependent on the relative alignment between the electrodes' magnetization. He measured for the first time what is known today as the tunnel magnetoresistance (TMR) effect in FM/I/FM trilayers, also known as a magnetic tunnel junctions (MTJs). At the time, SDT didn't attract the attention of the scientific community mainly due to the experimental difficulties to fabricate thin film heterostructures, the need for cryogenic temperature and the relatively small amplitude of the effect.

The second experimental breakthrough that definitely triggered the rapid development of SDT was the discovery of giant magnetoresistance (GMR) in 1988<sup>8,9</sup>. The GMR effect occurs in ferromagnetic-metallic-ferromagnetic trilayers and refers to the resistance change depending on whether the magnetization of the electrodes point toward the same direction or in opposite directions. As we discussed previously, magnetoresistive effects are not limited to GMR devices only, but occur in magnetic tunnel junctions too. Because both TMR and GMR have many potential applications, tremendous efforts were made in order to improve the devices performance. After the first experiments done by Jullière

in 1975, the next realization of magnetic tunnel junctions with sizable TMR at room temperature was developed in 1995<sup>10,11</sup>. GMR and TMR device are already used in various industrial applications<sup>12-14</sup>, but they are also intensively investigated for their potential application for new generation devices with advanced functionalities<sup>15</sup>.

The detailed understanding of SDT was first limited by theoretical difficulties in modelling the amorphous barrier. Progress in the fabrication of crystals and refinements in experimental techniques allowed the growth of epitaxial heterostructures, allowing to confront theoretical models and rapidly improved our understanding of SDT. Theoretical models dress a clear picture of spin dependent tunnelling in epitaxial systems, and the relatively large values of TMR obtained in crystalline Fe/MgO/Fe MTJs appear to confirm these models<sup>16</sup>.

However, several discrepancies between theory and experiments are still unexplained. For examples, first principles calculations predict TMR values as large as 30 000 %<sup>17</sup> while the maximum experimental value reaches 600 % (1100 %) <sup>18</sup> at room (low) temperature. Moreover, the temperature and bias dependence of magnetotransport properties are also not well understood. Finally, one of the most surprising result concerns the tunnel barrier height reported in MgO based MTJs. While the optical gap of MgO suggest a 3.9 eV barrier height, values reported in the literature range from 0.4 to 1.1 eV, 3 to 10 times smaller than expected.

Naturally, these discrepancies can be explained by the fact that first principles calculations consider perfect crystals while realistic devices contain different kind of defects. However, the importance of defects on devices performance of oxide based MTJs is not acknowledged as much as it is in the field of semiconductors, and the impact of structural defects in MgO on tunnelling is only emerging in this otherwise widely studied canonical system.

This thesis focuses on a very specific kind of such defects, namely oxygen vacancies present within oxides. In particular, our work aims to characterize the effect of such defects on spin dependent tunnelling in MgO based magnetic tunnel junctions. The study of oxygen vacancies is motivated by the fact that this type of structural defects is difficult to avoid, but also because they may result in advanced device functionalities<sup>2-6</sup>. For example, the presence of localized states induced by oxygen vacancies may be responsible of the low barrier height observed experimentally<sup>19</sup>. However, applications that rely on spin transfer torque<sup>20</sup> (STT) require high current densities that can only be accommodated in a MgO MTJ thanks to this low barrier height. More than just an academic matter, resolving this discrepancy, by correlating the nature of the defects to their impact on the devices' properties, might have a strong impact in applications based on SST.

The objectives of this work can be divided in two points: we first aim to characterize the impact of localized states induced by oxygen vacancies on the properties of CoFeB/MgO/CoFeB magnetic tunnel junctions and secondly, we want to use optical excitation as an additional degree of freedom of the system in order to probe the presence and impact of these defects. Additionally, driving the devices' properties by exploiting the optical activity of localized states could also be used as additional device functionalities, in photonics applications for example.

The first part of this thesis introduces the theoretical and experimental background of

this work and is divided in three chapters. [Chapter 1](#) first introduces phenomenological models in order to explain the giant and tunnel magnetoresistance effects. The second part details the first principle calculations of the magnetic and electric properties of crystalline Fe/MgO/Fe heterostructures and discuss the symmetry filtering effect at the origin of large TMR values measured in this system. [Chapter 2](#) dresses a detailed overview of the intrinsic or extrinsic effect that limit the performance of realistic MgO based MTJs. We first focus on interfaces, and investigate how interfacial resonant states, interface contamination and interface disorder impact the tunnel current. We then discuss how temperature and applied bias impact the electrical properties of the devices. The last part of the chapter is dedicated to the impact of localized states induced by defects or impurities in the insulating barrier. The last section is dedicated to a discussion of the optical activity of localized states induced by oxygen vacancies in MgO. [Chapter 3](#) describes the samples' growth and the devices fabrication by UV photolithography. The magnetotransport bench used to characterize the electrical properties of our devices is presented. Finally, the experimental setup of the synchrotron facility used in the last chapter of this thesis is briefly introduced.

The second part of the thesis is dedicated to experimental results and is divided in three chapters. [Chapter 4](#) presents our bias and temperature dependent magnetotransport measurements. We first discuss the photoluminescence spectra of our rf-sputtered MgO thin films. We detail the experimental technique used in order to extract the effective barrier height. Finally, we describe how we attempted to identify the impact of specific localized states on the tunnel current by relating photoluminescence spectra and magnetotransport measurements. In [Chapter 5](#), we review our attempt to use the optical degree of freedom in order to excite a specific population of localized states from its ground to its excited state. [Chapter 6](#) discuss how we combined x-ray absorption spectroscopy and magnetotransport measurements in order to probe the devices' properties in real operating conditions.



# Introduction to Spintronic

In this chapter, we'll introduce several concepts to understand the interplay between magnetism and electrical conductivity in solid state devices.

I'll first start with a brief introduction to giant magnetoresistance (GMR) using classical and phenomenological notions initially developed to explain electrical transport in ferromagnetic materials.

In the second section, the discussion will focus on the mechanism of tunneling current in amorphous tunnel junctions. We'll first introduce historical concepts to tunneling current in non magnetic tunnel junctions and discuss the validity and limitation of different approaches. Secondly we'll focus on spin dependent tunneling in magnetic tunnel junctions. As a follow-up to the discussion on GMR, the phenomenological Jullière model of tunneling will be discussed to explain the tunneling magnetoresistance (TMR) effect. In order to have more insight into spin dependent tunneling, some key experimental results as well as more refined models will be examined.

Finally in the third section, we'll consider fully epitaxial magnetic tunnel junctions for which more realistic theoretical models can be developed. We'll talk in more details about *ab-initio* calculations obtained on the canonical Fe/MgO/Fe (001) system within the quantum mechanical framework.

This chapter will mainly focus on *perfect* systems, i.e. only intrinsic properties of layers, and their coupling, will be considered. [Chapter 2](#) will be dedicated to device imperfections and extrinsic effects.

## 1.1 Phenomenological theory of giant magnetoresistance

### 1.1.1 Electrical conductivity of rare earth elements

In the classical theory of Lorentz, the conductivity of metals is defined as<sup>21</sup>:

$$\sigma = \frac{ne^2}{\mu}\tau \quad (1.1)$$

where  $n$  is the number of electrons per unit volume,  $\mu$  the effective mass of electrons,  $\tau$  the relaxation time (time before collision) and  $e$  the charge of one electron. This formula is still valid in quantum mechanics provided that the electron's effective mass and the relaxation time are calculated within the quantum mechanical framework. In particular, the relaxation

time will depend on (i) the displacement of atoms due to thermal motion (interaction with lattice vibrations) and (ii) the density of available states at the Fermi level (inter band scattering processes occur when empty states of unfilled bands are available).

All electrons belonging to shells that are not fully occupied and are at or near the Fermi energy will participate in the electric current and in transition metals the  $s$  as well as  $d$  electrons will be responsible for electrical conductivity. However, the effective mass and the relaxation time will be different for both states and the electrical conductivity of transition metals can be written:

$$\sigma = \frac{n_s e^2}{\mu_s} \tau_s + \frac{n_d e^2}{\mu_d} \tau_d \quad (1.2)$$

Experimental results on noble and alkaline earths metals established that the effective mass of  $s$  electrons is close to the mass of free electrons  $\mu_s = \mu_0$ . Owing to the fact that  $s$  electrons are delocalized, the interaction of electrons with lattice vibrations will be less likely and the overlap of orbitals between neighboring atoms higher. On the other hand,  $d$  electrons are more localized resulting in higher effective mass, higher scattering probability by atoms and a poor overlap with neighboring  $d$  orbitals. The contribution of  $s$  electrons to the conductivity is thus larger than the contribution from  $d$  electrons ( $\tau_s > \tau_d$ ).

Despite the fact that transition metals have more states at the Fermi level compared to noble metals ( $s$  conduction as well as  $d$  conduction), their measured electrical resistivity is higher than that of noble metals or alkaline earths elements. This apparent contradiction was first explained by Mott (1936)<sup>22</sup>, who took into account the interaction of electrons with the crystal lattice vibrations (phonons), and more particularly emphasized the importance of the  $s \rightarrow d$  scattering process.

In a very simple form, the scattering probability from an initial state 1 to a final state 2 can be written as:

$$\int \Psi_2^* \Delta V \Psi_1 d\tau \quad (1.3)$$

where  $\Delta V$  is the perturbing potential due to lattice vibration. If we suppose the transition matrix elements to be the same for  $s \rightarrow s$  and  $s \rightarrow d$  scattering processes, the transition probability will be directly proportional to available density of  $s$  ( $N_s$ ) and  $d$  ( $N_d$ ) states at the Fermi level. In transition metals,  $N_d$  being much greater than  $N_s$  (see Figure 1.1), the  $s \rightarrow d$  transition will be more important. As a consequence,  $\tau_s$  will be much smaller in transition metals than in noble metals in which the  $d$  band is full and only  $s \rightarrow s$  transitions are possible. Finally, we can see from equation Equation 1.2 that the decrease of  $\tau_s$ , in addition to the low conductivity of  $d$  electrons, results in a decrease of electrical conductivity in transition metals.

At that time, Mott was already aware that  $d$  electrons were responsible of ferromagnetism in transition elements, and that there was a direct connection between magnetic properties and electrical conductivity.

In the following, we'll use the same reasoning to consider the electrical properties of ferromagnetic materials, and how their integration within thin film heterostructures led to the discovery of giant magnetoresistance.

### 1.1.2 Electrical conductivity of ferromagnets

**Origins of ferromagnetism:** In isolated atoms, magnetism is essentially due to electrons from unfilled shells. The magnetic moment arises from (i) the motion of negatively charged electrons through the so called orbital magnetic moment and (ii) the electrons' intrinsic magnetic moment, the spin. The magnetic state of isolated atoms can be determined by taking into account the Pauli exclusion principle, the Coulomb interaction and the interaction between electrons' intrinsic spin and their orbital motion (spin-orbit coupling). A set of rules, called *Hund's rules*, have been established to determine the magnetic ground state.

When single atoms are brought together to form solids, the interactions between many electrons result in a variety of possible stabilized magnetic states. Since it depends on many-body interactions, magnetism in solids will depend on various parameters (constituent elements, crystal structure, bonds distance and angle, doping and so on...) resulting in very complex but also very rich physics.

A ferromagnet is a solid characterized by a spontaneous magnetic moment. The spontaneous magnetization is the macroscopic manifestation of magnetic order that originates from long range electron-electron interactions, called *exchange* processes. Among exchange interactions, we can mention the *direct* exchange that describes the direct coulomb interaction between neighboring ions. The *super* exchange interaction happens in material where the magnetic ions (M) are separated by nonmagnetic ions (NM). The interaction between magnetic ions is mediated by electrons in their common nonmagnetic neighbors<sup>23</sup>. The *indirect* exchange is characteristic of rare earth metals with partially filled f-shells, where the magnetic ions are coupled through their interaction with conduction electrons. The *double* exchange interaction arises in materials where magnetic ions occur in mixed valence states (for example  $Mn^{3+}$  and  $Mn^{4+}$  in Lanthanum strontium manganite or LSMO). It involves the simultaneous exchange of two electrons in a  $M^n - NM^p - M^{n-1}$  chain<sup>24</sup>. This is not an exhaustive list of exchange interactions. Moreover, in complex systems the stabilized magnetic order can result from the competition between several such interactions.

In the case of transition metals such as Fe, Ni or Co which will be of interest in this thesis, the microscopic process underlying the magnetic order is called *itinerant* magnetism and results from the strong interaction of itinerant 3d-shell electrons<sup>25</sup>.

**Electrical conductivity:** A characteristic property of ferromagnets is an imbalance in the density of states ( $D(E)$ ) of spin up ( $\uparrow$ ) and spin down ( $\downarrow$ ) electrons at the Fermi level. Figure 1.1 represent the spin resolved density of states of a ferromagnet. As it was discussed in the previous section, in transition metals the electrical conductivity depends on the density of states at the fermi level. Since  $D_{\uparrow}(E_F) \neq D_{\downarrow}(E_F)$  the conductivity of spin up and down electrons will not be the same in a ferromagnet, and usually (but not necessarily)  $\sigma_{\uparrow} > \sigma_{\downarrow}$ . As a result, a ferromagnet can be considered as two materials possessing different electrical conductivity occupying the same coordinate in space. A simple *two current* model with two resistances in parallel can be applied to describe electrical conductivity as shown in Figure 1.1. This model supposes that the spin of electrons is conserved.

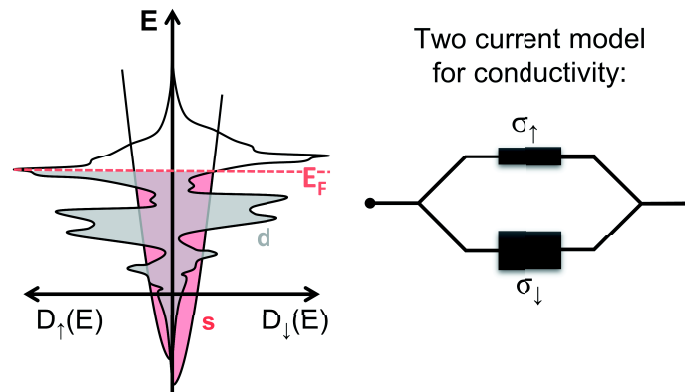


Figure 1.1: **Spin resolved density of states of 3d Ferromagnets:** In a ferromagnet, the net magnetization proceeds from an imbalance in the density of states (DOS) of spin up ( $\uparrow$ ) and spin down ( $\downarrow$ ) electrons at the Fermi level ( $E_F$ ). Here, arbitrary  $s$  (red) as well as  $d$  (grey) states are represented. Electrons with spins parallel to the local magnetization are called the *majority* spin population while electrons with spins antiparallel are called *minority* spin population. The conductivity can be described by a simple two current model.

This assumption is justified for low temperatures. As the temperature increases, scattering processes like electron-electron, electron-phonon and electron-magnon interactions can reverse the spin of electrons (*spin-flip* events).

### 1.1.3 Giant magnetoresistance

Progress in the fabrication of crystals and refinements in experimental techniques allowed the growth of thin films heterostructures at the nanoscale, making it possible to combine material with different properties within the same device. The archetypal Spintronic device is composed of two ferromagnetic electrodes (FM) separated by a metallic (M) spacer, as represented in Figure 1.2. If we assume that the spin is conserved during the electrical transport, it is possible to explain transport properties in FM/M/FM structures using the arguments developed in Sections 1.1.1 and 1.1.2.

Since electrical transport is a non-local process, when current flows in plane (CIP), it is possible for electrons to move from one electrode to the other through the metallic film. For electrodes with an in-plane easy axis magnetization, two cases can be distinguished: (i) when both electrodes have a parallel (P) magnetization, the spin referential between electrodes is unchanged and majority (minority) electrons in the first electrode will remain majority (minority) in the collecting electrode. The electrical current can be divided in two channels with relatively low and high resistivity for spins up and down electrons respectively. (ii) When the two electrodes have an antiparallel (AP) magnetic configuration, the spin referential is reversed and majority (minority) electrons in the emitting electrode become minority (majority) in the collecting electrode and their resistivity in the collecting electrode decreases (increases). Both P and AP magnetic states are represented in Fig-

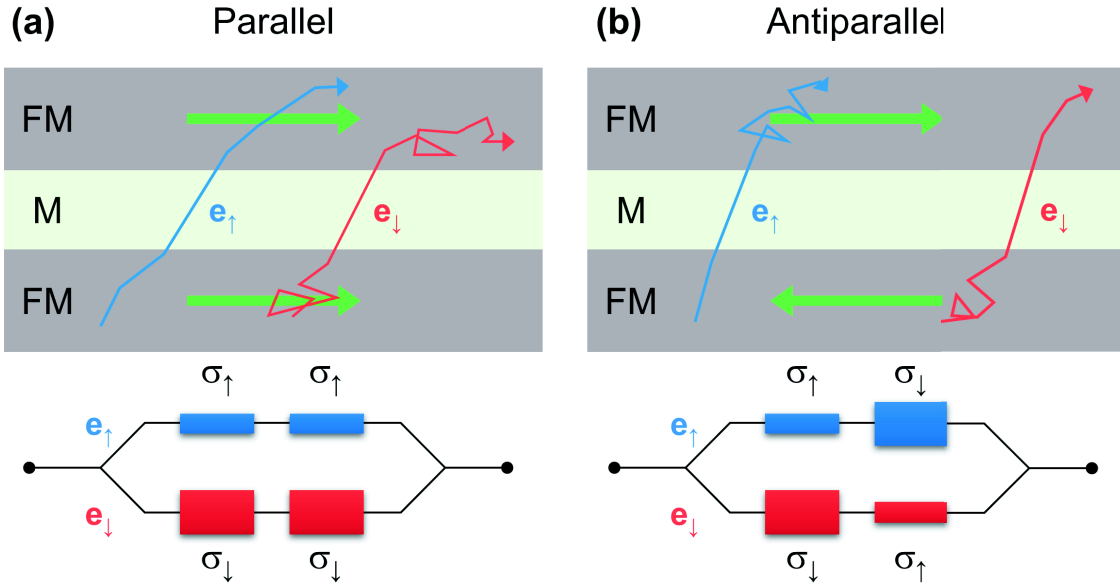


Figure 1.2: **Magnetoresistive properties of a GMR device:** The archetypal spintronic device is composed of two ferromagnetic electrodes (FM) separated by a metallic (M) spacer. The magnetization (green arrows) between electrodes can be (a) parallel or (b) antiparallel. In (a) the spin referential is the same within both electrodes, a majority electron will encounter less scattering processes compared to a minority electron and will contribute more to conduction. In (b) the spin referential is inverted. Majority electrons with good conductivity in the initial electrode will become minority electron in the second one, and their electrical conductivity will be reduced. The two current model is schematized for both cases. Finally, we can see that the resistance in the parallel state will be smaller than in the antiparallel magnetic state.

ure 1.2a-b as well as their two current models. A simple calculus of the output resistance for both cases shows that the P state has lower resistivity than the AP state or  $R_{AP} > R_P$ .

Finally, another fundamental interaction to take into consideration in FM/M/FM trilayers is the coupling of the magnetic electrodes through exchange coupling<sup>26,27</sup>. The amplitude and strength of the coupling depends on the spacer thickness. It is possible to tune the spacer thickness in order to obtain antiparallel alignment in absence of external magnetic field ( $H = 0$  Oe), resulting in a device with a high resistance state ( $R_{AP}$ ). One can then apply a magnetic field to align both magnetic layers and obtain a low resistance state ( $R_P$ ).

The giant magnetoresistance (GMR) is defined as the relative resistance difference between the parallel and antiparallel magnetic states:

$$GMR = \frac{R_{AP} - R_P}{R_P} \quad (1.4)$$

In 2007, A. Fert and<sup>8</sup> and P. Grünberg<sup>9</sup> conjointly received the Nobel prize for the dis-

covery of GMR. This discovery quickly resulted in industrial applications and triggered intensive research in the field of spintronic.

## 1.2 Tunneling magnetoresistance in amorphous magnetic tunnel junctions

The anatomy of a magnetic tunnel junction (MTJ) is similar to a GMR device except that the metallic spacer layer is replaced by a dielectric material. In the case of MTJs, the current will be perpendicular to plane (CPP) and the transfer of electrons between electrodes is realized through the *tunneling* effect.

We'll first consider tunneling in junctions with nonmagnetic metal electrodes. An early model was developed by Bardeen to explain experimental measurements involving tunneling from a metallic layer to a superconductor. We'll then give a small introduction to spin dependent tunneling (SDT) and discuss a simple phenomenological model to understand the tunneling magnetoresistance in MTJs. Finally, some key experimental results and theoretical refinements will be addressed in order to get a better understanding of solid state spin-dependent tunneling.

### 1.2.1 Tunneling basics

#### 1.2.1.1 Quantum tunneling

The tunneling effect refers to a quantum mechanical process where a particle can overcome a potential step that it could not overcome in the classical framework. The simple case of a plane wave (free electron) encountering a rectangular potential is schematized in Figure 1.3. In quantum mechanics, electrons are described by a wave-function that accounts for their wave-particle duality. When the wave-function encounters a potential step higher than its kinetic energy, it'll not be fully reflected as in classical mechanics. Instead, the probability density of the particle position decreases exponentially within the

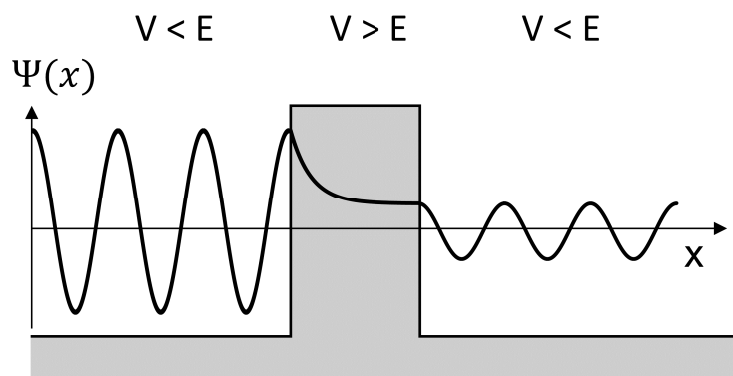


Figure 1.3: **Tunneling effect:** Simple case of a free electron encountering a rectangular potential.

potential step. For thin barriers, the probability for the electrons to *be* on the other side is non-zero, resulting in a reduced amplitude of the wave function for tunneling particles. The wave-function of the electron satisfies the Schrödinger equation and it is possible to calculate reflection and transmission coefficients by using the continuity conditions of the wave-function and its derivative (or *matching* of the wave-functions)<sup>28</sup>.

The simplest experimental realization of the model represented in Figure 1.3 is the tunneling in a metal-insulator-metal trilayer. The theoretical treatment of tunneling in a M/I/M will be briefly discussed in the next paragraph.

### 1.2.1.2 Bardeen's approach of solid state tunneling

Bardeen<sup>29</sup> considered the tunneling between two metallic (M) layers separated by an insulating layer (I). Instead of solving the equations for the whole system, he makes a clever use of the perturbation theory. A schematic of Bardeen approach is represented in Figure 1.4. Panel (a) represents the potential landscape of the metallic tunnel junction when a bias  $V$  is applied,  $\phi$  is the barrier height electrons have to overcome to tunnel through the dielectric. Panel (b) and (c) show how Bardeen separates the tunneling in a M/I/M structure into two distinct problems with well-known Hamiltonians and solutions. The electronic states of the isolated subsystems are obtained by solving the stationary Schrödinger equation. The wave functions on the left (L) and right (R) electrodes satisfy:

$$\left( -\frac{2\hbar^2}{2m_e} \nabla^2 + V_{L,R} \right) \psi_{\mu}^{L,R} = E_{\mu}^{L,R} \psi_{\mu}^{L,R} \quad (1.5)$$

where  $V_i$  is the potential in the electrodes, the  $\psi_{\mu}^i$  are the stationary solutions and  $E_{\mu}^i$  the eigenvalues ( $i = L, R$ ). Bardeen's model is based on the assumption that the tunneling probability between both electrodes is small, such that the coupling between electrodes can be considered as a small perturbation. The tunneling rate is then determined by the overlap of evanescent wave-functions within the insulating barrier (dotted line across panel (b) and (c)). Using the time dependent perturbation theory, the probability for an electron in a state  $\psi_{\mu}^L$  with energy  $E_{\mu}^L$  in the left electrode to tunnel into a state  $\psi_{\nu}^R$  with energy  $E_{\nu}^R$  in the right electrode is given by the Fermi golden rule (detailed calculation in Lounis<sup>30</sup>):

$$w_{\mu\nu} = \frac{2\pi}{\hbar} |M_{\mu\nu}|^2 \delta(E_{\mu}^L - E_{\nu}^R) \quad (1.6)$$

where the delta function ensures that an electron can move only to a state with the same energy level only and  $M_{\mu\nu}$  is the tunneling matrix element.  $w_{\mu\nu}$  expresses the tunneling rate of a single electron state  $\mu$  to a single state  $\nu$ . In order to extract an expression of the tunneling current, we have to sum over all the  $\mu$  and  $\nu$  states. At finite temperature, occupied states in both electrode are described by the Fermi-Dirac distribution  $f(E - E_F)$ , while unoccupied states by  $1 - f(E - E_F)$  and the tunneling from the left to the right electrode  $P_{L \rightarrow R}$  is written:

$$P_{L \rightarrow R} = \frac{4\pi}{\hbar} \sum_{\mu\nu} f(E_{\mu}^L - E_F^L) [1 - f(E_{\nu}^R - E_F^R)] |M_{\mu\nu}|^2 \delta(E_{\nu}^R - E_{\mu}^L) \quad (1.7)$$

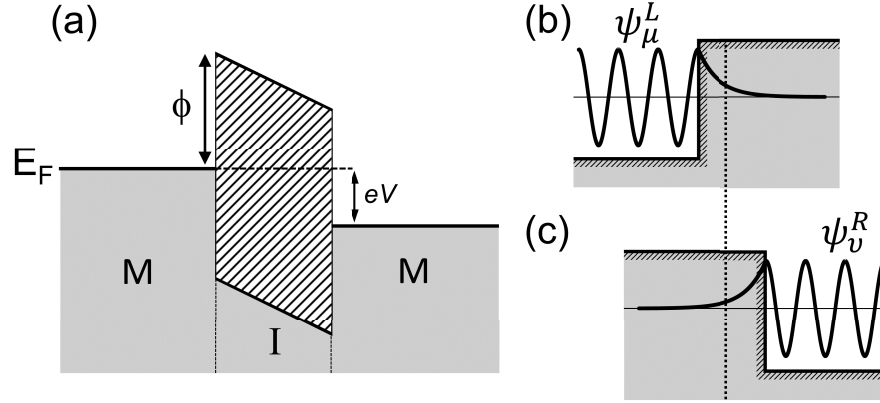


Figure 1.4: **Bardeen's approach of tunneling:** (a) Bardeen separates the tunneling in metal-insulator-metal device in two problems with well-known solutions, (b) and (c). The tunneling rate between electrodes is proportional to the overlap of evanescent wave-functions within the potential step (dotted line between panel (b) and (c)). For low tunneling probabilities, the time dependent perturbation theory can be used to treat the problem. The figure is adapted from [Julian Chen \(1993\)](#)<sup>31</sup>.

A similar expression can be derived for  $P_{R \rightarrow L}$ . The current can be obtained by multiplying these transmission rates by the charge  $e$  of one electron. The summation over discrete states can be replaced by an integral over the density of states in both electrodes. Finally, at finite bias we can write:

$$I_{L \rightarrow R}(V) = \frac{4\pi e}{\hbar} \int \rho^L(E) \rho^R(E + eV) |M(E, V)|^2 f(E) [1 - f(E + eV)] dE \quad (1.8)$$

where  $\rho^i$  is the density of states of electrode  $i = 1, 2$ . The net tunneling current is given by  $I_{L \rightarrow R} - I_{R \rightarrow L}$ .

Originally, Bardeen derived these equations to discuss experimental results obtained by Giaever<sup>7</sup> in metal-insulator-superconductor trilayers. In his experiment, Giaever was able to switch the behavior of a Pb layer from superconducting to metallic by applying an external magnetic field. He then measured  $I$ - $V$  characteristic in the M/I/M and M/I/S device states and evidenced a strong decrease in the tunneling current at low bias when the Pb layer was superconducting. Giaever interpreted his results as a direct dependence of the tunneling current to the density of states of the superconducting layer, i.e. he supposed that the tunneling matrix element  $|M_{\mu\nu}|^2$  in Equation (1.6) was constant. Since the quasi-particle DOS of superconductors is characterized by a gap  $2\Delta$  at the Fermi energy (see Figure 1.5a), there are no available states for metallic electrons to tunnel and the current is reduced within  $V = \pm\Delta$ . These results are important in that they demonstrated the ability of tunneling to measure many body effects. In other words, Bardeen confirmed that the assumption made by Giaever resulted in an expression of tunneling current dependent on the DOS in each electrode.

As we will see thereafter, many models are based on Bardeen's approach. In order to compare models with experimental  $I$ - $V$  characteristic (or its derivative), assumptions have

to be made to evaluate Equation (1.8). We'll see that careful attention has to be made when approximating the matrix element  $|M|^2$  for Equation (1.8) to account for many body effects as measured by Giaever.

As a quick example, we can mention Harrison's<sup>32</sup> use of Equation (1.8). He evaluated the matrix elements in the independent-particle framework and found that  $|M|^2$  was inversely proportional to the density of states of the electrodes. As a result the DOS factors in Equation (1.8) are canceled out, and the dependence of the tunneling current to the electrodes' DOS is suspiciously absent in his formula. There is a key difference between both approaches. Bardeen supposes that the tunneling rate is proportional to the overlap between wave functions within the potential step. This approximation still accounts for the *character* of the tunneling wave-functions. For instance, because *d* electrons are more localized than *s* electrons, their overlap in the insulating barrier will be smaller, resulting in a lower tunneling rate. On the other hand, Harrison's approach, as well as other models that will be discussed in the following, totally disregard the fact that the electrical conductivity in electrodes arises from the contribution of electrons belonging to various bands.

### 1.2.1.3 Simmons' formula of tunneling current

Simmons<sup>33</sup> used the WKB approximation to calculate the transmission matrix element  $|M|^2$  and derived a formula of conductance in metal-insulator-metal for barriers of arbitrary shape.

The WKB approximation is a quasi-classical approximation of the tunnel effect that accounts for slowly varying potentials or reciprocally, when the de Broglie wavelength of the tunneling particle is short compared to the distance over which the potential is changing. He calculated the tunneling current within the free electron framework in the electrodes and supposed  $T = 0 K$  such that the Fermi-Dirac distribution is replaced by a step function. He applied his results to the case of an *ideal* rectangular potential and obtained the following expression of the tunneling current<sup>33</sup>:

$$J(V) = \frac{J_0}{d^2} \left( \bar{\phi} - \frac{eV}{2} \right) \exp \left[ -Ad \sqrt{\bar{\phi} - \frac{eV}{2}} \right] - \frac{J_0}{d^2} \left( \bar{\phi} + \frac{eV}{2} \right) \exp \left[ -Ad \sqrt{\bar{\phi} + \frac{eV}{2}} \right] \quad (1.9)$$

where  $A = \pi \sqrt{2m_e^*/\hbar}$  and  $J = e/2\pi\hbar$  are constants,  $m_e^*$  is the electron effective mass,  $d$  the barrier thickness and  $\bar{\phi}$  the average barrier height. He then considered the tunneling current for different applied bias ranges and obtained a formula of  $J(V)$  that successfully accounts for *general* features of experimental results; At low bias, Equation (1.9) results in a linear dependence of  $J$  to  $V$  while in the intermediate bias range a  $J \propto V + V^3$  dependence is found which is a *signature* of tunneling transport. Finally a strongly nonlinear dependence is obtained at high bias. Simmons developed his model for identical electrodes and a symmetric barrier. Brinkman<sup>34</sup> further improved the model to account for trilayers with different electrodes by introducing an additional parameter,  $\Delta\phi$ , the barrier asymmetry between both metal-insulator interfaces.

Simmons' and Brinkman's approaches suffer from the same shortcomings as the aforementioned Harrison's model, i.e. the expression of the tunneling current is independent of

the electrodes DOS. Again, this is due to an inadequate use of the independent electron and semi-classical WKB approximations. Moreover these formulas are derived for ideal barriers for which inelastic processes are not considered. In spite of the many deficiencies of these models, they are still widely used to extract average barrier height and thickness. In Section 4.2.2, we'll discuss another approach to determine the effective barrier height experimentally that is free of the aforementioned deficiencies.

## 1.2.2 Phenomenological theory of tunneling magnetoresistance

### 1.2.2.1 Spin-dependent tunneling

Meservey *et al.*<sup>36</sup> quickly understood the importance of Giaever's<sup>7</sup> work. They used the peculiar density of states of superconducting electrodes as spin detectors to measure the spin polarization (SP) of ferromagnetic layers in FM/I/S heterostructures, where  $S = Al$ ,  $I = Al_2O_3$  and  $FM = Co, Ni, Fe...$  Figure 1.5 summarizes the idea behind their experiment.

Panel (a) represents the quasi-particle density of states of the superconducting  $Al$  layer.

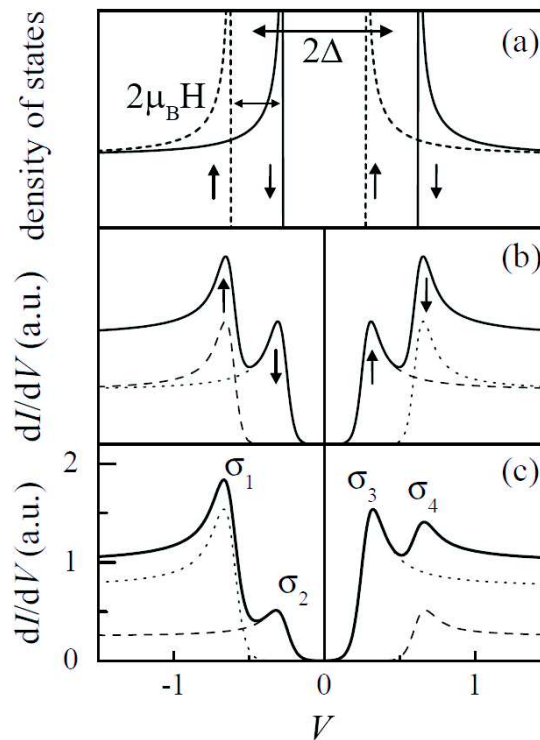


Figure 1.5: **Spin-dependent tunneling:** Panel (a) represents the Zeeman-split density of states of a superconducting layer. Panel (b) depicts the expected conductance spectra of unpolarized electrons from a metal to a superconducting layer. Panel (c) shows the conductance from a ferromagnet to a superconducting layer. See text for more details. Figure adapted from LeClair<sup>35</sup>.

The DOS features a gap ( $2\Delta$ ) around the Fermi energy and characteristic singularities at  $\pm\Delta$ . For thin Al layers, when a magnetic field is applied in the plane of superconducting electrodes, a Zeeman splitting appears between the DOS of spin up ( $-\mu_B H$  dotted lines) and down ( $+\mu_B H$  solid lines) quasi-particles. The four sharp features obtained in the DOS allow to discriminate the contribution of spin up and down electrons to tunneling current. If the spin is conserved during tunneling, the conductance will be the simple sum of spin up and down channels.

Panel (b) illustrates the conductance of unpolarized electrons from a metal to a superconducting electrode. Since  $D_{\uparrow}(E_F) = D_{\downarrow}(E_F)$  in metals, the contribution of both spin channels is equal, resulting in symmetric peaks in the conductance. On the other hand, panel (c) epitomize the conductance from a ferromagnet to a superconducting material. Since  $D_{\uparrow}(E_F) \neq D_{\downarrow}(E_F)$ , the four peaks in the conductance are asymmetric.

Meservey *et al.* (1970)<sup>36</sup> assumed that the conductance was directly proportional to the density of states of both electrodes and defined the polarization of the ferromagnetic electrode as:

$$P = \frac{(\sigma_4 - \sigma_2) - (\sigma_1 - \sigma_3)}{(\sigma_4 - \sigma_2) + (\sigma_1 - \sigma_3)} \quad (1.10)$$

### 1.2.2.2 The Jullière model of tunneling magnetoresistance

In 1971, Jullière<sup>1</sup> applied the concepts developed by Meservey and Tedrow to magnetic tunnel junctions. His idea was to use the exchange split DOS of a ferromagnet as a spin detector, instead of the magnetic field induced splitting in superconductors.

The Jullière model is based on two assumptions. First, he assumes that the electron spin is conserved during tunneling (no spin-flip events). Second, the probability for an electron to tunnel through the insulating barrier is directly proportional to the number of initial and final states accessible. According to the first point, an electron originating from the first electrode is accepted in the second electrode only if states with identical spin and energy are available. It allows to apply the two current model for the contribution of spin up and spin down electrons. The second point allows to define the conductance in terms of densities of states:

$$G_P \propto \rho_1^{\uparrow} \cdot \rho_2^{\uparrow} + \rho_1^{\downarrow} \cdot \rho_2^{\downarrow} \quad (1.11a)$$

$$G_{AP} \propto \rho_1^{\uparrow} \cdot \rho_2^{\downarrow} + \rho_1^{\downarrow} \cdot \rho_2^{\uparrow} \quad (1.11b)$$

where  $\rho_i^{\uparrow}$  and  $\rho_i^{\downarrow}$  are the tunneling DOS of the ferromagnets ( $i=1, 2$ ) for majority and minority electrons respectively. Note that Equation (1.11) can be derived from Equation (1.8) by considering  $T = 0K$  and  $|M|^2$  constant in addition to Jullière's assumptions.

Figure 1.6 represents electrons tunneling between two ferromagnetic electrodes through an insulating layer represented by a potential step (striped area) when a bias  $V$  is applied to the magnetic tunnel junction. Panel (a) and (b) distinguish the parallel and antiparallel magnetic states respectively. In this example the density of states of majority electrons is larger than for minority electrons.

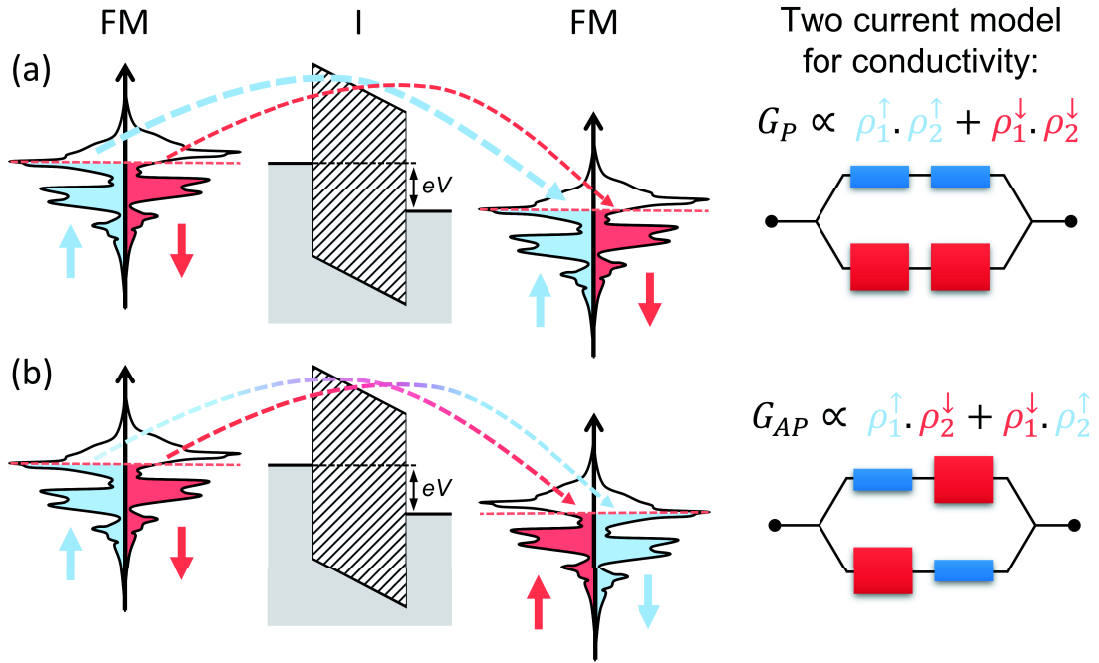


Figure 1.6: **The Jullière model for TMR:** The figure represents electrons tunneling between ferromagnetic (FM) electrodes through an insulating layer represented by a potential step (striped area) when a bias  $V$  is applied to the magnetic tunnel junction. Both parallel and antiparallel magnetic states are represented in (a) and (b) respectively. The model is based on two hypothesis that allow to apply the two current model (represented on the right hand side). See text for more details.

In the parallel state (panel a), majority electrons, which are in greater number in the emitting electrode, will find more available states in the collecting electrode than sparse minority electrons in both electrodes. As a consequence the majority  $\rho_1^\uparrow \rho_2^\uparrow$  channel will have more weight in the tunneling current compared to the minority  $\rho_1^\downarrow \rho_2^\downarrow$  channel. In the antiparallel state (panel b), the relative spin referential between the two electrodes is reversed. Majority electrons in the emitting electrode can tunnel only to minority states in the collecting electrode. Since minority states are in lower number, it results in a decrease of the majority conduction channel ( $\rho_1^\uparrow \rho_2^\uparrow > \rho_1^\uparrow \rho_2^\downarrow$ ). Despite the fact that the number of final available states is larger in the AP configuration, the minority channel conductivity will not substantially change because the number of initial states is still the same ( $\rho_1^\downarrow \rho_2^\downarrow \approx \rho_1^\downarrow \rho_2^\uparrow$ ).

The two current models for both magnetic states are represented on the right side of Figure 1.6. Again, it results in  $G_P \neq G_{AP}$ . Finally, the tunneling magnetoresistance is defined as the difference of conductance between P and AP states:

$$TMR = \frac{G_P - G_{AP}}{G_{AP}} = \frac{R_{AP} - R_P}{R_P} \quad (1.12)$$

Using Equation (1.11)a-b we obtain:

$$TMR = \frac{2P_1 P_2}{1 - P_1 P_2} \quad (1.13)$$

where  $P_i$  is the spin polarization of the ferromagnetic electrode defined as:

$$P_i = \frac{\rho_i^\uparrow - \rho_i^\downarrow}{\rho_i^\uparrow + \rho_i^\downarrow} \quad (1.14)$$

Using SP values measured by Mersevey, Jullière predicted 26 % of TMR for his samples, which is larger than the 14 % experimentally measured. He supposed that this difference was due to spin scattering processes and the coupling between electrodes.

Surprisingly, Jullière's results didn't have much impact on the scientific community at that time. This can be explained in part by experimental difficulties to fabricate MTJs, the need for low temperatures and the relatively small amplitude of the effect.

Despite the fact that the model was successfully applied to several ferromagnets and gave a qualitative comprehension of spin-dependent tunneling, it was totally failing to explain experimental results such as the positive spin polarization measured for Co and Ni. Both bulk Co and Ni are predicted to have more minority electrons at the Fermi level<sup>37</sup> and are expected to have negative spin polarization. More refined models were developed in order to account for unexplained experimental results. Some of them will be discussed thereafter.

In what follows, we'll discuss how experimental discrepancies and theoretical refinements pointed out the need to consider M/I/M structures as a whole system and not only as independent subsystems combined together.

### 1.2.3 Theoretical refinements

#### 1.2.3.1 Stearns' approach

Stearns<sup>38</sup> carefully analyzed realistic spin resolved band structure of transition metals ferromagnets to explain the positive spin polarization of Co and Ni measured by Mersevey and Jullière.

She supposed that the tunneling rate explicitly depends on the effective mass  $m_e^*$  of electrons, which is different for different bands. As a reminder, the electrical conductivity in  $3d$  ferromagnets arises from  $s$  as well as  $d$  electrons. She argues that, while  $3d$  electrons are responsible for most of the magnetic moment, they will not participate much in the tunneling current due to their large effective mass (localized electrons). On the other hand, the decay rate of dispersive  $s$ -like electrons will be much lower. She then assumed that for thick barriers  $s$ -like electrons carry most of the tunneling current and that the contribution of  $d$ -like electrons may be neglected. Actually her argument is similar to the one developed in [Section 1.1.1](#) to explain electrical conductivity in transition metal.

As a result, the quantity measured by Julliere and Mersevey is not the bulk spin polarization of Co and Ni, but the polarization of the band with the slowest decay rate within the insulating barrier. In Co and Ni the  $s$ -like  $T_{2g}$  band, responsible of the tunneling current, is polarized through hybridization between  $s$  and  $d$  bands and results in a polarization with opposite sign compared to bulk values. This in turn explains the positive measured spin polarization.

Recent calculations proved that Stearns was right. Moodera *et al.*<sup>39</sup> calculated the tunneling spin polarization between Co electrodes separated by a vacuum barrier as a function of the barrier thickness. For thin barriers,  $d$  electrons have a strong weight in the tunneling current and the spin polarization is found negative. As the barrier thickness increases, the weight of the  $3d$  electrons decreases and for sufficiently large barriers, the spin polarization is found positive reflecting the predominance of  $s$  electrons to the tunneling current.

Stearns' work emphasizes the fact that one should not interpret spin polarization values measured by spin-dependent tunneling techniques as reflecting the dependence of the tunneling current on the total DOS polarization at the Fermi level but on the DOS weighed by the tunneling matrix elements  $|M|^2$  instead. Her results were also an early indication of the fact that the understanding of spin-dependent tunneling requires a detailed knowledge of the electronic properties of the whole heterostructure, including the insulating barrier.

### 1.2.3.2 Importance of interfaces

Stearns' work emphasized the importance to take into account the *character* of the tunneling particles. However, theoretical models were still not satisfactory as they didn't take into account the importance of interfaces. Indeed, the intrinsic properties of the electrodes are predicted to be strongly perturbed in the presence of interfaces and it was expected that interfaces should play an important role in driving the tunnel current. Actually, it was anticipated that the tunneling current in MTJs is probing a few monolayers of the electrodes at each interface, and thus depends on the properties of the strongly perturbed regions and not on the bulk properties of electrodes.

Moreover, experiments on magnetic tunnel junctions with identical electrodes but different barriers indicated that the tunneling current was sensitive to the type of barrier used. This was interpreted as the fact that different barriers may act differently on tunneling particles but also that the *coupling* of the electrodes to the insulating barrier was different, i.e. the interfacial properties of the electrodes depend on the coupling of the electrode with the barrier.

Actually it was demonstrated in later works<sup>40</sup> that the amplitude and even the sign of spin polarization depends on the type of bonds at the electrode-barrier interface. It was shown in  $Co/Al_2O_3$  junctions that the  $sp-d$  bonding at the interface *permits* mostly  $s$ -like electrons to tunnel. However in  $Co/STO$  magnetic tunnel junctions,  $d-d$  bonding between Co and Ti at the interface mostly selects  $d$  orbitals. As it was discussed before, since in Co  $s$  electrons are positively polarized, the measured SP in  $Co/Al_2O_3$  MTJs is positive, while it is negative in  $Co/STO$  due to the weight of negatively polarized  $d$  electrons to the tunnel current.

### 1.2.3.3 Slonczewski model

From the discussion above, we can see that, in order to describe the tunneling current across a MTJ, one has to treat the heterostructure as a whole-quantum mechanical system. Slonczewski was the first to do develop such a global approach of spin-dependent tunneling.

He considered tunneling between two ferromagnetic electrodes separated by a rectangular potential step (see Figure 1.3). He used the free-electron approximation to describe the wave-functions in the electrode. In order to simulate the magnetism in the electrodes, he introduced a rigid shift in the band structure of spin up and down electrons that mimics the Stoner splitting in ferromagnetic layers. He supposed perfect translational symmetry in the plane of the electrodes. In other words  $\vec{k}_{\parallel}$ , the projection of  $\vec{k}$  in the  $xy$  plane, is conserved during tunneling. He calculated the transmission coefficient by using the continuity conditions of the wave-functions across the whole structure (approach introduced in most quantum mechanics textbooks).

The Schrödinger equation can be separated in two independent equations and the wave-functions can be represented in the form  $\Psi(\vec{r}) = \chi(\vec{k}_{\parallel}, \vec{r}_{\parallel})\varphi(z)$  where the  $\varphi(z)$  are the solutions of the one dimensional Schrodinger equation with potential  $V(z)$  and with energy  $E_z = E - \hbar^2 k_{\parallel}^2 / 2m$ .

Finally, the conductance was calculated by using Landauer-Büttiker formula:

$$G^{\sigma} = \frac{e^2}{h} \sum_{k_{\parallel}} T^{\sigma}(k_{\parallel}) \quad (1.15)$$

where  $\sigma$  is the spin index, and the sum is taken over all the transverse modes.

He obtained an expression of the conductance as a function of the relative magnetization alignment  $\theta$  of the two electrodes:

$$G(\theta) = G_0 (1 + P^2 \cos(\theta)) \quad (1.16)$$

where  $P$  is the effective tunneling spin polarization defined as:

$$P = \frac{k^{\uparrow} - k^{\downarrow} \kappa^2 - k^{\uparrow} k^{\downarrow}}{k^{\uparrow} + k^{\downarrow} \kappa^2 + k^{\uparrow} k^{\downarrow}} \quad (1.17)$$

and  $\kappa = \sqrt{(2m/\hbar^2)(U - E_F)}$  is the decay constant of the wave-functions in the barrier.

The principal result of Slonczewski's calculation is that the polarization  $P$  now depends on the height of the barrier through the imaginary vector  $\kappa$ . In the limit of a high barrier, this term tends to unity, reducing this expression to Jullière's formula. However if the barrier is not very high, the magnitude of TMR decreases with decreasing  $U$  and can even change sign.

One disadvantage of his approach is that the calculation requires predetermined wave-functions, which are easily obtained in the case of free electrons but hard to generalize for more complex or realistic systems. This approach also makes it hard to account for disorder within the junction. Finally a major drawback of this model is the use of a *perfect* potential step to model the insulating layer that doesn't take into account the electronic structure of the insulating layer (a crucial point as it will be discussed in the next sections).

## 1.2.4 Summary

In this section, we briefly considered spin-dependent tunneling across magnetic tunnel junctions. Experimental results and theoretical consideration mainly stressed the fact that

SDT is sensitive to many parameters such as the *character* of the tunneling particle, the coupling at the electrode-barrier interface but also to the electronic properties of the insulating barrier itself. This makes SDT tunneling very complex and rich, but it also makes it possible to tune each of these parameters and engineer MTJs with desired properties.

After the first experiments on MTJs of Jullière in 1975, the next realization of magnetic tunnel junctions with sizable TMR at room temperature were developed in 1995 independently by Moodera *et al.*<sup>10</sup> and Miyazaki and Tezuka<sup>11</sup>. More recent theories on GMR and TMR in amorphous junctions can be found in the literature<sup>41</sup>.

The drawback of the semi-classical models originate from the fact that they don't treat the junction as a single quantum-mechanical system. In the next section, we'll discuss first principles theoretical models of epitaxial junctions. It'll arise from the discussion that the electronic structure of the insulating layer plays a central role in tunneling.

## 1.3 Tunneling magnetoresistance in crystalline Fe/MgO/Fe(001) magnetic tunnel junctions

In the former section, the discussion focused on early models and experimental results, and pointed out that the tunneling current is very sensitive to several parameters such as the characters of the tunneling particles, interface considerations and even the electronic structure of the insulating layer. In this section, we'll see that the more realistic ab-initio calculations improves the simple models in various ways. They account for the complicated electronic structure of transition metals that are mostly used in spintronic devices. They also consider the properties of interfaces with more accuracy. Finally one of the most important advantage of epitaxial systems is the possibility to treat the electronic structure of the insulating barrier.

In this section, the discussion will focus on the canonical Fe/MgO/Fe (001) system. We'll first consider the structure of the Fe/MgO (001) interface and briefly talk about the methods used to calculate the electronic structure and the tunneling current. In the second part we'll describe the electronic structure of the whole stack with an emphasis on interface layers. In the third part we'll talk about the tunneling current throughout the heterostructure. The conductance as a function of  $k_{\parallel}$  will be discussed. The importance of lateral symmetry as well as the complex band structure of the insulating layer will also be addressed. These consideration naturally point to the need to consider the tunneling current at  $\mathbf{k}_{\parallel} = (0, 0)$ . Finally tunneling for  $\mathbf{k}_{\parallel} \neq (0, 0)$  and through resonant surface states will be briefly addressed.

### 1.3.1 Theoretical model and formalism

#### 1.3.1.1 Crystal structure

MgO crystal is formed by a charge transfer between Magnesium atoms and Oxygen atoms forming  $Mg^{2+}$  cations and  $O^{2-}$  anions, with each of the atoms types forming a face-centered cubic, or fcc structure that dovetails to form a rock-salt structure with a lattice pa-

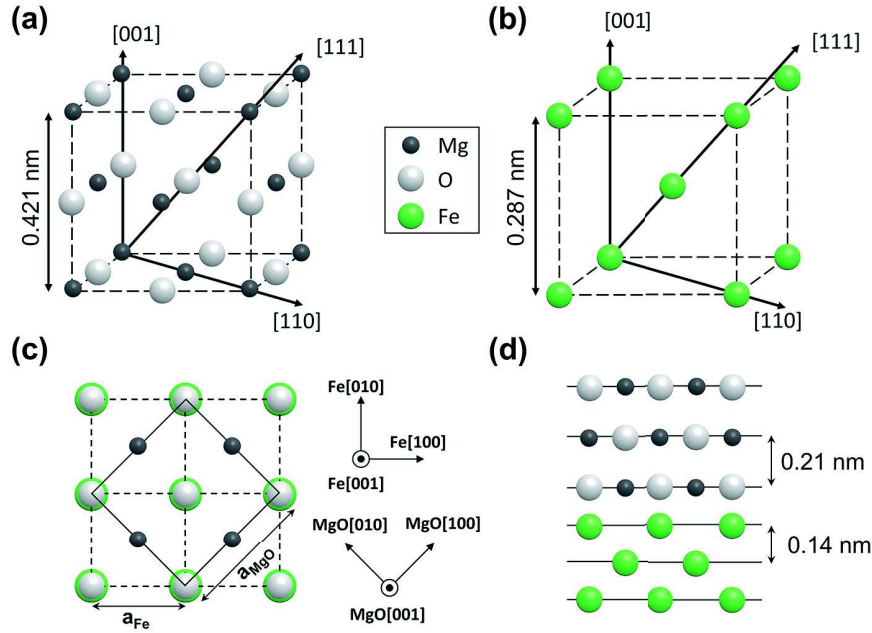


Figure 1.7: **Structure of the Fe/MgO (001) interface** The Rock-salt and the bcc crystal structure of MgO and iron are shown in panel (a) and (b) respectively. Top view and cross section of the Fe/MgO(001) interface are schematized in panel (c) and (d). We can see that MgO[100] is parallel to Fe[110]. Figure adapted from Yuasa and Djayaprawira<sup>45</sup>.

parameter  $a_{MgO} = 0.421$  nm. The crystal structure of MgO is represented in Figure 1.7a. The electron transfer results in both ions having the very stable electronic structure  $1s^2 2s^2 2p^6$ , that qualitatively explain the strong localization of electrons and the large optical band gap of MgO.

Magnesium oxide is a direct gap insulator with the valence band (VB) maximum and the conduction band (CB) minimum situated at the  $\Gamma$  point of the Brillouin zone. The amplitude of the gap has been determined experimentally and estimated to be around  $E_g = 7.8$  eV<sup>42</sup>. It is also established<sup>43,44</sup> that the MgO band gap is underestimated when using DFT techniques to values around  $\sim 5$  eV. The crystal structure of body-centered cubic (bcc) iron is represented in Figure 1.7b. The lattice parameter of the unit cell is  $a_{Fe} = 0.287$  nm.

Detailed experimental results<sup>46</sup> show that MgO(001) grows pseudomorphically on Fe(001) up to six monolayers with an epitaxial relationship Fe(001)[110]//MgO(001)[100] meaning that there is a 45° rotation between MgO[100] and Fe[100] axis. As a result, the lattice mismatch between  $a_{MgO}$  and  $\sqrt{2}a_{Fe}$  is only 3.7%. A scheme of the Fe(001)/MgO(001) interface is shown in Figure 1.7c (top view) and Figure 1.7d (cross section). After six monolayers a partial lattice relaxation appears resulting in misfit dislocations at the Fe/MgO interface. The impact of misfit dislocation on magnetotransport will be discussed later (Section 2.1.4). Other experiments<sup>47</sup> as well as theoretical studies<sup>48</sup> suggested that the oxygen atoms of MgO are sitting above Fe atoms with a distance of 0.20-0.23 nm.

### 1.3.1.2 Formalism

Butler *et al.*<sup>44</sup> used the layer-Korringa–Kohn–Rostoker method (LKRR) approach to calculate the electronic structure of the Fe/MgO/Fe heterostructure from first principles.

The LKRR method is based on the density functional theory (DFT), and incorporates the atomic sphere approximation. The extended solid is viewed as one composed with an infinite stack of layers, each of which has translational symmetry. Thus, this approach is particularly suited to the problem at hand, namely semi-infinite epitaxial leads separated by a thin tunnel barrier. Magnetism is treated within the local spin-density approximation.

The calculation proceeds as follow: First the bulk calculation is performed for the two electrodes. Then an interface containing the tunnel barrier with few iron layers on each side is introduced, Fe layers in the additional *sample* region have the properties of the bulk calculated in the previous step. Finally spin up and down potentials near the interfaces are allowed to relax until electrostatic self-consistency is achieved throughout the system. Usually, the calculated potentials don't differ significantly from those of the bulk three or four layers away from the interface.

In the leads, it is possible to take advantage of the two-dimensional periodicity to ease the calculation by using the Bloch's theorem to determine the electronic wavefunctions. Within the LKRR method, the electron wavefunctions are described by the product of two functions (i) the wavefunction that describe the electrons inside the radius defined by the atomic sphere approximation, where the potential due to on-site atoms is large and (ii) another function that describes the electron in the interstitial region, where the potential of the on-site atoms is negligible. The resulting Bloch wavefunctions are converted to a plane wave basis and propagated through the system by means of transmission and reflection coefficient between layers. Each layer is characterized by four scattering matrices describing the exchange of electrons with the neighboring layers.

When considering the scattering in the sample region, the LKRR method allows to express the reflection and transmission coefficient at the Fe/MgO interface as a function of the aforementioned scattering matrices. This property also makes LKRR very convenient for this kind of calculation.

Once the transmission coefficient are obtained for each Bloch state, it is possible to use the Landauer-Büttiker formula that relates the conductance to the transmission probability. In the case of perfect translational symmetry  $k_{\parallel}$  is conserved and the simplified Landauer-Büttiker<sup>49</sup> formula can be written:

$$G = \frac{e^2}{h} \sum_{k_{\parallel}, j} T(k_{\parallel}, j) \quad (1.18)$$

where  $e$  is the charge of the electron,  $h$  Planck's constant and  $T(k_{\parallel}, j)$  the tunneling probability of electrons with a given transverse mode  $k_{\parallel}$  and a given symmetry  $j$ . This formula expresses the conductance in a very simple form: electrons with a given symmetry and a given transverse mode form an independent conduction channel. The total conductance is the direct sum of all these channels.

For more details on the calculations and methods see MacLaren *et al.*<sup>50</sup>, Zhang and Butler<sup>49</sup> and references therein.

### 1.3.2 Electric and magnetic properties

It was found that there is very little charge transfer from MgO to the first Fe layer. The magnetic moment of Fe atoms at the interface is  $3 \mu_b$  which is higher than the  $2.2 \mu_b$  of bulk bcc iron under normal conditions.

The density of states is calculated for each layer. Figure 1.8 summarizes the result obtained on interface layers for both iron and MgO. In the case of Fe, we can see that the interface DOS is substantially changed compared to bulk values. For majority electrons (panel a), the DOS is reduced close to the interface, while a larger peak appears well below the Fermi level, represented by a dashed line at .35 Hartree. In the minority channel (panel b), a large and sharp peak appears just above the Fermi level. The position of this peak is consistent with other calculations and attributed to surface states appearing in the minority channel of *bcc* iron. This feature seems to be general as it was found for

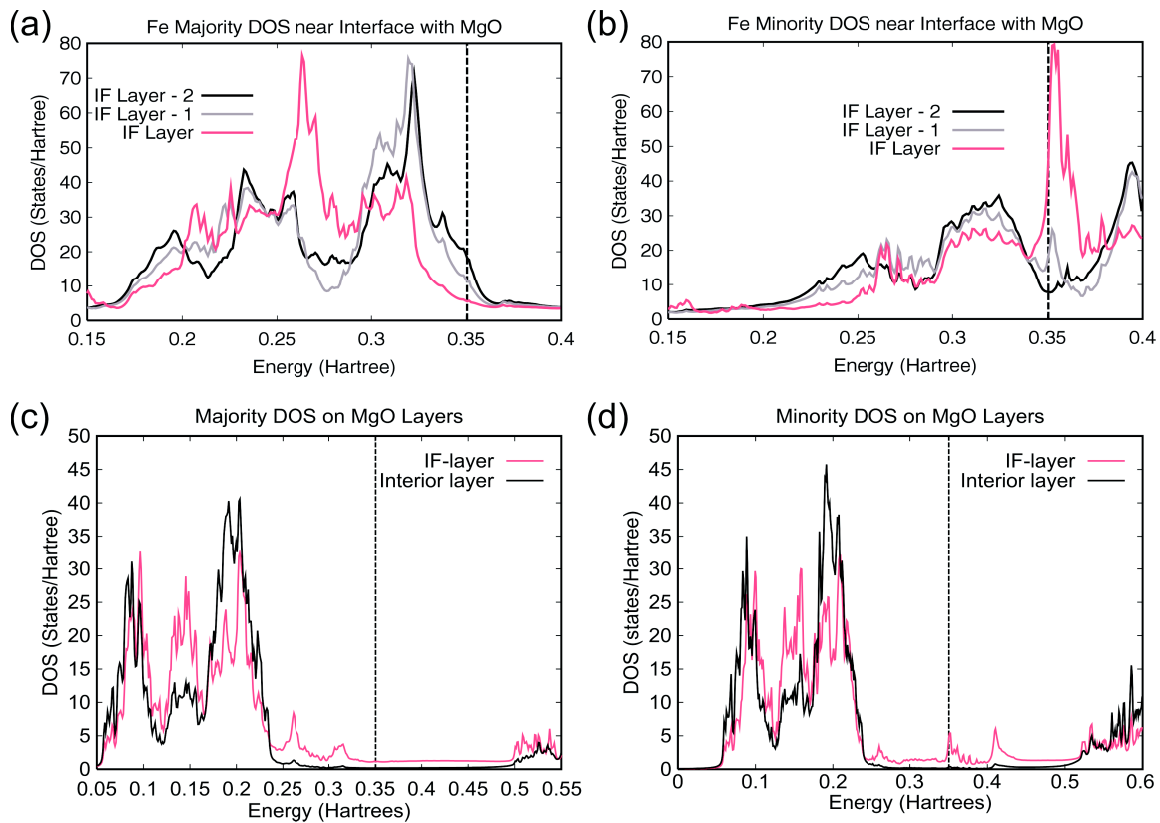


Figure 1.8: **Density of states at the Fe/MgO interface:** The majority and minority DOS is represented for Fe interface layers in panel (a) and (b). The presence of the MgO at the interface has opposite effects for majority and minority DOS. At the interface, the majority DOS is reduced close to the Fermi level (dashed line at .35 Hartree) while a sharp peak appears in the minority DOS. Similar results are plotted for MgO majority and minority DOS in panel (c) and (d) respectively. The gap of MgO is  $\sim 5.5$  eV, and small features in the gap of MgO result from the large peaks seen in the interface Iron layer. Figure adapted from [Zhang and Butler](#)<sup>49</sup>.

several Fe interfaces<sup>48–51</sup>. The general trend is that, moving toward the interface, the DOS decreases for majority electrons while a sharp peak appears in the minority channel.

For MgO, the interior layer is characterized by a large gap extending from .244 Hartree to 0.446 Hartree corresponding to a 5.5 eV gap, lower than the 7.8 eV experimental value but similar to other DFT calculations. Features at .26 and .31 Hartree in the majority channel (panel (c)) and peaks at .35 and .41 Hartree in the minority channel (panel (d)) are believed to be faint "echos" of peaks in the DOS of the interfacial iron layer.

### 1.3.3 $k_{\parallel}$ -resolved tunneling current

The conductance was calculated using Equation (1.15). Figure 1.9 represents the tunneling conductance as a function of  $\mathbf{k}_{\parallel} = (k_x, k_y)$  for both parallel (panel (a) and (b)) and antiparallel (panel (c)) magnetic configurations.

We can see in panel (a) that the results for the majority electrons are similar to what is expected for the free electron model, i.e the conductance is mainly situated at the  $\Gamma$  point of the 2D Brillouin zone that correspond to the  $\mathbf{k}_{\parallel} = (0, 0)$  point. Although the distribution of the conductance looks similar, we'll see in Section 1.3.5 that the more realistic model results in more complicated physics than simple models.

In panel (b), we can see that the main contribution in the minority channel are for values of  $\mathbf{k}_{\parallel} \neq (0, 0)$ . More precisely, it seems like these peaks form part of a circle centered at the

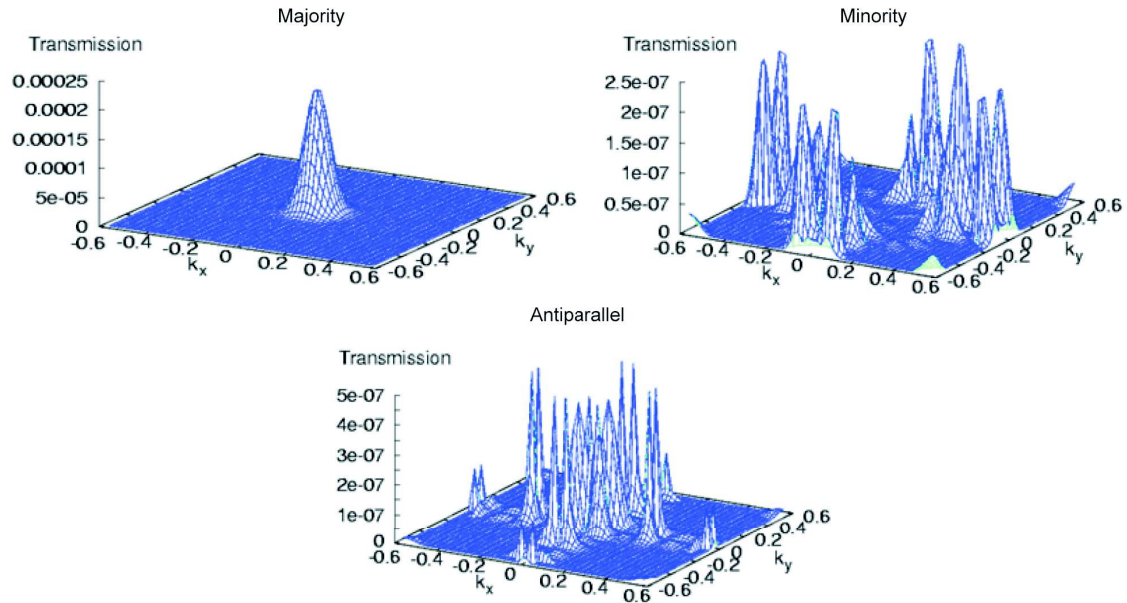


Figure 1.9: **Distribution of conductance as a function of  $k_{\parallel}$** :  $k_{\parallel}$ -resolved conductance for eight monolayers of MgO. Conductance in the parallel magnetic configuration for majority and minority spin channels are represented in top right and top left panels respectively. Conductance in the antiparallel configuration is shown in the bottom panel. See text for more details. Figure adapted from Butler *et al.*<sup>44</sup>.

origin of the zone. It was determined that this structure correspond exactly to the surface state that appears in the minority DOS of the interface iron layer (see [Figure 1.8b](#)). The thickness dependence of the tunneling current<sup>49</sup> showed that the conductance for larger values of  $\mathbf{k}_{\parallel} \neq (0, 0)$  is suppressed as the thickness is increased meaning that the resonant surface states that dominates the minority channel conductance at small thicknesses do not contribute in the limit of large barriers.

The conductance in the case of antiparallel alignment of the electrodes magnetization is shown in [Figure 1.9](#). We can see that the conductance has features of both spin channels.

Although the tunneling is more complicated for these first principle models, we can see from the conductance plots that the tunneling in the parallel magnetic configuration is larger than that in the antiparallel configuration and that the former is mostly centered around  $\mathbf{k}_{\parallel} = (0, 0)$ . In the following we'll distinguish two cases. We'll see that the tunneling for  $\mathbf{k}_{\parallel} = (0, 0)$  essentially explains the large TMR expected in the Fe/MgO/Fe (001) system while considering conductance for  $\mathbf{k}_{\parallel} \neq (0, 0)$  provides more insight into the complex physics underlying the electrical properties of epitaxial systems.

### 1.3.4 Electrical transport for $\mathbf{k}_{\parallel} = (0, 0)$

#### 1.3.4.1 Effect of lateral symmetry of incident Bloch states

As a quick reminder, when tunneling through a simple potential step is treated within the free electron model, the wavefunctions decay as  $\exp(-\kappa d)$  where  $d$  is the barrier thickness and

$$\kappa = \sqrt{(2m/\hbar^2)(V - E_F) + \mathbf{k}_{\parallel}^2} \quad (1.19)$$

is the decay constant. It is clear from the [Equation \(1.19\)](#) that the amplitude of the tunneling in the two dimensional Brillouin zone is centered around the point  $\mathbf{k}_{\parallel} = (0, 0)$ , for which  $\kappa$  is minimum. A simple explanation is that the  $\mathbf{k}_{\parallel}$  component of the wave vector  $\mathbf{k} = (\mathbf{k}_{\parallel}, k_z)$  has an energy  $\hbar^2 \mathbf{k}_{\parallel}^2 / 2m$  associated with the lateral motion of the electron that is not used to tunnel through the barrier. Moreover, one expect a single decay rate for a given value of  $\mathbf{k}_{\parallel}$  for the free electron mode.

In their detailed theoretical treatment, [Butler et al.](#)<sup>52</sup> determined that in addition to the value of  $\mathbf{k}_{\parallel}$ , the decay rate also depends on the symmetry of the tunneling electron. For  $\mathbf{k}_{\parallel} = (0, 0)$  they found that the decay parameter could be written:

$$\kappa^2 = \frac{2m}{\hbar^2} (V - E) - \frac{\langle \phi | \frac{\partial^2}{\partial x^2} + \frac{\partial^2}{\partial y^2} | \phi \rangle}{\langle \phi | \phi \rangle} \quad (1.20)$$

where  $\phi(x, y)$  is the planar component of the wavefunction  $\psi(x, y, z) = \phi(x, y)\exp(-\kappa z)$ . The second term of [Equation \(1.20\)](#) is positive and causes an increase in the decay rate, similarly as a nonzero value of  $\mathbf{k}_{\parallel}$  would. The amplitude of this additional term correlate with the number of nodes of  $\phi(x, y)$  in the plane. In this picture, it is useful to consider the tunneling Bloch states with respect to their symmetry as it allows to determine the number of nodes of the wavefunctions in the plane and their ensuing decay rate.

Bloch state	Character & symmetry	Decay rate
$\Delta_1$	$s, p_z$ and $d_{2z^2}$	$\kappa = \sqrt{(2m/\hbar^2)(U - E_F)}$
$\Delta_5$	$p_x, p_y, d_{xy}$ and $d_{yz}$	$\kappa = \sqrt{(2m/\hbar^2)(U - E_F) + g_1^2}$
$\Delta_2$	$d_{x^2-y^2}$	$\kappa = \sqrt{(2m/\hbar^2)(U - E_F) + g_1^2}$
$\Delta_{2'}$	$d_{xy}$	$\kappa = \sqrt{(2m/\hbar^2)(U - E_F) + g_2^2}$

Table 1.1: **Effect of lateral symmetry of Bloch states at  $k_{\parallel} = (0, 0)$ :** This table summarizes the different Bloch states at  $k_{\parallel} = (0, 0)$ , their character and their decay rate. The decay rate depends on the number of nodes of the planar component of the wavefunction. In turn, the number of nodes can be determined from symmetry considerations. Here  $g_1$  and  $g_2$  are additional terms due to the symmetry of the wavefunctions. In conclusion, it is important to note that  $\Delta_1$  have the slowest decaying rate,  $\Delta_5$  and  $\Delta_2$  states will decay faster and  $\Delta_{2'}$  states will decay even faster.

Table 1.1 summarizes the incident Bloch waves at  $k_{\parallel} = (0, 0)$ . What is important to retain from the symmetry considerations is that  $\Delta_1$  have the slowest decaying rate,  $\Delta_5$  and  $\Delta_2$  states will decay faster and  $\Delta_{2'}$  states will decay even faster.

The variation of lateral symmetry is not the the dominant effect in determining the decay rate of electrons. Mavropoulos *et al.*<sup>53</sup> showed that the decay rate can be precisely determined from the the complex band structure of the barrier. It will be used, together with the band structure of iron, to explain the large tunneling magnetoresistance in this system.

### 1.3.4.2 Wave-functions matching at interfaces

In addition to the previous discussion on the lateral symmetry of impinging Bloch states, electrical transport in heterostructures can also be understood in terms of metal-induced gap states (MIGS) in the barrier. In this picture, transport is explained by coupling incident metallic states to evanescent states within the insulator's band gap.

**MgO Complex band structure:** The electrical structure of the insulating barrier can be described from the standpoint of tunnelling transmission by the *complex band structure*<sup>53,54</sup>. In the bulk of the barrier, the periodicity of the crystal structure requires that the Bloch states must have free electron-like real  $\mathbf{k}$  vectors. Near the crystal surface however, it is possible to match Bloch states within the crystal with evanescent wave-functions outside the crystal. Again the problem can be simplified if one considers a perfect epitaxial layer in the  $xy$  plane and the interfaces perpendicular to the  $z$  direction. It is possible to decompose  $\mathbf{k} = (k_{\parallel}, k_z)$  such that  $k_{\parallel}$  is conserved and only  $k_z$  is allowed to have complex values.

In the case of magnetic tunnel junctions, the current is mostly carried by charge carriers at the Fermi level. That's why we'll mostly focus our discussion on states at the Fermi level. As it was mentioned before, when incident metallic states at  $E_F$  are scattered through the barrier, they couple to the insulator's state with complex  $k$ . In the case of

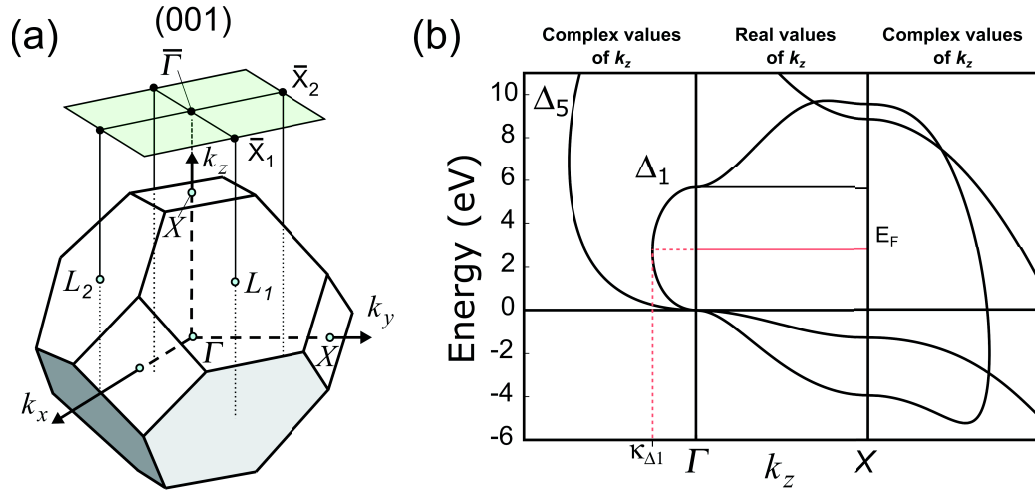


Figure 1.10: **MgO symmetry resolved complex band structure:** The 3D Brillouin zone of rock-salt structures is shown in panel (a). We are interested in electrical transport in the  $k_z$  direction that corresponds to the  $\Gamma - X$  line in reciprocal space. Panel (b) represents the complex band structure of MgO. The central part of the graph corresponds to wave-functions with real wave vectors while left and right panels shows the evanescent wave-functions with complex  $\kappa$  values starting from the  $\Gamma$  and  $X$  points in reciprocal space. The decay rate can be easily extracted by choosing the minimal  $\kappa_{min}$  for a given energy.  $\Delta_1$  states have the slowest decay rate at the Fermi energy. Figure adapted from [Tsymbal and Zutic<sup>41</sup>](#).

ballistic transport, the transverse properties of the tunneling particle are conserved during scattering, therefore tunneling particles can only couple to evanescent gap states with identical  $k_{\parallel}$  and symmetry only. The 3D Brillouin zone of rock-salt structures and the complex band structure of MgO are represented in Figure [Figure 1.10](#).

The advantage of this approach is that it allows to extract the extinction coefficient of wave-functions at a given energy and for a given symmetry easily, without the need of time consuming calculations. In order to do that, it is enough to select the energy of the tunneling particle (we are interested in electrons at the Fermi level) and select the minimum complex  $k$  value that has the same symmetry as the tunneling particle. The example of  $\Delta_1$  decay rate is shown in [Figure 1.10](#) assuming that the Fermi level of MgO is in the middle of the gap (calculated gap of 5 eV). The Bloch states in the electrode compatible with this evanescent state will have the slowest decay rate in the insulating barrier. Using the same procedure in [Figure 1.10](#), we can see that electrons with  $\Delta_5$  symmetry have the second slowest decaying rate. The transport for  $k_{\parallel} = (0,0)$  is characterized by two additional symmetries  $\Delta_2$  and  $\Delta_2'$ . Data for these two states is not shown in [Figure 1.10](#), but it was established that they decay much faster than  $\Delta_1$  and  $\Delta_5$  states, with  $\Delta_2'$  decaying even faster than  $\Delta_2$ .

**Fe (001) bcc band structure:** Now that the order of decaying rates within the insulating barrier has been established, we have to look at the Bloch states in the electrode compatible with these evanescent states, i.e. electrode states at  $E_F$  in the  $k_z$  direction.

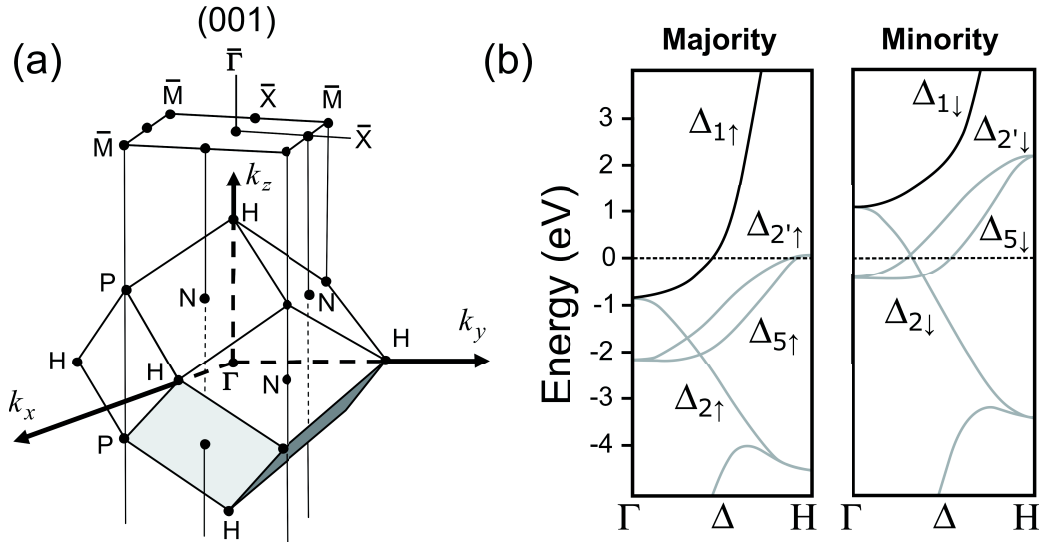


Figure 1.11: **bcc iron (001) symmetry resolved band structure:** The 3D Brillouin zone of bcc structures is shown in panel (a). We are interested in electrical transport in the  $k_z$  direction that corresponds to the  $\Gamma - H$  line in reciprocal space, also denoted  $\Delta$ . Panel (b) represents the spin- and symmetry-resolved band structure of bcc iron in the  $\Delta$  direction. In the majority population  $\Delta_1$ ,  $\Delta_5$  and  $\Delta_{2'}$  are involved at the Fermi energy, while  $\Delta_2$ ,  $\Delta_5$  and  $\Delta_{2'}$  are involved in the minority channel. Figure adapted from Papaconstantopoulos<sup>37</sup>.

Figure 1.11a schematizes the 3D Brillouin zone of bcc structures with all the lines of high symmetry. We are interested in the tunnel transport in the  $k_z$  direction, i.e. [001] direction, perpendicular to the (001) planes of the structure. This particular line corresponds to the  $\Gamma - H$  direction of the reciprocal space, also denoted  $\Delta$ . The spin- and symmetry-resolved band structure of bcc iron in  $k_z$  direction is represented in Fig. Figure 1.11b. We can see that the Fermi level crosses the  $\Delta_1$ ,  $\Delta_5$  and  $\Delta_{2'}$  in the majority channel and the  $\Delta_2$ ,  $\Delta_5$  and  $\Delta_{2'}$  in the minority channel.

As we thoroughly discussed previously, the  $\Delta_1$  states will have the slowest decaying rate. Thus, electrical transport in the parallel and antiparallel configuration of MTJs and ensuing TMR will depend on either the  $\Delta_1$  conduction channel is open or not. We can see from Fig. Figure 1.11b that the  $\Delta_1$  state is totally spin polarized at  $E_F$ . Keeping this in mind, we'll now discuss the tunneling DOS calculations of Butler *et al.*<sup>44</sup>, and show how MgO acts as a symmetry filter in this system.

### 1.3.4.3 Tunneling DOS across the junction

Figure 1.12 and Figure 1.13 plot the tunneling density of state (TDOS) for the parallel and antiparallel magnetic configurations, respectively. The tunneling DOS is defined as the electron density of states at each layer due to a single incident Bloch state and is roughly proportional to  $|\Psi|^2$ .

Upon interpreting these results, it is important to remember that coupling impinging

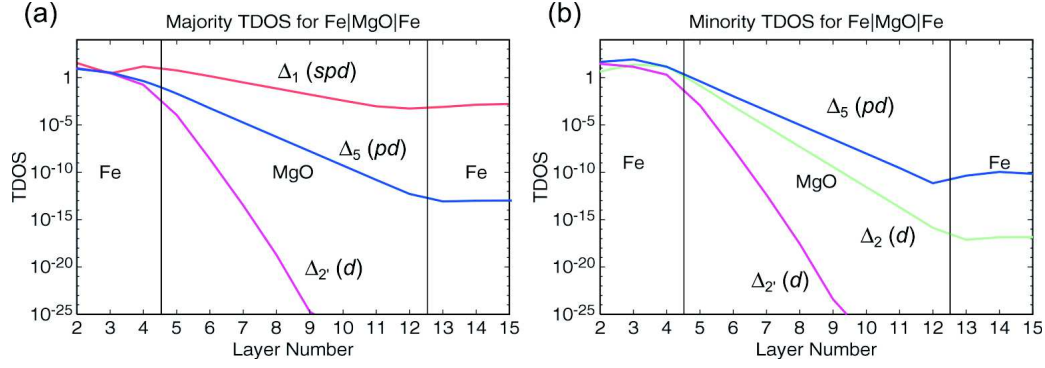


Figure 1.12: **Fe/MgO/Fe tunneling DOS in the parallel magnetic state:** Panels (a) and (b) plot the tunneling DOS as a function of the position in the Fe/MgO/Fe tri-layer in the parallel magnetic state, for majority ( $G^{\uparrow\uparrow}$ ) and minority ( $G^{\downarrow\downarrow}$ ) channels respectively. There is no  $\Delta_1$  channel in the minority channel. See text for more details. Figure adapted from Zhang and Butler<sup>49</sup>.

electrons from the emitting electrode to evanescent states inside the barrier at the first interface is not sufficient to ensure effective tunneling. In order to efficiently tunnel across the barrier, the decaying wave-functions must also couple to compatible Bloch state in the collecting electrode at the second interface.

Moreover, incoming  $\Delta_1$  and  $\Delta_5$  Bloch states will decay as evanescent states with the same symmetry in MgO. However,  $\Delta_2$  states in iron will decay as  $\Delta_2'$  states in MgO. Similarly  $\Delta_2'$  states in the electrode will decay as  $\Delta_2$  states in the barrier. This change in symmetry properties is due to the fact the the MgO[001] grows with an angle of  $45^\circ$  with respect to the Fe [001] direction (refer to Figure 1.7).

Figure 1.12(a) plots the tunneling DOS for majority electrons when both electrodes have their magnetization in the same direction ( $G^{\uparrow\uparrow}$ ). In the parallel magnetic configuration, the two electrodes have similar Bloch states at the Fermi level, namely  $\Delta_1$ ,  $\Delta_5$  and  $\Delta_2'$  (see Figure 1.11). As it was previously discussed, each state will be transmitted with a probability that depends on the interfacial transmission coefficient but also on the symmetry-dependent decay rate in the barrier. We can see from the slope of the tunneling DOS inside the barrier that  $\Delta_1$  states have the slowest decay rate while  $\Delta_5$  and  $\Delta_2'$  states decay much faster, consistent with the previous discussion on lateral symmetry and MgO complex band structure (see Figure 1.10).

In panel (b) the same quantity is represented for the minority channel ( $G^{\downarrow\downarrow}$ ). The main difference is that the  $\Delta_1$  state is not present in the minority channel, and the contribution of a  $\Delta_2$  state appears. For both ( $G^{\uparrow\uparrow}$ ) and ( $G^{\downarrow\downarrow}$ ) we can see that each state couples effectively at the second interface to available states with identical symmetry in the collecting electrode. In the parallel magnetic configuration, the current is mainly due the  $\Delta_1$  state present in the majority channel.

Panels (a) and (b) of Figure 1.13 represent the tunneling DOS in the antiparallel magnetic configuration for both majority  $\rightarrow$  minority ( $G^{\uparrow\downarrow}$ ) and minority  $\rightarrow$  majority ( $G^{\downarrow\uparrow}$ ) channels, respectively. In the case of  $G^{\uparrow\downarrow}$  we can see that each of the  $\Delta_1$ ,  $\Delta_5$  and  $\Delta_2'$  states

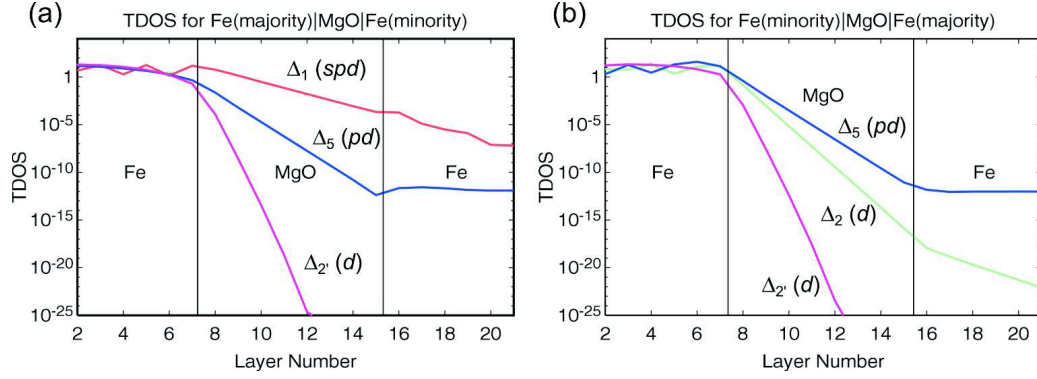


Figure 1.13: **Fe/MgO/Fe tunneling DOS in the antiparallel magnetic state:** Panels (a) and (b) represent the tunneling DOS in the antiparallel magnetic configuration for  $G^{\uparrow\downarrow}$  and  $G^{\downarrow\uparrow}$  respectively. See text for more details. Figure adapted from Zhang and Butler<sup>49</sup>.

couples effectively at the first interface and decays similarly to the  $G^{\uparrow\uparrow}$  case (compare panel Figure 1.12(a) and Figure 1.13(a)). However, since the  $\Delta_1$  state is not available in the minority channel, it continues to decay in the collecting electrode, resulting in a strongly reduced tunneling current for  $G^{\uparrow\downarrow}$ . Similar conclusions can be made for ( $G^{\downarrow\uparrow}$ ), again there is no  $\Delta_1$  state in the emitting electrode.  $\Delta_5$  states tunnel effectively since this state is present in both spin population at the Fermi level. The  $\Delta_2$  state, present in the minority channel but not in the majority channel, will continue to decay in the counter electrode.

Finally, we saw in Section 1.3.1.2 that the Landauer-Büttiker formula expresses the conductance as a simple sum of the different channels at the Fermi level. We can thus write:

$$G_P = G_{\Delta_1}^{\uparrow\uparrow} + G_{\Delta_5}^{\uparrow\uparrow} + G_{\Delta_5}^{\downarrow\downarrow} + G_{\Delta_2}^{\downarrow\downarrow} \quad (1.21a)$$

$$G_{AP} = G_{\Delta_5}^{\uparrow\downarrow} + G_{\Delta_5}^{\downarrow\uparrow} \quad (1.21b)$$

where  $G_P$  and  $G_{AP}$  are the conductance for the parallel and antiparallel alignments of ferromagnetic electrodes magnetization, respectively. The contribution of  $\Delta_2'$  states is neglected in Equation (1.21). In this frame work, the tunneling magnetoresistance defined as:

$$TMR = \frac{G_P - G_{AP}}{G_{AP}} \quad (1.22)$$

is expected to be very large. Indeed,  $G_P$  is predicted to be much larger the  $G_{AP}$  because the tunneling current is mainly carried by  $\Delta_1$  electrons that have a strong weight in the P majority conduction channel while they are filtered away in the antiparallel configuration.

### 1.3.5 Electrical transport for $k_{\parallel} \neq (0, 0)$

The electrical properties of Fe/MgO/Fe(001) MTJs cannot be explained in simple terms of symmetry for  $k_{\parallel} \neq (0, 0)$ . In this thesis we'll discuss two interesting cases that illustrate

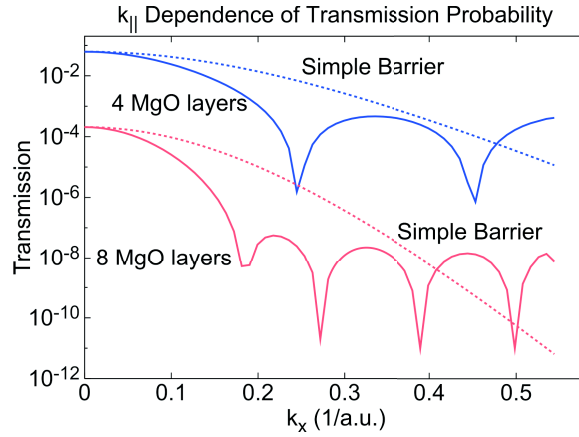


Figure 1.14: **Interference of tunneling states:** Tunneling DOS as a function of  $k_x$  for  $k_y = 0$ . The LKKR decay rate (solid lines) is compared to the simple barrier model (dashed lines) for 4 and 8 MgO monolayers (blue and red respectively). The oscillatory dependence of the TDOS can't be explained by simple models. Figure adapted from Zhang and Butler<sup>49</sup>.

the fact that simple models are not appropriate to describe tunneling in magnetic tunnel junctions.

The first effect addressed in this section is the interference of tunneling states. The second effect, focuses on interface resonant states and will be addressed in Section 2.1.1. Referring to Figure 1.12a, we saw that the  $\mathbf{k}$ -resolved tunneling DOS (TDOS) of the majority channel was similar to that for the free electron model, i.e. the conductance is mainly centered around the  $\Gamma$  point of the two-dimensional Brillouin zone.

The tunneling DOS as a function of  $k_{||}$  (for  $k_y = 0$ ) on a logarithmic scale is plotted in in Figure 1.14. LKKR results (solid lines) are compared to the simple barrier model (dashed lines) for four and eight MgO monolayers (blue and red respectively). For small values of  $k_x$ , the decrease in TDOS is faster than the simple model, while it becomes slower for large values of  $k_x$ . The most striking difference is the oscillatory dependence of the tunneling DOS with  $k_x$  that cannot be explained by standard models. This oscillatory behavior can be understood by the complex band structure of MgO<sup>44</sup>.

### 1.3.6 Co and CoFe electrodes

Similarly to bcc Fe electrodes Zhang and Butler<sup>17</sup> studied the transport properties of MTJs including bcc Co and CoFe electrodes from first principles. In general, similar properties are found, that is to say transport properties are described in terms of symmetry filtering by the insulating barrier at the  $\bar{\Gamma}$  point of reciprocal space.

A critical difference lies in the symmetry-resolved band structure of Cobalt. Figure 1.15 compares the band structure of bcc Iron and bcc Co. We can see that, conversely to bcc Fe, all states are totally spin polarized at  $E_F$  in Co. In Fe electrodes,  $\Delta_5$  as well as  $\Delta_2$  states are present in both minority and majority channels. Despite the fact that they decay faster than

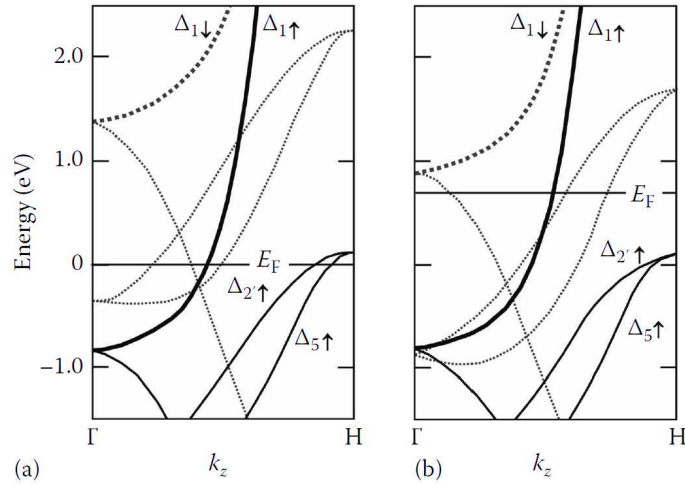


Figure 1.15: **Spin- and symmetry-resolved band structure of bcc Fe and Co:**  $\Delta_5$  and  $\Delta_{2'}$  are present in both majority and minority spin population of bcc Fe electrodes while they are totally spin polarized in bcc Co. This is expected to further reduces  $G_{AP}$  increasing the conductance asymmetry between P and AP and the resulting TMR. Figure taken from [Tsymbal and Zutic](#)<sup>41</sup>.

$\Delta_1$  states, they still contribute to conductance in both P and AP magnetic configuration. In Co, the total spin polarization of  $\Delta_5$  and  $\Delta_{2'}$  states (present in majority spin population only) reduces  $G_{AP}$  and is expected to increase TMR.

From conductance calculations, they predict TMR of 5000 %, 13000 % and 34000 % for Fe/MgO, Co/MgO and CoFe/MgO MTJs respectively<sup>17</sup>. These values are calculated without taking into account the conduction of the minority channel. The authors state that taking into account the minority channel should increase the TMR because of interface resonant states (IRS). However, we'll see in [Section 2.1.1](#) that IRS are in fact reducing the TMR. Moreover, in the model used by [Butler et al.](#), the lattice parameters of electrodes and MgO are exactly matched and the crystal structure in their simulation is allowed to relax out of plane only. As we mentioned previously, above a critical thickness, the MgO layer relaxes and misfit dislocations appear at the interface. Finally, other shortcomings to these theoretical models have to be taken into account in order to properly describe transport properties in realistic MTJs. Some of them will be addressed in [Chapter 2](#).

### 1.3.7 Experimental confirmation

The first sizable TMR values (27 %) at room temperature were obtained in 2001 by [Bowen et al.](#)<sup>55</sup>. In 2003, TMR of 67 % were achieved at RT using molecular beam epitaxy (MBE)<sup>56</sup>. Finally in the late 2004 200 % TMR at room temperature were announced using MBE<sup>57</sup> and sputtering techniques<sup>58</sup>.

Also, Co/MgO/Co(001) MTJs with metastable bcc Co layers were realized<sup>59</sup>. The junctions exhibited TMR values higher than 400 % at room temperature, confirming theoretical predictions that the bcc Co or bcc FeCo electrodes should improve MTJs performances

compared to the Fe/MgO couple<sup>17</sup>.

In Section 1.4 we'll see the importance of sputtered techniques for industrial applications.

### 1.3.8 Summary

The advantage of epitaxial systems over their amorphous counterparts is that they can have a detailed theoretical treatment, including modeling of the tunneling barrier.

In epitaxial systems, each layer has perfect two-dimensional symmetry in the  $xy$  plane while interfaces are perpendicular to the  $z$  direction. The periodicity of the crystal structure makes it possible to describe the electrons in the leads with Bloch wave-functions. The electrical properties of impinging Bloch states can be reduced into groups by symmetry considerations, with each symmetry having a different decay rate inside the dielectric. The distribution of tunneling conductance in the two dimensional Brillouin zone shows that electrical transport in first principle models is way more complicated than the classical models.

The large TMR expected in this system can be understood from transport properties at  $k_{\parallel} = (0, 0)$ . At the corresponding  $\bar{\Gamma}$  point of reciprocal space, only few Bloch states are allowed to tunnel across the barrier. Of these states,  $\Delta_1$  electrons have the slowest decay rate. From the band structure of bcc iron we know that these states are totally spin polarized at the Fermi level. In the parallel magnetic configuration,  $\Delta_1$  states in the emitting electrode will couple to  $\Delta_1$  evanescent states in the barrier and in turn couple to available  $\Delta_1$  states in the collecting electrode. In the antiparallel configuration however, no  $\Delta_1$  states are available in the collecting electrode, resulting in a much lower conductance in the antiparallel magnetic configuration. The ensuing TMR, defined as the relative difference of conductance between P and AP, is expected to be very large (more than 10 000 %).

Transport at  $k_{\parallel} \neq (0, 0)$  is characterized by (i) oscillations of the tunneling DOS as a function of  $k_{\parallel}$  and (ii) interface resonant states (IRS) that can have a strong impact on the tunneling current.

After the first predictions in 2001, spectacular experimental confirmation came just few years later. The challenge was the realization of epitaxial structures with high crystalline quality, particularly at interfaces. We'll see that both the realization of perfect interfaces as well as the characterization of their detailed structure is challenging.

## 1.4 From Epitaxial to textured magnetic tunnel junctions

As discussed in Section 1.3, several groups calculated the electronic properties of fully epitaxial heterostructures<sup>44,53,60</sup> and predicted very high TMR ratio in Fe(001)/MgO(001)/Fe(001) epitaxial MTJs. This triggered a lot of effort in the fabrication of fully epitaxial systems, followed by spectacular experimental confirmation few years later<sup>56,61,62</sup>. The mechanisms underlying symmetry filtering in epitaxial MgO-based heterostructures can

be summarized as follows:

1. In epitaxial systems electrons are subject to a periodic potential, therefore Bloch's theorem can be used to calculate the electrons wavefunctions. The properties of the resulting Bloch states can be unified and reduced into sets of families by symmetry consideration.
2. Within the heterojunction, interfacial continuity is required for the incoming Bloch wave functions to couple at the interfaces and propagate.
3. By matching the symmetry dependent electronic properties of the ferromagnetic electrodes and the insulating barrier, it is possible to obtain very high tunneling spin polarization and ensuing high TMR ratios.
4. From a technological point of view, a strong decoupling between electrodes is necessary. This requirement usually result in pinning one of the electrodes with an antiferromagnetic pinning layer by exchange coupling.

Although epitaxial system are useful for fundamental studies and comparison with theoretical simulations, they are not compatible with mass production techniques and hard to integrate into real life applications. If we look carefully into the results obtained in ref. 44 and weight them to available growth techniques, point 1 and 2 can be reformulated as:

- 1'. In first approximation, only electrons with  $k_{\parallel} = 0$  (electrons moving perpendicular to plane) participate in the tunneling current. This suggest that atomic arrangement in the z direction (in the direction of current flow) is needed, while it is *irrelevant* in the xy plane.
- 2'. Concerning interfaces, two critical points have to be taken into account: (i) Atomic periodicity has to be maintained and careful attention has to be given to interfacial arrangements (matching of crystal structure of electrodes and insulating barrier) (ii) Interfaces have to be flat, and defect free.

In parallel to the development of epitaxial MTJs, another technique fulfilling point 1' and 2' and compatible with mass production was used to fabricate MTJs, namely the *sputter* deposition technique.

Parkin *et al.*<sup>58</sup> were the first to report high MR ratio (i.e. > 100 %) with fully sputtered MTJs in 2004. They used a combination of ion beam and magnetron sputtering to grow Si(100)/SiO<sub>2</sub>/TaN/IrMn/CoFe/MgO/CoFe/TaN(Mg) heterostructures. The as deposited samples had low TMR that increased dramatically after annealing at 400 °C under magnetic field. The annealing step was necessary to pin the bottom CoFe electrode by exchange coupling with the underlying antiferromagnetic IrMn layer. Pinning allows to get the necessary antiparallel alignment between electrodes in order to obtain magnetoresistance (point 4.). In their growth process all layers deposited on top of the amorphous TaN buffer layer, including the IrMn pinning layer, were polycrystalline with high (001) texture but random in plane orientation (point 1'). They reported very high MR values (220 %

at room temperature) in their exchange-biased spin valve (EB-SV). The increase of TMR with increasing annealing temperature also suggested an improvement of the sample crystal structure.

In 2005, Djayaprawira *et al.*<sup>63</sup> fabricated Ta(10)/PtMn/CoFe/Ru/CoFeB/MgO/CoFeB/Ta/Ru heterojunctions that exhibited 230 % TMR at room temperature. Contrary to aforementioned CoFe based samples, they obtained amorphous electrodes. Surprisingly, MgO grew with a (001) rock-salt texture on top of the amorphous CoFeB electrode. As shown in Figure 1.16, the annealing step is necessary to trigger two processes: the first one is to pin the bottom electrode, as mentioned before. The other one is to extend the crystal structure of MgO(001) to the neighboring amorphous CoFeB layers<sup>64</sup>. The fact that the as deposited CoFeB electrodes are amorphous make this technique very versatile (the CoFeB/MgO/CoFeB trilayer can be grown on many materials) and compatible with mass production techniques.

By comparing samples with textured CoFe electrodes and samples with amorphous CoFeB, they concluded that the latter ones have several advantages: First, by optimizing the deposition parameters, amorphous samples allow to get very flat layers and sharp interfaces. Note that the equilibrium crystal structure of CoFeB should be fcc, but the crystallization of electrodes during the annealing step is driven by the highly (001)-oriented rock-salt structure of MgO. This process is called *solid phase epitaxy*. Finally, the amorphous layer below the bottom CoFeB electrode acts as a buffer layer that separates the crystal structure of the underlying AF pinning layers that can otherwise act as a template for layers grown above. This allows to get rid of possible lattice mismatch at the IrMn/CoFeB interface that can cause dislocations propagating through the heterostructure.

From that point, several technological issues were addressed to increase the TMR up to 1000 %. Hayakawa *et al.*<sup>65</sup> showed that although the annealing step was necessary to create and improve the crystal structure of interfaces it was also causing diffusion of elements such as Mn or Ta (or Ru) from lower layers, limiting the performance of the device for annealing temperatures above 450 °C. By designing a sample without the AF pinning layer (a pseudo spin valve, or PSV), they got rid of the IrMn layer and increased TMR to 472 % at room temperature.

Attention was then focused on the composition of the electrodes<sup>66</sup>. Co layers have higher polarization compared to Fe layers, in addition to  $\Delta_1$  electrons  $\Delta_5$  states are also totally spin polarized at  $E_F$ . In principle doping iron electrodes with cobalt allows to obtain higher spin polarization. However doping can change the stabilized crystal structure after annealing, increase lattice mismatch between electrodes and the insulating barrier, and can consequently reduce the TMR. It is therefore important to optimize the Co concentration as to obtain the highest TMR possible while maintaining the favorable b.c.c. (001) structure of electrodes. Boron concentration above 10% is required in order to make the layers amorphous. Lee *et al.* measured a TMR ratio of 500 % at room temperature for  $(\text{Co}_{25}\text{Fe}_{75})_{80}\text{B}_{20}$  electrodes (numbers are nominal concentrations in %) and a 2.1 nm thick MgO layer.

Another progress was made when Ikeda *et al.*<sup>18</sup> showed that diffusion of Ta atoms from the buffer layer was also limiting TMR. By increasing the thickness of the bottom CoFeB layer they limited Ta diffusion and obtained TMR ratio of 604 % at room temperature.

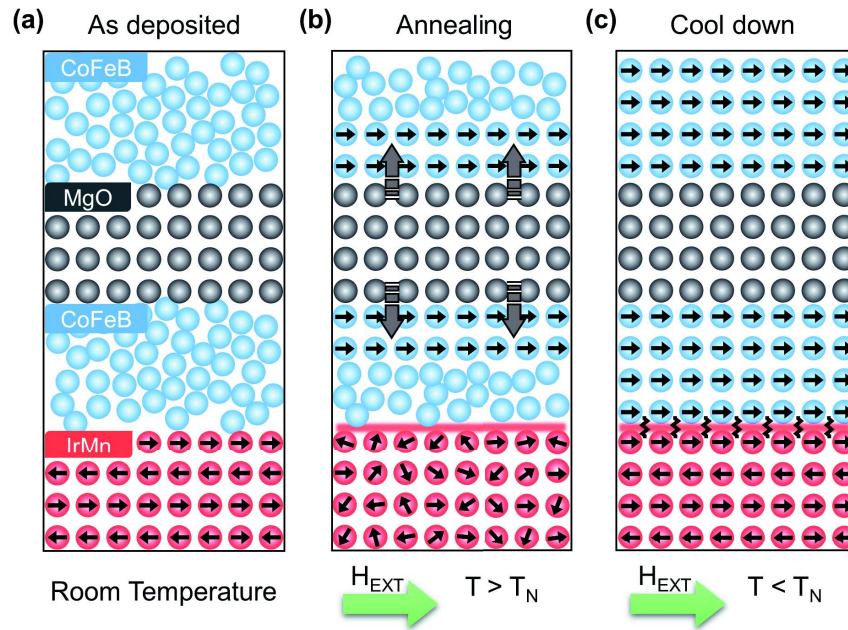


Figure 1.16: **Annealing of CoFeB based MTJs:** Panel (a) shows the samples as deposited, both CoFeB electrodes are amorphous while the pinning antiferromagnetic (AF) layer and MgO are textured. In panel (b), the sample is annealed above the Néel temperature ( $T_N$ ) of the IrMn layer. The AF layer is magnetically disordered and the (001) rock-salt structure of MgO extends to the electrodes that slowly crystallize in b.c.c (001). Panel (c) shows the cool down of the sample under external magnetic field ( $H_{EXT}$ ). In the final state, the bottom electrode and the AF layer are coupled to some extent (the amplitude and the sign of the coupling depend on annealing temperature) and interfaces are crystallized (layers are fully crystallized for small thicknesses).

Finally, samples with magnetization out of plane were obtained. The same deposition technique and materials were used. They obtained this specific magnetic anisotropy of the electrodes by fine-tuning the electrodes thickness<sup>67</sup>.

It is generally accepted that the large TMR in CoFeB based MTJs results from the same mechanisms that governs transport properties of epitaxial Fe/MgO tunnel junctions. Although large TMR measured in these systems support this interpretation, many details are still ambiguous. For instance, HRTEM images showed interface crystallization but the question of what happens to Boron is still not explained. Again, these points will be addressed in Chapter 2.

## 1.5 Conclusion

In this chapter, we took an historical approach to introduce tunneling in solid state devices. Although simple models failed to accurately describe spin-dependent tunneling, we saw

that early theories were successfully leading the field of spin-dependent tunneling in the right direction. These works put all the mechanism behind SDT on firmer ground and undoubtedly contributed to the fast development of the field when sophisticated theoretical tools and experimental techniques became available.

Although theoretical predictions were successfully confirmed, ideal systems cannot be obtained in reality, resulting in theoretical vs experimental discrepancies. Despite refinements to experimental techniques, device fabrication always introduces some amount of defects making small deviation in the crystal structure compared to perfect models. Besides, we are mostly interested in textured CoFeB/MgO/CoFeB magnetic tunnel junctions for which the annealing step makes the detailed knowledge of crystal and interface structures difficult. Even though the mechanism behind spin-dependent tunneling and TMR are the same for epitaxial and textured samples, it is clear that their transport properties will be different.

The goal of the following chapter is to present a general picture of electrical transport in realistic tunnel junctions, taking into account deviations compared to ideal systems. We'll mainly focus on experimental results, sometimes backed with theoretical consideration, in order to understand the complex electrical properties of realistic junctions.



# Spin dependent tunneling in realistic junctions

In the preceding chapter, we introduced the field of spin dependent tunneling. In particular, we examined spin dependent transport in fully epitaxial MgO based magnetic tunnel junctions. We saw that in perfect systems and in the coherent tunneling regime, i.e. in a framework where inelastic processes that induce incoherent tunneling (loss of spin and symmetry information) are disregarded, the symmetry filtering effect of MgO coupled to transition metal electrodes with an appropriate band structure results in large tunneling magnetoresistance.

Although theoretical models accurately describe general properties of MTJs, some experimental results are still unexplained and their interpretation open to debate. For example, the bias and temperature dependence of magnetoresistive properties are complex and a detailed and accurate description is still missing. Another important property that is not well understood is the barrier height in MgO based MTJs: it is found to be one order of magnitude lower than the value expected from the optical gap. Besides, experimental TMR values are always at least one order of magnitude lower than TMR predicted by theory.

The difficulty to explain these discrepancies stems from the fact that, on the one hand, it is challenging from an experimental point of view to characterize the detailed structure of buried interfaces. On the other hand, the impact of disorder is very hard to take into account from a theoretical point of view. Both predicaments makes it difficult to compare experimental results and theoretical models.

Nevertheless tremendous efforts have been made, both from experimental and theoretical point of views, to carefully design samples and models in order to evaluate the impact of intrinsic and extrinsic inelastic processes. In this chapter we'll review various works related to these aspects.

This chapter is outlined as follows. We'll first consider deviation from the perfect Fe/MgO/Fe epitaxial structure by considering interface effects. We'll then focus on other intrinsic and extrinsic features occurring in the non-equilibrium regime, that is the impact of bias voltage on coherent as well as non-coherent (inelastic) tunneling. More precisely, we'll focus on the low bias region where interaction of electrons with magnons, phonons and impurities takes place. Moreover, we'll discuss the impact of temperature on magnetotransport. In addition to the smearing of the Fermi energy and decrease of electrode's polarization with increasing temperature, we'll see that temperature dependent measurements underscore other inelastic processes. Once the understanding of spin dependent

tunneling in MgO is put on firmer ground, we'll consider the impact of impurity-induced localized states in the gap of MgO on spin dependent tunneling (SDT). We'll see that Oxygen vacancies are the most expected defects in MgO and discuss their characteristics in detail. Most of our discussions and interpretations of experimental measurements will be based on results described in this section.

The last section of this chapter will detail the scientific motivations of this thesis.

## 2.1 Interface considerations

Since the beginning of the field of spin dependent transport across magnetic tunnel junctions, the importance of structural quality and chemical bonding at the metal-insulator interface has always been emphasized (see Section 1.2.3.2). However, since interfaces are embedded within the device, it is generally difficult to characterize, let alone control the quality of interfaces.

On the one hand, the sensitivity of SDT to interface properties is subtle and makes any attempt of systematic studies tedious and difficult, mainly due to the fact that interfacial quality is very sensitive to small fluctuations in growth parameters. On the other hand, this extreme sensitivity to interfaces is also a very interesting playground to tune device properties by interface engineering.

In this section we'll review various aspect of metal-MgO interfaces and discuss their impact on transport properties both from experimental and theoretical viewpoints.

### 2.1.1 Tunneling through interface resonant states

In a crystal with infinite dimensions, symmetry considerations describe the charge carriers in an efficient and elegant manner. When the dimensions of the crystal are finite, the introduction of discontinuities such as surfaces or interfaces are expected to change the electrical properties of the material in the vicinity of the discontinuity.

In addition to simple evanescent states, other solutions to Schrödinger's equation can be found for systems with finite dimensions. We'll be interested in states that appear in metals *local gaps* that exist between the ordinary allowed bands. Since these states are present in forbidden energy regions, they decay both inside and outside the metal, making them strongly localized near the interface. These states are called *Surface states*.

When dealing with surface states in transport experiment, *normal* surface states are distinguished from interface resonant states (hereafter denoted IRS). The former are states located in regions of the two-dimensional Brillouin zone where no bulk states are available, while the latter are located in regions where bulk states can occur. Since normal surface states are much localized, they usually don't impact transport properties. On the other hand, resonant surface states can hybridize with bulk states, extend away from the interface and participate to tunneling current. In this paragraph we'll mostly focus on IRS.

In the equilibrium transport regime (no bias voltage applied), owing to the fact that IRS are present away from the  $\bar{\Gamma}$  point they are generally negligible in the asymptotic limit, i.e. limit of large barriers thicknesses for which contributions of features at  $k_{\parallel} \neq 0$  are

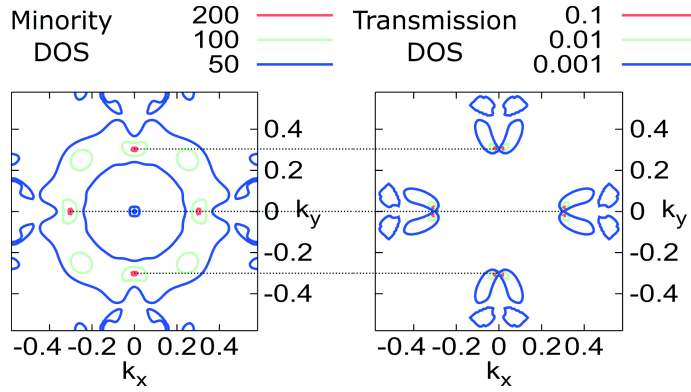


Figure 2.1: **Contour plot of the minority DOS and TDOS.** DOS (left panel) in states/hartree and TDOS (right panel) of the minority channel in the parallel magnetic configuration. The complex structure of the tunneling DOS (left panel) in the two-dimensional Brillouin zone can be related to peaks in the DOS of minority electrons (right panel). Interface resonant states are expected to play an important role in the tunneling current as they can open conduction channels at finite bias in both P and AP magnetic configurations. Figure adapted from [Zhang and Butler](#)<sup>49</sup>.

filtered out. Nevertheless, they can be the dominant transport mechanism for intermediate and thin barriers. Moreover, it was shown that IRS are indeed present at the  $\bar{\Gamma}$  point of the reciprocal space ( $k_{\parallel} = 0$ ) but at higher energies than  $E_F$  ( $\sim 0.2$  eV above  $E_F$ <sup>68</sup>). As a consequence, they can participate in the tunneling current in the non-equilibrium regime (when a bias voltage is applied) and even dominate transport properties as we'll see hereafter. Furthermore, IRS are very sensitive to surface and interface structures, they can be quenched or suppressed with very small amount of disorder<sup>69</sup>.

In [Section 1.3.3](#), we briefly mentioned that the complicated structure of the tunneling DOS in the minority channel is related to interface resonant states present in the minority channel at the interface iron layer (see [Figure 1.8b](#)). [Figure 2.1](#) shows a contour plot of the minority channel DOS (left panel) and the tunneling DOS (or TDOS, defined as the electron density of states at each layer due to a single incident Bloch state) of the minority channel (right panel) as a function of  $k_{\parallel}$ . Although DOS and TDOS plots don't have a one-to-one correspondence, it is possible to straightforwardly identify the maximum in the tunneling DOS to peaks in the density of states of the minority channel.

It is clear that IRS have a non-negligible contribution to the tunneling current. It was also established that the states corresponding to the peaks in the TDOS have significant  $s$ -character and are effectively transmitted since they can couple to the  $\Delta_1$  states evanescent within the barrier.

An early experimental and theoretical evidence of IRS was found by [Stroscio et al.](#)<sup>68</sup>. A scanning tunneling microscope (STM) is used to measure topological and electrical properties of Fe (001) single crystal whiskers. In their experiment, electrical transport is carried by electrons tunneling from the tip to the Fe surface through a vacuum barrier. They compared their conductance spectra to theoretical surface DOS calculations and identified a strong peak in their  $dI/dV$  spectra at 0.2 eV as a strong peak in the minority DOS of bcc

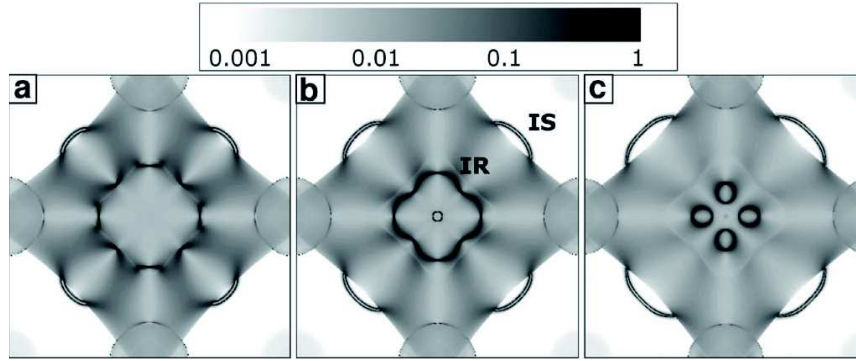


Figure 2.2: **Fe (001)  $k_{||}$ -resolved minority DOS:** Minority DOS of the topmost Fe layer in a Fe/MgO/Fe (001) trilayer for three energies: (a) 0.02eV below  $E_F$  (b) at  $E_F$  and (c) 0.02eV above  $E_F$ . Regular surface states and resonance states are marked IS and IR respectively. Figure reproduced from [Belashchenko \*et al.\*<sup>72</sup>](#).

Fe (001), supporting result found by [Butler \*et al.\*<sup>44</sup>](#). They attribute the origin of the peak in the minority DOS to  $3d_{z^2}$  orbitals at the interface, that form *dangling* bonds away from the surface in the vacuum region.

Another group studied the impact of IRS on electrical properties of Fe/MgO/FR MTJs at zero bias from first principle<sup>70</sup>. In particular, it is shown that the barrier can be totally transparent to IRS resulting in a transport regime dominated by resonant states in the parallel magnetic configuration, while their contribution is limited in the antiparallel configuration. This is mainly due to the fact that the theoretical model assumes that the barrier is *perfect* and *symmetric*. Consequently, large DOS induced by IRS are present at both interfaces and are perfectly matched. Because tunneling is supposed to be coherent (no spin flip), conduction channels induced by IRS are open only in the parallel magnetic configuration and IRS are predicted to effectively increase TMR. However, perfect and symmetric barriers are almost impossible to obtain in realistic junctions as interfaces are never defect free and growth conditions make it very difficult to obtain identical quality at the bottom and top interfaces.

[Tiusan \*et al.\*<sup>71</sup>](#) studied the transport properties of high quality Fe/MgO/Fe (001) magnetic tunnel junctions. Similarly to [Stroscio \*et al.\*](#) they report an IRS at 0.2 eV. They show that this state is present at the bottom Fe/MgO interface only, demonstrating the lower quality of the top interface. They show that the activation of the IRS conduction channel increases the conductance in the antiparallel magnetic configuration, making  $G_{AP} > G_P$  hence inverting the sign of TMR. These results are in contradiction with the aforementioned first principle calculations<sup>70</sup>.

Based on the results of [Tiusan \*et al.\*](#), [Belashchenko \*et al.\*<sup>72</sup>](#) clarified the apparent contradiction. As seen in [Figure 2.2](#), they show that the IRS present in the Fe (001) minority DOS are very sharp and extremely sensitive to carrier's energy. Moreover, IRS are present in regions where the DOS of bulk states is very low.

In order for the sharp IRS peaks in the emitting electrode to effectively tunnel, they have to (i) couple with barrier states at the first interface and (ii) find a large amount of

available states in the collecting electrode. Point (i) can be satisfied in the non-equilibrium tunneling regime: when a bias voltage is applied and the energy  $E_F + eV$  of the tunneling electrons matches that of resonant states, IRS will couple to bulk states and decay as evanescent states inside the barrier. Besides, it was shown that IRS originate from  $3d_{z^2}$  orbitals compatible with the slow decaying  $\Delta_1$  states within MgO. Because the IRS are present in regions where DOS of bulk states is low, point (ii) is satisfied only when the large IRS peak in the emitting electrode matches that in the collecting electrode (or another sharp feature in the DOS of the collecting electrode).

In symmetric junctions, these conditions are fulfilled only at zero bias, but we already discussed the fact that in realistic junctions bottom and top interfaces are not strictly identical and thus IRS conduction channels in the parallel magnetic configuration are quenched. Moreover, when a small bias is applied, IRS at both interface are mismatched, as seen in [Figure 2.2](#) small bias voltages as low as  $0.02\text{ eV}$  strongly modifies the contribution of IRS to the  $k_{\parallel}$ -resolved transmission. On the other hand, in the antiparallel configuration, minority IRS at one interface are compatible with majority states in the collecting electrode (inversion of the spin referential between electrodes in AP) that are present in large number and thus IRS are expected to increase the conductance in the AP magnetic configuration. Briefly, in opposition to the conclusions of [Wunnicke \*et al.\*<sup>70</sup>](#), in realistic junctions IRS increase the conductance of the AP channel only and are expected to reduce TMR.

Finally, a more recent work<sup>73</sup> identified a second IRS at  $1.1\text{ eV}$ . Similarly to [Tiusan \*et al.\*](#), this peak is present in the AP configuration and for positive bias only. They show that the amplitude of the peak is inversely proportional to MgO thickness. They also estimated the decay rate as a function the MgO thickness and confirm that these IRS decay similarly to  $\Delta_1$  states. We'll see that this peak can also be ascribed to electrodes DOS effects ([section 2.2.1.2](#)), or localized states induced by impurities or defects ([section 2.4.2](#)).

We'll see in a coming section ([Section 2.1.3](#)) on interface Carbon contamination that interfaces can be chemically engineered and IRS tuned in order to obtain interesting device properties.

## 2.1.2 Interface oxidation

As it was briefly mentioned before, MgO is a good candidate as a tunnel barrier because it is relatively easy to grow and has stable chemical, mechanical and thermal properties. Moreover, MgO has a small lattice mismatch compared to bcc iron, and is predicted to be weakly interacting with the iron layer. Actually MgO is commonly used as a non-interacting substrate for studies on Fe layers. Although it is known that the Mg-O bond is energetically more favorable than the Fe-O bond, detailed chemical and structural studies of the Fe/MgO interface revealed the presence of a FeO layer<sup>74,75</sup> at the interface. Following experimental evidences of interface oxidation, [Zhang \*et al.\*<sup>76</sup>](#) studied its impact from first principle.

They based the structure of the interface on [Meyerheim \*et al.\*<sup>74</sup>](#) results and calculated the electronic structure and the tunneling conductance as a function of  $x$ , the oxygen concentration in the additional  $FeO_x$  interface layer. Their results are summarized in [Figure 2.3](#).

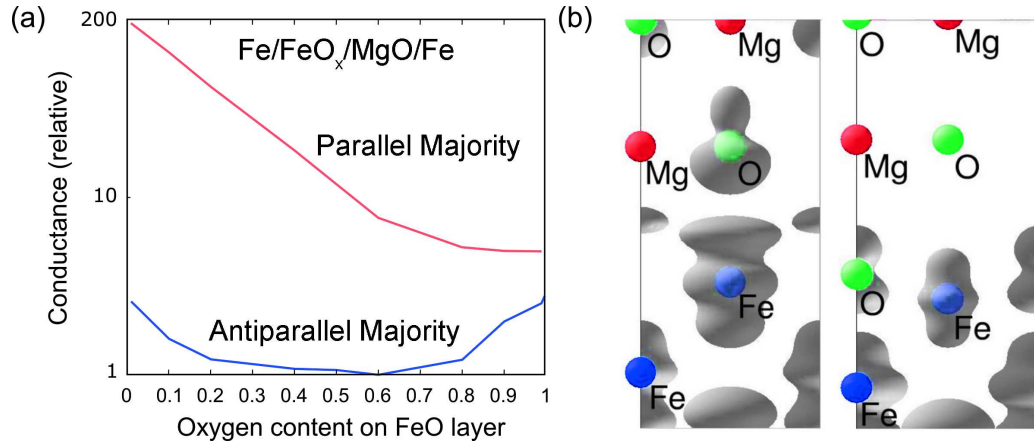


Figure 2.3: **Impact of interface oxidation:** (a) conductance as a function of oxygen content within the interface  $FeO_x$  layer and (b) the partial DOS of  $\Delta_1$  states in the minority spin channel in the interface region for both clean (left panel) and oxidized (right panel) interfaces. The interface oxidation dramatically reduces the parallel conduction channel for majority spins while it scarcely modifies the antiparallel channel. The TMR is expected to drop exponentially as the content of oxygen in the oxidized layer increases. Figure taken from *Zhang et al.*<sup>76</sup>.

Panel (a) plots the relative conductance in both parallel and antiparallel magnetic configurations as a function of oxygen concentration in the  $FeO_x$  layer. We can see that the main effect of the additional oxidized layer is the reduction of conductance in the parallel channel. In comparison, there are little changes in the antiparallel conduction channel.

The origin of this reduction can be found in panel (b) of Figure 2.3 that plots the partial DOS of  $\Delta_1$  states at the interface for both clean and oxidized interfaces. As it was previously mentioned, transport properties in Fe/MgO MTJs in the P state are mainly determined by  $\Delta_1$  electrons. It is crucial for these states to couple at the interface in order to effectively tunnel across the barrier.

As we can see from Figure 2.3b, the presence of the oxidized layer (right panel) strongly reduces the  $\Delta_1$  density of states in the interface interlayer region compared to the clean interface (left panel). As a consequence, the coupling of the  $\Delta_1$  states is affected, resulting in a reduction of conductance in the parallel magnetic configuration. In other words, the presence of oxygen at the interface strongly localizes the electron DOS within the FeO layer. The injection of electrode states is then carried through the oxygen atoms of the FeO and MgO layer that are mismatched, compared to the more favorable interface Fe-O overlap in the case of clean interfaces. The antiparallel channel, carried by  $\Delta_5$  ( $d$ ) electrons, is hardly modified because the injection of  $\Delta_5$  electrons in the barrier is little altered by the additional FeO layer.

More recently, *Bonell et al.*<sup>77</sup> experimentally studied the impact of interface oxidation on magnetotransport properties. In order to do so, the authors tuned the oxygen coverage of the topmost Fe layer of the bottom electrode by controlling oxygen adsorption prior to the barrier deposition. They also controlled the crystal quality of the as deposited

amorphous oxygen layer by thermal treatment. In doing so they are able to discriminate the detrimental impact of interface oxidation and interface disorder on magnetotransport. They report a decrease of TMR as the interface oxygen content increases. Corroborating Zhang *et al.*<sup>76</sup>'s prediction, they find that the TMR decrease is caused by a decrease of the parallel conduction channel, while the antiparallel conduction channel is barely altered. However, Zhang *et al.*<sup>76</sup> predicts a drastic effect of the oxidized layer on magnetotransport in Fe/MgO/Fe (001) MTJs, reducing the TMR from 4000 % to 100 %. Based on this assumption, many works explain the low experimental TMR values compared to theory in terms of interface oxidation. In their work, Bonell *et al.* suggest that although interface oxidation and disorder have a negative impact on TMR, they are not the principal source of the experimental vs theoretical discrepancy.

As a concluding remark, we note that the structure of the samples, and particularly its interfaces, is extremely sensitive to many parameters. Furthermore, the presence of the FeO layer is controversial as other groups confirmed very clean and sharp Fe/MgO interfaces<sup>78,79</sup>. As a consequence it is difficult to make general conclusions concerning the impact of an additional interface FeO layer. In general, accurate structural studies for each specific case is necessary. We will reassess this point from the vantage of a new operando technique that combines X-ray absorption spectroscopy (XAS) with spintronics in Chapter 6.

### 2.1.3 Effect of interface carbon contamination

Detailed experimental analysis of the Fe/MgO interface<sup>80</sup> revealed the presence of Carbon contamination at the bottom interface. It was determined that the additional C atoms originate from the single crystal MgO substrate on which the 50 nm-thick iron bottom electrode is deposited. A postdeposition thermal treatment is performed in order to improve the crystal quality as well as the surface flatness of the electrode. During the annealing step, the carbon atoms originally at the surface of the MgO substrate diffuse throughout the Fe layer and end up at the surface of the electrode.

It was first shown that it is possible to get a carbon-free Fe surface by adding an additional MgO trapping layer<sup>81</sup>, before the bottom electrode deposition, that prevents the C atoms' diffusion. In order to estimate the impact of additional carbon atoms at the bottom interface on spin dependent tunneling, magnetotransport experiments on clean and contaminated surfaces were carried out and results for both interfaces compared<sup>82</sup>. As we will see hereafter, the impact of Carbon on magnetotransport is rather complex and result in peculiar transport properties.

**Clean Fe/MgO interface:** Figure 2.4 summarizes results obtained on clean Fe/MgO interfaces. Panel (a) and (c) plot the TMR and its derivative as a function of bias voltage. The zero bias TMR reaches 150 % at room temperature, attesting to the good crystalline quality of the structure. The small asymmetry between positive (electrons injected from top to bottom electrode) and negative (electrons injected from bottom to top electrode) bias results from the difference in interface quality at both interfaces. These differences are inherent to the growth process, the top interface being of lower quality in general.

Panel (b) and (d) plot the conductance and the  $d^2I/dV^2$  spectra as a function of bias

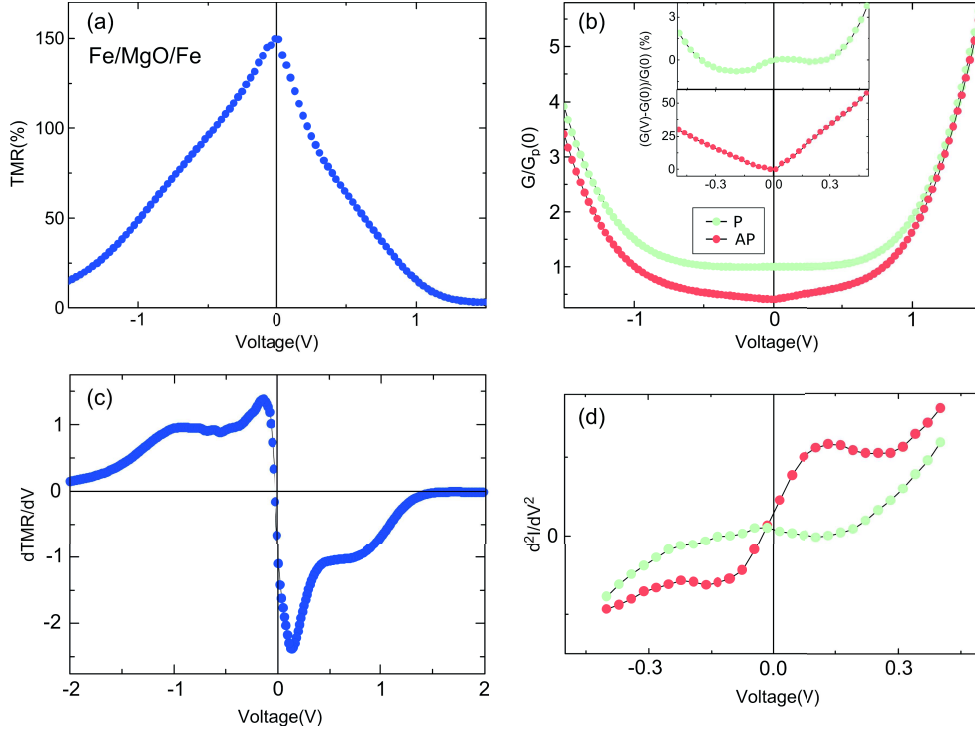


Figure 2.4: **Magnetotransport properties of Fe/MgO/Fe with clean interfaces:** TMR and its derivative are plotted in panels (a) and (c). The normalized conductance and current second derivative are plotted in panels (b) and (d) respectively. See text for more details. Figure taken from [Tiusan \*et al.\*](#)<sup>82</sup>.

voltage for both parallel (green) and antiparallel (red) magnetic configurations. In the low bias range (see inset of panel (b)), we can see a 40 % increase of the AP conduction channel compared to the zero bias conductance, while the P channel barely changes (+ 4 %). The two local minima in the P conduction channel around  $\pm 0.2$  V are attributed to DOS features of bcc Fe majority spin. Indeed, the top of the  $\Delta_5$  conduction band is  $\sim 0.2$  eV above  $E_F$  for a Fe electrode in a Fe/MgO/Fe MTJ. When the applied bias voltage becomes larger than this energy, no  $\Delta_5$  states are available in the collecting electrode anymore and the  $\Delta_5$  conduction channel is totally closed, resulting in a dip in the conductance (see [section 2.2.1.2](#) for more details). The amplitude of this minimum compared to the zero bias conductance quantifies the impact of  $\Delta_5$  electrons in the majority channel. Features at the same bias voltage can be seen in the  $d^2I/dV^2$  spectra of the P channel.

The strong increases of conductance in AP for  $|V| > 0.2$  V is ascribed to interface resonant states (IRS) at  $\sim 0.2$  eV (panel (d)), which in turn reduces the TMR in the same energy region (peaks in panel (c)). The impact of IRS was already addressed in [Section 2.1.1](#). In conclusion, the TMR decreases because (i) reduction of conductance in the P state due to closing of  $\Delta_5$  channel and (ii) matching of tunneling electrons with IRS at 0.2 eV in the AP channel.

**Fe-C/MgO interface:** [Figure 2.5](#) presents similar results for C contaminated surfaces. We can see that the TMR features in panel (a) and (c) are very different compared to

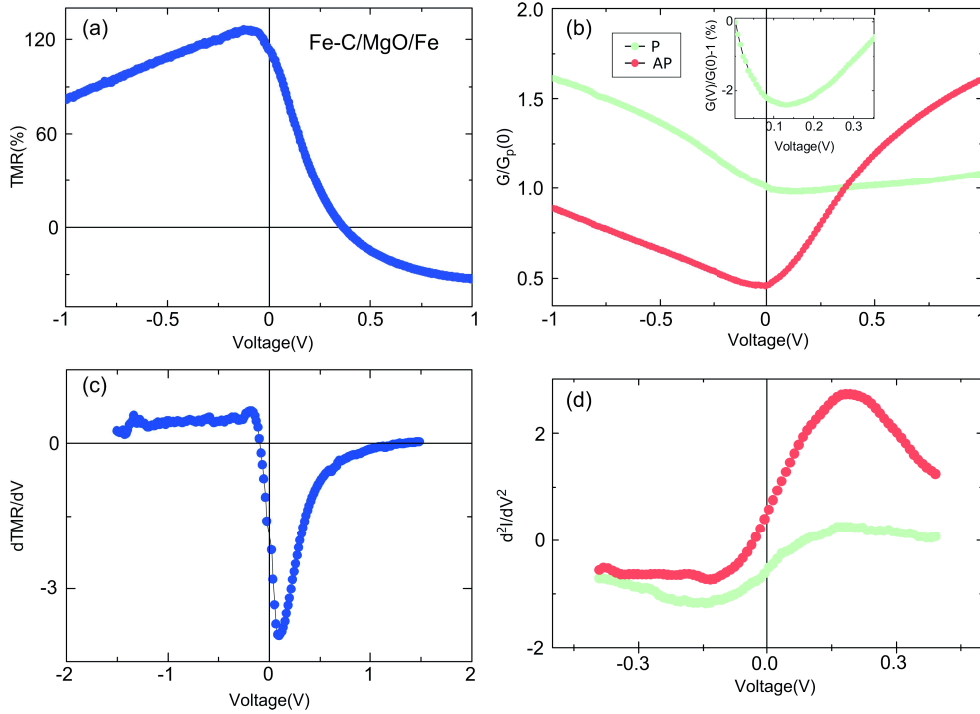


Figure 2.5: **Magnetotransport properties of Fe/MgO/Fe with carbon at the bottom interface:** Similar results as Figure 2.4 for carbon contaminated MTJs. See text for more details. Figure taken from Tiusan *et al.*<sup>82</sup>.

samples with clean bottom interface.

We note that the  $TMR(V)$  becomes strongly asymmetrical and has a maximum of 126%. For positive bias (electrons tunneling from top to bottom electrode), transport properties are again strongly influenced by the interface states. When the energy of tunneling electrons *matches* that of IRS (0.2 eV above  $E_F$ ), the AP channel dominates the P channel and the sign of TMR is inverted. For negative bias, the absence of a peak attests of the absence of IRS due to the lower crystal quality of the top interface compared to clean samples. The absence of IRS also results in a slower TMR decrease with increasing bias (the slow TMR decrease is not explained either, this point will be addressed in section 2.2.1.1).

Similarly to clean junctions, the conductance in the parallel magnetic configuration shows a local minimum for positive bias, (inset of panel (b)) but has a larger amplitude. The authors ascribe the TMR reduction as well as the stronger impact of IRS to the influence of the Fe-C bonds at the interface. Indeed, the Carbon atoms will interact with the Fe layer mainly through  $s$  and  $p$  bonds affecting  $\Delta_1$  states while barely impacting processes originating from  $d$ -like orbitals. The additional C atoms result in the reduction of  $\Delta_1$  transmission across the barrier, reducing the TMR and making transport properties more sensitive to the other conduction channels, e.g. IRS (originating from  $d_{z^2}$  orbitals) have more weight in the transport properties.

Finally, the maximum TMR is not centered around zero, and increases at small negative bias. This effect was already discussed by Zhang *et al.*<sup>83</sup>, that predicted an in-

crease of TMR with increasing bias voltage due to the contribution of electrons between  $[E_F, E_F + eV]$ . This contribution of this effect is usually dominated by IRS and other inelastic processes when they are present.

From the discussion of Section 2.1.1 on IRS and these experimental results, it appears that improving the interface crystalline quality increases TMR. However, concurrent to the improvement of coherent tunneling and symmetry filtering, improving crystalline quality also results in the apparition of IRS, which are known to be rapidly quenched or suppressed by interface disorder and impurities. In the non-equilibrium regime, when the applied bias voltage equals the energy of IRS,  $G_{AP}$  is strongly increased resulting in a sharp decrease of TMR within this energy range. It appears that adding carbon atoms at the interface does not significantly affect the interface quality but deteriorates  $s$ - and  $p$ -like states tunneling due to bonding of C with interface Fe atoms. This hypothesis is supported by the fact that IRS are still present and dominate the tunneling current when activated (inversion of TMR) while the zero bias TMR, which strongly depends on the tunneling of  $\Delta_1$  electrons ( $s$ ,  $p_z$  and  $d_{z^2}$  orbitals), is decreased but not suppressed. In conclusion, Carbon atoms affect the tunneling of  $s$  and  $p$  orbitals while allowing tunneling of  $d_{z^2}$  states that appear to have more weight in Fe-C/MgO samples.

A recent theoretical study<sup>84</sup> investigated the impact of Carbon on transport properties in Fe/MgO/Fe tunnel junctions. Their approach is similar to the theoretical treatment of a single FeO layer at the Fe/MgO interface discussed in Section 2.1.2. The authors considered the insertion of a single FeC layer and computed  $G_p$ ,  $G_{AP}$  and TMR for clean Fe/MgO/Fe as well as Fe/FeC/MgO/Fe MTJs. They find similar general trend as Tiusan *et al.*<sup>82</sup> experimental results, that is a strong increase of  $G_{AP}$  when the bottom interface is probed. They also confirmed that IRS could be activated when the applied bias voltage matches the energy of resonant surface states.

### 2.1.4 Impact of misfit dislocations

In Fe/MgO (001) tunnel junctions, it is generally favorable to be in the asymptotic limit in order to exploit the symmetry filtering effect of MgO at  $k_{\parallel} = 0$  and thus obtain the maximum TMR possible. Nevertheless, it is well established that above 5 or 6 monolayers of MgO the epitaxial strain that originates from the small lattice mismatch between the Fe layer and MgO (about 3.7%) is released, and misfit dislocations start to form<sup>62,85,86</sup>. In general, any lattice imperfection is expected to have detrimental effects on magnetotransport.

Bonell *et al.*<sup>87-89</sup> experimentally investigated the impact of dislocations on spin dependent tunneling in Fe/MgO/Fe MTJs. One way to decrease the dislocations density at the interface is to tune the lattice mismatch between the electrodes and the MgO barrier. Changing material in order to obtain a lower lattice mismatch compared to iron is possible, but the new electrode must keep the bcc structure, that is favorable to the symmetry filtering effect in the  $\Delta$  direction of the reciprocal space, and have comparable spin polarization.

An alternative and more elegant way to engineer the electrode properties while conserving its general characteristic is the use of alloys. Bonell *et al.*<sup>87</sup> used the bcc  $Fe_{1-x}V_x$  alloy, known to have a larger lattice parameter than Fe. When increasing the Vanadium content

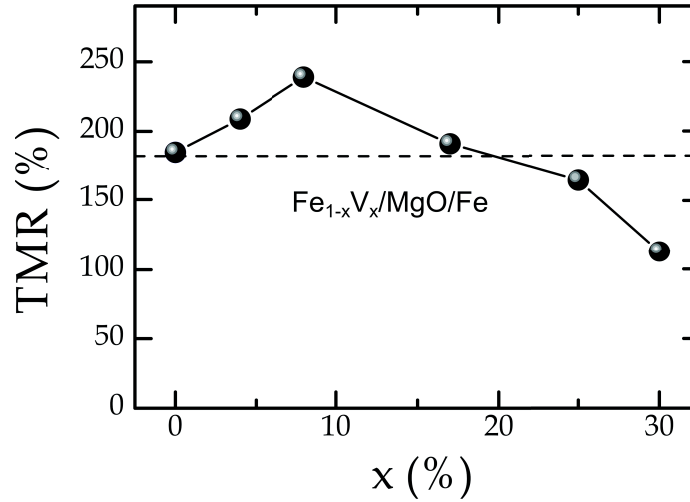


Figure 2.6: **Impact of interface dislocations on magnetotransport:** Plot of the room temperature TMR as a function of  $x$ , the Vanadium (V) concentration in the bottom  $Fe_{1-x}V_x$  electrode. The TMR is improved compared to the perfect Fe/MgO couple up to 20 % of Vanadium content, and starts to decrease for larger values of  $x$ . At first, the TMR increases because the density of dislocation decreases with increasing  $x$ . The beneficial improvements of crystalline quality has a stronger weight on magnetotransport than the detrimental impact due to the deterioration of the electrode electrical and magnetic properties. For  $x$  larger than 10 %, the reduction of spin polarization in the  $Fe_{1-x}V_x$  layer becomes the dominant effect and TMR starts to decrease. Figure taken from Bonell *et al.*<sup>89</sup>.

in the  $Fe_{1-x}V_x$  electrode, two changes have opposite effects on TMR: (i) as the concentration of V increases, the lattice mismatch between FeV and MgO layers decreases along with the density of dislocations and identical lattice parameters are obtained for  $x=70$  % and (ii) the saturation magnetization and spin polarization of the alloy electrode decreases with increasing  $x$ , the layer becoming almost nonmagnetic at  $x=50$  %.

The first point is expected to increase TMR values as decreasing the density of dislocations improves the overall crystalline quality and thus reinforces coherent tunneling and symmetry filtering. Concerning the second point, it is well established that reducing the spin polarization reduces the TMR, which is by definition related to the spin polarization. In order to distinguish the impact of both effects, the authors carried out a careful study by measuring the density of dislocation with high resolution tunneling electron microscopy (HR-TEM) and the impact of vanadium on the electrical and magnetic properties of iron by using spin resolved ultraviolet photoelectron spectroscopy (SR-UPS) and first principles calculations on the spin- and symmetry-resolved DOS of  $Fe_{1-x}V_x$  layers. Finally, electrical properties are measured as a function of Vanadium content.

Bonell *et al.*<sup>87</sup> measured the impact on magnetotransport as a function Vanadium content. Figure 2.6 plots the TMR as a function vanadium/Fe content in the FeV alloy. We can see that the TMR is improved from 180 % to 240 % for V content of  $x = 10$  % and decreases for larger V concentrations. Their results can be interpreted as follow: as we mentioned

previously the impact of vanadium content on TMR result from the competition between two effects. At first the TMR increases because the crystalline quality is improved while there is only little change to the electrical properties of the Fe layer. Above  $x = 10\%$  the deterioration of the iron layer spin polarization starts to be the dominant effect and TMR decreases monotonously with increasing  $x$ .

To summarize, Bonell *et al.*<sup>87</sup> show that the crystalline quality at the interface has a relatively strong impact on TMR. As they mention in their paper, dislocations seem to be localized defects but actually deteriorate the crystal structure over extended regions. Taking into account the deterioration of electrical properties due to V doping, one would expect an even larger TMR increase caused by improvement of interface structure.

### 2.1.5 Interface disorder from first principle

Velev *et al.*<sup>69</sup> theoretically considered the effect of disorder on the electrical properties of perfect and *symmetric* epitaxial MTJs. The aim of the paper was to discuss results obtained by Tusche *et al.*<sup>90</sup> on symmetric junctions for which very high TMR was predicted, principally due to the contribution of perfectly matched surface resonant states in the parallel magnetic configuration. However, as Velev *et al.*<sup>69</sup> correctly pointed out, IRS are rapidly quenched in the presence of disorder, resulting in lower TMR than predicted. In order to support their argument, Velev *et al.* studied the impact of disorder on surface states. In order to describe scattering due to disorder, they use a phenomenological approach by introducing a small random imaginary part to the energy that increases the damping of tunneling states. Although their result is not quantitative, it qualitatively supports their hypothesis.

Another phenomenological approach was used by Itoh<sup>91</sup> who considered the impact of lattice distortion within the MgO and at the Fe/MgO interface. We remind that misfit dislocations at interfaces are responsible for lattice distortion in extended region<sup>87</sup>. In general, their result are similar to Velev *et al.*, but are also in line with our discussion on surface resonant states. Indeed, the introduction of disorder quenches IRS in the parallel conduction channel while it increases the antiparallel conduction channel and thus reduces TMR.

More sophisticated tools were used to rigorously study the impact of disorder in the equilibrium<sup>92</sup> and non-equilibrium<sup>93</sup> transport regime. Probably due to the complexity of the calculations, both works considered the tunneling between two epitaxial Fe leads separated by a vacuum barrier. In order to introduce disorder, Xu *et al.* added single Fe atoms at the iron interface layers. Adding Fe atoms at the interface has two effects (i) it breaks the crystal periodicity, making the description of transport in terms of symmetry incorrect and suppressing resonant surface states, (ii) it reduces the width of the vacuum barrier and increases the conductance that has an exponential dependence on barrier thickness. In order to circumvent the latter effect, disorder is introduced by moving Fe atoms from the first interface to the second one so that the barrier width is unchanged on average. The studied system is  $\text{Fe}/\text{Fe}_{1-x}\text{Vac}_x/\text{Vacuum}/\text{Fe}_x\text{Vac}_{1-x}/$  where  $x$  represents proportion of atoms moved from the right lead to the left lead. For a given  $x$ , they calculated and averaged transport properties for several configurations.

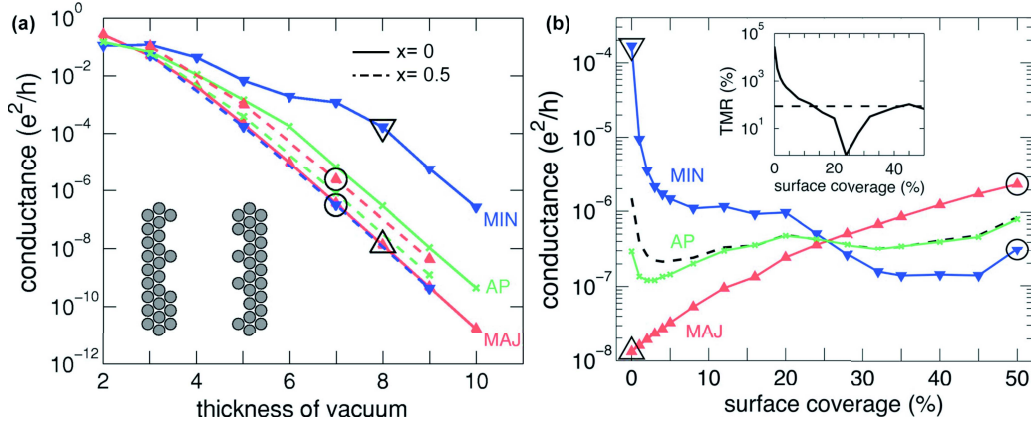


Figure 2.7: **Impact of interface disorder in the equilibrium regime:** Conductance as a function of vacuum barrier thickness for  $x = 0.5$  (maximal disorder) (a) and conductance and TMR as a function of interface disorder  $x$ . See text for more details. Figure taken from Xu *et al.*<sup>92</sup>.

Figure 2.7 compiles their results obtained in the equilibrium regime. Panel (a) plots the conductance as a function of the thickness of the vacuum barrier for perfectly flat MTJs and for  $x = 0.5$  (maximal disorder). We first concentrate on perfectly flat systems (solid lines) and immediately note the anomalous behavior of the minority channel in the parallel configuration  $G_P^{min}$  (solid blue line). As it was discussed before, this behavior originates from the matching of surface resonant states in symmetric models at zero bias voltage. We also remind that Xu *et al.*<sup>92</sup> performed their calculations for a vacuum barrier in which no symmetry filtering effects take place. For small thicknesses, we can see a non-exponential behavior for all conduction channel due to the impact of features away from the center of the 2D Brillouin zone ( $\bar{\Gamma}$  point or  $\mathbf{k}_{\parallel} = (0, 0)$ ). Above 6 monolayers of vacuum,  $G_P^{min}$  and  $G_{AP}^{min}$  decrease exponentially, as expected from the exponential dependence of tunneling current on barrier thickness.

The main difference for  $x = 0.5$  (dashed lines) is the absence of the anomalous behavior of  $G_P^{min}$  and the inversion of polarization of the P conduction channel as  $G_P^{min}$  become smaller than  $G_P^{maj}$ . However, the TMR remains positive because  $G_P$  is still larger than  $G_{AP}$ . This is a strong indication that IRS are mismatched by disorder.

In Figure 2.7b Xu *et al.* examined transport properties as a function of disorder  $x$ . We can see from the sharp decrease of  $G_P^{min}$  that IRS are quenched for a small amount of disorder. In general,  $G_P^{min}$  is decreased by three orders of magnitude, while  $G_P^{maj}$  steadily increases by two orders of magnitude with increasing disorder. Comparatively, the AP conduction channel is barely changed. Inset of panel (b) plots the dependence of TMR to  $x$ . TMR is also strongly reduced with interface disorder, with a minimum around 25 % coverage ( $x = 0.25$ ). In general, we note that disorder has a strong impact on TMR, above 5 % coverage the TMR is already below 1000 %.

Ke *et al.*<sup>93</sup> took the calculation one step further, and considered the impact of interface disorder on magnetotransport in the non-equilibrium regime. The model used is similar the one of ref<sup>92</sup> and similar results are obtained in the equilibrium regime.

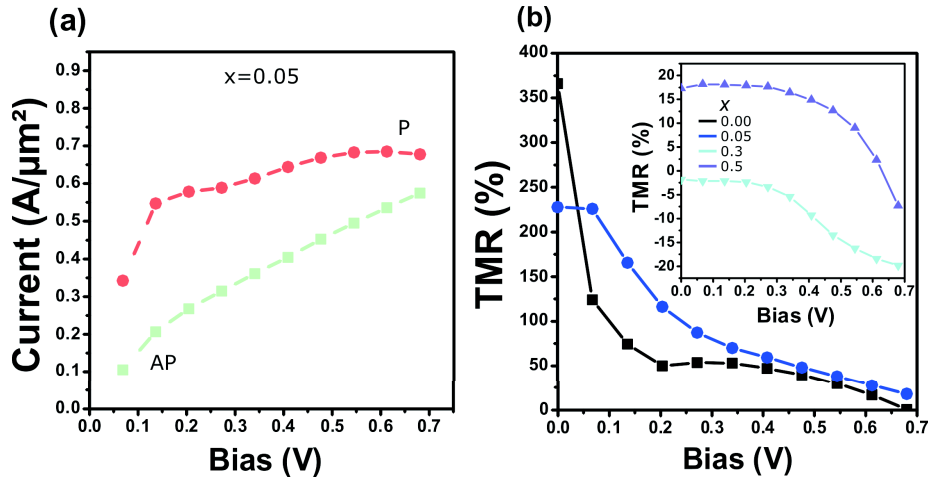


Figure 2.8: **Impact of interface disorder in the non-equilibrium regime:** Conductance (a) and TMR (b) as a function of bias voltage for various  $x$ , the proportion of atoms moved from the right electrode interface to the left electrode interface. See text for more details. Figure reproduced from *Ke et al.*<sup>93</sup>.

Panel (a) and (b) of Figure 2.8 plot the bias dependence of the conductance for  $x = 0.05$  and the TMR for various  $x$  respectively. For small disorder, e.g.  $x = 0.05$ , we can see that  $G_P$  and  $G_{AP}$  both increase with increasing bias voltage but the asymmetry between the two channels slowly decrease, resulting in a TMR drop.

Interestingly, they find that for clean interfaces, the TMR is higher but decreases faster with bias compared to disordered interfaces. Again this behavior is ascribed to IRS present at a perfect interface but are quenched when disorder is introduced.

In general, these results confirm that disorder has a strong impact on spin dependent tunneling. TMR is reduced because disorder allows scattering between otherwise independent conduction channels, reducing the effective spin- and symmetry-polarization. The detrimental impact of disorder on resonant surface states is also corroborated. We also remind that these works considered the tunneling in a vacuum barrier, so one has to be careful when drawing conclusions concerning tunneling in MgO from these results.

## 2.2 Effect of bias voltage

In order to characterize the electrical properties of MTJs, one has to perform electrical measurements, either by applying a bias voltage or a current. The most common way to do so is to measure electrical current as a function of applied bias voltage, resulting in the well-known  $I$ - $V$  characteristics. In the Fe/MgO/Fe MTJs, most experimental results established the fact that TMR decreases with increasing bias voltage due to a strong increase of the AP conduction channel. This is not always the case as some groups measured a TMR sign inversion or even TMR oscillations (but for doped interfaces)<sup>94</sup>. Additionally, *anomalies* at low bias are always reported, often refereed as zero bias anomalies (ZBA). The bias voltage dependence of TMR is essentially interpreted in terms of DOS effects as

well as inelastic processes. In this section we'll review bias induced changes to electric structure and transport properties of MTJs in order to accurately interpret these spectroscopic measurements.

First we'll discuss the effect of bias voltage on coherent tunneling. We'll see that applying a bias voltage induces changes in the potential landscape felt by tunneling electrons. The bias dependence as well as sharp features in the DOS of the ferromagnetic leads are also affecting transport properties. Secondly, the non-coherent tunneling regime will be considered, in particular we'll see that bias induced elastic and *inelastic* processes have a strong impact on magnetotransport. In order to discuss these anomalies, we'll briefly introduce inelastic electron tunneling spectroscopy (IETS), a powerful experimental technique used to investigate inelastic processes in magnetic tunnel junctions.

## 2.2.1 Impact of bias on coherent tunneling

### 2.2.1.1 Modification of the potential landscape

The first theoretical calculations on transport properties in magnetic tunnel junctions were always carried within the linear response regime. As a bias voltage is applied in a trilayer composed of two ferromagnetic electrode separated by a thin insulating spacer, the system enters a non-equilibrium regime and the aforementioned calculations are not valid anymore. Several groups tackled the problem of calculating transport properties of epitaxial MTJs at finite bias from first principle<sup>83,95-97</sup>.

It was shown that the main effect of applying a bias voltage is an accumulation of charge at interface layers. As it is emphasized by Zhang *et al.*<sup>83</sup> and later by Rungger *et al.*<sup>97</sup>, this charge accumulation doesn't significantly change the DOS of electrodes, except for a nearly constant shift in energy in the leads concurrent to a linear potential drop within the dielectric. These results are consistent with the rigid shift of the electrodes chemical potential  $\mu$ , usually considered to model the influence of bias voltage in non self-consistent approaches.

The effect of bias voltage on the potential landscape of MTJs is sketched in Figure 2.9. Note that this is a very simple sketch in which only the Fermi level of the electrodes is represented and the barrier is modeled by a simple rectangular potential step. Although this representation is oversimplified, it is often used to discuss qualitatively bias induced changes to tunneling transport. As we can see, applying a bias voltage results in two main changes: (i) the linear potential drop in the dielectric transforms the rectangular barrier into a trapezoid. As we'll see hereafter, this will modify the scattering probabilities of tunneling electrons. (ii) As the bias is increased and the chemical potentials in both electrodes are shifted relative to each other, more states tunnel out of the emitting electrode and more empty states in the collecting electrode are probed. This is represented by thick blue arrows in Figure 2.9. Note that if the bias voltage exceeds the interfacial barrier height, part of the dielectric becomes metallic and electrical transport enters the so called Fowler-Nordheim regime<sup>98</sup>. This effect will not be addressed in this thesis because the energy gap of MgO is large enough so that MTJs usually suffer electrical breakdown before being able to reach the necessary bias voltage.

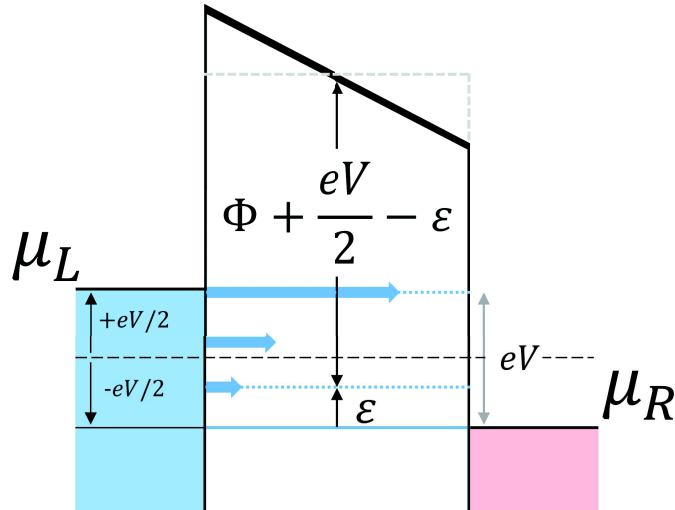


Figure 2.9: **Impact of Bias voltage on the potential landscape of tunnelling electrons:** Simple model to discuss bias induced changes to MTJs potential landscape and electrical properties. The bias voltage causes a simple shift in energy in the electrodes and a linear potential drop in the dielectric (verified from self consistent first principle calculations<sup>83</sup>). As bias voltage is increased, additional states below  $\mu_L$  in the left electrode can tunnel into the right electrode. Simple considerations show that filled states at  $\mu_L$  in the left electrode as well as empty states at  $\mu_R + eV$  in the right electrode dominate transport properties. Nevertheless, sharp feature in the DOS of electrodes should have a significant impact as they enter the bias window  $eV$ . See text for more details. Adapted from Voigtländer<sup>99</sup>.

As we can see from Figure 2.9, the electrodes chemical potential are shifted by  $\pm 1/2 eV$  relative to their absolute energy position for  $V = 0$ , where  $V$  is the applied bias. At zero bias, only states at  $\mu_{L,R}$  participate in the tunneling current. When a bias voltage is applied, states between  $\mu_L - eV$  and  $\mu_L$  in the left electrode will participate in the tunneling conductance. In a very simple approximation, the tunneling barrier height felt by tunneling particles in the left electrode can be written as  $\Phi + eV/2 - \epsilon$  (see Figure 2.9), where  $\epsilon$  represents the energy of tunneling particles relative to  $\mu_R$ . Electrons at  $eV/2$  below  $E_F$  will feel the equilibrium barrier height, that is  $\Phi$ . For tunneling carriers above (below)  $eV/2$ , the barrier height will be decreased (increased) compared to the equilibrium value. As a result, the main contribution still arises from carriers at  $\mu_L$  for which the interface barrier height is  $\Phi - eV/2$ . On the other hand, the barrier height felt by electrons in the left electrode at the same level as  $\mu_R$  is equal to  $\Phi + eV/2$  resulting in a reduced scattering probability. However, even if the scattering probability is reduced below  $\mu_L$ , sharp features in the DOS should still have a significant impact on electrical transport when they enter the bias window.

Concerning this matter, it is interesting to consider the work Valenzuela *et al.*<sup>100</sup> on spin dependent tunneling. They used a clever non-local architecture to discriminate the effect of tunneling *in* or *out* of a ferromagnetic material. Combining their results with a

simple theoretical model, they found that, when tunneling out of the FM layer, the main contribution to tunneling current arises from strongly polarized electrons at and slightly below the Fermi energy. When tunneling *in* the FM, hot electrons are probing states above  $E_F$ , the spin population asymmetry of these states is not as large as states at  $E_F$  resulting in a depressed spin selectivity and thus lower TMR. Other inelastic processes due to hot electrons and detrimental to TMR will be considered in the following section.

To summarize, applying a bias voltage across the heterostructure modifies the potential landscape, reducing the interface barrier height felt by tunneling electrons at the Fermi energy. As the bias voltage is increased, additional states are allowed to tunnel. The interface barrier height felt by tunneling particles increases with their energetic distance to the Fermi energy. As it is pointed by Valenzuela *et al.*<sup>100</sup>, as the bias voltage is swept, tunneling electrons at the Fermi energy in the emitting electrode probe empty states at  $E_F + eV$  in the collecting electrode. Consequently the current intensity as a function of bias voltage should be related to the electrodes' DOS.

### 2.2.1.2 Density of states effects

We remind that transport properties in the coherent and equilibrium regime are explained in terms of band structure matching across the whole heterostructure. As bias voltage is swept and the voltage window increased (represented by  $eV$  in Figure 2.9), it is possible to open or close conduction channels by matching (mismatching) bands of compatible symmetry between both electrodes. Although the transmission of lead states are weighed by their transmission probability (that depends on barrier height), bias induced DOS effects arise from intrinsic properties of the ferromagnetic electrodes. As a consequence, it is possible to relate peaks in the conductance to sharp features, like band edges or interface resonant states, in the DOS.

To illustrate this fact, we represent in Figure 2.10 the bias window induced by a bias  $U = 2 V$  on the spin- and symmetry-resolved band structure of bcc Fe, for a device parallel magnetic state. The same drawing for the antiparallel magnetic states is represented in Figure 2.11. The red and blue regions represent filled and empty states respectively and the dotted line correspond to the Fermi energy  $E_F$ . The colorshading emphasize the fact that transport properties are mainly defined by tunneling electron at  $E_F$  and empty states in the right electrode at  $E_F + eV$  (opaque red and blue). Filled states lying below  $E_F$  in the left electrode have a lower tunneling probability. Since we are in the coherent regime (conservation of energy), states below  $\mu_R + eV$  are less likely to be probed (transparent red and blue). Green circles emphasize sharp regions of DOS where changes in the tunneling current should be visible.

We first consider the case of the majority conductance in the parallel magnetic configuration,  $G_P^{\uparrow\uparrow}$  (Figure 2.10 left panels). When a small Bias is applied, more  $\Delta_1^{\uparrow}$  states in the emitting electrode are able to tunnel into available  $\Delta_1^{\uparrow}$  in the counter electrode and  $G_P^{\uparrow\uparrow}$  is expected to increase. When the bias is further increased, tunneling electrons start to probe states above  $\Delta_5$  and  $\Delta_{2'}$  bands in the collecting electrode (green circle in the right panel of  $G_P^{\uparrow\uparrow}$ ). Because no  $\Delta_{5,2'}$  states are available in the collecting electrode, the corresponding conduction channels are closed and  $G_P$  is expected to decrease. Note that the

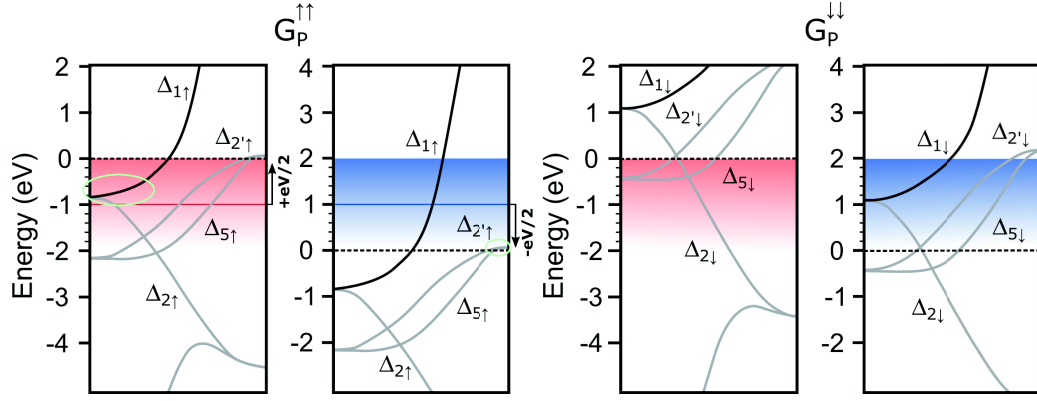


Figure 2.10: **Impact of bias voltage related to the band structure of the ferromagnetic leads:** Bias window induced by a bias  $U = 2\text{ V}$  on the spin- and symmetry-resolved band structure of bcc Fe for the parallel magnetic state and for both spin channels. As the bias is swept, tunneling electrons at  $E_F$  in the emitting electrodes probe the density of states of the collecting electrode. Sharp features in the density of state, emphasized by green circles, are expected to have a strong impact on  $G_P$  and  $G_{AP}$ . See text for a detailed discussion.

the main contribution to  $G_P$  comes from the tunneling of  $\Delta_1$  states such that the closing of  $\Delta_{5,2'}$  channels should have a minor impact.  $G_P^{\uparrow\uparrow}$  is expected to increase rapidly until the  $\Delta_1^{\uparrow}$  band edge in the emitting electrode enters the bias window (green circle in the left panel of  $G_P^{\uparrow\uparrow}$ ) resulting decrease of  $G_P^{\uparrow\uparrow}$  because the number of additional conduction channels with increasing bias is reduced.

Another strong impact of the DOS structure is expected in the majority conductance of the antiparallel magnetic configuration,  $G_{AP}^{\uparrow\downarrow}$  (Figure 2.11 left panels). Once the minority  $\Delta_1^{\downarrow}$  enters the bias window ( $\sim 1.2\text{ eV}$  above  $E_F$ ), the conductance should increase as  $\Delta_1^{\uparrow}$  states are able to tunnel into  $\Delta_1^{\downarrow}$  in the AP conduction channel (reversed spin referential). In this bias range, the conductance of  $G_{AP}$  should be similar to that of  $G_P$  resulting in a quenched TMR.

One more feature should be visible in  $G_{AP}^{\downarrow\uparrow}$  (Figure 2.11 right panels). The tunneling conductance in this channel is mostly carried by  $\Delta_{5,2'}^{\downarrow}$  tunneling into  $\Delta_{5,2'}^{\uparrow}$  states, but when the bias voltage exceeds  $\sim 0.2\text{ eV}$  the bands are mismatched and  $G_{AP}^{\downarrow\uparrow}$  is expected to decrease. Finally, the conduction of the minority channel is not characterized by sharp features.

We emphasize that this discussion is based on simple approximations as one should consider interface rather than bulk DOS (for example IRS are not considered here) as well as the changes in tunneling probability. A full quantitative discussion is given in [Runger et al.](#)<sup>97</sup>.

The general results obtained from first principle calculations in the non-equilibrium regime, applied on clean interfaces and in the ultrathin tunneling regime<sup>97</sup>, can be summarized as follows: The zero bias parallel conduction channel is dominated by the minority spin channel  $G_P^{\text{min}}$  because of interface resonant states, resulting in TMR of several thousand percent. When a small bias voltage is applied ( $< 100\text{ mV}$ ),  $G_P^{\text{min}}$  decreases dramati-

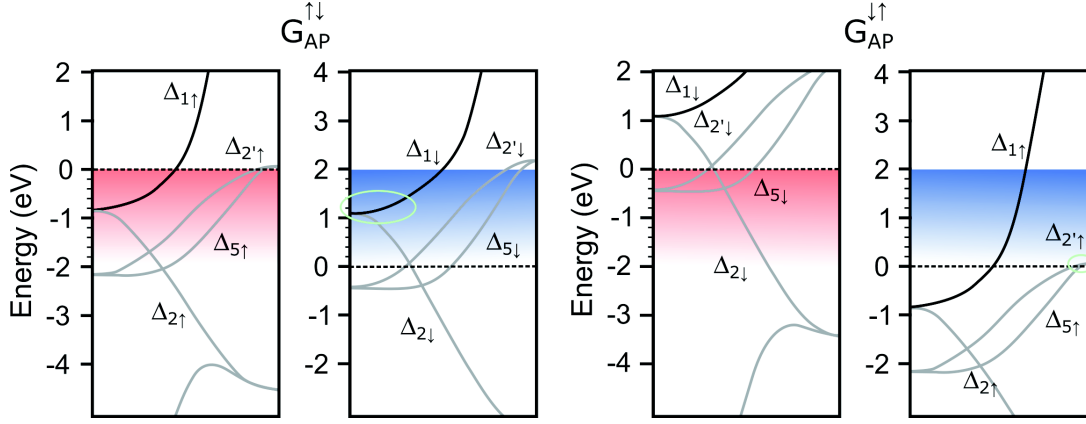


Figure 2.11: **Impact of bias voltage related to the band structure of the ferromagnetic leads:** Similar drawing as Figure 2.10 for the AP magnetic state. See text for more details.

cally due to IRS mismatch, producing a strong TMR decrease in the very small bias range. As discussed previously in this thesis (see section 2.1.1), this feature is likely absent in real junctions, at least in the parallel conduction channel, and the zero bias TMR should be lower than predicted in ref<sup>97</sup>, and the TMR decrease smoother. Between 0.1 V and 0.3 V, the increase in  $G_P$  is nearly constant while  $G_{AP}$  decreases resulting in a slow TMR increase within this bias range. The decrease of  $G_{AP}$  is due to the  $\Delta_{5,2}^{\uparrow\downarrow}$  bands mismatch in the minority channel as discussed previously. The high bias region is characterized by a slowing down in the  $G_P$  increase rate, while  $G_{AP}$  increases faster with a sharp increase at 1.5 V coincident with a quenching of TMR. The sharp increase of  $G_{AP}$  above 1.5 V is due to the matching of the  $\Delta_1^{\uparrow}$  and  $\Delta_1^{\downarrow}$  bands as schematized in Figure 2.11 left panels. In Figure 2.11, the  $\Delta_1^{\downarrow}$  lies  $\sim 1.2$  eV above  $E_F$ , one would then expect an impact at 1.2 V but we remind that (i) Figure 2.10 and Figure 2.11 plot bulk DOS of bcc Fe, whereas interface states should be considered and (ii) the correspondence of sharp features in the DOS don't have a one to one correspondence to the tunneling probability, DOS features can impact tunneling current at slightly different bias voltages.

At first sight, these result seems inconsistent with experimental measurements. Indeed, all experimental data indicate a decrease of TMR with increasing bias voltage. Moreover, the increase of TMR in the low bias region has never been observed in Fe/, CoFe/ nor CoFeB/MgO/Fe MTJs to our knowledge. However, we should emphasize that these calculations are limited to coherent tunneling only. In the following section, we'll see that various inelastic processes are involved in the non-equilibrium regime, especially at low bias. In general, these processes have a detrimental impact on spin dependent tunneling and could possibly compensate the small coherent TMR increase predicted in the 0.1-0.3 V range.

Our discussion of DOS features concerned Fe/MgO/Fe MTJs. In the case of CoFeB/MgO MTJs, after the annealing step, a CoFe alloy is expected to form at the interface with MgO. Several works<sup>101,102</sup> investigated the symmetry resolved band structure of  $\text{Fe}_{1-x}\text{Co}_x$ . These works suggest that the minority  $\Delta_1^{\downarrow}$  band lies closer to the Fermi energy in  $\text{Fe}_{1-x}\text{Co}_x$

alloys and thus the opening of the  $\Delta_1$  conduction channel in the AP magnetic state is expected to occur at lower bias voltages.

## 2.2.2 Bias induced inelastic processes

The previous section focused on bias induced changes to coherent tunneling, i.e. on elastic and intrinsic properties of MTJs. In this section, we'll review other ways for tunneling particles to scatter across MTJs. These processes, may they be intrinsic or extrinsic, will interact with charge carriers in a way that will modify the otherwise conserved particle properties, i.e. its energy, spin or symmetry.

These processes are hard to take into account in first principle approaches and are generally investigated by developing empirical models which are then confronted to experimental results.

### 2.2.2.1 Inelastic electron tunneling spectroscopy

As the name suggests, Inelastic electron tunneling spectroscopy (IETS) uses quantum tunneling itself to probe inelastic processes in tunnel junctions. In elastic and coherent tunneling, electrons in the emitting electrode are directly transmitted into the collecting electrode. In the process, only the amplitude of wavefunctions is exponentially reduced within the dielectric material, i.e. incoming wavefunctions are transmitted to the collecting electrode with a small probability but the particle's energy, spin and symmetry are conserved. Unlike elastic tunneling, inelastic processes are characterized by the fact that tunneling particles lose energy due to interactions with additional degrees of freedom in the system.

As we'll see in the following, additional degrees of freedom originate from various intrinsic and extrinsic properties of the heterostructure under study. For example, electrons can interact with lattice vibrations (phonons), collective spin wave excitations (magnons) or interface impurities but also with quantum well states present in the collecting electrode or trapping states (due to structural defects) within the dielectric.

The main impact of inelastic processes is that they create additional tunneling paths that will add to the coherent conduction channel, except for trapping states that will be considered separately. However, in order for the tunneling particles to interact with a vibrational mode, their energy should be at least equal to that of the mode. In other words, there is an energy *onset*  $E$  for which inelastic processes are activated, and a change of the tunnel current is expected at this precise energy. Similarly, vibrational modes have an energy *cutoff*  $E_m$  that depends on intrinsic properties of the electrode and barrier materials. In the case of ferromagnetic materials, it was shown that the energy cutoff of magnons is related to the Curie temperature of electrodes,  $E_m = 3k_b T_C / (S + 1)$  where  $T_C$  is the effective Curie temperature. For example,  $E_m$  is estimated to be  $\sim 165 \text{ meV}$  in CoFe<sup>103</sup>. In MgO based MTJs, the impact of phonons and magnons are generally limited to the  $\pm 300 \text{ mV}$  bias range.

The working principle of IETS is schematized in [Figure 2.12](#). As the bias is swept and the energy of electrons is sufficient to activate additional conduction channels, the rate of tunneling current is accelerated, resulting in a small step in the first derivative

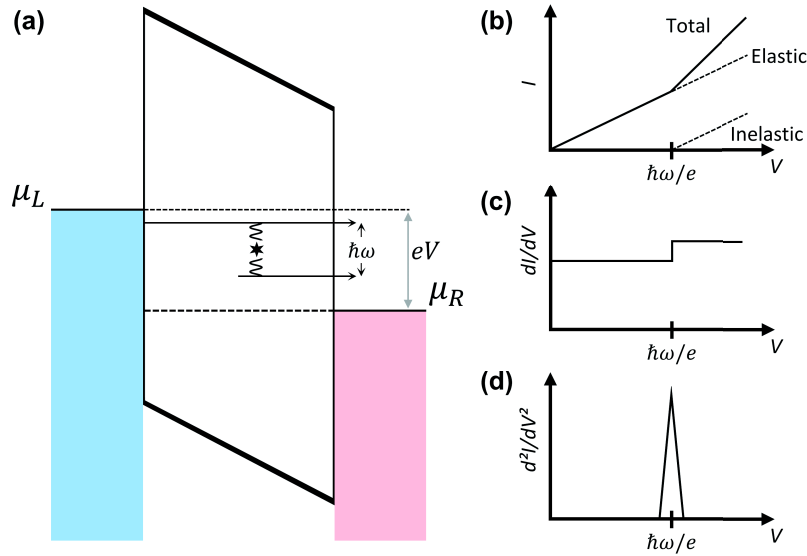


Figure 2.12: **Principle of inelastic electron tunneling spectroscopy:** (a) Both elastic and inelastic tunneling processes are represented. In inelastic processes, tunneling particles lose energy due to interaction with vibrational modes in the system. The additional conduction channel is opened only when the energy of the tunneling particle equals the one of the vibrational mode, i.e. when  $eV = \hbar\omega$ . Panel (b), (c) and (d) sketch the impact of this additional channel on  $I(V)$ ,  $dI/dV$  and  $d^2I/dV^2$  respectively. A feature is apparent at  $V = \hbar\omega/e$ , note that the signal is more prominent in the second derivative.

and in a sharp peak in the second derivative as represented in panels (b), (c) and (d) of Figure 2.12. Note that we represented a linear dependence between the current and the bias voltage. Although oversimplified, this approximation is true at low bias. For larger bias, an additional nonlinear background is superimposed onto IETS peaks.

The measurement principle is very simple: a modulation voltage is superimposed onto a constant bias voltage. The signal measured at first and second harmonic of the oscillation frequency are directly proportional to current first derivative and second derivative respectively. The second derivative is sometimes computed numerically. The measurement can be carried out by a lock-in technique that has better signal-to-noise ratio compared to conventional  $I$ - $V$  because noise signal at frequencies other than modulation frequencies are rejected.

The resolution of IETS is limited by temperature ( $k_bT$ ), which is related to thermal smearing of electrodes Fermi energies, as well as modulation voltage ( $V_m$ ). It was determined that the full width at half maximum (FWHM) of IETS peaks scale as  $5.4 k_bT$ , resulting in an energetic resolution of  $2 mV$  at 4 K and  $140 mV$  at room temperature. Generally, IETS measurement are carried at the lowest temperature possible. The modulation voltage is also detrimental to IETS resolution. However,  $V_m$  cannot be arbitrarily reduced because the IETS signal, and thus the signal-to-noise ratio, are related to  $V_m$ . The modulation voltage is usually chosen to be equal to  $5.4 k_bT$  in order to obtain the best resolution

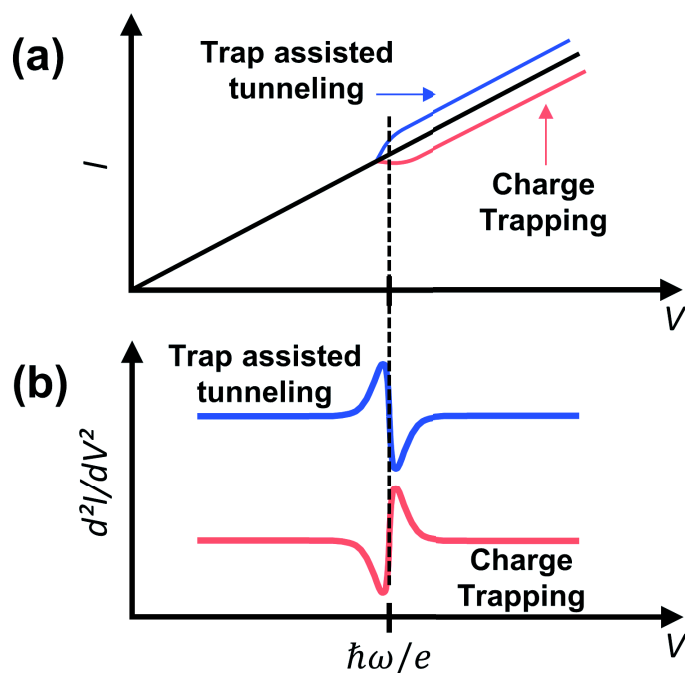


Figure 2.13: **Impact of trapping states on tunnel transport:** Trapping states impact the tunnel current in two ways: (i) they promote trap-induced tunneling, a process that increases the tunnel current and (ii) they induce charge trapping that slows down the current increase. The impact of both processes on  $I(V)$  and  $d^2I/dV^2$  are sketched in panels (a) and (b) respectively. The two processes can be distinguished in IETS spectra because they are always characterized by a peak-dip couple. Adapted from He and Ma<sup>107</sup>.

with the best signal to noise ratio.

When a bias is applied, electrons will tunnel in the collecting electrodes as hot electrons. They can either absorb magnons or phonons in the emitting electrode or emit magnons or phonons in the collecting electrode. At low temperature, the density of magnons and phonons is low, making the latter process more likely. It is often supposed that IETS probes inelastic processes in the positively biased (collecting) electrode.

One of the best advantages of IETS is its sensitivity. For example, IETS is widely used to measure molecular vibrational modes of adsorbates at interfaces of Metal-Insulator-Metal structures<sup>104–106</sup>. A small amount of molecules at one interface, typically  $< 1 ML$ , is sufficient to get a nice IETS spectrum.

Recently, electron tunneling spectroscopy was used to investigate trapping states within the oxide barrier of metal-oxide-semiconductor (MOS) devices<sup>108–110</sup>. Trap states can impact the tunneling current in two opposite ways: (i) trap assisted tunneling, process that increase the tunnel current and (ii) charge trapping, mechanism that slows down the increase of tunnel current. Panel (a) and (b) of Figure 2.13 represent the impact of both effects on tunnel current and its second derivative respectively. The signature of trapping states is different compared to other inelastic processes. While other contributions are

characterized by single peaks, trap induced changes are always characterized by a peak-dip couple. We'll see that this approach can easily be extended to magnetic tunnel junctions.

IETS's main disadvantage is that, in order to be identified, peaks have to be compared to other spectroscopic data. For example, to study vibrational modes of molecules IETS spectra have to be compared to optical measurements. In the case of MTJs, one has to carefully consider the electrodes and barrier phonon spectra as well as interface magnon in the ferromagnetic leads. Another difficulty, inherent to the technique, is that many effects are convoluted in the IETS spectra. The previously discussed *coherent* features as well as inelastic processes both shape the IETS spectra.

Nevertheless, it might be possible to discriminate some of the peaks by careful considerations. For example, it is possible to change the electrodes material to ascertain the position of phonon and magnon or discriminate DOS features. As we'll see in the next section, theoretical models were also developed in an attempt to explain the bias and temperature dependence of MTJs magnetotransport properties.

More generally, the designation *inelastic electron tunneling spectroscopy* can be reduced to electron tunneling spectroscopy (ETS). Indeed, the technique uses the fundamental quantum mechanical tunneling process itself to probe elastic, inelastic, intrinsic and extrinsic features in a tunneling device. The main advantage of the technique is that it can probe interface properties and other buried structures, otherwise hard to characterize with conventional means, with high sensitivity.

More details can be found in ref<sup>104–106,110</sup> and references therein.

### 2.2.2.2 Zero bias anomaly, phonons and magnons

Zhang *et al.*<sup>111</sup> first tried to explain the fast TMR drop at low bias in AlO, Al<sub>2</sub>O<sub>3</sub>, AlO<sub>x</sub> ...-based magnetic tunnel junctions. They derived an expression for the contribution of magnetic excitations (magnons) on the tunnel current and showed that the magnon contributions to  $G_P$  and  $G_{AP}$  conduction channel are linear with increasing bias voltage, but with a stronger contribution in AP that results in a TMR decrease. They didn't explicitly calculate the contribution of magnons, but rather derived an empirical expression to fit experimental data. The model was used to investigate amorphous AlO<sup>112</sup> MTJs and extended to study MgO based MTJs<sup>113</sup>.

Nevertheless, Wei *et al.*<sup>114</sup> later showed that magnon assisted tunneling alone couldn't explain sharp peaks observed at very small bias. In order to improve Zhang's model, they considered the impact of magnetic impurity scattering already developed decades ago to explain the so called zero bias anomaly (ZBA) in metal-insulator-metal structures. They compare IETS spectra measured on CoFeB/MgO and CoFeB/AlO MTJs and show that magnon contribution in both devices are similar. The main difference between the two stacks is the impurity induced peak at very low bias. In MgO, the splitting of the peak is ascribed to the antiferromagnetic coupling of magnetic impurities to electrodes magnetization. This coupling is supposedly absent in AlO based MTJs. In order to reinforce the validity of their model, they determined all the parameters of their model at low temperature, and successfully fitted data at higher temperatures.

Similarly, Bratkovsky<sup>115</sup> investigated the impact of phonons on tunnel transport and

showed that, conversely to magnon assisted tunneling, phonon assisted processes conserve the spin of electrons. Consequently,  $G_P$  is expected to increase faster than  $G_{AP}$  resulting in a TMR increase. [Dimopoulos \*et al.\*<sup>116</sup>](#) used a model that combine both magnon and phonon contributions to fit experimental data. Phonons are believed to attenuate the detrimental effect of magnon assisted inelastic processes.

It is also noteworthy to mention the work of [Du \*et al.\*<sup>117</sup>](#) on fully epitaxial Fe/MgO/Fe MTJs. The authors measured IETS spectra as a function of MgO thickness for various temperatures and magnetic fields. Interestingly, they saw very little change in IETS peak positions. The fact that IETS spectra are thickness and sample independent suggests that scattering processes and interference of tunneling states in the tunneling barrier are negligible. Moreover, the fact that peaks are insensitive to temperature and magnetic field implies that features in IETS spectra are not due to magnon nor phonon processes. In order to identify the underlying processes behind IETS peaks, they calculated transport properties in the non-equilibrium regime for perfect Fe/MgO/Fe, Fe/FeO/MgO/Fe and Fe/MgO/Vacancy/MgO structures and compared experimental results to theoretical predictions. They find that it is possible to relate IETS peaks to changes induced by oxygen contamination at the bottom interface and the presence of oxygen vacancies at the top interface.

On the one hand, these empirical models are useful to determine if a given inelastic process might impact the tunnel current. On the other hand, the fact that they can more or less fit experimental data in which the number, position and intensity of peaks are different shows the limitations of these approaches. Another approach to extract qualitative information of IETS spectra is to carry systematic studies as a function of some parameters of the system.

[Ando \*et al.\*<sup>118</sup>](#) measured IETS spectra in single crystal Fe/MgO/Fe as a function of MgO spacer thickness  $t_{MgO}$ . The  $I(V)$  second derivative as a function of bias voltage and  $t_{MgO}$  for both magnetic configuration are presented in [Figure 2.14](#). In panel (a), the IETS spectra of  $\Delta G_{AP}$  is slightly asymmetric due to the asymmetry of interface quality. More interestingly, they evidenced a feature appearing around 1V in the AP channel for thicker barriers. They argue that DOS effects should become more prominent as the thickness of the barrier increase and thus ascribe this peak to the matching of  $\Delta_1^\uparrow$  and  $\Delta_1^\downarrow$  bands as discussed in [section 2.2.1.2](#). However, trap assisted tunneling due to localized states in the dielectric can also play a role for large thicknesses.

Additionally, they evidenced clear oscillations in  $\Delta G_P$  (see panel (b)). Since peaks position are independent of MgO thickness, interference of tunneling states in the barrier can be ruled out. Moreover, the Fe DOS doesn't show sharp features in this bias region. Finally, they verified that these peaks are not related to molecular vibrational modes that could arise from interface contamination during the growth process. While they didn't clearly identify the origin of these oscillations, the authors propose that IRS can have a complex structure that could possibly account for such oscillations. We note that this can be due to quantum well states present in the collecting electrode (see [Section 2.2.2.3](#)).

[Nishioka \*et al.\*<sup>119</sup>](#) used bcc Co electrodes coupled to a MgO tunnel barrier. As it is expected, they find a peak at 0.5 V that is not present in MTJs with Fe electrode. This peak is a signature of Co DOS and is related to the  $\Delta_1^\uparrow$  and  $\Delta_1^\downarrow$  bands matching of  $G_{AP}^{\uparrow\downarrow}$  that occurs

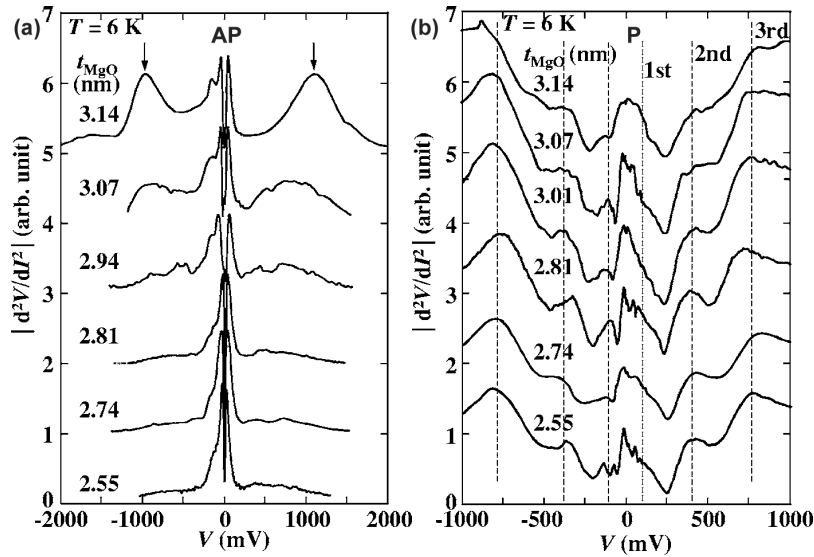


Figure 2.14: **IEST spectra of single crystal Fe/MgO/Fe MTJs:** IETS measured in (a) AP and (b) P magnetic configurations. In AP, sharp peaks at very low bias are ascribed to impurity scattering, while the shoulder at 0.2 meV is attributed to inelastic scattering by interface dislocations. Additionally, a DOS feature appears around 1 eV for thicker MgO. In the parallel magnetic state, oscillations of IETS spectra are tentatively ascribed to the complex DOS of interface states, but can also be explained by quantum well states in the collecting electrode. Reproduced from Ando *et al.*<sup>118</sup>

at 1.2 V in Fe (see section 2.2.1.2).

**Characteristics of CoFeB/MgO MTJs:** As it was quickly reviewed in Section 1.4, the highest TMR in MgO-base MTJs are obtained in sputtered CoFeB/MgO/CoFeB magnetic tunnel junctions with values reaching 600 % at room temperature and more than 1100 % at low temperature<sup>18,66</sup>. As discussed in Section 1.4, the CoFeB/MgO architecture takes advantage of the fact that the sputtered MgO grows with a (001) texture on amorphous CoFeB layers. In this system, an effective spin filtering effect is obtained by post growth-annealing, a necessary step to crystallize the electrodes, improve the MgO crystal quality and sometimes pin one of the electrodes with an antiferromagnetic layer by exchange coupling. Typically, the TMR ratio first increases with annealing temperature ( $T_a$ ) reaching a maximum and decreasing for higher  $T_a$ , see Figure 2.15. This behavior stems from the competition between crystal structure improvements, i.e. interface crystallization as well as MgO crystal structure<sup>120,121</sup>, and diffusion processes of light elements across the heterostructure. For example, the TMR in CoFeB/MgO pseudo spin valves (PSV) was greatly improved by removing the IrMn antiferromagnetic layer required in exchange biased samples, thus suppressing Mn atoms diffusion<sup>65</sup>. The diffusion of Boron present in the electrodes is more controversial. It is established that a CoFe layer is created at the interfaces with MgO while B is *pushed out* of the electrodes<sup>123</sup>. Two B diffusion scenarios are discussed in the literature: (i) Boron atoms diffuse at the interfaces and within the MgO

barrier, resulting in interface and bulk impurities or in a MgBO layer at the interface<sup>124–126</sup> or (ii) B atoms segregate into neighboring Ta layers, resulting in very clean and defect free CoFe and MgO layers as well as sharp and impurity free interfaces<sup>123,127</sup>. Ta atoms are expected to diffuse at higher temperatures compared to B and Mn. Nevertheless, it was shown that preventing Ta diffusion by increasing electrodes thickness was improving magnetotransport properties. This support the fact that Ta diffuses even at relatively small annealing temperatures<sup>18</sup>.

Briefly, due to their unrivaled TMR performance, CoFeB/MgO MTJs are systems of choice to study fundamental aspects of spin dependent tunneling across MgO. But the impact of the annealing step is complex<sup>128,129</sup> and depends strongly on the type of structure studied. In particular, in exchange biased samples that are required for device applications, additional layers required to establish a well defined AP state makes detailed and systematic studies more difficult.

Concerning DOS effects, the band structure of CoFe has to be taken into account. Although the nominal Co concentration in the CoFe layer is known, the structure and the alloy composition at the interface is hard to characterize, making comparison to calculated transport properties or DOS difficult. Any interpretation of magnetotransport studies in such samples should be backed with detailed knowledge of electrodes, MgO barrier and interface crystal structure.

Keeping in mind these distinctive characteristics of CoFeB/MgO MTJs compared to Fe/MgO/Fe structures, we'll discuss several IETS studies measured on this system.

**IETS in CoFeB/MgO MTJs:** We first present Drewello's<sup>130</sup> results on CoFeB MTJs. We discuss this paper first because their IETS spectra present almost all the features discussed in the literature. The authors prepared three samples with different structure: sam-

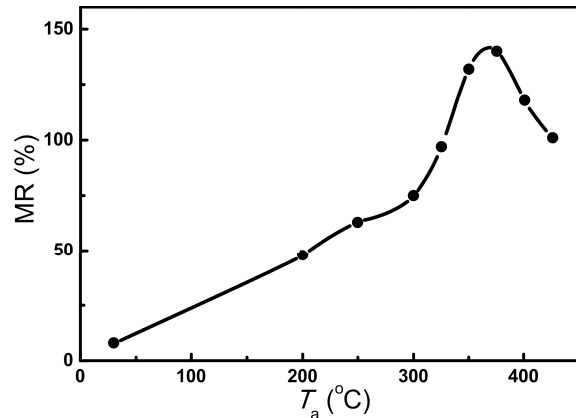


Figure 2.15: **TMR as a function of annealing temperature in CoFeB/MgO MTJs:**

TMR first increases with increasing annealing temperature ( $T_a$ ), reaches a maximum around 500 °C and decreases for higher  $T_a$ . This behavior is explained by the competition between two processes upon annealing: (i) improvement of crystal structure that tends to increase TMR and (ii) diffusion of light elements across the heterostructure resulting in degraded transport properties. See text for more details. Reproduced from *Ma et al.*<sup>122</sup>.

ples 1# and 2# are exchange biased samples with the bottom or top electrode pinned respectively. Sample 3# is a pseudo spin-valve in which the AP state is obtained by changing the electrodes thicknesses, resulting in dissimilar coercive fields in both electrodes. Samples 1#, 2# and 3# are annealed at 375°C, 350°C and 400°C respectively. Annealing temperatures were chosen in order to get higher TMR possible.

Figure 2.16 panels (a), (b) and (c) represent IETS spectra measured on sample 1#, 2# and 3# respectively for both magnetic states. Top panels show IETS spectra within the  $\pm 300$  mV bias window, while bottom panels represent the same data in the restricted  $\pm 60$  mV bias region. Except for different amplitudes, the three samples feature similar peaks in the IETS spectra. First at very low bias (bottom panels), sharp peaks are present around  $\pm 10$  mV in both magnetic states and are attributed to the zero bias anomaly (ZBA). These peaks are followed by other maxima around  $\pm 20$  mV, usually ascribed to magnons excitation (M). Additional peaks emerge around  $\pm 80$  mV and correspond to a peak in MgO phonon DOS (P) at  $81$  meV<sup>131</sup>. Finally, a smaller peak appears at higher voltages,  $\pm 200$  mV and denoted C. In samples 2#, all the peaks intensities are smaller in P compared to AP, but overall positions are similar to those of sample 1#. IETS spectra of Sample 3#, look like an intermediate state between sample 1# and 2#. In P state, the ZB peak is similar to that of sample 1#, while other peaks are similar to sample 2#. AP is also similar to sample 2# except for the feature at  $\pm 200$  meV which is not distinguishable anymore.

The main difference in these spectra resides in the ZBA peaks at very low bias, while this peak is very prominent in sample 1#, it is strongly reduced in sample 2# (making the shoulder around  $\pm 20$  meV (M) more visible) and just slightly reduced in sample 3#. Since the peaks positions are the same overall, the inelastic processes responsible of IETS features are supposed to be the same in each samples.

The ZB peak intensity is similar for both magnetic states in all samples suggesting that the underlying process is field independent. This peak is ascribed to magnetic impurities scattering. They are more prominent in sample 1# because of Mn diffusion from the antiferromagnetic layer close to the bottom interface. In sample 2# the amplitude of the ZB peak is reduced because additional Ru and CoFe layers partially prevent Mn diffusion toward the top interface, this is also supported by the fact that this sample can be annealed at higher temperatures compared to sample 1#. In sample 3# there is no Mn, but the peak is still larger than in sample 2#, the authors claim that other impurities might contribute at higher annealing temperatures.

Conversely to the field-independent ZB peaks, the second peak (M) is always more prominent in the AP state, which is consistent with the fact that magnon assisted tunneling is predicted to be dependent on the device magnetic state<sup>111</sup>.

Finally, in order to identify the third peak (C) around  $\pm 200$  mV, the authors attempted to compare NiFe/AlO/CoFe, CoFeB/AlO/CoFeB and as deposited CoFeB/MgO/CoFeB structures. While they successfully identified phonon peaks related to MgO and AlO barriers, they couldn't identify the origin of this peak with certainty.

Matsumoto *et al.*<sup>132</sup> measured IETS spectra in exchange-biased (EB) MTJs. They obtained similar spectra to the ones previously discussed, except for the phonon peak which is absent in their spectra, and for the unidentified feature at  $\pm 200$  mV that was observed at  $\pm 400$  mV instead. In line with Drewello *et al.*, they observe sharp peaks at very low bias

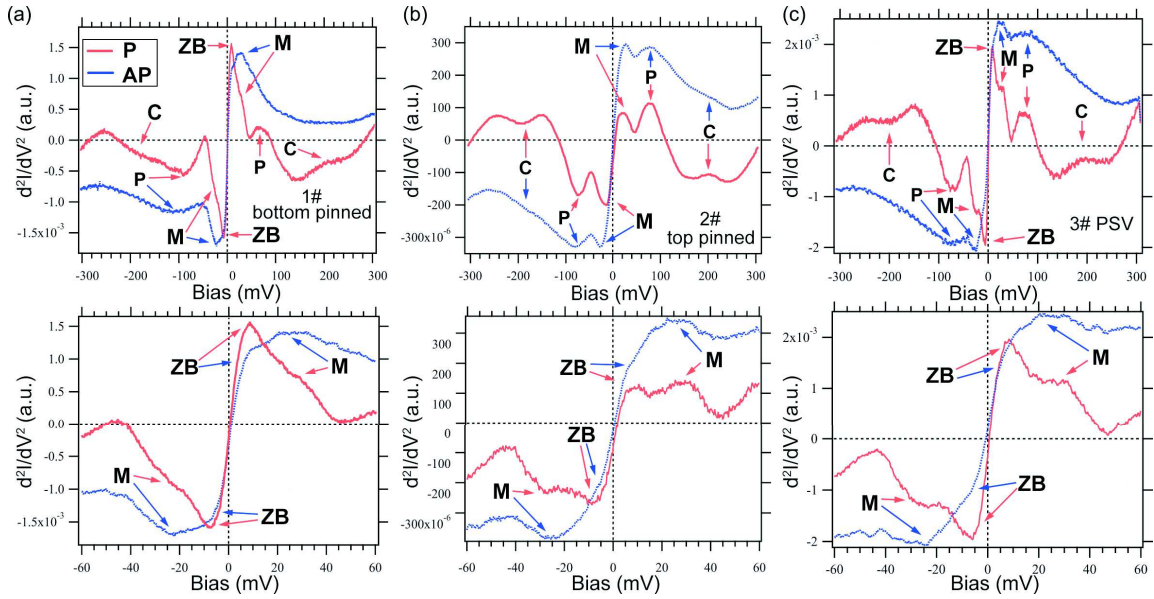


Figure 2.16: IETS spectra of MgO-based MTJs with various architectures<sup>130</sup>

IETS spectra measured on exchange biased MTJs with bottom (a) or top (b) electrode pinned and pseudo spin-valve junctions (c). At very low bias, sharp peaks are ascribed to impurity scattering (ZB). The following peaks around  $\pm 20$  mV are attributed to magnons excitation (M). Peaks at  $\pm 80$  mV are associated with a peak in MgO phonon DOS<sup>131</sup> (P). Peaks at  $\pm 200$  mV are tentatively ascribed to the CoFe DOS (C). Taken from Drewello *et al.*<sup>130</sup>.

followed by broader peaks related to magnon excitations. Again, the magnon contribution to the tunnel current is larger for the AP magnetic state. Concerning the peak at  $\pm 400$  mV, the authors couldn't determine its origin with certainty but speculate in terms of a CoFe DOS effect or a modification of the tunneling probability due to the MgO barrier itself. Additionally, they changed the boron concentration from 20 % to 12 % in the electrodes in order to investigate the impact of Boron diffusion, but measured similar IETS spectra and concluded that Boron diffusion has a negligible impact on the electrodes magnetization.

Miao *et al.*<sup>133</sup> measured IETS spectra in exchange-biased CoFeB/Mg/MgO/CoFeB structures as a function of an additional interface Mg layer thickness at the bottom interface. For standard samples (no Mg insertion), IETS spectra are similar to Figure 2.16, expect for the unidentified peak measured around  $\pm 300$  mV in this case. We note that the authors interpret all the low bias peaks in terms of magnon contributions without considering magnetic impurity scattering (ZBA). The unidentified peak is, again, uncertainly attributed to electrode DOS effects. The purpose of an additional Mg layer is to prevent the bottom electrode oxidation during MgO sputtering and to suppress tunneling through interface resonant states. They report that all IETS peaks are still present after Mg insertion. This result is not surprising concerning magnons and phonons peaks because they depend on the ferromagnetic electrode and the MgO barrier respectively. The fact that the third peak survives suggest that the Mg layer may conserve the electrons spin and symmetry and pro-

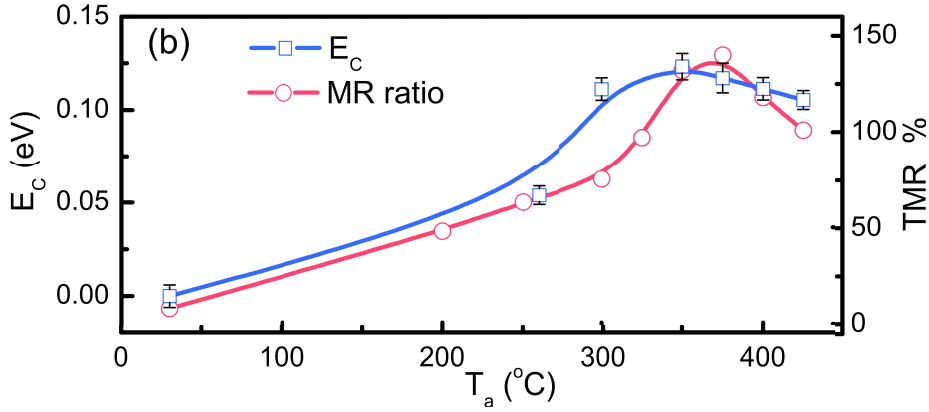


Figure 2.17: **Magnon activation energy and TMR as a function of annealing temperature in CoFeB/MgO based MTJs:** An apparent correlation is visible between magnon activation energy  $E_c$  and TMR. TMR increases with magnon activation energy, suggesting that magnon have a strong impact on magnetotransport properties. Reproduced from *Ma et al.*<sup>122</sup>.

mote coherent tunneling even for thicknesses as large as 1 *nm*. This could be explained by the fact that the Mg layer acts as an oxygen sink, actually protecting the bottom electrode but eventually resulting in an MgO layer.

Another interesting process that can impact the low bias region of IETS spectra is discussed by *Bernos et al.*<sup>134</sup>. They suggest that the ZBA is related to electron-electron interactions due to sub-total crystallization of the amorphous CoFeB electrodes. Indeed, X-ray characterization as well as HR-TEM pictures show that CoFeB layers are not totally crystallized with remaining amorphous regions after annealing. Their hypothesis is based on the fact that the amorphous CoFeB metal-insulator transition has a clear signature on the junction resistance at low bias. In amorphous electrodes, as the temperature decreases, electron-electron interactions lead to a DOS depletion at the Fermi level and tend to increase the resistance. As  $T_a$  increases, the crystal structure improves and the effect of electron-electron interaction vanishes. These considerations are of particular interest as we investigated devices developed by the same group and with similar structure in this thesis.

*Ma et al.*<sup>122</sup> emphasized the contribution of magnon excitation on magnetotransport. In order to do so, they used Wei's model<sup>114</sup>, that take into account impurity scattering as well as magnon excitation, to fit their experimental data and extract the magnon activation energy  $E_c$  as a function of annealing temperature. Figure 2.17 plots  $E_c$  and TMR as a function of annealing temperature  $T_a$ . We can see that the magnon activation energy follows the same trend as TMR with increasing  $T_a$ , suggesting a strong correlation between TMR and  $E_c$ .

Recently, *Teixeira et al.*<sup>135</sup> focused on the unidentified conductance dips located around  $\pm 300$  *mV*. They suppose that the band structure of the bcc CoFe alloy can be obtained by a rigid shift of bcc Fe and bcc Co band structures. They explain the conductance decrease by the bias-induced quenching of the  $\Delta_{5,2}^\uparrow$  and  $\Delta_2^\downarrow$  bands located at 0.2 *eV* and 0.3 *eV* above

$E_F$  in Fe and Co respectively (see Section 2.2.1.2). The band structure scenario is also supported by Ringer *et al.*<sup>136</sup>.

### 2.2.2.3 Quantum well states

Teixeira *et al.*<sup>137</sup> reported the contribution of majority spin  $\Delta_1$  quantum well (QW) states present in the free top electrode. Indeed in CoFeB/MgO/CoFeB/Ru MTJs, it is established that electrons can be reflected at the CoFeB/Ru interface. The problem is similar to one of the simplest system of quantum mechanics, i.e. a quantum particle in a box of finite size. The interaction of tunneling  $\Delta_1$  electrons with reflected  $\Delta_1$  electrons at the CoFeB/Ru results in quantum well states (similar to standing waves) in the sandwiched CoFeB layer. The energy position of QW states in the potential well depends on the MgO/CoFeB and CoFeB/Ru interface barrier height as well as the free CoFeB layer thickness. The quantum well states are clearly identified as oscillations in the parallel IETS spectra in which the majority  $\Delta_1$  band dominates the tunnel current. The contribution of other states is ruled out by simple considerations: first QW oscillations are absent in the AP magnetic state because the  $\Delta_1$  channel is closed in  $G_{AP}$  in which the conductance is carried by  $\Delta_{5,2}$  bands. Secondly,  $\Delta_{5,2}$  bands are closed for biases larger than 0.2 V in  $G_P$  and thus cannot be responsible of QW states measured above 0.2 V.

The impact of quantum well states on tunnel current is similar to inelastic processes: resonant tunneling through QW states occurs when the applied bias voltage equals the energy of the state, resulting in an additional conduction channel that increases the conductance. In addition to the fact that QW states impact  $G_P$  only and increase TMR they

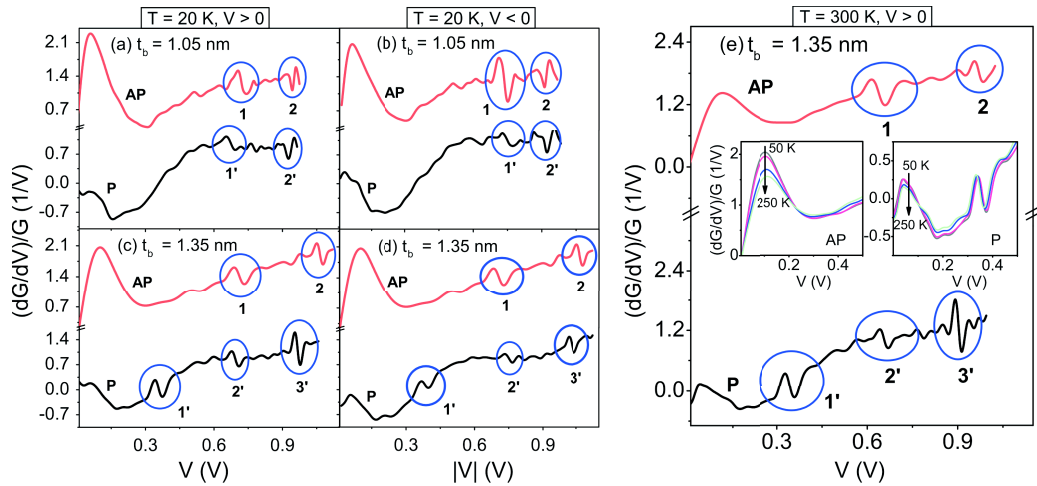


Figure 2.18: **Impact of trap states on IETS in CoFeB/MgO based MTJs:** (a) and (b) plot IETS spectra measured at low temperature for positive and negative bias voltage for  $t_{MgO} = 1.05$  nm. (c) and (d) plot similar data for  $t_{MgO} = 1.35$  nm for which additional room temperature measurements are presented in panel (e). Clear signature of trap states are emphasized with blue circles. See text for more details. Reproduced from Teixeira *et al.*<sup>138</sup>.

can be switched on and off by an external magnetic field.

#### 2.2.2.4 Trapping states

Usually, the presence of defects within the insulating layer is detrimental to spin dependent tunneling in MTJs because it promotes inelastic and incoherent tunneling processes. In addition to local perturbations in the insulating layer crystal structure, defects can also induce discrete energy states within the dielectric band gap, usually referred as trap states or localized states.

Similarly to aforementioned inelastic processes, when the bias voltage is swept and the Fermi energy of the emitting electrode equals the energy of defect induced localized states, resonant tunneling can occur. Resonant tunneling through trap states can impact the tunnel current in two ways: (i) trap assisted tunneling can be promoted, opening a new conduction channel and increasing the conductance and (ii) charge trapping on the localized state can occur, process that reduce the tunnel current due electron retention on the trap state.

The impact of both processes on IETS spectra is discussed in 2.2.2.1. The former process is characterized by a peak followed by a valley while the latter is characterized by a valley followed by a peak (see Figure 2.13). The impact of resonant trap assisted tunneling is restricted to a small bias range which is related to the state energy smearing. The theory of trap assisted tunneling will be discussed more thoroughly in a dedicated section. Here we report the work of Teixeira *et al.*<sup>138</sup> on trap states to emphasize the fact that IETS may be a technique of choice to characterize defect induced localized states in the dielectric.

Teixeira *et al.* measured IETS spectra on exchange-biased CoFe/MgO/CoFeB MTJs in which the presence of defects located in the middle of the MgO layer was confirmed by HR-TEM pictures. In Figure 2.18, IETS spectra measured at 20 K for both bias polarity for a barrier thickness of  $t_{MgO} = 1.05 \text{ nm}$  are represented in panel (a) and (b) respectively. Panels (c) and (d) represent similar data for  $t_{MgO} = 1.35 \text{ nm}$ , for which additional room temperature spectra are plotted in panel (e). First we note the presence of a wide peak present in the 0 – 350 mV bias region ascribed to impurity scattering, magnon and phonon assisted tunneling and possibly a dip around 350 meV due to electrodes DOS effects. For  $t_{MgO} = 1.05 \text{ nm}$ , clear signatures of trap assisted tunneling, denoted 1 and 1', as well as charge trapping, denoted by 2 and 2', are visible for both magnetic configurations. For a thicker MgO barrier, an additional trap assisted tunneling process occurs at lower bias in the parallel magnetic state. The absence of this process in the AP state can be explained by the fact that the signal is buried by the wide peak that extends in the 0 – 350 mV bias region. Nevertheless, the absence of peak in one of the magnetic state could also suggest tunneling through spin-polarized localized states. Panel (e) represent similar measurements at room temperature. The fact the peaks are still present at RT and that peak positions are temperature independent suggest that the hopping process is elastic<sup>138</sup>.

### 2.2.3 Summary

In this section, we first considered the effect of applying an electric field on coherent tunneling.

We saw that the main effect was an accumulation of charge at both interfaces resulting in a relative shift between the Fermi energies in both electrodes and in a linear potential drop in the dielectric. The potential drop in the dielectric result in a modification of the effective barrier height felt by tunneling electrons. As the bias voltage is swept and the Fermi energies of both electrodes are shifted relative to each other, additional energy regions of the DOS in both emitting and collecting electrodes are involved in the tunnel current, and thus the intrinsic electrodes DOS should be reflected in electrical spectroscopic measurements.

Secondly, it is well established that many other intrinsic and extrinsic inelastic processes impact the tunnel current. In particular, tunneling particles can interact with magnon present in ferromagnetic electrodes, phonons within the dielectric spacer, impurities but also other modes of the system such as quantum well states that might be present in the collecting electrode.

Usually, all these effects (when they are present) might jointly affect the electrical properties of the devices and can make the interpretation of experimental data very hard. Additionally, these effects originate from various microscopic processes such as collective excitation of electrons' spin (magnons), lattice vibrations induced by temperature (phonons) or localized states induced by impurities and are very challenging to take into account from a theoretical point of view.

## 2.3 Effect of temperature

As it is emphasized in the previous section, electrical measurements in MTJs reflect the combined contributions of many processes induced by the interaction of tunneling particles with various intrinsic and extrinsic properties of devices. It is usually difficult to discriminate the impact of a specific tunneling process. Nevertheless, each mechanism has a particular temperature dependence and temperature dependent measurements can be used to distinguish the impact of specific processes.

First, the impact of temperature on amorphous AIO based MTJs is reviewed. In a second part, the temperature dependence of MgO based MTJs in discussed.

### 2.3.1 AIO based MTJs

Shang *et al.*<sup>139</sup> first discussed the temperature dependence of electrical properties in AIO based MTJs. In order to do so, they considered three thermally induced changes on devices properties. Firstly, as the temperature is increased, additional thermal energy provided to electrons smears the Fermi energy. Because the additional thermal energy reduces the effective barrier height felt by electrons, the thermal smearing of the Fermi energy is predicted to increase the tunnel current. Using classical models<sup>140,141</sup> developed for metal-insulator-metal structures, the conductance dependence on temperature is written:

$$G_T = G_0 \frac{CT}{\sin(CT)}, \quad (2.1)$$

where  $G_T$  is the total elastic conductance,  $G_0$  the conductance at  $T = 0 K$  and  $C \propto d/\sqrt{\phi}$

with  $d$  the barrier thickness and  $\phi$  the barrier height. This process is predicted to increase the tunnel current by a few percent between 10K and 300K<sup>139</sup>. In first approximation, this contribution can be neglected in devices in which the tunnel current increases by more than 20% in the same temperature range. Secondly, the authors considered the impact of temperature on the electrodes polarization  $P$ . We remind that the polarization is related to the majority and minority spin population imbalance at the Fermi level. In order to model the temperature dependence of  $P$ , the polarization is assumed to be proportional to the electrode magnetization ( $M$ ), whose temperature dependence is well known. With increasing temperature, thermally induced spin waves excitation reduce the magnetization of the ferromagnetic layer according to Bloch's law. The hypothesis  $P \propto M$  allows to write the temperature dependence of  $P$  as:

$$P(T) = P_0(1 - \alpha T^{3/2}), \quad (2.2)$$

where  $\alpha$  is a constant that depends on the material intrinsic properties and  $P_0$  the material polarization at  $T = 0$  K. Lastly, [Shang \*et al.\*](#) extended Slonczewski's model (see [Section 1.2.3.3](#)) by introducing an additional spin independent conduction channel.

$$G(\theta) = G_T \{1 + P_1(T)P_2(T)\cos(\theta)\} + G_{SI} \quad (2.3)$$

where  $P(T)$  is the polarization of the electrodes with a temperature dependence defined by [Equation \(2.2\)](#),  $\theta$  is the relative orientation between the electrodes magnetization and  $G_{SI}$  the additional spin independent channel. Temperature dependent measurements can easily be exploited with this simple model.

Indeed, the measured quantity

$$\Delta G = G(\theta = 0^\circ) - G(\theta = 180^\circ) = G_P - G_{AP} = 2G_T P_1(T)P_2(T) \quad (2.4)$$

is independent of  $G_{SI}$  and allows to weigh the impact of the temperature dependent polarization of electrodes on tunnel current. Additionally, this expression can be used to evaluate  $G_T$  from the knowledge of  $P(0$  K), which is usually estimated from spin dependent tunneling experiment at low temperature. In turn,  $G_T$  can be used to probe the impact of  $G_{SI}$ :

$$G_{SI} = \langle G \rangle - G_T, \quad (2.5)$$

where  $\langle G \rangle$  is the average conductance between the P and AP magnetic states. They fitted the spin independent conductance to a power-law  $G_{SI} \propto T^\gamma$  and obtained  $\gamma = 1.33$ , suggesting hopping through a chain of two localized states (see [Section 2.4](#) for more details). However, the authors emphasize that several mechanisms can be responsible of  $G_{SI}$ , such as magnetic impurities within  $\text{Al}_2\text{O}_3$  or the presence of pinholes resulting from inhomogeneity in the AlO layer. Later, [Dimopoulos \*et al.\*](#)<sup>116</sup> used the same model and compared temperature dependent measurements carried before and after a post growth annealing step. They found that  $\Delta G$ , and thus the TMR, increases in annealed samples, suggesting an additional spin conserving channel compensating the impact of  $G_{SI}$ . They ascribe this additional channel to phonon assisted tunneling<sup>115</sup> which promotes spin conserving scattering.

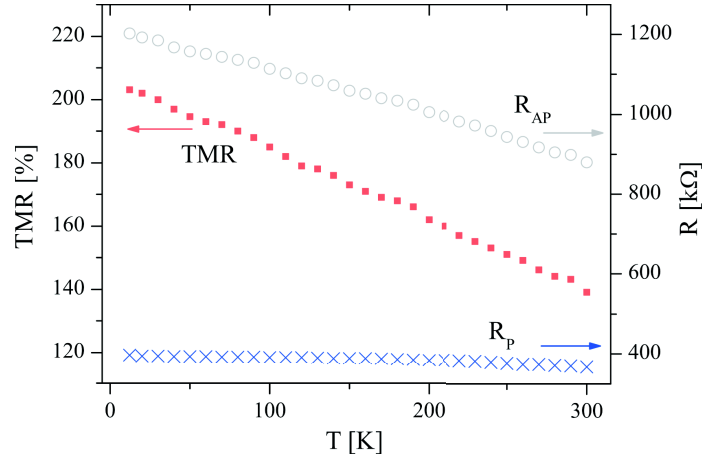


Figure 2.19: **Temperature dependence of electrical transport in MgO based MTJs:** The resistance of both P and AP magnetic state as well as TMR as a function of temperature in exchange biased CoFeB/MgO/CoFeB MTJs. The TMR decrease is principally due to the strong decrease of  $R_{AP}$ . In comparison  $R_P$  is almost temperature independent. Reproduced from [Drewello \*et al.\*](#)<sup>113</sup>.

Alternatively, [Han \*et al.\*](#)<sup>112</sup> used the model developed by [Zhang \*et al.\*](#)<sup>111</sup>, which considers the absorption or emission of magnons during the tunnel process, in order to explain the temperature dependent electrical properties of AlO based MTJs. Note that magnon assisted tunneling is different from the impact of magnon excitation on the electrodes magnetization considered in ref<sup>139</sup> and used in [Equation \(2.2\)](#). They explain the behavior of conductance and TMR in terms of anisotropic magnon cutoff energy, i.e. the magnon cutoff energy  $E_c$  is different between P and AP magnetic state.

### 2.3.2 MgO based MTJs

[Figure 2.19](#) plots the resistance in both P and AP magnetic state as well as the TMR as a function of temperature in CoFeB/MgO/CoFeB MTJs<sup>113</sup>. We can see that the temperature dependence of electrical properties in MgO based magnetic tunnel junctions is different compared to devices with Al<sub>2</sub>O<sub>3</sub>. The main difference resides in the fact the strong TMR decrease is principally due to a strong decrease in the resistance (conductance increase) of the antiparallel channel with increasing temperature, while the resistance in the parallel magnetic configuration is almost independent of T.

Similarly to AlO based MTJs, Shang's model applied to MgO tunnel junctions shows that the temperature dependence of conductance and TMR cannot be explained in terms of elastic tunneling only, and that an additional spin independent term has to be introduced<sup>142</sup>. Furthermore, [Kou \*et al.\*](#)<sup>142</sup> mention that the impact of magnon<sup>112</sup> and phonon<sup>115,116</sup> assisted tunneling alone cannot explain their experimental results.

[Wang \*et al.\*](#)<sup>143</sup> developed a model slightly different compared to the one developed for AlO MTJs<sup>139</sup>. The difference resides mainly in that [Wang \*et al.\*](#) introduced individual angular terms to define the direction of electrode magnetization with respect to the applied

magnetic field. This allows to take into account an additional process related to the impact of electrode magnetization misalignment induced by thermal disorder. Conversely to Shang's model, this empirical model allows to fit experimental data without resorting to a spin independent conduction channel. They used their empirical formula to fit temperature dependent data measured on Fe(25nm)/MgO(3nm)/Fe(10nm) MTJs. The model suggests that the thermally induced misalignment of electrodes magnetization is greater for AP magnetic configuration. The fact that the P magnetic state is more resilient to thermal disorder can be explained by the fact that the indirect exchange coupling (IEC) between the two electrodes through the MgO layer favors a parallel alignment for barrier thickness greater than 0.8 nm.

Backed with IETS spectra measured at low temperature, [Drewello \*et al.\*](#)<sup>113</sup> show that magnon assisted tunneling has a strong impact on tunnel transport. Furthermore, the authors note that, since  $G_P$  is almost temperature independent, the impact of the Fermi energy thermal smearing cannot be overlooked in MgO based MTJs. [Drewello \*et al.\*](#)<sup>113</sup> extend the magnon assisted tunneling model<sup>111,112</sup> by taking into account the effect of [Equation \(2.2\)](#) in order to accurately fit experimental result. In line with ref<sup>142</sup> [Drewello \*et al.\*](#)<sup>113</sup> show that magnon assisted tunneling alone cannot describe experimental data, but the extended model accurately describes the temperature dependence of MgO based MTJs electrical properties.

[Ma \*et al.\*](#)<sup>144</sup> systematically measured the temperature dependence of electrical properties in Fe/MgO/Fe MTJs as a function of the MgO barrier thickness  $t_{MgO}$ . Interestingly, they see that the temperature dependence of the parallel magnetic state  $G_P$  changes sign as  $t_{MgO}$  decreases. From a slight increase as a function of temperature for thick MgO (see [Figure 2.19](#)),  $G_P$  start to decrease with increasing temperature for thinner MgO. Among all the elastic and inelastic processes discussed previously only [Wang \*et al.\*](#)<sup>143</sup> predict such a decrease of  $G_P$ . This supports the strong influence of the electrode magnetization misalignment on tunnel transport and suggests that the spin independent conductance channel is not significant in fully epitaxial Fe/MgO/Fe MTJs.

Finally, similarly to ref<sup>144</sup>, [Teixeira \*et al.\*](#)<sup>145</sup> measured the temperature dependence of electrical properties in exchange biased CoFeB/MgO/CoFeB MTJs as a function of  $t_{MgO}$ . Again, they find that  $G_P$  is almost temperature independent except for thin MgO thicknesses for which  $G_P$  decrease as T increases. Additionally,  $G_{AP}$  becomes almost temperature independent, and the TMR decrease is mostly due to  $G_P$  decrease. They ascribe this peculiar behavior to the onset of pinhole induced metallic conductance for small MgO thicknesses.

## 2.4 Impact of localized states on spin dependent tunneling

In condensed matter physics, delocalized states refer to mobile charge carriers in a solid. The mobility of these particles stems from the overlap of their wave-function with many atoms, i.e. the spatial expansion of the wave-function is larger than the distance between

atoms in the solid. Conversely, the term *localized state* encompasses immobile charges that are trapped by attractive potentials. The wave functions of such states are confined within a narrow volume in space and have a limited overlap with neighboring atoms.

Many intrinsic and extrinsic features of solids can result in localized states. In crystals, any deviation (disorder) from the perfect periodic potential breaks the symmetry of the system and can induce localized states. As an example, in [section 2.1.1](#) we already mentioned that the presence of surfaces or interfaces breaks the crystal symmetry and results in interface states present in local gaps of the metallic electrodes. We also mentioned that these states have a strong impact when the energy of the tunneling particle is similar to the energy of the surface state. Other source of disorder, such as impurities (interstitial or substitutional atoms) or defects (vacancies or misfit dislocations) can act as electron traps. As for disordered systems, they are characterized by a high density of localized states uniformly distributed over a wide energy band. Similarly to IRS, we'll see that the impact of localized states on tunnel transport is different depending on whether or not their energy falls in the vicinity of the Fermi energy.

The impact of localized states was first considered by Anderson<sup>146</sup> to explain the absence of conductivity in some disordered solids. In amorphous systems, it was shown that the lowest states of the conduction band are localized. Above a threshold energy, electrons enter a high mobility region of the conduction band. At high temperatures, the conductivity is described in terms of thermal excitation of electrons in localized states to the high mobility region of the conduction band. As the temperature decreases and the Fermi energy falls below the threshold energy, the dominant transport mechanism crosses over to hopping through localized states. When estimating the tunneling probability between two localized states, in addition to the physical distance between the two states, their energetic distance has to be taken into account. A careful analysis by Mott<sup>146</sup> (who got his Nobel prize for his work on amorphous systems) showed that the temperature dependence of the conductance in the hopping regime, also known as variable range hopping (VRH), is:

$$\ln G_{VRH} \propto -1/T^{1/4} \quad (2.6)$$

[Equation \(2.6\)](#) is valid in the bulk but becomes irrelevant when the dimensions of the system are reduced.

In this section, we'll consider the impact of localized states located in the energy gap of very thin insulating layers integrated in magnetic tunnel junctions. In that case, we'll see that another mechanism than VRH dominates the tunnel current. First, the impact of localized states on spin dependent tunneling is considered both from theoretical and experimental points of view. Secondly, several mechanisms that can induce localized states in crystalline MgO are reviewed. In particular, oxygen vacancies are thoroughly discussed. The section is concluded by a brief summary.

### 2.4.1 Impact of localized states: Early models

In insulating materials, defect- or impurity-induced localized states can be located within the band gap of the dielectric. In tunnel junctions, as the thickness of the insulating layer

increases, the dominant tunneling mechanism crosses over from direct tunneling to resonant tunneling to hopping via chains of localized states, and eventually to VRH when the properties of the bulk are recovered.

Direct elastic tunneling is thoroughly discussed in [chapter 1](#), and many other inelastic processes are examined in the previous sections of this chapter. We remind that elastic tunneling differs from inelastic tunneling in that it conserves the energy of the tunneling particle. The impact of localized states located in the forbidden energy gap of the dielectric is different depending on the energy position of the localized state ( $\epsilon_i$ ) compared to the Fermi energy ( $E_F$ ) of the emitting electrode.

Resonant tunneling refers to the case  $E_F = \epsilon_i$ , the process is similar to resonance interaction in optics: the photon absorption probability, or equivalently a given transition probability, is greatly enhanced when the energy of the probe equals the energy  $\Delta\epsilon$  required to promote the transition. For excitation energies below or above  $\Delta\epsilon$  the transition is greatly reduced. Resonant tunneling refers to the fact that the DOS as well as the conductance are greatly enhanced when the energy of the tunneling particle equals that of the defect state. Conversely, non-resonant tunneling refers to the case  $E_F \neq \epsilon_i$ , but also has a non-negligible impact on tunnel current.

Resonant tunneling can be elastic or inelastic depending on the temperature and the strength of the coupling between localized states and phonons in the barrier.

#### 2.4.1.1 Resonant tunneling through a single localized state

**Elastic resonant tunneling:** The conductance due to a tunneling electron, with initial energy  $\epsilon$  in the emitting electrode, via a localized state with energy  $\epsilon_i$  to the collecting electrode with final energy  $\epsilon'$  can be written<sup>147</sup>:

$$g(\epsilon \rightarrow \epsilon') = \frac{e^2}{2\pi\hbar} \frac{4\Gamma_L\Gamma_R}{(\epsilon - \epsilon_i)^2 + \Gamma^2} \delta(\epsilon - \epsilon') \quad (2.7)$$

The delta function ensures the conservation of energy (elastic tunneling),  $\Gamma = \Gamma_L + \Gamma_R$  and

$$\Gamma_{L,R} = E_0 e^{(-2\alpha z_{L,R})} \quad (2.8)$$

where  $E_0$  is the depth of the localized state,  $\alpha$  is the attenuation length ( $\alpha^{-1}$  is also called the localization length) and  $z_{L,R}$  the distance of the impurity from the left or right electrode.

From [Equation \(2.7\)](#), we can see that the conductance is maximum when  $\Gamma_L = \Gamma_R$ , i.e. when the single impurity is located at the middle of the barrier (for a symmetric barrier), and when  $\epsilon_i = \epsilon = \epsilon'$ , i.e. when the energy of the tunneling particle (the Fermi energy in the emitting electrode) equals the one of the localized states. Moreover, resonant tunneling through localized state contribute to tunneling only when the localized state (LS) energy falls in the vicinity of the Fermi energy.

When many localized states are present in the barrier, the total resonant tunneling  $G_1^{res}$  can be obtained by taking the sum of all the resonant channels:

$$G_1^{res} = A e^{-\alpha d}, \quad (2.9)$$

where  $A$  is a constant related to the area of the junction and the density of localized states. From Equation (2.9) we can see that  $G_1^{res}$  is temperature independent but has a different thickness dependence compared to elastic tunneling:

$$G_0^{elastic} \propto e^{-2ad} \quad (2.10)$$

The subscripts refer to the number of localized states involved in the resonant tunneling, 0 corresponding to elastic tunneling and 1 to resonant tunneling through a single localized state. The crossover between the dominant tunneling process as a function of the spacer thickness is reported in the literature<sup>148</sup>.

Larkin and Matveev<sup>147</sup> derived a similar equation for elastic resonant tunneling through two impurities,  $G_2^{res}$ . Again, resonance is reached when the energy of both localized states is equal and falls within  $k_bT$  of the emitting electrode Fermi energy. Moreover, the two impurities have to be aligned in space. Although  $G_2^{res}$  should dominate tunnel current for large thicknesses or large impurity concentration, in practice this conduction channel is overshadowed by other inelastic processes which will be discussed in Section 2.4.1.2.

**Inelastic resonant tunneling:** Glazman and Shekhter<sup>149</sup> investigated the coupling between localized states and the phonon field of the dielectric. The same problem was considered by Wingreen *et al.*<sup>150</sup>. Although the studied system (double barrier system) and the mathematical treatment are different, the impact of electron-phonon interaction (EPI) is essentially the same. Interestingly, we note that in double barrier systems, discrete energy states in the potential well between the two barriers also result in resonant tunneling. If we compare the equations derived in ref 149 and ref 150, we can see that the process is essentially the same as resonant tunneling through a single localized state. Actually, a point defect in the tunnel barrier can be viewed as a potential well of infinitesimal width resulting in a single resonant state.

Without going into the details, it was shown that the electron-phonon interaction (EPI) affects resonant tunneling through a single localized states ( $G_1^{res}$ ) in two ways: it broadens the resonance peak and it divides resonant tunneling into an elastic and an inelastic conduction channel. When the EPI is strong, the amplitude of the resonance peak is reduced, while when it is weak the inelastic contribution introduces a temperature dependent correction to resonant tunneling which scales as  $T^2$ . The contribution of this term is discussed in ref 148: it is shown that the temperature dependence of the resistance due to this term is similar to the smearing of the Fermi energy (see Section 2.3.1) and can be neglected in some cases.

The electrical transport is referred as hopping transport when inelastic resonant tunneling occurs in chains composed of two or more impurities.

#### 2.4.1.2 Hopping via chains of localized states

Glazman and Matveev<sup>151</sup> considered hopping transport in certain limiting case. They supposed  $eV$  smaller than  $k_bT$  (low bias) and a high density of localized states with energy positions close to the Fermi energy. In practice, the model can be used to treat experimental

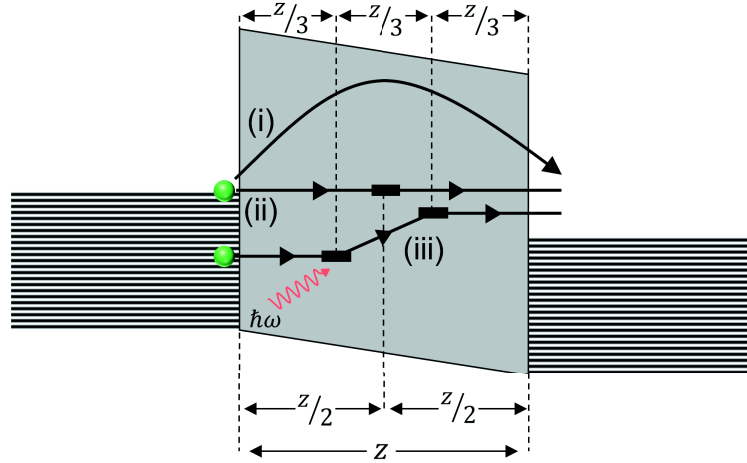


Figure 2.20: **Different tunneling path induced by localized states:** Paths (i), (ii) and (iii) respectively represent direct tunneling, resonant tunneling through a single localized states (LS) and inelastic hopping through a chain of two LS. The red arrow represents the absorption of a phonon during the hopping. Adapted from Xu *et al.*<sup>148</sup>.

data measured in MTJs with an amorphous dielectric. They suppose elastic tunneling from the emitting electrode to the first localized state and from the last localized state to the collecting electrode. Electrons can hop into localized states of different energies by absorbing or emitting a phonon, the process is schematically represented in Figure 2.20.

The authors derived an expression for hopping via a chain of two localized states,  $G_2^{hop}$ . They find that resonance conditions are obtained when: (i) the localized states are aligned in space (in the direction of the current flow) (ii) when the position of the localized states in the  $z$  direction divide the barrier in equal parts. More important for experimentalist, they find that  $G_2^{hop}$  has a peculiar temperature dependence:

$$G_2^{hop} \propto (k_b T)^{4/3} \quad (2.11)$$

$G_2^{hop}$  has different temperature and thickness dependencies compared to  $G_0^{elastic}$  and  $G_1^{res}$ . This peculiar temperature dependence allows to study deviations from the expected tunnel current due to elastic tunneling. Compared to resonant tunneling, hopping allows inelastic transitions between localized states. As a consequence, the alignment of the states in energy is not required anymore, making the opening of inelastic channels more probable compared to elastic ones (for  $N > 1$ ).

The authors discussed hopping via a chain of  $N$  localized states and showed that the temperature and thickness dependence scale as  $T^\gamma$  and  $e^{\gamma ad}$  respectively, where  $\gamma = N - [2/(N + 1)]$  and  $N$  is the number of localized states in the chain. Finally, the total conductance can be written as the some of all the contributions:

$$G(T) = G_0^{elastic} + G_1^{res} + \sum_N G_N^{hop}(T) \quad (2.12)$$

Actually, these models are the one mentioned in Section 2.3.1 to explain the temperature dependence of amorphous AlO and in some cases crystalline MgO based MTJs. Temperature dependent measurements are one way to characterize the impact of localized states.

More recently, Bratkovsky<sup>152</sup> considered the impact of resonant tunneling through a single impurity level on TMR in magnetic tunnel junctions. He showed that when  $G_1^{res}$  dominates the tunnel current, the TMR is not defined by the effective polarization of the electrodes but rather by a quantity that he defines as the polarization of the impurity channels. Introducing localized states near the Fermi level of the device enhance the conductance but greatly reduce TMR.

Finally, we emphasize that the aforementioned models don't take into account spin-flip scattering events, an inelastic process that can occur if impurities are magnetic.

### 2.4.1.3 Resonant tunneling with spin-flip scattering

Spin-flip scattering due to magnetic impurities located in the spacer layer was investigated by several groups<sup>153–155</sup>. In addition to the simple resonant tunneling mentioned previously, Guinea<sup>153</sup> considered the possible interaction between the spin of the electron and the magnetic moment of impurity states. At resonance, they show that the TMR is reduced by a factor  $\sigma_I/\sigma_0$ , where  $\sigma_0$  and  $\sigma_I$  are the elastic and impurity-induced conductance respectively. Finally, they note that if  $\sigma_I$  dominates, a high applied magnetic field is expected to align the magnetic moments of the impurities and result in a TMR increase.

Vedyayev *et al.*<sup>154</sup> made a more rigorous treatment of spin flip scattering on paramagnetic impurities. In order to derive the expression of the tunnel current, they treat the problem within the Kubo formalism of linear response theory. They suppose an exchange interaction between the spin of tunneling electrons and the spin of the impurities. Free electrons are assumed in the electrode while ferromagnetism is taken into account by introducing an exchange splitting between majority and minority spins in the electrodes. Moreover, the impurity levels are coupled to the electrode magnetization, resulting in different value of the potential at the impurity site depending on the electrode magnetic configuration. They restricted their calculations to the case of a resonant tunneling through a single localized state and obtain the same expression as Equation (2.7) in the case of nonmagnetic impurities.

The authors finally compute the transport properties of amorphous Co/AlO/Co MTJs as a function of temperature and applied bias voltage. Interestingly, they show that the low temperature TMR is larger in systems containing paramagnetic impurities compared to perfect impurity-free trilayers. Within their models, the enhancement of TMR is principally due to the coupling between the impurity spin and the magnetization of the electrodes which tend to magnetically order the magnetic moments of impurities. The temperature dependence shows that the TMR decreases due to a conductance increase in the antiparallel magnetic configuration while the parallel magnetic configuration is nearly constant. Finally, they find that the TMR is strongly asymmetric and decreases with increasing bias voltage. The asymmetry is ascribed to the impact of impurities located close to interfaces that have a dissymmetric impact when the bias voltage is reversed.

#### 2.4.1.4 Impact of localized states induced by boron impurities in CoFeB/MgO/CoFeB MTJs

More recently Lu *et al.*<sup>156</sup> extended the Glazman-Matveev model to investigate the impact of boron impurities in CoFeB/MgO/CoFeB MTJs. The model was modified to account for spin polarized tunneling through ferromagnetic electrodes. The authors find a temperature dependence similar to unpolarized systems for chains composed of more than 1 localized states,  $N > 1$ . Similarly to Shang *et al.*<sup>139</sup> the temperature dependence of the electrodes polarization is considered. Moreover, the temperature behavior of the elastic tunneling channel  $G_0^{elastic}(T) \propto \frac{CT}{\sinh(CT)}$  related to the smearing of the Fermi energy is taken into account. Finally, an expression of TMR related to spin polarized tunneling through chains of  $N$  localized states is derived:

$$TMR(N) = \frac{(1 + P)^{2\beta N} + (1 - P)^{2\beta N}}{2(1 - P^2)^{\beta N}}, \quad (2.13)$$

where  $N$  is the number of localized states,  $P$  is the spin polarization of the electrodes (assumed identical for both electrodes) and  $\beta = 1/(N + 1)$ . The authors show that Equation (2.13) is a decreasing function of  $N$ , meaning that TMR decreases even if hopping through chains of localized states is a spin conserving process. When different varieties of conduction channels occur, the total TMR can be written as the sum of each TMR weighed by their fractional contribution:

$$TMR = \sum_N \rho_N \times TMR(N), \quad (2.14)$$

where  $\rho_N$  and  $TMR(N)$  are the weight and TMR related tunneling through chains of  $N$  localized states.

In order to confront their model with experimental data, the authors fabricated CoFeB/MgO/CoFeB MTJs with different MgO thicknesses (sample A  $t_{MgO} = 2.5$  nm; sample B  $t_{MgO} = 3$  nm; sample C  $t_{MgO} = 4$  nm). The presence of oxidized boron within the MgO barrier is confirmed by in depth x-ray photo-emission spectroscopy (XPS). Temperature dependent conductance and TMR are then interpreted using the aforementioned model.

First the authors emphasize the different temperature dependence of TMR for the three samples. In sample A, the TMR drops from 129 % at 3 K to 79 % at room temperature. The temperature dependence of sample C is stronger, the TMR drops from 108 % at low temperature to 11 % at 300K. Sample B has an intermediate behavior. The TMR drop with increasing temperature is ascribed to the crossover from elastic to inelastic tunneling possesses through localized states induced by boron impurities.

Figure 2.21(a) and (b) plot the conductance of the antiparallel magnetic configuration as a function of temperature. Using their generalized Glazman-Matveev model, they extract the impact of the different conduction channels related to inelastic tunneling from their specific temperature dependence (see Equation (2.12)). In sample A,  $G_{AP}$  can be fitted with  $A + BT^{4/3}$  and is related to an inelastic channel containing 2 localized states (see Equation (2.11)). In order to fit  $G_{AP}$  in sample C, an additional term related to tunneling through a chain of 3 localized states was required. Finally, Figure 2.21(c) and (d)

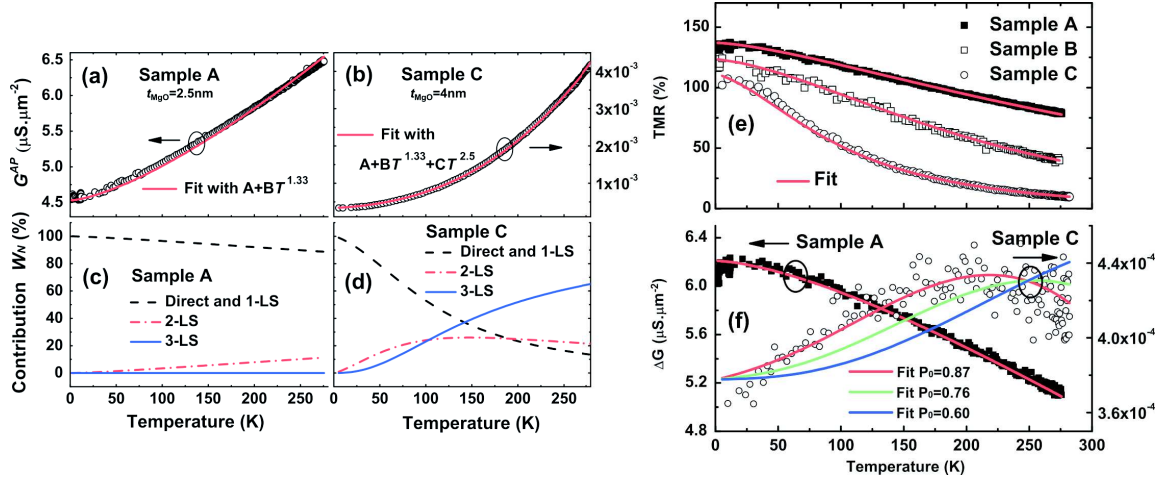


Figure 2.21: **Impact of boron impurities in CoFeB/MgO/CoFeB MTJs:** Temperature dependence of  $G_{AP}$  for  $t_{MgO} = 2.5$  nm and  $t_{MgO} = 4$  nm in panel (a) and (b) respectively. Red lines are fit after Equation (2.12) allowing to extract  $N$ , the number of localized states involved in the dominating hopping chain. Panel (c) and (d) plot the weighted contribution of all conduction channels. Panel (e) plot the temperature dependence of TMR as well as fit after Equation (2.14). Finally, panel (f) represent  $\Delta G = G_P - G_{AP}$ . See text for more details. Reproduced from Lu *et al.*<sup>156</sup>.

represent the contribution of each conduction channel to  $G_{AP}$  as a function of temperature for samples A and C respectively. The contribution of chains with larger  $N$  is increased when the barrier is made thicker or when temperature is increased. Besides, in sample C the dominant conduction channel crosses over from elastic tunneling to inelastic tunneling through 3 localized states at  $T = 150$  K. This explains the large TMR drop in this sample. Eventually TMR is fitted using Equation (2.14) as represented in Figure 2.21(e).

One of the main argument supporting the interpretation of Lu *et al.*<sup>156</sup> is the temperature behavior of  $\Delta G = G_P - G_{AP}$ , which is related to the temperature dependence of the electrodes polarization (see Section 2.3.1).  $\Delta G$  is plotted in Figure 2.21(f) for sample A and C. We can see that in sample A,  $\Delta G$  decreases with increasing temperature as expected from the temperature dependence of the electrodes magnetization. Surprisingly, in sample C  $\Delta G$  increases up to 220 K before decreasing up to RT. This peculiar behavior of  $\Delta G$  cannot be explained by depolarization of the electrodes nor by unpolarized inelastic processes<sup>139</sup>.  $\Delta G$ 's increase in sample C can be understood in terms of thermally activated spin conserving inelastic channels. The graph can be interpreted as follow: Spin conserving tunneling through a chain of  $N$  localized states induce a non-zero  $\Delta G$  and thus a non zero  $TMR(N)$  related to a specific channel. However, concurrent to the increase of  $\Delta G$ , the total tunnel current is also greatly increased and thus the total TMR is lowered.

In amorphous systems, it is well established that a large density of localized states induced by disorder are located near the Fermi energy. In that case, the aforementioned models are suited to describe the temperature and bias dependence of such systems. In the

case of crystalline systems and in particular Fe-, CoFe- and CoFeB-MgO based MTJs, the high TMR values observed attest that most of the tunnel current is coherent, i.e.  $G_0^{elastic}$  dominates and higher order terms have a secondary impact at best. Moreover, the previously discussed models are usually developed in the low bias regime, this makes it difficult to characterize the impact of localized states located far away from the Fermi energy, as it can be the case for some impurities or defects. In the following section, we'll discuss more sophisticated theoretical treatment of localized states induced by oxygen vacancies in MgO based MTJs.

### 2.4.2 Impact of oxygen vacancies in MgO based MTJs from first principles

MgO is integrated in many electronic systems such as advanced hard drives, nonvolatile magnetic memories, magnetic sensors or flat screen technologies. Because the material is used in so many devices, it is one of the most extensively studied oxide both from experimental and theoretical point of views. At first glance, it seems like the electrical properties of MgO are well understood, but a closer look at the literature shows that the origin of many properties of this apparently simple oxide are not well established. A first example is related to the anomalous optical activity of MgO. Another peculiar characteristic of MgO pertains to the catalytic properties of its surface that attracted the attention of the chemistry community and triggered a tremendous amount of work on this topic<sup>157</sup>. These particular properties are mainly ascribed to defects in the MgO crystal, and more particularly to oxygen vacancies. Oxygen vacancies are the most common and as such the most studied intrinsic defect in oxides. In this section, we are particularly interested in the impact of oxygen vacancies on the electrical transport of MgO based magnetic tunnel junctions.

#### 2.4.2.1 Electrical properties of MgO containing oxygen vacancies

Velev *et al.*<sup>19,158</sup> investigated the impact of localized states induced by oxygen vacancies on the magnetic and electric properties of crystalline Fe/MgO/Fe MTJs. First, the impact of localized states induced by oxygen vacancies (F centers) on electrical properties of MgO was examined. In order to calculate the electrical properties of bulk MgO in the presence of oxygen vacancies, the authors use the pseudopotential plane-wave method within the local density approximation (LDA). Vacancies are introduced by removing neutral oxygen atoms from the supercell. Velev *et al.*<sup>158</sup> mention that a slight deformation of the lattice occurs in the vicinity of vacancies without further considerations, we'll see later that the defect-induced lattice distortion have important consequences.

The band structure of MgO for the ideal case and in the presence of F centers is plotted in Figure 2.22(i). We can see that the presence of F centers results in two localized states in the band gap of MgO. The first state, denoted  $F_s$  (red line), is located at  $\sim 1$  eV below the Fermi energy (0 eV) and is doubly occupied. The second state, denoted  $F_p$  (blue line), overlaps with the bottom of the conduction band approximately 4 eV above  $E_F$  and is unfilled.

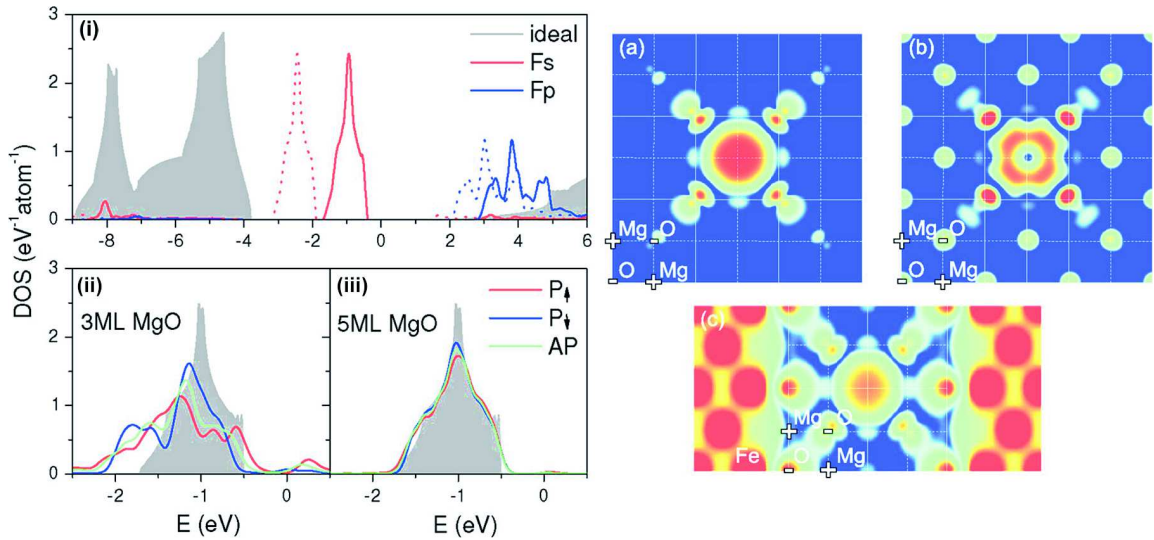


Figure 2.22: **Impact of localized states on electronic properties of bulk MgO:** (i) Electrical properties of bulk MgO for an ideal crystal (solid grey) and a sample containing oxygen vacancies (red and blue line). Oxygen vacancies result in two states in the band gap of MgO, the first one  $-1$  eV below  $E_F$  ( $F_s$ ) and the second one  $4$  eV above  $E_F$  ( $F_p$ ). Panel (a) and (b) plot the charge density of both states at the defect site, allowing to determine their orbital character. The scale goes from blue for low density to red for high density. Panel (ii) and (iii) plot  $F_s$  for oxygen vacancies introduced in the middle of a 3ML and 5ML thick MgO slab sandwiched between two Fe electrodes. Panel (c) plot the charge density of  $F_s$  in a Fe/MgO(5ML)/Fe MTJ. Reproduced from *Velev et al.*<sup>19</sup>.

The charge density at the defect site plotted in Figure 2.22(a)-(c) allows to unambiguously determine the orbital character of the localized states. States below and above  $E_F$  have  $s$  and  $p$  characters respectively.

From panel (a), it is also clear that  $F_s$  hybridizes with the nearest neighbors only and is strongly localized around the defect site, this behavior is expected for sharp localized states in the gap. Conversely, because  $F_p$  partially overlaps with the conduction band, the state is less localized and interacts with atoms far away from the defect position (see panel (b)).

Figure 2.22(ii), (iii) and (c) plot similar results for a MgO slab integrated in a Fe/MgO/Fe device. The vacancies are placed in the middle of the MgO layer. The DOS of  $F_s$  is plotted for 3 and 5 monolayers (ML) of MgO in panel (ii) and (iii) respectively. The width of the localized state depends on its coupling to electrodes and depends on the magnetic configuration of the electrodes. When the coupling is strong (small thicknesses), the peak broadens due to a large escape rate between the localized state and the electrodes. From panel (iii), we can see that the properties of  $F_s$  in the bulk are recovered when defects and electrodes are separated by 2 ML. The charge density of the defect in the Fe/MgO/Fe trilayer is plotted in panel (c). Similarly to the bulk,  $F_s$  interacts with the nearest neighbors only and interface O atoms are not affected.

### 2.4.2.2 Impact of oxygen vacancies on spin dependent tunneling in Fe/MgO/Fe MTJs

In a second step, *Velev et al.*<sup>158</sup> calculate the tunneling transport properties of MgO containing oxygen vacancies. Figure 2.23(a)-(c) shows the transmission as a function of energy for majority and minority channels for both magnetic configuration in ideal MTJs and in devices containing oxygen vacancies in the middle layer of the 5 ML thick MgO slab. The ensuing TMR as a function of tunneling particle energy is plotted in Figure 2.23(d).

First, we see that F centers produce a large peak when the energy of tunneling electrons equals the energy of the localized states  $E = E_i = -1$  eV. A similar peak occurs 3.5 eV above  $E_F$  and corresponds to the F centers p state located near the conduction band (not shown). At resonance, the tunnel current is dominated by the resonant conduction channel, in that case TMR is defined in terms of polarization of the resonant channel. From Figure 2.23, we can see that the resonant channel has a similar impact on  $G_P$  and  $G_{AP}$  (small asymmetry) resulting in a reduction of TMR close to the resonance (panel (d)). Secondly, O vacancies strongly affect the majority conduction channel away from resonance. From

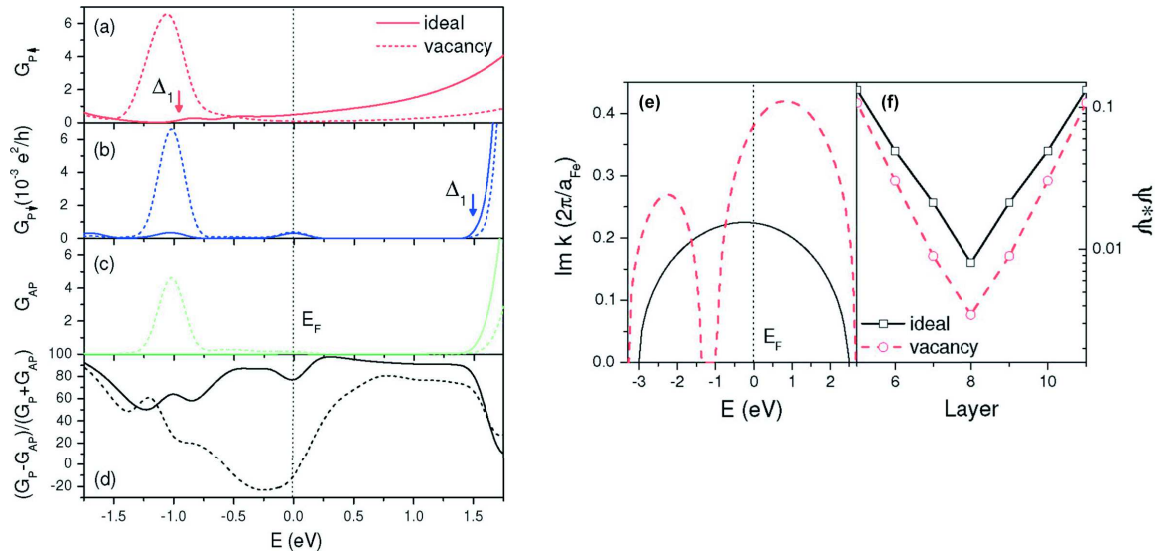


Figure 2.23: **Impact of localized states on spin dependent tunneling in crystalline Fe/MgO/Fe MTJs:** Tunneling conductance as a function of energy in a Fe/MgO/Fe MTJ with (dashed line) and without O vacancies (solid lines). The conductance is plotted for (a)  $G_P^\uparrow$  (b)  $G_P^\downarrow$  and (c)  $G_{AP}$ , TMR is plotted in panel (d). The main effect of F centers is (i) a resonant peak located around the defect energy level in all conduction channels and (ii) a strong decrease of  $G_P^\uparrow$  off resonance. Panel (e) plots the decay rate of  $\Delta_1$  states in both ideal MgO (solid black) and MgO with O vacancies (dashed red line). The decay rate is strongly reduced at resonance and related to conductance peaks in panels (a)-(c). Off resonance,  $\Delta_1$  states decay rate is increased explaining the decrease of  $G_P^\uparrow$ . Finally panel (f) plots the probability density and is an alternative way to extract the decay rate of  $\Delta_1$  states. Reproduced from *Velev et al.*<sup>19</sup>.

panel (a), we can see that  $G_P^\uparrow$  is reduced by a factor of 5-7 off resonance. This reduces the asymmetry between  $G_P$  and  $G_{AP}$  as well as the ensuing TMR. The reduction of the majority channel is due to inelastic tunneling induced by oxygen vacancies, allowing scattering to states with  $\mathbf{k}_{\parallel} \neq (0, 0)$ . As a consequence, the conductance is decreased because states with  $\mathbf{k}_{\parallel} \neq (0, 0)$  are more attenuated in the barrier.

This interpretation is further supported by analyzing the complex band structure of bulk MgO with and without vacancies. Figure 2.23(e) plots the decay rate of  $\Delta_1$  states as a function of energy in bulk MgO for both cases. At resonance, slightly below  $-1$  eV, the decay rate is strongly reduced and corresponds to the large peak in conductance at the same energy in panels (a), (b) and (c). Off resonance, the decay rate is increased, confirming that F centers effectively increase the decay constant. Similarly, the decay rate can be estimated by the slope of the probability density  $|\psi|^2$  as a function of  $t_{MgO}$ . Figure 2.23(f) plots  $|\psi|^2(t_{MgO})$  for  $\Delta_1$  state showing the decay rate for electrons tunneling at the Fermi energy for a Fe/MgO/Fe MTJ, is increased in MgO containing O vacancies.

The minority conduction channel, which is smaller compared to the majority channel, is dominated by tunneling electrons with  $\mathbf{k}_{\parallel} \neq (0, 0)$ . Consequently, off resonance scattering contribute both constructively and destructively and is not expected to significantly change the minority channel.

### 2.4.2.3 Systematic study of the effect of oxygen vacancies in Fe/MgO/Fe MTJs

We report the investigation of Ke *et al.*<sup>159</sup>'s on the effect of oxygen vacancies in Fe/MgO/Fe MTJs from first principles.

The authors use a non-equilibrium vertex correction in order to average many configurations when disorder is introduced in the system. The atomic structure of their model is composed of two semi-infinite iron electrodes separated by 13 monolayers of MgO. Oxygen vacancies are introduced by randomly replacing an oxygen atom with a vacuum sphere with the same radius. The small lattice distortion due to the vacancy (Va) is neglected. As it is mentioned before we'll see that lattice distortion is crucial to explain the properties of oxygen vacancies (Section 2.4.3). The substitutional disorder is realized by an alloy model  $O_{1-x}Va_x$ . Finally, transport properties are calculated as a function of oxygen vacancies concentration  $x$ .

In ideal MTJs, they find that the TMR increases with MgO thickness and reaches 10000 % for  $t_{MgO} = 13 ML$ , in line with other theoretical studies<sup>17,49,160</sup>. The inset of Figure 2.24 panel (c) plots the impact of introducing 3 % (green squares) or 5 % (black triangles) of oxygen vacancies (OV) in  $n$  layers of MgO. We can see that OV cause a 50- or 220-fold resistance increase for 3 % and 5 % concentrations respectively. Figure 2.24 panels (a) and (b) represents the effect of introducing 3% OV at the bottom MgO interface layer while varying the concentration  $x$  of OV in the topmost MgO layer, for  $G_P^\uparrow$  and  $G_{AP}^\uparrow$  respectively. Similar results are plotted for  $G_P^\downarrow$  and  $G_{AP}^\downarrow$  in insets of panel (a) and (b). The coherent (red), vertex correction (black) and total conductance (green) are plotted. The main observation is that the vertex correction (related to diffusive scattering) dominates all conduction channels.  $G_P^\downarrow$ ,  $G_{AP}^\uparrow$  and  $G_{AP}^\downarrow$  are almost entirely due to diffusive scattering. These results are ascribed to interchannel scattering promoted by interface oxygen

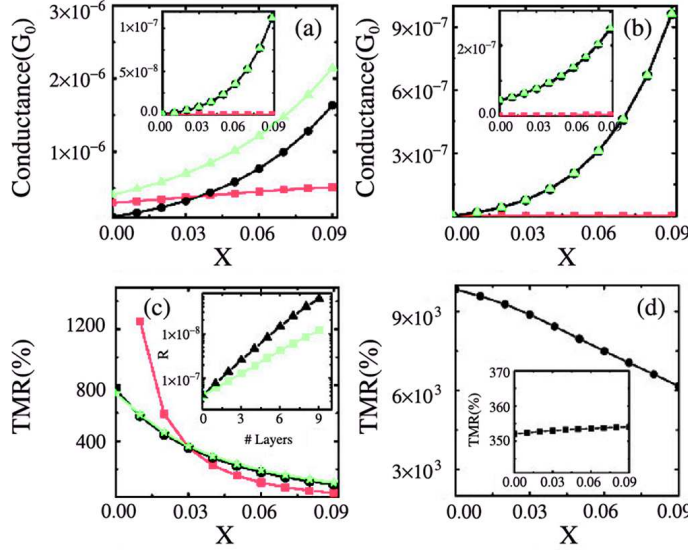


Figure 2.24: **Electrical properties of Fe/MgO/Fe MTJs as a function of O vacancy concentration:** Panels (a) and (b) plot the conductance for  $G_P^\uparrow$  and  $G_{AP}^\uparrow$  as a function of oxygen vacancy concentration  $x$ , located at the interface layer. 3 % of oxygen vacancies are introduced at the bottom MgO layer and the concentration  $x$  is varied in the topmost MgO layers. The coherent (red), vertex correction (black) and total conductance (green) are plotted. Insets represent similar data for  $G_P^\downarrow$  and  $G_{AP}^\downarrow$ . Panel (c) plots the TMR related to data of panel (a) and (c) for various samples. Panel (d) shows the effect of substituting OV by nitrogen atoms (the large TMR is recovered). The inset of panel (d) shows that TMR is almost independent of oxygen vacancies introduced in the middle of the MgO layer. Reproduced from *Ke et al.*<sup>159</sup>.

vacancies. As a consequence, minority Fe states (which are normally filtered by the MgO barrier) are allowed to couple to the slowly decaying  $\Delta_1$  states. The ensuing increase of  $G_{AP}$  strongly reduces the TMR to a few hundred percent, as shown in panel (c) for several junctions. Finally, panel (d) plots TMR as a function of  $x$  in the case where OV are replaced by nitrogen atoms. We can see that scattering induced by nitrogen impurities are less effective than OV, and TMR stay above 8000 % even for 4 % impurities.

Secondly, the author investigate the impact of OV location in the MgO layer. 3 % of OV are placed at both MgO interface layers while the OV concentration in the middle layer is varied. We remind that these calculations are done in the equilibrium regime (no applied bias voltage). From our discussion of the previous section, we know that this situation corresponds to off resonance conditions. Results are presented in the inset of Figure 2.24(d), TMR is almost independent of the OV concentration in the middle layer. Moreover, the location of OV was systematically varied, and it was found that the impact of OV lessens with their distance from the interfaces. As it was mentioned previously, OV allow interchannel scattering, effectively increasing  $G_{AP}$  due to scattering of minority electrons with  $k_{\parallel} \neq 0$  to slow decaying to states with  $k_{\parallel} = 0$ . As the oxygen vacancies

are moved into the interior layers, the overlap between the localized states and incoming Bloch states in the electrodes lowers, especially for fast decaying minority electrons, and thus the impact of interchannel scattering is reduced.

Finally, comparing the impact of oxygen vacancies to interface disorder<sup>93</sup>, *Ke et al.*<sup>159</sup> show that interface oxygen vacancies are more efficient in reducing the TMR than interface disorder.

#### 2.4.2.4 Effect of oxygen vacancies on interlayer exchange coupling in Fe/MgO/Fe MTJs

The interlayer exchange coupling (IEC) refers to the interaction between the magnetization of two ferromagnetic layers separated by a thin spacer layer. It was first observed in trilayers with a metallic spacer and later in devices with an insulating spacer.

The most general formalism describes IEC in terms of spin dependent reflections at the ferromagnetic (FM)-spacer interface<sup>161</sup>. In a FM-spacer-FM trilayer, a charge carrier moving from the left to the right electrode is reflected with a given probability at the right interface. The reflected particle is again reflected with a given amplitude at the left interface and so on. Interactions between forward and backward moving particles result in interferences that induce changes in the density of states (DOS). The change in DOS, which in turn drives the interlayer exchange coupling, has an oscillatory dependence on the spacer thickness. Note that this approach can be applied to evanescent states within an insulating spacer. A detailed review on the subject can be found in ref<sup>161</sup>. In the simplest form, the energy related to IEC can be written:

$$E_{IEC} = J_1 \cos(\theta), \quad (2.15)$$

where  $J_1$  represent the strength of the coupling and  $\theta$  is the relative angle between the magnetization of the electrodes. Positive and negative values of  $J_1$  correspond to ferromagnetic and antiferromagnetic coupling respectively.

Theoretical models accurately describe the coupling of ferromagnetic layers separated by a metallic spacer, in which case the coupling oscillates and decreases with increasing spacer thickness<sup>26,161</sup>. For insulating spacers, theoretical models anticipate a nonoscillatory exponential decrease of the coupling reflecting the evanescent nature of the interaction. Moreover, the strength of the coupling is expected to increase with increasing temperature. This peculiar temperature dependence can be understood in terms of numbers of electrons participating in IEC. Indeed in MTJs, the tunneling probability of electrons depends exponentially on the barrier height. As the temperature increases, additional electrons within  $k_b T$  of the Fermi energy contribute to the tunnel current and thus to IEC.

Figure 2.26(a) plots the magnetic coupling between two Fe layers within crystalline Fe/MgO/Fe<sup>19,162</sup> stack as a function of MgO thickness  $t_{MgO}$ . At very small thicknesses (below 0.5 Å), the coupling is ferromagnetic due to pinholes present in the spacer layer. The coupling is antiferromagnetic between 0.5 – 0.8 Å and crosses over to ferromagnetic coupling for  $t_{MgO} > 0.8$  Å. The origin of this inversion is not well understood and cannot be explained within the framework of the aforementioned model.

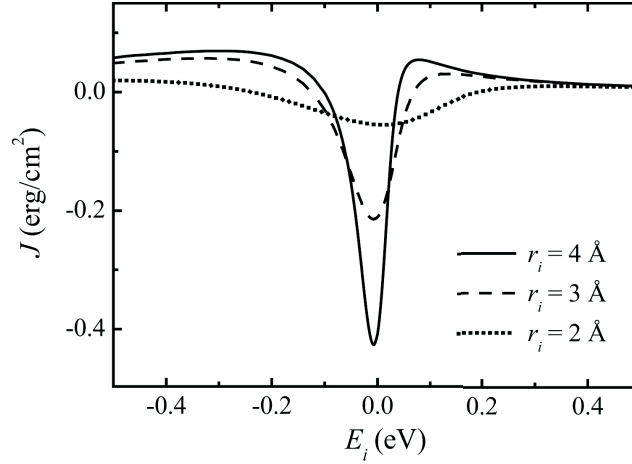


Figure 2.25: **Interlayer exchange coupling mediated by resonant tunneling:** The exchange coupling constant  $J$  is calculated for a magnetic tunnel junction containing a square tunnel barrier of width  $t_b = 8 \text{ \AA}$ . The figure plots  $J$  as a function of the localized state energy position for various positions of defects within the barrier ( $4 \text{ \AA}$  correspond to the middle of the barrier). The coupling is stronger when resonant conditions are satisfied, i.e. when the defect is located in the middle of the barrier and when the defect energy level is positioned at the Fermi energy. Reproduced from [Zhuravlev \*et al.\*](#)<sup>163</sup>.

[Zhuravlev \*et al.\*](#)<sup>163</sup> propose a mechanism involving resonant tunneling through localized states in order to explain these inconsistencies.

In order to compute  $E_{IEC}$ , the authors consider two semi-infinite electrodes separated by a square barrier of thickness  $d$ . The electronic structure of the electrodes is modeled by free electrons and ferromagnetism is introduced by artificially inserting an exchange splitting term in order to split the band structure of spin up and down electrons. Impurities are modeled by delta functions located in the barrier. As we discussed previously, impurities introduce a localized states with energy  $E_i$  compared to the Fermi energy.

First, the authors compute  $J$  as a function of  $E_i$  for different defect locations within the  $8 \text{ \AA}$  thick tunnel barrier. Results are plotted in [Figure 2.25](#). We can see that the coupling becomes larger (i) when  $E_i = E_F$  and (ii) when the defect is located in the middle of the dielectric layer. Both observations are consistent with our discussion on resonant tunneling through a single impurity level (see [Section 2.4.1.1](#)). We can thus conclude that IEC strength is increased due to additional tunneling electrons promoted by resonant tunneling.

Concerning the sign of the coupling, it can be understood from the spin dependent impurity-induced DOS in the gap of the insulating layer represented in [Figure 2.26\(f\)](#) and (g) for  $E_i = 0.3 \text{ eV}$  and  $E_i = 0 \text{ eV}$  respectively. We remind that the the width as well as the position of localized states depend on their coupling with the electrodes. Since the density of evanescent states is larger for majority electrons (defined by the exchange splitting term in the electrodes), the coupling with majority electrons is stronger and results in a broader peak compared to minority electrons. Similarly, majority and minority peaks in the DOS are shifted in opposite directions due to spin dependent interactions between

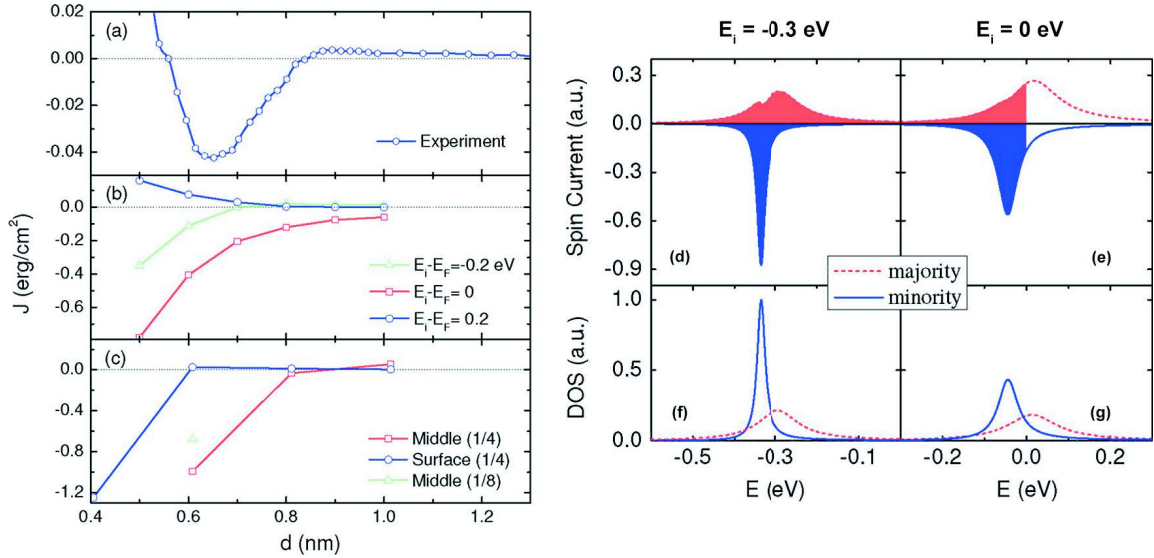


Figure 2.26: **Interlayer exchange coupling mediated by defects:** (a) Experimental measurement of IEC in a wedge-shaped Fe/MgO/Fe trilayer. The ferromagnetic coupling at small thicknesses is due to the presence of pinholes in the MgO layer. The antiferromagnetic coupling for intermediate thicknesses as well as the crossover to ferromagnetic coupling at larger thicknesses cannot be explained with conventional models. Panel (b) plots IEC calculated using an empirical model for various energetic positions of the localized state. We can see that localized states positioned 0.2 eV below  $E_F$  reproduce experimental data. Panel (c) plots similar results from first principle calculations for Fe/MgO/Fe MTJs containing oxygen vacancies. Panels (d) and (e) represent the resonant spin current related to defect-induced DOS within the band gap of the tunnel barrier, as shown in panels (f) and (g), for two localized states energy positions,  $E_i = -0.3$  eV and  $E_i = E_F$  respectively. Reproduced from *Velev et al.*<sup>19</sup>.

impurity states and electrodes.

In turn, the ensuing spin current due to localized states is also spin dependent and has approximately the same shape as the DOS features, as shown in Figure 2.26(d) and (e). Moreover, we can see that both spin channels have opposite contributions to the spin current. Majority and minority spin currents contribute in ferromagnetic (FM) and antiferromagnetic (AF) exchange coupling, respectively. It follows that, when majority or minority channel dominate the total current, the exchange coupling will be FM or AF, respectively.

Besides, the total net current is the integral over all the energies up to  $E_F$  (weighed by their transmission probability) as represented by the red (majority) and blue (minority) areas in Figure 2.26(d) and (e). When the impurity level lies below the the Fermi level (panel (d)), both resonant channels fully contribute to the total current but the majority channel dominates and the coupling is expected to be FM. However, if the impurity lies close to  $E_F$  such that the majority resonant peak contributes only partially to the current while the minority resonant peak is fully integrated, the minority channel dominates and

the exchange coupling is expected to be AF.

Finally, Figure 2.26(b) plots IEC strength as a function of spacer thickness for different energy positions of the localized state. For  $E_i = 0.2$  eV and  $E_i = 0$  eV =  $E_F$ , the coupling is FM or AF respectively but decreases exponentially without crossover in both cases. When  $E_i = -0.2$  eV a crossover between FM and AF coupling occurs, similar to Figure 2.26(a) and IEC measured by Faure-Vincent *et al.*<sup>162</sup>.

In order to confirm results obtained with this simple model, which has the advantage of being transparent, Katayama *et al.*<sup>164</sup> calculated IEC in ideal and defective Fe/MgO/Fe MTJs from first principles. As expected from theory, they find that IEC is ferromagnetic for ideal MgO and decreases exponentially with MgO thickness. Moreover, they find that the decay rate of the coupling is similar to the decay rate of  $\Delta_1$  electrons<sup>49</sup> in MgO, meaning that IEC is mainly mediated by the slowest decaying states in MgO. O vacancies are then introduced by removing a neutral Oxygen atom and replacing it by an empty sphere of the same radius. The concentration of vacancies is varied from 1 vacancy per 8 oxygen atoms to 1 vacancy per 4 oxygen atoms. Additionally, defects position is varied from middle layer to the surface layer. Results are plotted in Figure 2.26(c). We can see that the coupling becomes stronger when (i) the defect concentration increases and (ii) defects are located in the middle of the MgO slab. Furthermore, similarly to experimental results, the calculated coupling is AF in the presence of F centers at small thicknesses and crosses over to FM slightly above  $t_{MgO} = 0.8$  Å. This is also consistent with the DOS of F centers presented in Figure 2.22. Indeed, we see that, for 3 ML of MgO, the width of the localized state around  $-1$  eV increases due to its coupling with the electrodes, and a non negligible DOS is present around  $E_F$ . At larger thicknesses, the F centers are more localized and do not induce DOS at the Fermi energy, and IEC becomes FM as expected from theory<sup>161</sup>.

Briefly, Zhuravlev *et al.*<sup>163</sup> show that defect-induced localized states situated  $-0.2$  eV below  $E_F$  are expected to promote an antiferromagnetic exchange coupling for small thicknesses. As the thickness increases, the impact of resonant tunneling progressively lessens and the coupling becomes ferromagnetic as expected from theory. Katayama *et al.*<sup>164</sup> clearly identify F centers as possible candidate to explain the antiferromagnetic exchange coupling mediated by resonant tunneling through localized states located near  $E_F$  from first principle. Nevertheless, we must emphasize that DFT approaches do not correctly account for self-interaction. As it is discussed in ref<sup>158</sup>, when self interaction is taken into account, the energy position of LS is greatly modified. This is illustrated in Figure 2.22(a), the dashed line represent the energy position of the localized states induced by oxygen vacancies when self-interactions are taken into account. Other shortcomings of DFT limit the direct quantitative comparison between theory and experiments.

### 2.4.3 Optical activity of oxygen vacancies in MgO

In the previous section, we saw that any deviation from the perfect crystal structure can result in localized states positioned in the band gap of the insulating material. In particular, we discussed the influence of oxygen vacancies on the properties of MgO and on the electrical as well as magnetic properties of crystalline Fe/MgO/Fe devices.

A large part of the results presented in this thesis are temperature dependent electrical measurements from which changes due to localized states are identified. As it is thoroughly discussed in this chapter, many processes can potentially impact the tunnel current. In order to discriminate the impact of oxygen vacancies from other processes, their characteristics have to be clearly identified. It is the purpose of this section to review the characteristics of localized states induced by the presence of oxygen vacancies in MgO.

First, the peculiar optical activity of MgO induced by the presence of localized states is discussed both from experimental and theoretical points of view. Then, a small section is dedicated to a model that predicts coherent tunneling between oxygen vacancies in MgO.

### 2.4.3.1 Photoluminescence of point defects

Photoluminescence (PL) is one of the first experimental tools used to characterize localized states in the band gap of semiconductors or dielectrics. The principle behind PL induced by localized states is very simple. A basic PL scenario is schematized in Figure 2.27(a).

An electron occupying a localized state in the gap ( $E_g$ ) of the dielectric can be excited to an empty state with higher energy by absorbing a photon of energy  $\hbar\omega = E$ , where  $\hbar$  is the Planck constant,  $\omega$  the photon frequency and  $E$  the energy difference between the initial and the final state. The excited electron can then recombine to available states with lower energies. This relaxation process can be accompanied by the emission of a photon of energy  $\hbar\omega' = E'$  where  $\omega'$  is the frequency of the emitted photon and  $E'$  the energy difference between the initial (excited) and final (ground) state. When  $\hbar\omega' < \hbar\omega$ , it means that some energy was lost through interaction of the photo-excited particle with the phonon field of the crystal (heat). The energy difference between the absorbed and emitted light is called a Stokes shift. When  $\hbar\omega' > \hbar\omega$ , the photo-excited particle absorbed some energy from the crystal, and the process is called an anti-Stokes shift.

Moreover, exciting or removing an electron from an oxygen vacancy in MgO results in lattice distortion in the vicinity of the defect site. Figure 2.27(b) represents a configuration coordinate diagram that illustrates the interaction between localized electrons and the lattice of the MgO crystal. This diagram plots the energy of the crystal as a function of the position of the ions that interact with the defect center in the solid. In the simplest case the abscissa represents the distance between the center and its nearest neighbors. Since optical transitions are much faster than the motion of atoms in the crystal (Franck-Condon principle), it is assumed that electrons in the ground state are promoted to *unrelaxed* excited states (red arrow in Figure 2.27(b)). Once the lattice relaxes through the interaction with excited particles, electrons recombine to the (unrelaxed) ground state by emitting a photon with lower energy, resulting in a Stokes shift (blue arrow).

Additionally, we can see from Figure 2.27(b) that a small displacement in the ground state (due to thermal vibrations for example) results in a large spread in energy in the unrelaxed excited state, leading to a large absorption band. Similar conclusions can be drawn for the emission process.

We must emphasize that since the optical transitions always involve relaxed and unrelaxed states, the absorption and luminescence bands do not give the energy difference between ground and excited states, since the proportion of energy lost to the lattice during

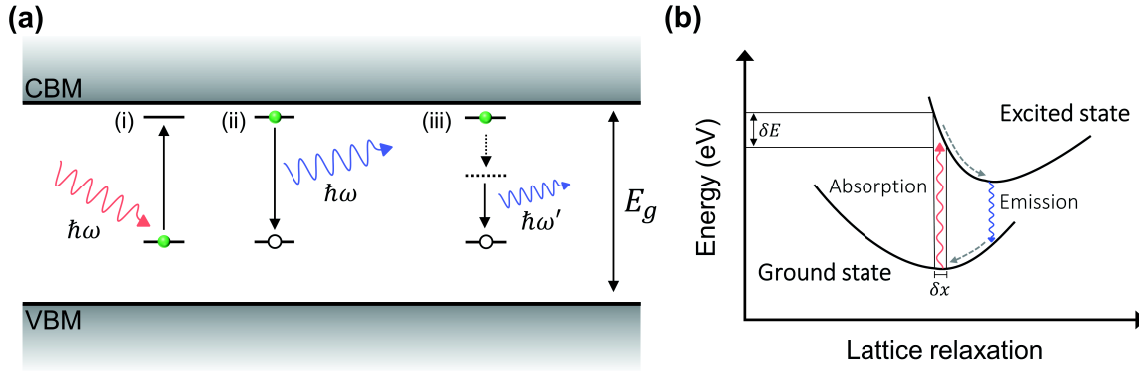


Figure 2.27: **Principle of photoluminescence measurements:** Panel (a) represents a simple schematic of a photoluminescence process. In the first step, an electron occupying the ground state of a localized state in the band gap of the dielectric absorbs a photon of energy  $\hbar\omega = E$  and is promoted to an excited state. In a second step, the excited electron can recombine with the ground state by emitting a photon with the same energy, as represented in (ii). In real materials the process can be more complicated due to the interaction between electrons and the crystal lattice. In this process electrons can lose energy to the crystal and emit a photon of lower energy. This is represented in (iii). Panel (b) represents a configuration coordinate diagram. When an electron occupying a defect state is excited or removed, the lattice around the point defect is distorted. Since optical transitions are much faster than the motion of atoms (Franck-Condon principle), the electron in the ground state is excited to an *unrelaxed* excited state (red arrow). After relaxation of the lattice, the electron can recombine with the ground state by emitting a photon with a lower energy, resulting in a Stokes shift (blue arrow).

the excitation and relaxation processes is not known. In some cases, a direct recombination between the relaxed excited and ground states is possible and results in a very sharp luminescence band, also called the zero phonon line. Although no zero phonon lines characterize the luminescence of single oxygen vacancies, we'll see that it is the case for the emission of  $M$  centers (double oxygen vacancies).

Monitoring the time and temperature dependence of a luminescence peak allows to get useful information on the various states that may be present in the band gap of the material under study. Although the technique was successfully applied to semiconductors and divalent dielectrics such as CaO, its application to the case of MgO has proven very difficult and is discussed hereafter.

### 2.4.3.2 Single oxygen vacancies

Several works investigated the optical activity of MgO induced by single oxygen vacancies ( $F$  centers) in pristine crystals as well as crystals with varying type and concentration of defects<sup>165–169</sup>. The goal of this section is not to give a complete overview of the results obtained from PL measurements, but rather introduce several important characteristics

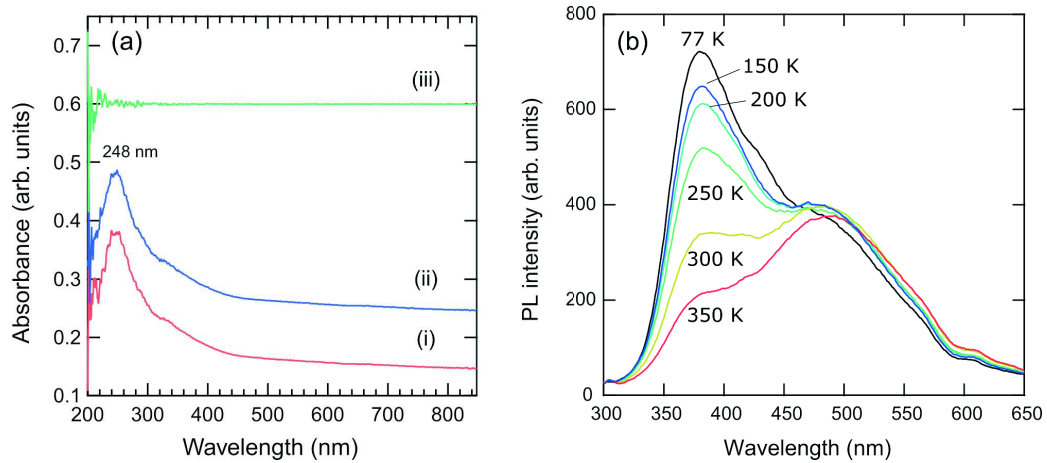


Figure 2.28: **Absorption and photoluminescence of MgO:** Absorption spectra (a) and photoluminescence spectra of MgO for various temperature (b). In panel (a), cruves (i) and (ii) are the absorption of MgO before and after long exposure to 5 eV photons. Cruve (iii) result from the difference between (i) and (ii). A single absorption peak at 248 nm (5 eV) results in two luminescence peaks located around 2.3 eV (540 nm) and 3.2 eV (390 nm) related to the luminescence of  $F$  and  $F^+$  bands respectively. The  $F^+$  peak has a strong temperature dependence. Reproduced from Uenaka and Uchino<sup>169</sup>.

that will be used to discuss different models proposed in the literature to explain the optical activity of MgO.

A typical absorption spectra of MgO is plotted Figure 2.28 panel (a). We can see that MgO has a single absorption band centered around 248 nm (5 eV). The fact that the absorption is the same after long exposure to 5 eV photons exclude the presence of other defects in large concentrations (Mg vacancies or other impurities). The steady state photoluminescence spectra related to the 248 nm absorption peak is presented in panel (b). Interestingly, we can see that the single absorption peak results in two luminescence bands located at 2.3 eV (540 nm) and 3.2 eV (390 nm). These have been attributed to the emission of the  $F$  and  $F^+$  bands respectively.

The identification of these two bands was not easy. It required the careful preparation of crystal containing a specific defect population. Two techniques were mainly used to introduce  $F$  and  $F^+$  centers, the first one consists in annealing MgO crystals at high temperatures ( $\sim 2000$  K) under a strongly reducing environment (background pressure of Mg). This so called thermochemical reduction (TCR) result in a crystal that contains mainly  $F$  centers. A second technique consist in exposing high quality MgO crystals to neutron radiations, producing mainly charged  $F^+$  centers. Additionally, it was found that long exposure of TCR samples to UV light resulted in the conversion of  $F$  to  $F^+$  centers and that a subsequent annealing step produced the inverse conversion,  $F^+$  to  $F$ .

Finally, the fact that  $F^+$  centers are paramagnetic (singly occupied state) was used to discriminate both bands. Indeed, concurrent electron paramagnetic resonance (EPR) and photoluminescence experiment established that the emission band at 3.2 eV (390 nm) is

related to an EPR signal and hence attributed to  $F^+$  states. When the EPR signal disappears, the absorption peak is still present but results in a single luminescence band located at 2.3 eV (540 nm) and is thus ascribed to  $F$  centers. Please refer to [Hughes and Henderson](#)<sup>170</sup> for a complete overview.

In addition to this particularity, the optical activity of MgO is special in several other ways. First of all, the optical transition between ground ( $s$ -like) and excited ( $p$ -like) states of  $F$  and  $F^+$  centers is allowed, thus the recombination is expected to be very fast and the PL signal very short. However, it was shown that the PL signal of these two bands is long-lived and can be measured several seconds after excitation. Secondly, the strong temperature dependence of the  $F^+$  states suggest a thermally activated process. Also, it was shown that the  $F$  to  $F^+$  relative emission intensities is dependent on the impinging photon flux, implying some sort of photoconversion process between the two centers. Finally, time resolved PL experiments established that the  $F^+$  luminescence (3.2 eV) has a fast decay component, in the ns- $\mu$ s timescale, while the  $F$  emission is detected only at longer detection delays.

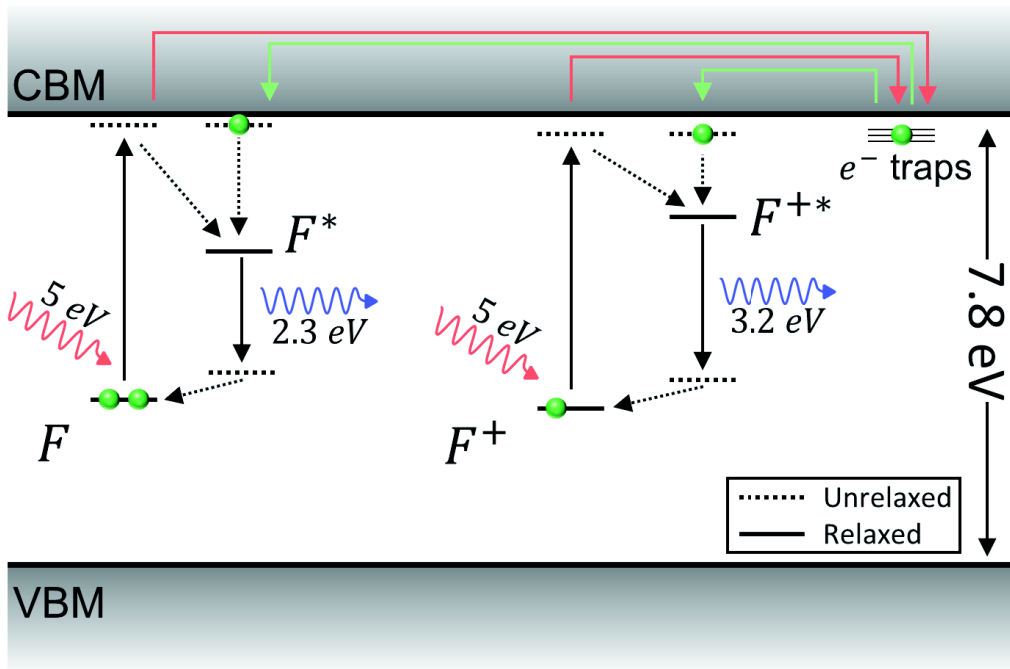


Figure 2.29: **Rosenblatt’s model to explain the PL spectra of MgO:** Both  $F$  and  $F^+$  states absorb 5 eV photons and promote electrons in their respective excited states. The excited states can either (i) radiatively recombine to the unrelaxed ground state after lattice relaxation (explaining the Stokes shift), or (ii) ionize to the conduction band due to thermal excitation. The electrons in the conduction band are then retained in trap states induced by other impurities (red arrows), constituting an electron reservoir that provides electrons to  $F^*$  and  $F^{+*}$  states and explain the long-lived photoluminescence (green arrow). Adapted from [Rosenblatt et al.](#)<sup>167</sup> and [Uenaka and Uchino](#)<sup>169</sup>.

In order to explain these unconventional results, Rosenblatt *et al.*<sup>167</sup> proposed a model involving trap states and lattice relaxation to explain the delayed PL signal and the strong Stokes shift reported. The model is schematized in Figure 2.29 and can be summarized as follows. Oxygen vacancies result in neutral  $F$  centers located in the band gap of MgO. The localized states are occupied by two electrons and can absorb 5 eV photons resulting in *unrelaxed*  $F^*$  excited states. The excited  $F^*$  states can either radiatively decay by emitting photons of energy  $\hbar\omega = 2.3$  eV (some energy is lost due to the interaction between the photo-excited electron and the the crystal structure, resulting in the relaxation of the lattice) or ionize by promoting an electron to the conduction band minimum (CMB), resulting in  $F^+$  states. This suggests that  $F$  states are located approximately 5 eV below the conduction band minimum (CBM) and that the excited  $F^*$  state is very close the CBM, such that a small thermal energy  $k_bT$  is sufficient to ionize the state. The resulting  $F^+$  centers can also absorb 5 eV photons, resulting in *unrelaxed*  $F^{+*}$  excited states. Again, the excited  $F^{+*}$  states can either radiatively recombine by emitting photons with energy  $\hbar\omega = 3.2$  eV (Stokes shift due to lattice relaxation) or ionize, resulting in doubly charged  $F^{2+}$  states. This implies that the  $F^+$  states lies at the same level as the  $F$  centers, that the excited  $F^{+*}$  states lies close to the CBM and that the  $F^{2+}$  exists. Finally, in order to account for the long-lived photoluminescence, the authors suggest the presence of trap states located near the conduction band. Electrons promoted to the conduction band after ionization of  $F^*$  and  $F^{+*}$  states can be retained in these electron traps (red arrows in Figure 2.29), resulting in a reservoir of electrons available for delayed  $F$  and  $F^+$  emission (green arrow in Figure 2.29).

Uenaka and Uchino<sup>169</sup> slightly modified this model in order to explain the temperature dependence and the fast decay component of the  $F^+$  band. In order to explain the absence of a fast decay component of the  $F$  band, they suppose that  $F^*$  always ionizes to the conduction band, which thus precludes direct recombination.

Trap states can originate from  $H^-$  impurities that induce localized states near the conduction band minimum. Even at low concentrations,  $H^-$  centers can effectively trap electrons and result in delayed PL. Uenaka and Uchino<sup>169</sup> also propose the excited *unrelaxed*  $F^{+*}$  states that can act as shallow traps. Other candidates can be double oxygen vacancies, denoted  $F_2$  or  $M$  centers, or weakly coupled  $F - F$ ,  $F^+ - F$  and  $F^+ - F^+$  pairs.

As it emphasized by Gibson *et al.*<sup>171</sup>, the main deficiency of this model is related to the impact of the lattice relaxation. Indeed, to account for the large Stokes shift of the emission bands compared to the 5 eV absorption, the energies involved by the lattice reconfiguration in the vicinity of the defect site should be 2.7 eV and 1.8 eV for the  $F$  and  $F^+$  emission processes respectively. Although the relaxation of atoms around the defect site is expected, such large values are surprising.

Gibson *et al.* proposed an alternative model to explain the optical activity of MgO. In this model,  $F$  and  $F^+$  centers are actually 1.22 eV and 1.4 eV below the conduction band minimum. The 5 eV absorption peak is related to the excitation from doubly or singly occupied  $F$  and  $F^+$  states in the gap of MgO to unoccupied states induced by oxygen vacancies in the conduction band of MgO approximately 5 eV above  $F$  and  $F^+$  centers. The excited electrons can then nonradiatively relax to the bottom of the conduction band and finally radiatively recombine with ground states. Although the calculated energy differ-

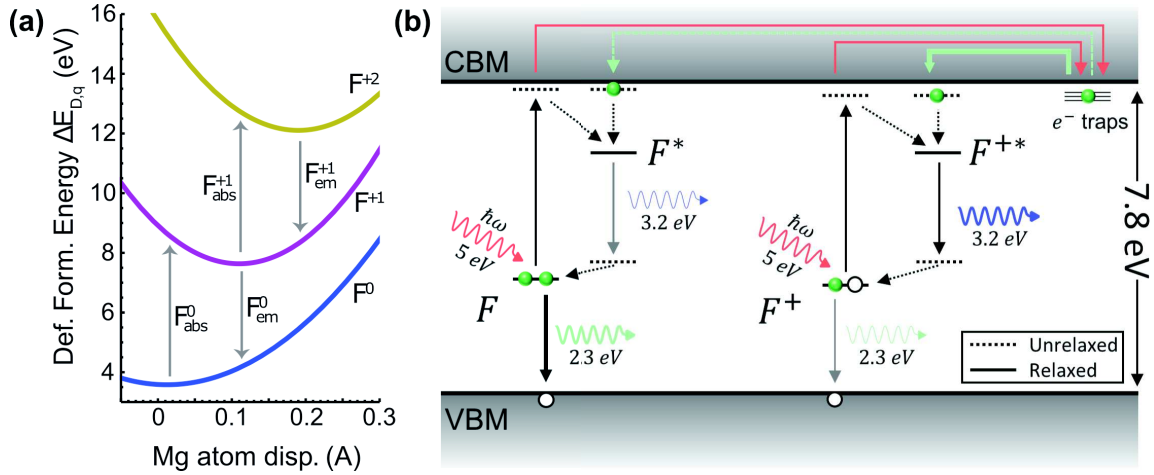


Figure 2.30: **Extension of Rosenblatt's model:** Panel (a) plots the configuration coordinate diagram related to the absorption of 5 eV photons by  $F$  and  $F^+$  centers in MgO (Reproduced from Ertekin *et al.*<sup>173</sup>). The corresponding absorption and emission values obtained from first principles are summarized in Table 2.1. Panel (b) represents the scenario proposed by Rinke *et al.*<sup>172</sup>. The broad emission peak centered around 3.2 eV is associated with both  $F$  and  $F^+$  emission bands. In order to explain the emission peak centered around 2.3 eV, they propose the relaxation of electrons from  $F$  and  $F^+$  states to the valence band. See text for more details. Adapted from Rinke *et al.*<sup>172</sup>.

ences are not consistent with experimental values, the authors argue that their model is consistent with the formation energy of oxygen vacancies in MgO.

Recently, two papers tackled the problem of  $F$  and  $F^+$  emission from a theoretical point of view<sup>172,173</sup>. First, Rinke *et al.*<sup>172</sup> used many-body perturbation theory in the  $G_0W_0$  approximation to calculate the optical absorption and emission spectrum of  $F$  and  $F^+$  centers in MgO. In a second paper, Ertekin *et al.*<sup>173</sup> used a different computational method based on a Quantum Monte-Carlo (QCM) approach to compute the same quantities. Quantitative values obtained in the two papers are essentially the same. In particular, the calculated absorption values of  $F$  and  $F^+$  centers are very close to experimental results. In order to obtain absorption value similar to experiment, both the lattice relaxation and the interaction between the excited electron and the hole present in the ionized state are considered. The fact that two papers that use different computational methods yield similar values, which are additionally consistent with experiments, reinforce the reliability of these theoretical works.

Similarly to many theoretical treatments of oxygen vacancies in MgO<sup>171,174–176</sup>, it is found that removing an oxygen atom result in a  $s$ -like doubly occupied localized state in the gap of MgO. In addition to the ground state located approximately 5 eV below the conduction band minimum (CBM), a  $p$ -like excited state is found just below the CBM.

When an oxygen atom is removed and a  $F$  center is created, calculations show that neighboring Mg atoms move slightly outward while next neighbors O atoms are attracted

Table 2.1: **Absorption and emission of F and F<sup>+</sup> centers in MgO:** Computed absorption and of  $F$  and  $F^+$  centers confronted to experimental values.

	$F_{\text{abs}}$	$F_{\text{em}}$	$F^+_{\text{abs}}$	$F^+_{\text{em}}$
Rinke <i>et al.</i> <sup>172</sup>	4.95 eV	3.4 eV	4.92 eV	3.6 eV
Ertekin <i>et al.</i> <sup>173</sup>	5.1 eV	3.5 eV	5 eV	3.8 eV
Experimental values	5 eV	2.3 eV	4.95 eV	3.2 eV

and move slightly inward. The lattice distortion is accentuated as the charge of the defect state is increased ( $F^+$  and  $F^{2+}$ ). Figure 2.30(a) represents the configuration coordinate diagram related to the distortion of the lattice. The corresponding absorption and emission values are summarized in Table 2.1.

As we can see from Table 2.1, the computed absorption values are in very good agreement with experiment. Moreover, the fact that the  $F^+$  states absorb at slightly lower energies than the  $F$  centers is also reported in the literature<sup>165</sup>. Since both  $F$  and  $F^+$  states absorb at the same energy, the luminescence related to the two bands is expected to be similar. This is actually what is found theoretically, the emission related to the  $F$  and  $F^+$  centers peak at 3.4 eV and 3.6 eV respectively. As it was already reported by Gibson *et al.*<sup>171</sup>, it is found that the lattice relaxation does not account for 2.7 eV stoke shift to explain the 2.3 eV emission as proposed by Rosenblatt *et al.*.

In order to explain the 2.3 eV emission, Rinke *et al.*<sup>172</sup> propose an extension to Rosenblatt's model. The model is schematized in Figure 2.30(b). The difference of this model lies in the fact that the 3.2 eV luminescence is attributed to both  $F$  and  $F^+$  centers. Additionally, the authors propose the relaxation of electrons in  $F$  and  $F^+$  centers to holes present in the valence band, that would yield an emission peak close to 2.3 eV. Besides, the fact that 2.3 eV and 3.2 eV peaks are associated with  $F$  and  $F^+$  centers can also be rationalized. Indeed, ionized electrons in the conduction band will preferably interact with charged  $F^+$  states. Similarly holes in the valence band will be repelled by charged states and will preferably interact with  $F$  neutral centers. Finally, the model predicts an additional absorption peak near 3.6 eV that would correspond to the excitation of electrons from the valence band to  $F^+$  centers.

The only weakness of this model is related to the presence of holes in the valence band. This point was discussed by Rosenblatt *et al.*<sup>167</sup>, but the creation of holes in the valence band with 5 eV light would require a state near midgap but no such state is reported in the literature. Rinke *et al.*<sup>172</sup> also propose a photobleaching effect induced by 5 eV photons but the proposed mechanism is not further discussed in their paper.

To quickly summarize, oxygen vacancies induce an  $s$ -like occupied state in the band gap of MgO, 5 eV below the conduction band. These neutral states, named  $F$  centers, can be singly ( $F^+$ ) or doubly charged ( $F^{2+}$ ). Different theoretical works established that the position of the ground state of  $F$  states in the gap was not very sensitive to the charge, i.e.  $F$ ,  $F^+$  and  $F^{2+}$  are energetically close to each other<sup>172,174,175</sup>. In addition to the ground state, a  $p$ -like excited state is located close to the bottom of the conduction band. Besides,

experimental and theoretical work emphasized the importance of the coupling between photo-excited electrons and the lattice of the MgO crystal. The most reasonable model to explain the complicated PL spectra of MgO is schematized in [Figure 2.30](#).

### 2.4.3.3 Double oxygen vacancies

As the concentration of oxygen vacancies increases, the distance between defect sites decreases, isolated defects start to interact with each other and may eventually form double oxygen vacancy, also called M centers, when point defects are on adjacent sites on the oxygen sublattice. Similarly to *F* centers, double oxygen vacancies can be in charged ( $M^+$ ,  $M^{2+}$ ) and/or excited states (denoted \*). Although *M* centers are discussed in several experimental and theoretical papers<sup>169,177–182</sup>, they didn't receive as much attention as *F* centers and absorption and emission peaks related to *M* centers are not unambiguously identified.

First, [Chen et al.](#)<sup>177</sup> observed additional absorption peaks at 355 nm (3.47 eV), 574 nm (2.16 eV) and 975 nm (1.27 eV) in neutron irradiated samples. At low Temperature, these bands are accompanied by zero phonon lines (direct recombination between unrelaxed excited and ground states). Zero phonon lines (ZPL) are characterized by very sharp peaks, similarly to the transition in isolated atoms, and deliver much more information concerning the emitting center than wide luminescence bands, e.g. the energy separation between ground and excited states. Besides, modification induced to ZPL peaks induced by uniaxial stress experiments that consist in applying a stress in a given crystal direction, allows to probe the anisotropy of charge distribution of localized states. Additionally, polarized luminescence experiments can also be used to extract supplementary information on the emitting center. Using the aforementioned techniques, two absorption peaks at 355 nm (3.5 eV) and 325 nm (3.81 eV) associated with luminescence peaks at 375 nm (3.3 eV) and 441 nm (2.8 eV) are tentatively ascribed to  $M^{179}$  and  $M^{+2}$ <sup>178</sup> centers.

*M* centers were also investigated theoretically<sup>181</sup>. [Figure 2.31](#) represent a simple diagram of the energy levels involved in the optical excitation of M centers. In the ground state, both lowest lying states of *M* centers are fully occupied, and the optical transition is expected to occur between the highest occupied state and the lowest unoccupied state lying 4.4 eV higher in energy. When an electron is removed to create a  $M^+$  center, an additional absorption peak is expected between the lowest doubly occupied state and the now partially filled state separated by 1.3 eV. As it is discussed by [Domínguez-Ariza et al.](#)<sup>181</sup>, calculations tend to overestimate the absorption energy and theoretical results cannot be qualitatively compared to experimental values. Indeed, we can see that predicted absorption values are rather far away from the 3.5 eV observed experimentally.

As a concluding remark concerning the optical activity of MgO, it should be emphasized that the different models proposed in the literature and presented in this section are not totally unambiguous. Besides, a lot of photoluminescence experiments report additional absorption and emission peaks in MgO<sup>183,184</sup>. However, the origin of additional peaks should be interpreted carefully because the PL of MgO is sample dependent and extremely sensitive to additional impurities. It is also reported that MgO nanocrystallites are characterized by additional peaks because the surface area of nano-powders is much

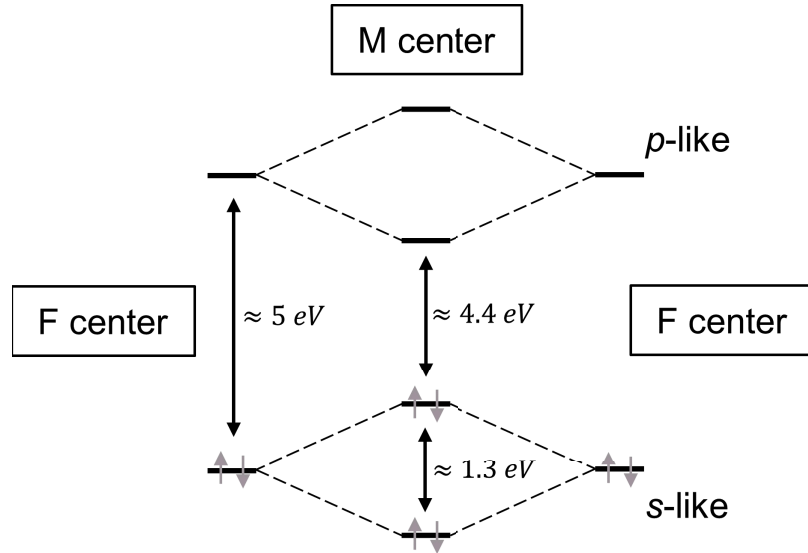


Figure 2.31: **Optical activity of double oxygen vacancies:** Simple representation of the energy levels involved in the electronic excitation of *M* centers (double oxygen vacancies). Adapted from Domínguez-Ariza *et al.*<sup>181</sup>.

larger than macroscopic sample, and many of the optical features are ascribed to surface vacancies located on different coordination sites of the surface that can absorb and emit at different energies. Finally, we note that the absorption coefficient related to the 250 nm (5 eV) absorption is always much larger than other absorption bands.

#### 2.4.3.4 Coherent tunneling between defects in MgO

Recently, McKenna and Blumberger<sup>185</sup> theoretically investigated the tunneling of electrons between *F* centers in MgO. More particularly, they considered the transfer of electrons between a neutral *F* center and a charged  $F^+$  state. The process can be written:



where the subscripts *i* and *ii* denote two oxygen vacancies located at  $r_i$  and  $r_{ii}$  respectively. The electron transfer rate is computed as a function of the distance  $d$  between two defects aligned along various crystal directions.

Their computational method involves the calculation of two key parameters determining the electron transfer rate: (i) the electronic coupling matrix element denoted  $H_{ab}$  and (ii) the reconfiguration energy, denoted  $\lambda$ , which is related to the distortion of the lattice around the defect when an electron is added or removed. Both quantities are then used to compute the electron transfer rate and the activation energy within Marcus theory of electron transfer.

Figure 2.32 plots the electronic coupling, the reconfiguration energy and the electron transfer rate as a function of  $d$  in panels (a), (b) and (c) respectively. The electronic coupling of the two defects is expected to decay exponentially with  $d$ , as represented by the

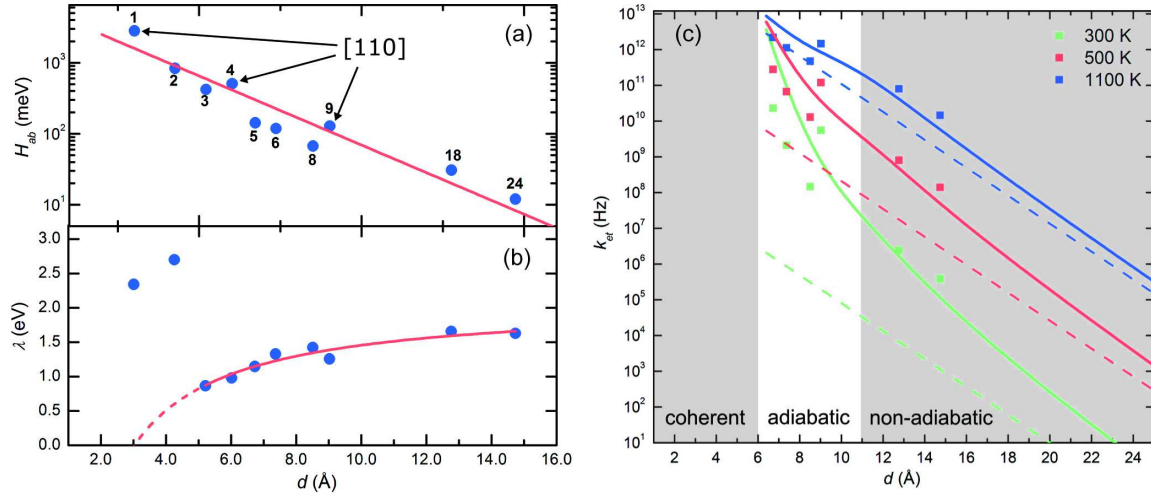


Figure 2.32: **Tunneling between oxygen vacancies in MgO:** (a) Electronic coupling matrix elements and (b) reconfiguration energy as a function of the distance  $d$  between  $F$  centers along various crystal directions. (c) Electron transfer rate between oxygen vacancies as a function of  $d$  in MgO plotted for three temperatures. Dashed lines are calculated assuming nonadiabatic electron transfer and constant activation energy. Reproduced from McKenna and Blumberger<sup>185</sup>.

red line in panel (a). We can see that the behavior of  $H_{ab}$  deviates significantly from the expected exponential decay. The authors emphasize that this is not due to inaccuracies in the calculation but to an intrinsic anisotropy of the system. Indeed, as it is indicated in panel (a), the coupling is larger when the distance between defects is along the [110] direction. The coupling of defects aligned in this direction can even be larger than that of defects which are closer but aligned along different directions. This is ascribed to the fact that the  $p$  orbitals of oxygen atoms in MgO extend along the [110] direction and mix more effectively with  $s$ -like orbitals at the defect site, resulting in a larger charge density in the [110] direction.

As shown in panel (b), the reconfiguration energy is very large when defects are separated by less than 5 Å. This is due to overlapping and opposing ionic distortion fields.  $\lambda$  becomes smaller for distances larger than 5 Å, and increases slowly with defect separation.

Panel (c) plots the electron transfer rate as a function of  $d$  for different temperatures. Three regimes can be distinguished. First, for defects separation above 11 Å, the electron transfer rate decays exponentially. In this non-adiabatic regime the decay is solely due to the reduction of the electronic coupling between defects. Secondly, for distances between 6 Å and 11 Å, the behavior deviates from the mono-exponential decrease because the electron transfer rate now depends on both the electronic coupling and to the strong increase in the reorganization energy which in turn defines the electron transfer activation energy. At  $T = 1100$  K the thermal energy is large enough to compensate the increase of the activation energy and the decay rate as a function of defects separation is monotonous and similar in both regimes.

Finally, McKenna and Blumberger identify a third regime for defects that are separated

by less than 6 Å. This regime is characterized by a negative activation energy, meaning that the electron is delocalized in the two defect sites. In this case, the electron transfer mechanism crosses over from incoherent to coherent tunneling and the computational method used by McKenna and Blumberger is not valid anymore.

This work emphasizes two important aspects concerning the impact of oxygen vacancies on magnetotransport. First, it is shown that the lattice relaxation plays a crucial role in the transfer of electrons between two defect, the energy related to lattice distortion induced by the transfer of one electron depends strongly on the distance between the two defects. Secondly, it is shown for the first time that defects can promote coherent tunneling. Although calculations are limited to electron transfer between two defects in bulk MgO and are not applied to MTJs, these results provide a proof that introducing defects in the dielectric of MTJs can be advantageous in terms of preserving an electron's quantum properties such as symmetry and spin, conversely to what is generally believed. This point will be further discussed in the section dedicated to the scientific motivations of this thesis (Section 2.6).

## 2.5 Conclusion

In the first chapter of this thesis, we reviewed theoretical models in order to explain the origins of high TMR values obtained in crystalline magnetic tunnel junctions. These models mostly consider perfect crystal structures and compute device properties in the equilibrium regime, i.e. when no bias voltage is applied. Very quickly, experimental results successfully confirmed the mechanism of symmetry filtering effect in devices composed of a crystalline MgO barrier coupled to ferromagnetic transition metal electrodes.

Following the first experimental breakthrough in achieving high TMR ratios, tremendous efforts were made in order to approach the very high TMR values predicted by theory. However, the highest TMR obtained in real device barely exceeds 1000 %, a value an order of magnitude lower than the 30 000 % expected from theory. The attention was then focused on all the deviations that realistic devices might have compared to the perfect systems considered in early first principle models.

The goal of this chapter was to review various imperfections present in realistic junctions and discuss their impact on magneto-electric properties of working devices. Firstly, considering the deviations from perfect systems is motivated by the desire to understand and explain various discrepancies between theory and experiment in order to eventually improve devices architectures and performances. Secondly, a closer look at this chapter shows the complexity and the concurrent impact of many processes on the device electrical properties, making the interpretation of a quantity as simple as the device conductance quite complicated. We remind that the main goal of this thesis is to characterize the effect of oxygen vacancies on electrical properties of MgO based MTJs. In order to accurately interpret bias- and temperature-dependent electrical measurements and unambiguously identify the impact of oxygen vacancies, it is essential to dress a detailed picture of tunneling in MTJs. Additionally, we'll see in the last section of this chapter that desirable device properties such as high TMR ratios combined with device low barrier height could be explained by the presence of device imperfections, e.g. oxygen vacancies.

Finally, we saw that spin dependent tunneling in MTJs is extremely sensible to many parameters such as interface properties, bias voltage, temperature as well as other intrinsic (magnon, phonon) and extrinsic (impurities, vacancies, disorder) device properties. Although this makes the fabrication and characterization of such devices complicated, it also provides an interesting playground, both from theoretical and experimental point of view, to engineer devices with new architectures and properties.

## 2.6 This thesis scientific motivations

This work was carried within the framework of a broader project in the field of inorganic spintronic that aims to develop materials for next generation devices. This thesis mainly focuses on the impact of oxygen vacancies present within oxide layers integrated in working electronic devices. In particular, it aims to characterize the effect of such defects on spin dependent tunneling in MgO based magnetic tunnel junctions. Basically, the objectives of this work can be divided in two fields: the first line of research aims to characterize the impact of localized states induced by oxygen vacancies on the properties of CoFeB/MgO/CoFeB magnetic tunnel junctions.

The second goal of our work is to use the knowledge acquired during the first stage of the project in order to actually use the effects induced by oxygen vacancies as additional devices functionality. Both research objectives are motivated by discrepancies and/or interesting phenomenon reported in the literature and are discussed hereafter.

### 2.6.1 Impact of localized states on electrical transport properties

Firstly, it is clear that oxides are very important from a technological point of view as they are already used in various type of applications such as read-head of hard drives or magnetic sensors. Additionally, oxides are also expected to play a strategic role in future applications because they exhibit various interesting properties. For instance, we can mention the class of transition metal oxides with the perovskite crystal structure. These oxides are characterized by more than one order parameters (ferromagnetic, ferroelectric and son on) that might be coupled to each other, opening new opportunities to design next generation multifunctional electronic devices. Although it is accepted that oxides are crucial for many existing and future applications, the importance of defects on their nominal properties is not acknowledged as much as it is in the field of semiconductors. Indeed, defects, and in particular oxygen vacancies (unavoidable defects in oxides), play a crucial role in devices reliability and performance.

From this perspective, it is essential to clearly identify their impact on the electrical transport properties of MTJs. As it is discussed in [Section 2.4.2](#), oxygen vacancies result in a variety of different localized states in the gap of MgO depending on the charge state of the defects and their separation. The first objective of this work is not only to unambiguously identify the impact of a specific defect population but also to determine the underlying physical process responsible for changes in devices properties. With the

acquired knowledge on the impact of oxygen vacancies, the goal is to discuss several discrepancies reported in the literature and recast the role of oxygen vacancies.

The first point that is unclear in the literature concerns the disagreement between predicted and experimental TMR values. While early first principle theories expects TMR values as large as 30 000 %<sup>17</sup>, the maximum experimental value reaches 600 % (1100 %)<sup>18</sup> at room (low) temperature.

The second point is related to the temperature dependence of magnetotransport properties and in particular the strong TMR decrease with increasing temperature. Although the point is intensively discussed in the literature (see Section 2.3), the origin of the TMR decrease is still uncertain.

Finally, the last point we want to discuss is related to the reported barrier height in MgO based magnetic tunnel junctions. Indeed, independent optical<sup>186</sup> and STM<sup>85,187,188</sup> experiments determined the band gap of MgO to be 7.8 eV in the bulk and in thin films. Furthermore, it is established that the barrier height felt by tunneling electron is specific to each symmetry and can be determined from the complex band structure of MgO (see Section 1.3.4.2). For instance, the barrier heights inferred from the complex band structure are 3.9 eV and 6 eV for  $\Delta_1$  and  $\Delta_5$  states respectively. Since the parallel and antiparallel magnetic configuration are characterized by tunneling electrons of different symmetries, namely  $\Delta_1$  and  $\Delta_5$  for P and AP respectively (see Section 1.3.4.3), their barrier height should be defined by the one specific to these states. Consequently, we expect the barrier height for the parallel magnetic configuration  $\phi_P$  to be much lower than the barrier height of the antiparallel magnetic configuration  $\phi_{AP}$  and in turn the resistance R to be lower in P than in AP.

Nevertheless, the barrier heights reported in the literature for both magnetic states are inconsistent with the aforementioned theoretical picture. Indeed, reported values are almost an order of magnitude lower than the 3.9 eV expected and are nearly identical for P and AP<sup>189,190</sup>. But what is even more surprising is the fact that  $\phi_P$  can be larger than  $\phi_{AP}$  while  $R_P < R_{AP}$ .

The discrepancy between theoretical and measured barrier heights can partially be explained by the fact that (i) the effective mass of tunneling electron in MgO can be lower the free electron mass<sup>191</sup> and (ii) the most common technique used to extract the effective barrier height consist in fitting experimental  $I - V$  curves with model based on the WKB approximation (see Section 1.2.1.3). The first point results in a lower effective barrier height, typically 1.5 eV, as discussed in ref 191 and ref 192. The second point is more critical. Indeed as it is reviewed in Section 1.2.1.3 and discussed by Miller *et al.*<sup>193</sup>, models based on the WKB approximation are oversimplified and fail to account for the dielectric barrier's complex band structure or the presence of localized states in the band gap that perturb the potential landscape. Using such models in crystalline structures, especially in the high bias regime, is not appropriate and yield unphysical parameters.

In Chapter 4, we discuss in detail the result of our temperature dependent photoluminescence experiment on sputtered MgO thin film and our bias and temperature dependent magnetotransport measurements on CoFeB/MgO/CoFeB magnetic tunnel junctions. In particular, we'll use an experimental technique in order to determine the effective barrier height. This technique is free of the deficiencies of models based on the WKB approxi-

mation. We'll see that the signature of localized states on the electrical properties of the device can be identified by comparing the optical activity of MgO thin films and the electrical properties of MgO based MTJs. Finally, the aforementioned discrepancies will be discussed from the point of view of spin dependent tunneling mediated by localized states.

### **2.6.2 An attempt to exploit the effect of localized states as additional functionality in working devices**

The second direction of the research project is the natural continuation of the first one and aims to actually take advantage of properties induced by oxygen vacancies in magnetic tunnel junctions. It is motivated by several elements in the literature suggesting that oxygen vacancies could in fact result in additional device functionality.

Indeed, it is reported that oxygen vacancies might play a central role in two interesting areas of oxides, namely the field of memristors and magnetic dilute oxides (DMOs). The former field concerns devices which electrical resistance is not constant but depends on the history of applied bias. The effect was demonstrated in  $\text{TiO}_2$  tunnel junctions, and the underlying microscopic process was ascribed to the diffusion of oxygen vacancies within the dielectric. The latter field encompasses oxide materials doped with 3d magnetic cations that exhibit ferromagnetism although the doping level remains well below the percolation limit<sup>194</sup>. Ferromagnetism in DMOs cannot be explained with standard theories and experimental results suggest magnetism induced by defects, and notably oxygen vacancies. Both examples suggest that the presence of oxygen vacancies can be desirable. Additionally, as it was mentioned before, oxygen vacancies could also explain some discrepancies in the literature concerning MTJs and their presence may actually be necessary in order to consistently explain the properties of MgO based MTJs. Finally, the main idea that motivated the second research field was to take advantage of the optical activity of MgO induced by oxygen vacancies, and more particularly to exploit the interplay between the optical properties of the oxide and the electrical properties of the device.

In [Chapter 5](#) we investigated the possible interaction between optical properties of MgO and electrical properties of MTJs. The idea is to combine the optical, electrical and temperature degrees of freedom in the same experiment. Exciting the MgO barrier with photons with a specific energy is expected change the defects population and thus modify the potential landscape. The concurrent temperature dependent electrical measurements allow to directly probe any optically induced change to the device properties. As it'll be discussed in details in [Chapter 5](#), our approach that consist in using continuous light excitation is challenging due to sample heating issues.

### **2.6.3 Combining X-ray absorption spectroscopy and electrical measurements**

In the last chapter of this thesis, I'll be briefly discuss some work that was carried on the DEIMOS beamline at the synchrotron SOLEIL.

The goal of the project was to use the newly installed versatile variable temperature insert (V<sup>2</sup>TI) that offers the possibility to perform *in operando* studies, i.e. measure the properties of our device using x-rays while applying external stimulus . More precisely, we combined the chemical selectivity of XAS to magnetotransport experiments on CoFeB/MgO based MTJs. Combining both techniques offer the possibility to probe the devices' properties when the device is close to real operating conditions.

The chapter focuses mainly on the details of the experimental setup. The last part of the chapter is dedicated to a brief discussion of results obtained during the synchrotron run.

## Experimental techniques

Most of this thesis work was done within the scope of a collaboration between my home institute, the Institut de Chimie et de Physique des Matériaux de Strasbourg (IPCMS) and the Institut Jean Lamour of Nancy (IJL). Our collaborators, specialists in the growth of thin film heterostructures by Molecular Beam Epitaxy and magnetron sputtering, provided us with samples while we fabricated micrometric size magnetic tunnel junctions and characterized their temperature-dependent magnetic, electrical and optical properties. To explore the large parameter space involved in our measurements we highly automated our magnetotransport experiment.

In this chapter, I'll first give a quick overview of sample growth and MTJ patterning by standard UV lithography. I'll then describe in more details the characteristics and automation of the magnetotransport bench. In the last section I'll briefly discuss the X-ray experiments carried at the synchrotron SOLEIL in Paris.

The experimental section supplies information for the purpose of knowledge transfer. Readers may skip parts of this section without disturbing the understanding of the thesis.

### 3.1 Sample Growth and device fabrication

#### 3.1.1 Introduction to sputtering

Sputtering is a physical vapor deposition (PVD) technique. The physical process consists in bombarding a target composed of the desired material with ions generated in a glow discharge plasma. Usually the deposition takes place in a vacuum chamber with partial pressure of rare earth gas such as Ar. The plasma is created by an electrical discharge that will ionize the gas. Ions are accelerated toward the target by an electric field applied between the target and the sample placed a few centimeters away. For sufficiently energetic particles, the bombardment of the target will generate several processes, one of which will be the ejections of neutral surface atoms (*sputtered* atoms) that will condense on the sample surface and may create a smooth layer. The bombardment of the target will also create secondary electrons that play a crucial role in maintaining the plasma and are also used in magnetron sputtering.

Magnetron sputtering uses permanent magnets to create strong magnetic fields near the surface of the target. The magnetic fields confine secondary electrons close to the surface. The electrons will follow a helical trajectory around the line of the magnetic field and encounter several ionizing collisions with the surrounding gas. These additional ions

will take part in the bombardment of the target and in turn create new electrons that will ionize more gas and so on. The use of the magnetron makes the deposition more efficient, faster and allows to maintain plasma in the chamber for lower partial pressure and lower operating voltage, resulting in a reduced sample contamination. The sputtered atoms are neutral and therefore insensitive to magnetic fields.

Sputtering also allows to make deposition of oxide by sputtering a metallic target under partial pressure of reactive gas that can oxidize the deposited species, for example Mg in a partial background pressure of oxygen to deposit MgO. In reactive sputtering, some regions of the target can get covered with atoms of the reactive gas. The process is known as target *poisoning*. The affected areas become insulating and charge build-up usually results in arc-discharge events, along with the ejection of droplets on the surface of the sample. The ejection of material can cause defects in the growing film.

A workaround for this issue is to use radio frequency sputtering (*RF*-sputtering) where an insulating oxide target is directly deposited. The polarization of the target is changed at radio frequency (13.56 MHz) to prevent charge build up. RF-sputtering produces high quality films but usually has a slow deposition rate.

For applications where the deposition rate is critical, reactive pulsed magnetron sputtering (PMS) can be used. The technique consists in pulsing the magnetron discharge in the mid-frequency range (10-200 kHz). The short pulse ON time limits the charge build-up on the poisoned regions of the metallic target, while the pulse OFF time allows to dissipate the charges through the plasma. PMS reduces the formation of arc and allows high deposition rates.

For an overview on sputtering, readers can refer to section II.4 of Vossen and Kern<sup>195</sup> and the review article on magnetron sputtering of Kelly and Arnell<sup>196</sup> and references therein.

### 3.1.2 Sample deposition

A commercial Alliance Concept DP850 magnetron sputtering system was used to deposit the samples studied in this thesis. The main chamber's base pressure was lower than  $10^{-9}$  mbar (UHV). A load lock allows to introduce samples without breaking vacuum, reduce sample contamination and gain subsequent pumping time. Six targets with diameter of 2 and 3 inches are available for deposition. The depositions are made with background pressure of  $5 \cdot 10^{-3}$  mbar of Argon. The insulating MgO layer was deposited using rf-magnetron sputtering. The deposition rates were calibrated by measuring the layers thickness with a *Dektak* profilometer and X-ray diffraction. The stack of the samples studied in this thesis is Ta(5)/Co(10)/IrMn(7.5)/FeCoB(4)/MgO(2.5)/FeCoB(4.5)/Ta(5)/Pt(5) (numbers in nm).

For more details on the deposition parameters of each layer, readers can refer to section III.3.2 and Annexe A of Bernos' thesis<sup>197</sup>.

### 3.1.3 MTJ patterning

In the previous sections, I emphasized important aspects concerning the growth of MgO based heterostructures by sputtering. In this section I'll give details on the patterning of

magnetic tunnel junctions (MTJs) by photolithography and how junctions were contacted for electrical measurements.

**Photolithography:** In UV photolithography, a lithographic mask and UV light are used to pattern a photosensitive material (called photoresist, or simply resist) into the desired architecture on the surface of a sample. In order to ease the tiresome alignment of the lithographic mask and define patterns as small as possible, clean and smooth layers are required. For this reason, the whole process takes place in a clean environment (*clean room*) to avoid atmospheric pollutions and samples are thoroughly cleaned with acetone and ethanol ultrasonic baths.

Each lithography step consists in first depositing resist on top of the sample with the help of a spin coater to get a flat and smooth deposition. The more homogeneous the layer the easier the alignment step will be. The accumulation of resist on the borders of the sample makes the alignment step particularly difficult for small samples. In order to circumvent this problem a detouring step can be performed to remove resist in the peripheral regions. The shadow mask, a transparent glass plate patterned with a very sharp chromium layer, is then carefully aligned on the sample with help of a microscope and alignment crosses defined in the previous steps (chromium side in contact with the sample). The position of the first step is usually chosen in the most homogeneous part of the sample. The sample is eventually exposed to 365 nm UV light, with the resist and the mask on top. Exposed regions of the resist will polymerize and, depending on whether the resist is positive or negative, exposed areas will dissolve faster or more slowly respectively, than those areas that have not been exposed. A solution in which the resist is soluble is used to develop the pattern. Finally, prepared samples are either etched (to define pillars or electrodes) or undergo a deposition step (passivation layer or metallization).

**Etching:** To remove material from the unprotected (resist free) areas and define the pattern on the sample, a dry etching technique is used. The ion beam etching (IBE) operating principle is similar to the sputtering technique introduced in [Section 3.1.1](#).

The process takes place in a vacuum chamber with a low background pressure of neutral gas, Argon in our case. A plasma of  $\text{Ar}^+$  and electrons is created in the discharge chamber, where electrons provided by a hot filament (cathode) are accelerated with a negatively biased anode. A magnetic field is used to confine electrons and make the ionizing event more likely. The ion beam is created by a negatively biased accelerator grid that attracts the  $\text{Ar}^+$  ions towards the sample. Within the ion beam, electrons move much faster than heavier ions and tend to leave the beam faster. This charge imbalance has to be neutralized for three reasons: (i) repulsive interactions between positive  $\text{Ar}^+$  causes defocusing of the ion beam, (ii) charge build up on the wall of the chamber ends up creating short duration arcs with nearby hardware or the etched samples and (iii) accumulation of positive charges on the surface of insulating layers can repel incoming ions and slow the etching down or degrade the tunnel barrier's dielectric properties. To circumvent these issues, the ion beam is neutralized by a hot filament placed on the way of the ion beam. The filament provides electrons that counterbalance the positive charges within the ion beam.

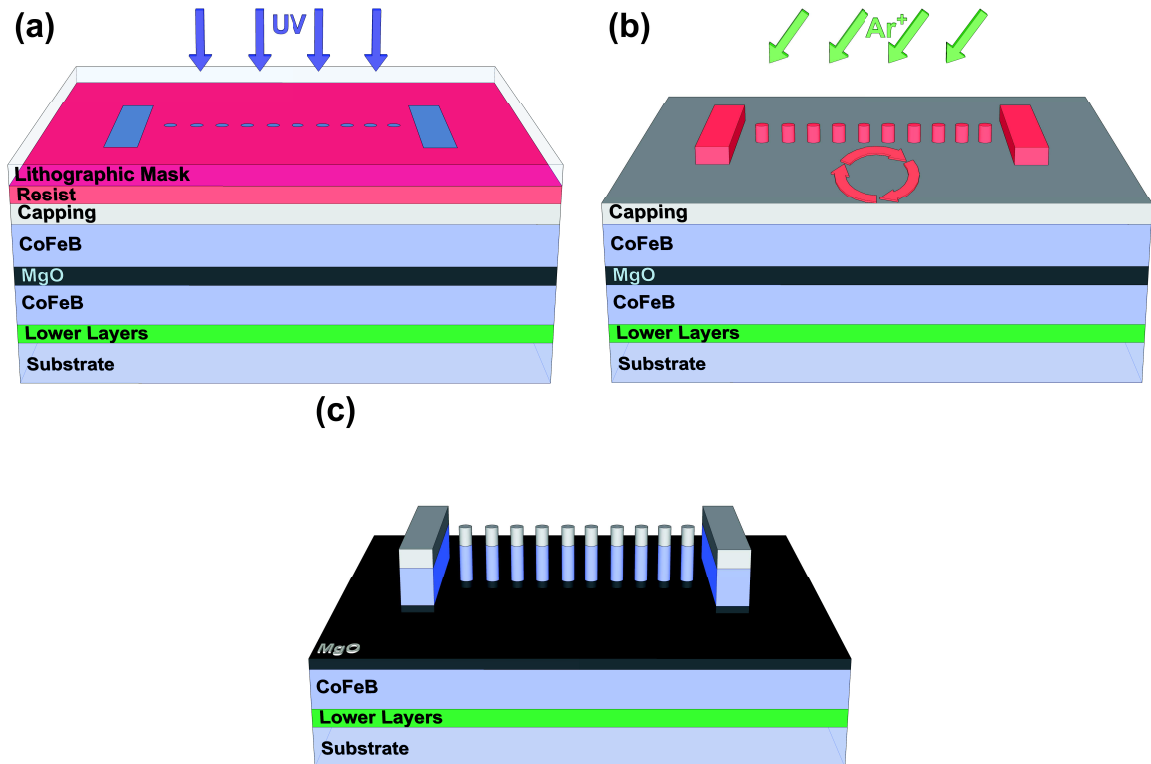


Figure 3.1: **Step I, Pillar definition:** Schematic view of (a) lithographic mask with desired pattern in contact with resist previously deposited on top of the sample and UV insulation step (b) sample etching after resist development and (c) sample after lift-off and cleaning in ultrasonic bath. Note that not all layers are shown and that picture is not to actual scale.

Samples were rotated and tilted with an angle of  $45^\circ$  compared to the incoming particles during etching to improve etching uniformity and to avoid redeposition issues that might shortcircuit the device. The etching was done in small steps and Auger electron spectroscopy (AES), a surface- and element-sensitive technique, was used to precisely determine the etching depth.

We used a four-step UV lithography process developed and optimized in our institute by my colleague Filip Schleicher. In what follows, I'll describe in more details each of these steps.

### 3.1.3.1 Step I: Pillars definition

The first step consists in defining junctions pillar and contact pads of the lower electrode. A mask that consists of circular (for pillars) and rectangular (for contact pads) opaque patterns on a transparent background is used as shown in Figure 3.1. In panel (a), the lithographic mask is placed in contact with the sample formerly covered with resist. The sample is then insulated with UV light. Panel (b) shows the sample after development of the UV exposed resist, we can see that only the desired pattern is left on the sample.

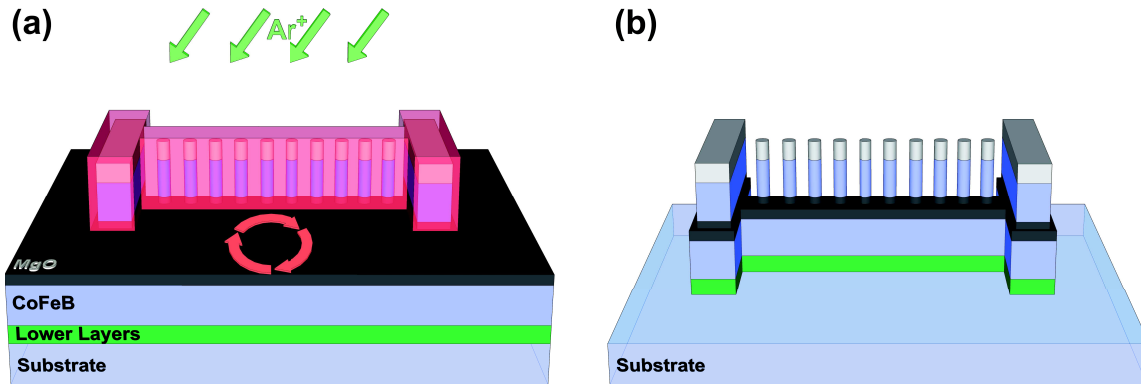


Figure 3.2: **Step II, Bottom electrode definition:** Schematic view of (a) sample with resist defining the bottom electrode (UV insulation step not shown) as introduced in the etching chamber and (b) sample after etching, lift-off and cleaning in ultrasonic bath.

The sample is then introduced in the etching chamber, where  $\text{Ar}^+$  ions will etch the sample down to the middle of the insulating MgO layer. The etching is done in small steps interspersed with Auger electron spectroscopy measurement to control the etching depth. Samples are tilted with an angle of  $45^\circ$  and rotated to ensure homogeneous etching and avoid redeposition issues on the sides of the pillars.

An important point in this step is to stop the etching within the insulating barrier as etching beyond would decrease the thickness of the lower electrode, affecting both its magnetic and electrical properties. Moreover etching the bottom electrode can result in redeposition of conductive material on the side of the insulating barrier within the pillars and cause a device short-circuit. Panel (c) shows the sample after removal of the resist and proper cleaning with ethanol and acetone ultrasound bath.

### 3.1.3.2 Step II: Lower electrode definition

The next step is similar to step I except that the resist pattern now defines the shape of the lower electrode as shown in panel (a) of Figure 3.2. It also protects pillars and pads defined previously. Again, the sample is introduced in the etching chamber and etched down to the substrate. Just as for step I, over-etching is not desired as it can make the substrate conductive. Contacts made with the wedge bonder usually go through the stack down to the substrate and consequently conductive substrate can cause shortcircuit during electrical measurements.

### 3.1.3.3 Step III: Passivation layer deposition

To avoid shortcircuiting the pillar when contacting the bottom and top electrodes, the sample is covered with a 150 nm thick layer of  $\text{SiO}_2$ . The passivation layer is deposited on the whole sample except where electrical contacts are desired. In order to do that, resist is deposited to define  $\text{SiO}_2$  openings on pads and pillars where metallic contacts will be

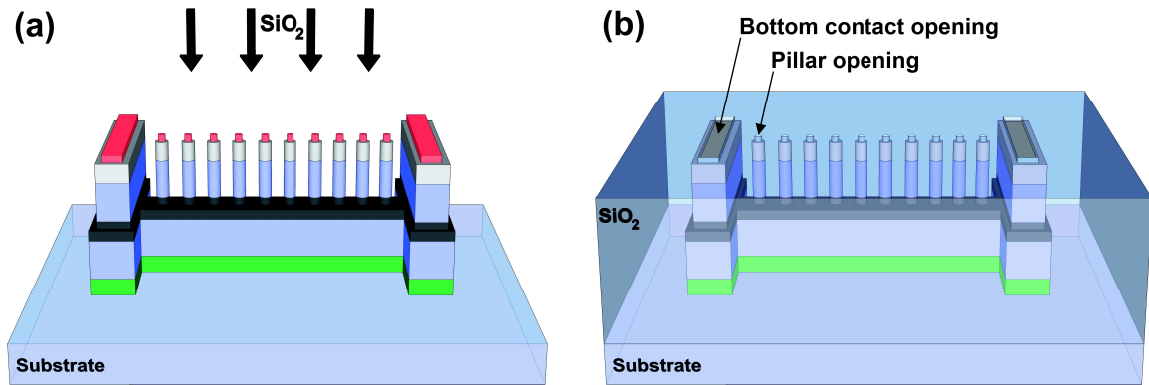


Figure 3.3: **Step III, Passivation layer deposition:** Schematic view of (a) sample with resist defining SiO<sub>2</sub> openings on pads and pillars for electrical contact and (b) sample after SiO<sub>2</sub> deposition and lift-off.

deposited in step IV, as shown in panel (a) of Figure 3.3. The sample is introduced into a commercial rf-sputtering system to deposit the insulating layer from a two inch SiO<sub>2</sub> target.

The resist lift-off after the deposition can be problematic. Actually, the resist is damaged to some extent during the deposition and the small pattern size on pillars makes the lift off difficult. In addition to that, the SiO<sub>2</sub> layer has a limited adhesion on the sample that precludes the use of ultrasonic bath. The samples were simply immersed in acetone bath at room temperature for few hours to dissolve the resist. Panel (b) shows the sample after lift-off and cleaning.

#### 3.1.3.4 Step IV: Electrode deposition

In order to electrically contact the sample, it is necessary to pattern electrical circuitry atop the structure. As some experiments in this thesis involve excitation of MgO in a working device with coherent light, it is desirable to have as little material as possible on top of the structure. In order to clear the optical path, our collaborators reduced the capping layers and top electrode thickness as much as possible, while maintaining identical physical properties of the device. We also slightly modified the fourth step of the lithography process in order to create an optical opening on the top electrode. Some reference junctions, without optical opening, are defined on the same lithographic mask in order to estimate the impact of this modification.

As shown in panel (a) of Figure 3.4, the sample is covered with resist except on pads and on rectangles above the pillars that define the top electrode contact. It is important to note the presence of resist on pillars that allow optical access. In order to ensure electrical contact between top electrodes and pillars, the radius of the circular resist pattern is smaller than the radius of the SiO<sub>2</sub> opening defined in step III (see inset of panel(b)). The sample is introduced in a commercial Plassys MEB 550S metallic evaporation system and a Al(110 nm)/Au(35 nm) bilayer is deposited. Al is used for lower metalization layer due to its better adhesion to the passivation layer. Gold is chosen to protect the Al layer from oxidation

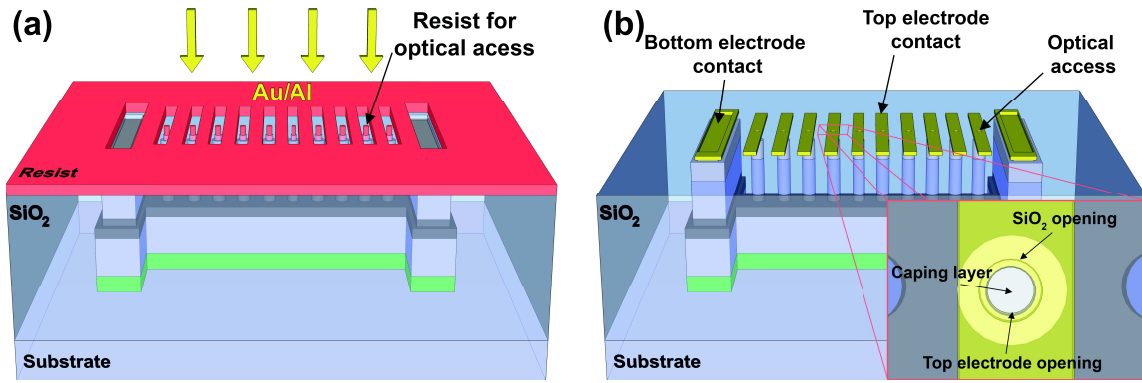


Figure 3.4: **Step IV, Metalization:** Schematic view of (a) sample with resist defining top electrode openings on pillars for optical access and (b) sample after metal deposition and lift-off. The inset of panel (b) represents a top view of the optical access on the pillar.

and enables good wire-bonding.

What is presented from step I to IV is in fact a small portion of the lithographic mask used in the laboratory. The real mask consists of ten such structures. It allows to pattern more than a hundred junctions in one process. Thanks to the development and optimization of the process over several years, the success rate of the process is very high. Figure 3.5 shows a sample after processing. The inset shows a top view over a pillar.

More details on lithography parameters can be found in section II.4.2 of Schleicher's thesis<sup>198</sup>.

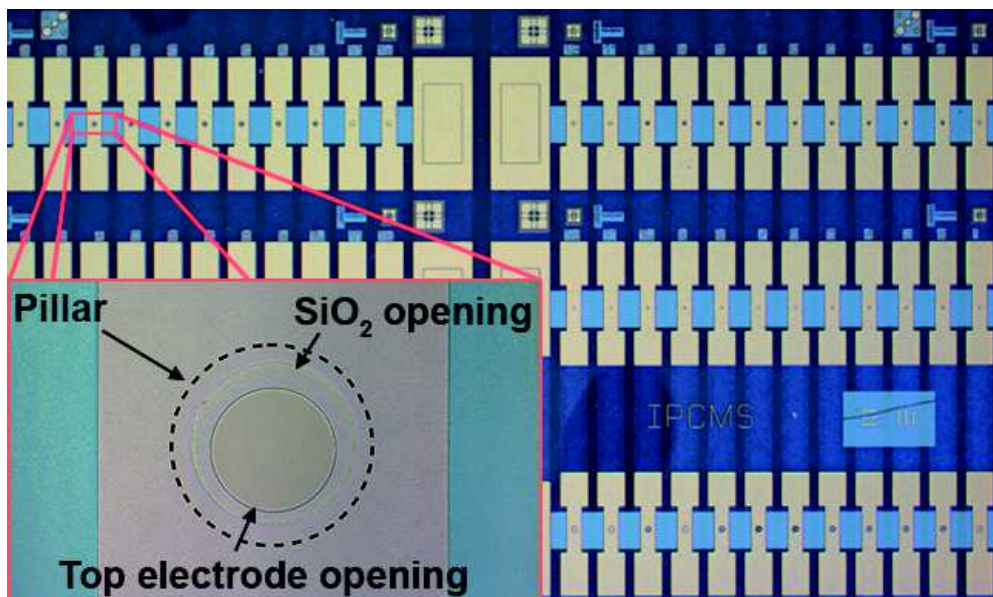


Figure 3.5: **Processed sample:** Picture (top view) of a sample after the four lithography steps.

## 3.2 Magnetotransport experiment

### 3.2.1 Setup general description

The setup is composed of standard elements necessary to measure the interplay between magnetic and electric properties of magnetic tunnel junctions, namely a cryostat, two magnets, a proportional–integral–derivative (PID) temperature controller, a source meter, a pumping and a cooling system (not shown) as shown in Figure 3.6.

In addition to the standard apparatus, the setup also have distinctive features: the cryostat is equipped with optical windows and mounted on a rotation plate, an optical table is coupled to the shelf of the cryostat, four precision motors allow XYZ displacement of the cryostat and magnets and finally an electrical multiplex transmitter will be briefly discussed later. In what follows I'll discuss in more details the different apparatus operation, integration and calibration.

#### 3.2.1.1 Gifford-McMahon cycle

Our cryostat is a pneumatically driven two stage Gifford-McMahon refrigerator (see Figure 3.6). The expander is the key component, as it is where the cooling takes place. A cold finger is directly attached to the second stage of the expander and cooled to 4.2K. A

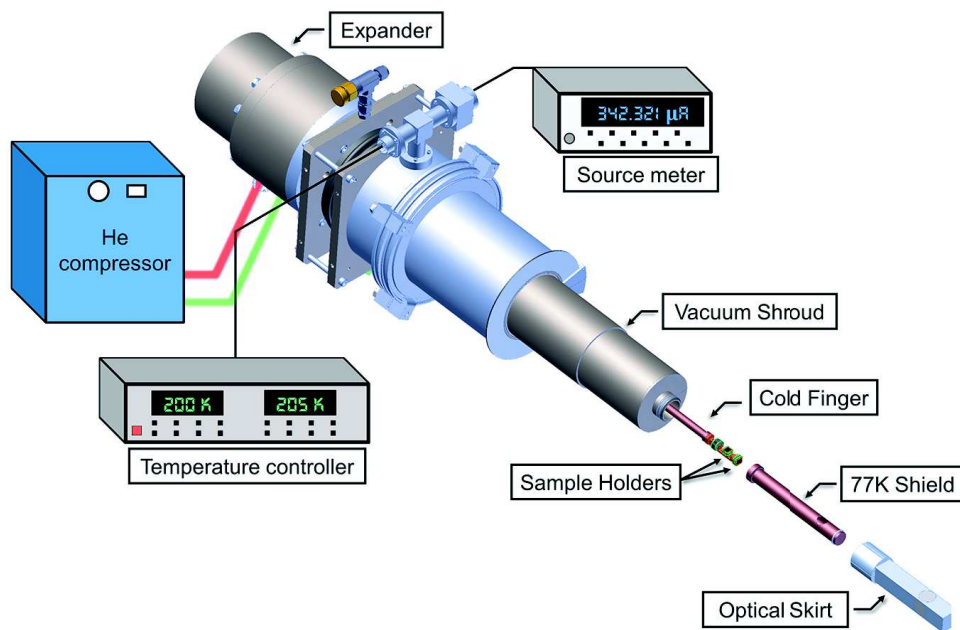


Figure 3.6: **4K Gifford-McMahon cryostat:** Standard magnetotransport bench composed of a cryostat, a temperature controller, a source meter, two magnets (not shown) and a computer with a LabView control program (not shown). Other elements such as an electrical multiplex transmitter, motors, optical tables and optical elements are not shown.

radiation shield is fastened to the expander's first stage and cooled to 77K (*77K shield*). It protects the cold finger from room temperature thermal radiations. Finally, a vacuum shroud protects the sample environment and limits thermal load due to conduction and convection. The radiant shield and the vacuum shroud allow for optical access on the vertical sample. Thirty four copper wires are electrically connecting both samples holders, two temperature sensors and the heater.

The operating principle of the cryostat is based on the Gifford-McMahon (GM) cycle. For the sake of simplicity, the thermodynamic equations will not be addressed, only the basic functioning of a single stage GM cooler will be explained. The principal components of the expander (or coldhead) are represented in [Figure 3.7](#). It consists in a chamber where the gas can be compressed or expanded, a *regenerator* (usually a porous body through which the gas passes back and forth), a *displacer* (piston), high and low pressure valves, a rotating valve and finally a motor allowing to drive the displacer. A compressor supplies the cold head with high pressure He. In the case of our cryostat, the regenerator and the displacer are combined (the displacer, usually a cylinder, contains the porous material). The rotating valve allows pressure variation by opening and closing the high pressure inlet and the low pressure exhaust and is carefully synchronized with the motion of the displacer. The GM cooling cycle can be divided in four steps schematized in [Figure 3.7](#):

1. Panel (a): The cycle starts with the displacer-regenerator down. The high pressure inlet is opened, letting high pressure He fill the upper part of the chamber. The whole system is at room temperature.
2. Panel (b): With the high pressure line opens, the displacer-regenerator starts to move upwards forcing the gas through the regenerator. (Note that if it's not the first cycle, the regenerator is already cold and will cool the gas at constant pressure, see step 4).
3. Panel (c): While the displacer is up, the High pressure valve is closed and the low pressure valve is opened. The high pressure gas in the lower part of the chamber will be able to expand and cool (Joule–Thomson process). Some gas is also forced to the exhaust through the regenerator hence generating work (impairs efficiency). This is the main cooling step, by direct thermal contact the gas will drive heat out of the cold finger.
4. Panel (d): Finally the displacer moves down forcing the gas to go through the regenerator. This process cools the regenerator (in turn, the regenerator cools the gas in step 2).

It's the constant repetition of this cycle that allows the system to cool. In the case of multiple stage GM coolers, each stage is fed with low pressure gas from the previous one, and all the displacer-regenerators move in phase. Our cryostat is composed of two stages. The first stage reaches 80 K (cools the radiation shield) while the second stage reaches temperatures as low as 2.9 K (cools the cold finger).

GM coolers have several advantages over other architectures. They work in a closed loop and can be used for extended periods of time without need of maintenance or He re-filling. They require simple equipment for functioning and are cheaper than other systems

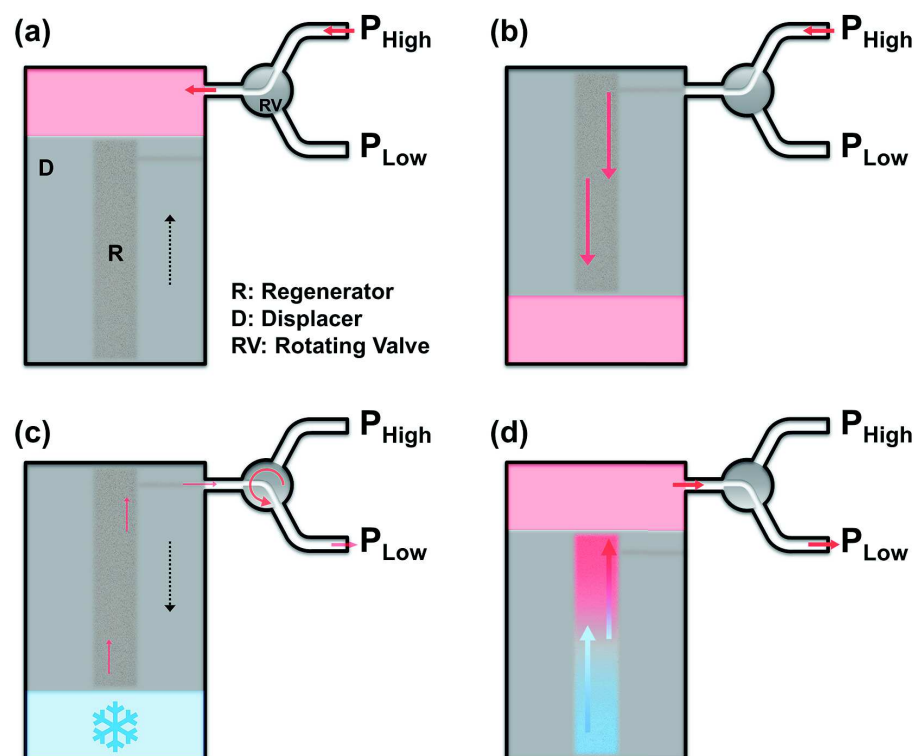


Figure 3.7: **Gifford-McMahon cycle:** (a) the high pressure He line is opened (b) the displacer (D) moves to the top position, forcing high pressure He to the lower part of the chamber through the regenerator (R). Panel (c), the rotating valve (RV) opens the low pressure He line. The gas is allowed to extend and cools by Joule–Thomson process. Panel(d), the displacer returns to initial position, the cold gas is forced through the regenerator. It cools the regenerator and leaves the expander at near room temperature.

with comparable cooling power. Drawbacks are also multiple: GM coolers are mechanical refrigerators. The motor of the rotating valve and the movements of the displacers induce vibrations. These vibrations are transmitted to the shelf of the cryostat and possibly to all other instruments in direct or indirect contact with the shelf. But vibrations are also transmitted directly to the second stage of the cryostat and cause the vibration of the samples themselves. The amplitude of the vibrations are on the order of  $20\ \mu\text{m}$  ( $5\ \mu\text{m}$ ) parallel (perpendicular) to the axis of the cold finger. GM coolers are suited for experiment where vibrations of  $10\text{--}20\ \mu\text{m}$  are acceptable. For experiments where sensitive apparatus are used (precision optics, spectrometers etc...) one has to decouple the expander from the body of the cryostat. In our case, it would be rather complex because additional position motors should be added and their movements synchronized with existing motors in order to move the upper and lower part of the cryostat at the same time.

Our cryostat uses internal pressure differential to move the displacer, it reduces general vibrations of the whole structure. We also installed pneumatic anti-vibration columns to further reduce vibrations transmitted through the mounting flange to the optical table.

## 3.2.2 Calibration and automation

### 3.2.2.1 Temperature calibration

Temperature dependent measurements, such as most of this thesis data sets, are an important tool to characterize the impact of defects on nominal material properties. In order to extract precise quantitative values, it is essential to measure the temperature as precisely as possible.

A resistive heater placed around the the second stage of the expander allows temperature control. Three output ranges are available, 0.5, 5 and 50 Watts. The heater is coupled to a Lake Shore cryotronics 332 PID controller. Two sensors allow temperature reading in two different places of the cryostat: the first one is placed on the heat station of the second cooling stage (at the top of the cold finger), while the other one is placed at the end of the cold finger, next to the sample holders. The latter gives the closest value to the real sample temperature. However, three thermal interfaces between the sample and the cold finger can worsen thermal conduction and lead to wrong temperature readings: (i) the sample holders are tightened to the cold finger with *molybdenum screws* (ii) samples are glued on chips identical to sample holders, the chips are plugged on the sample holders with twelve *copper contacts* (iii) finally, samples are contacted to the copper contacts of the chip with 200  $\mu\text{m}$  thick *aluminum wires*. Even if the temperature sensor is close to the sample holders, the real sample temperature can still be very different.

To measure the real sample temperature (hereinafter simply referred as *sample tempera-*

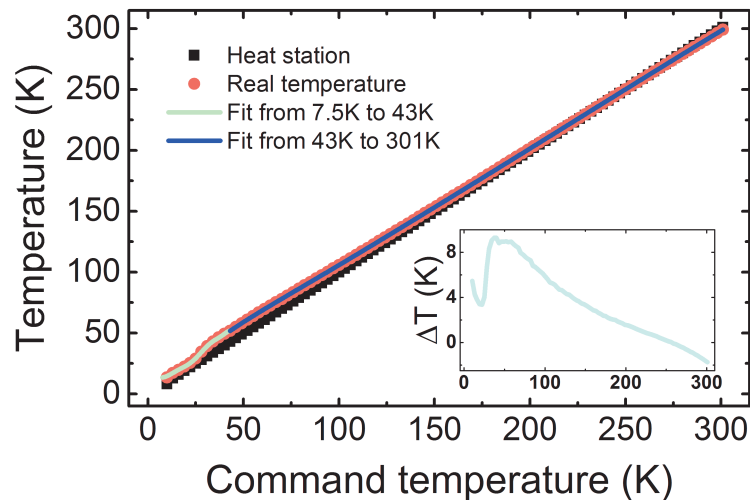


Figure 3.8: **Temperature calibration:** Temperature of the heat station (black line) and extrapolated *real* temperature of the top sample (red line) as a function of command temperature (set by user). Error bars lie within the thickness of the line. The real temperature was interpolated in two different regions. The inset shows the difference between both temperatures. The temperature offset is not constant and shows complex behavior within the whole temperature range confirming the need of an accurate temperature calibration.

ture), we glued a calibrated temperature diode on a chip using the same glue and the same electrical contacts as for standard samples. We then swept the temperature from 10 K to 300 K with steps of 3 K, measured the diode's voltage and extrapolated the real temperature for both sample holders. For each step, the temperature was stabilized for ten minutes in order to ensure thermal stability. We measured the voltage for three minutes, allowing to get statistics and verify that there was no temperature drift.

Results for the top sample are presented in [Figure 3.8](#). The temperature of the heat station and of the sample are plotted as a function of command temperature. The inset shows the difference between both temperatures ( $\Delta T$ ). At low temperatures the sample temperature is underestimated ( $\Delta T \approx 4K$ ): there is a rapid increase in  $\Delta T$  at 22K. This sharp increase is concurrent to a change in the output power range of the heater from low (0.5 W) to high (50 W) power.  $\Delta T$  then decreases monotonously from 58K to 256K, where it reaches 0 K. At 256 K the sample temperature starts to be overestimated and  $\Delta T \approx -2K$  at 300K. The sample temperature was interpolated and polynomial parameters were integrated to the acquisition program such that the real temperature was directly accessible to measurement protocols.

According to the specification of the cryostat, a base temperature of 2.9 K is accessible. However, optical access requires optical windows on the skirt of the cryostat and holes in the 77 K radiant shield, both modifications increase the apparatus base temperature. With the optical skirt, as it was, the base temperatures were 15 K and 33 K for the bottom and top sample respectively. Due to the optical windows and holes in the 77 K shield, the top sample is more exposed to room temperature thermal radiations and its base temperature is higher compared to the more protected bottom sample.

In order to increase the performance of the cryostat, we performed two modifications. We closed one hole in the 77 K radiation shield. We also drilled the back of the chip on which samples are glued and increased the height of the Molybdenum screws head to put the sample as close as possible to the screw (they are now separated by a few hundred microns of PCB). With the latter modifications, we were able to reach base temperature of 10 K and 16 K on the bottom and top samples respectively.

### 3.2.2.2 Dilation of the cold finger and optical device tracking

Results presented in [Chapter 5](#) involve temperature dependent optical measurements on micron-size junctions. In order to realize such experiments, the position of the light source and the sample have to stay fixed. However, when the temperature is changed, dilatation/contraction of the cold finger makes this task tedious and difficult. In order to ease the measurement protocol we calibrated the dilatation of the cold finger as a function of temperature.

In order to do so, we used a magnifying lens coupled to a digital camera to take pictures of a sample placed on the cold finger while sweeping the temperature from 10 K to 320 K with steps of  $\Delta T = 10$  K. Again, the temperature was stabilized for ten minutes in order to make sure that the system was stabilized. We then digitally processed each picture with ImageJ, an open source image processing software. Four reference points were monitored and averaged to extract the dilatation. Results are presented in [Figure 3.9](#). The dilatation

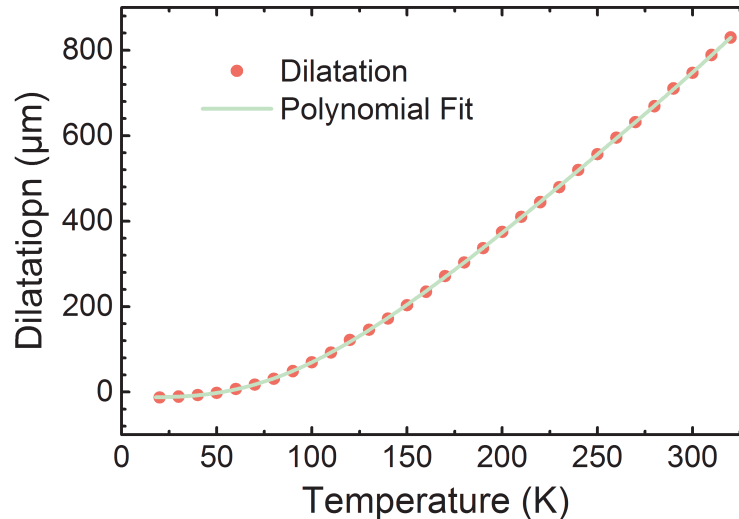


Figure 3.9: **Dilatation calibration:** The dilatation of the cold finger as a function of temperature was extracted by processing digital images of the sample taken while sweeping the temperature.

curve was interpolated and polynomial parameter integrated to the main control program.

The setup is equipped with four precision motors allowing XYZ displacement of the cryostat and displacement of the magnets in the X direction. An independent automaton controls the position of each motor. In order to have full control over the position of the sample in our experiment, we interfaced the program controlling the motors to the main control program.

The control program allows to align several devices on the fixed laser spot and save their position in space. The control over the motors allows to switch between devices during optical studies, i.e. *optical multiplexing*. Thanks to the dilatation calibration, the main program is also capable of dynamically correcting the position of the cold finger when the temperature is changed, and maintain the device under the laser spot.

### 3.2.2.3 Electrical multiplex transmitter

The optical multiplexing introduced before is useful only if we can, in parallel to that, automatically switch the electrical contact to the device under the laser spot, i.e. *electrical multiplexing*.

Twenty four wires connect the sample holder for electrical contact on the sample. This allows to connect ten (five) devices in two (four) points mode. The connector of the wires is plugged to an electrical multiplex transmitter, or a *multiplexor*, developed in our institute by V. Davesne and P. Panissod. To keep it simple, the multiplexor acts as a relay between the sourcemeter and the sample and allows to switch automatically between devices contacted on the sample. More details on the circuitry and the working principle of the multiplexor can be found in section III.7 of V. Davesne<sup>199</sup> thesis.

By combining electrical, optical multiplexing, control of the position of the sample

Parameter	Equipment	Implementation
Magnetic field	Magnet x2	Calibrated, Hardware and Software
	Hall probe x2	Calibrated, Hardware and Software
Magnet positioning	Precision motor	Hardware and Software
Electrical	Keithley 2636 sourcemeter	Hardware and Software
	Multiplexor	Hardware and Software
Temperature	Temperature sensors	Calibrated, Hardware and Software
	Resistive heater	Calibrated, Hardware and Software
Optical	Lasers	Hardware and Software
	Motorized rotation	Hardware and Software
	Other optics	Hardware
Sample positioning	Three precision motors	Hardware and Software
	Cryostat Rotation plate	Hardware

Table 3.1: **Appartus integration:** This table summarizes parameters accessible to the setup, ensuing apparatus needed and their implementation. More details can be found in the text.

and the dilatation calibration, it is possible to perform automated temperature dependent magnetotransport experiment coupled to optical excitation on several devices.

### 3.2.2.4 Setup automation

As it was already mentioned previously, a lot of external parameters are involved in our experiment. The control over each parameter involve integration of one or several devices. [Table 3.1](#) summarizes the list of equipment integrated to the setup. In this framework, probing the interplay between parameters becomes complex and difficult from an experimental point of view. In order to make the task possible, we systematically automated the experiment when it was possible. To do that, we wrote an advanced control and acquisition program in LabView. The program will be described in the following.

All the apparatus are integrated in a modular way. What it means is that all measurement protocols have access to external parameters so that we can probe one parameter while changing all the others easily. Standard protocols such as  $I(V)$ s,  $R(H)$ s and  $R(T)$ s are integrated to the main program. All protocols can be saved in a database, are editable and can be quickly reused. They can be used independently or integrated within a macro that will execute user defined lists of protocols and change to external parameters. Since the cryostat doesn't need He refilling or maintenance, it is possible to define macros that will measure for weeks. Results presented in [Chapter 4](#) were carried out by taking advantage of the aforementioned programmable features as well as electrical multiplexing and temperature control.

For optical measurements, in addition to lasers and focusing optics, two motorized rotation stages and a shutter were integrated. The angle between the two rotation stages

is synchronized. When a combination of quarter and half wave-plates is used the setup allows full control over the light polarization state (angle of linearly polarized light and circularly left and right polarized light).

More complex protocols involving optical parameters were developed. Two protocols involve measurement of current as a function of light polarization state called SHI and SHI++. Two protocols were also developed to ease optical measurements: (i) a 2D mesh allowing XZ scan in order to quickly align the device with the laser spot (ii) and a Knife Edge protocol that allows to determine the shape of the laser spot.

Finally, the program also features real time monitoring of the sample allowing to change all the external parameters to quickly extract useful information on the device under study.

## 3.3 Synchrotron Experiments

During the timespan of my PhD, my institute was in charge of developing a new technique on the DEIMOS beamline at the *SOLEIL* synchrotron in Paris. The goal was to design a new insert<sup>200</sup> allowing electrical access on the materials under study and compatible with the beamline capabilities. In the following section I first briefly describe the setup of the DEIMOS beamline and the principle of XAS measurements, I'll then discuss some technical aspect of the versatile insert and finally explain how we interfaced our homemade magnetotransport experiment to the DEIMOS setup.

### 3.3.1 DEIMOS X-ray absorption spectroscopy setup

DEIMOS, acronym that stands for *Dichroism Experimental Installation for Magneto-Optical Spectroscopy*, is a beamline located at the *SOLEIL* synchrotron facility that provides a large brilliance polarized and coherent X-ray source.

DEIMOS is dedicated to soft X-ray dichroic measurements. The principle of dichroic measurements is to compare two X-ray absorption spectra for two different sample magnetic states or two different light polarization states. The technique allows to get quantitative information on the sample's electronic and magnetic properties. Since the principle is to compare measurements made at different times and potentially look for very small effects, the beamline was specially designed for stability and reproducibility<sup>201,202</sup>. The insertion devices (undulators) and other optics were specifically chosen to get light with very high polarization rate. A turbo-scan (*on the fly* measurement) was also developed in order to minimize the acquisition time and the impact of instabilities due to experimental environment<sup>203</sup>.

When an electromagnetic wave interacts with matter, several processes can occur. [Figure 3.10](#) shows the cross section of possible light-matter interactions as a function of impinging photons energy. We can see that within the soft X-ray energy range accessible on the DEIMOS beamline, i.e 250-2500 eV, the cross section of photoelectric absorption is order of magnitude larger than other cross sections and that we can, in first approximation, neglect other processes.

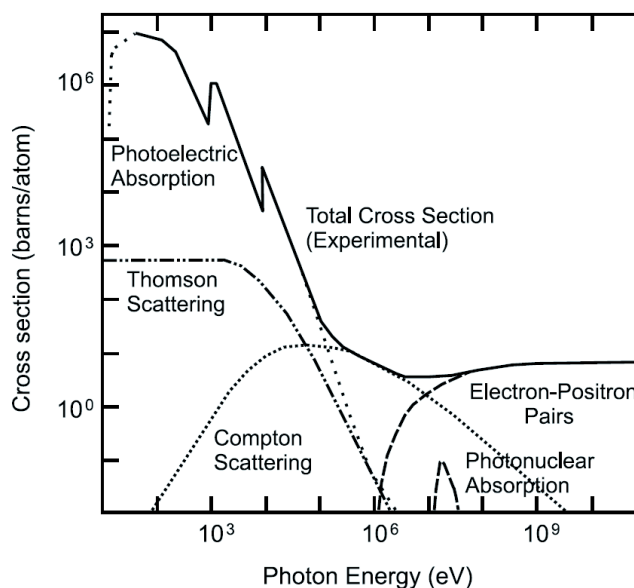


Figure 3.10: **Cross sections of light-matter interactions:** Cross section of the photoelectric absorption, Thomson and Compton scattering, electron-positron pairs creation and photomolecular absorption as a function of photon energy. Within the soft X-ray range, the photoelectric absorption is order of magnitude higher than other processes. Figure taken from C. Felix's thesis<sup>204</sup>.

The photoelectric effect is the property of a material to emit an electrons upon absorbing a photon. From quantum mechanics, we know that electrons, when bound to atoms, have discrete energy states allowed. From the law of conservation of energy, it is easy to conceive that in order for an electron to absorb light, the photon energy must equal the energy difference between the electron initial and final state. It is the reason why the photoelectric cross section shows resonance peaks at element specific energies.

When the photon energy exceed the electron binding energy, electrons can be excited to the continuum. It is possible to study the outgoing electrons and get surface sensitive and core-shell information on the sample. The technique is called X-ray photoemission spectroscopy (XPS). However, we focused on X-ray absorption spectroscopy that will be described in the following.

**X-ray absorption spectroscopy (XAS):** In this thesis we focused on the absorption coefficient of the material under study. In general, there are three ways to measure the absorption or quantities proportional to absorption. The first one consists in a direct measurement of the X-ray transmission through the sample. It is experimentally realized by placing a photon detector behind the sample but is limited to thin samples only. A second technique consist in measuring the photons resulting from electrons and X-ray induced core-holes recombination, called the total fluorescence yield (TFY). Finally, it is also possible to gain information on absorption by measuring the electron current generated by

X-ray absorption.

To measure this current, one can either measure electrons outgoing from the sample (photo-, Auger and secondary electrons) or measure the compensation current from the ground to the sample. The former technique requires an electron detector in close proximity to the sample with the limitation of a restricted solid angle. The latter technique is free from this limitation and easier to implement experimentally as it only requires to contact the sample to the ground. This technique is called the total electron yield (TEY).

DEIMOS beamline offers the possibility to use either of these techniques. In the following I'll briefly describe how electronic and magnetic properties can be extracted from dichroic XAS measurements.

**Light matter interaction and dichroism:** Dichroism is the property of a material whose absorption depends on the light polarization. Linear dichroism (LD) can be defined as the difference between the absorption of light polarized parallel and polarized perpendicular with respect to an orientation axis. It is used to characterize an eventual anisotropy of the charge distribution in the sample under study. LD arises from the interaction between the electric field  $\mathbf{E}$  of light and an anisotropic charge distribution through the so called *search light* effect. By changing the polarization, the electric field  $\mathbf{E}$  *searches* for the direction of maximum and minimum number of empty states.

In nonmagnetic materials, the charge distribution can be anisotropic due to the atomic environment (bonds), in which case we talk about natural linear dichroism (XNLD). In magnetic samples, an additional anisotropy due to the magnetization axis can also result in anisotropic charge distribution, in this case we talk about magnetic linear dichroism (XMLD). In all cases, linear dichroism (LD) arises from nonspherical charge distribution. When both effect coexist, it is possible to separate each contribution by temperature dependent measurements or, in the case of ferromagnets, by applying an external magnetic field.

Similarly to linear dichroism, circular dichroism (CD) is defined as the difference of absorption between circularly left (CL) and circularly right (CR) polarized light. When used to characterize magnetic materials, the technique is called X-ray magnetic circular dichroism (XMCD). XMCD arises from the fact that CR and CL polarized photons transfer opposite momentum to excited electrons, and thus excite electrons with opposite spins. When the density of final states is different for spin up and down electrons (e.g. the 3d shell of transition metals), the absorption of CR and CL light will be different and XMCD will provide detailed information on the magnetic properties of the sample.

As an example, we will consider the transition of an electron from  $2p_{3/2}$  and  $2p_{1/2}$  levels to a Stoner split 3d empty state (namely L3 and L2 edges respectively), as shown in [Figure 3.11](#). If we assume that the transition probability is proportional to the number of initial and final states, the L2 and L3 edge intensity have to be proportional to the number of valence 3d holes (available final state). Moreover, because the excitation process is spin dependent, it is possible to relate the difference of the acquired spectra (dichroic signal) to the 3d shell spin up and spin down holes imbalance. It is possible to preferentially excite either spin population by changing the helicity of circularly polarized light, or equivalently

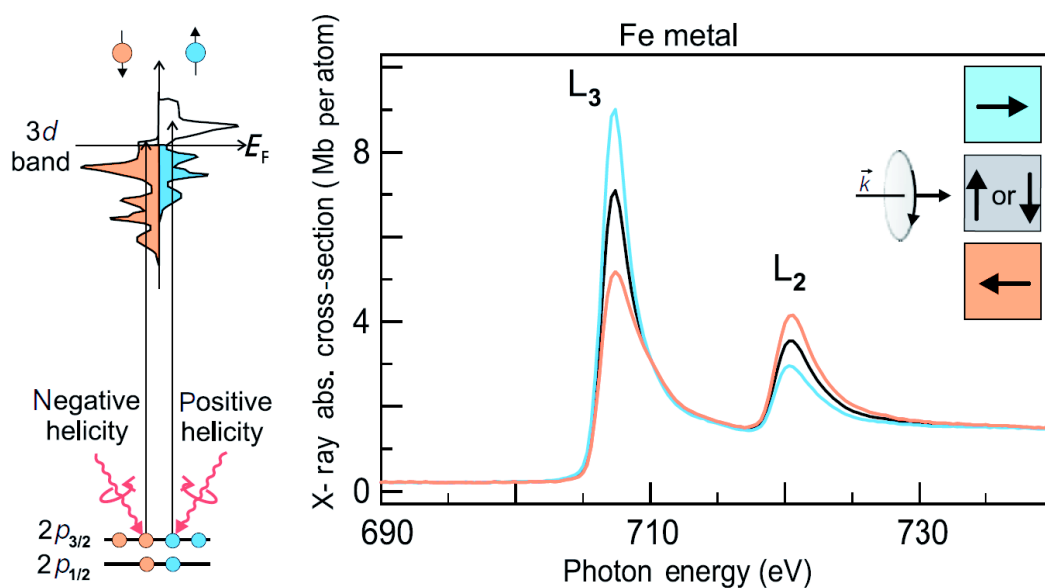


Figure 3.11: **Origin of XMCD:** On the left panel: Core shell  $2p_{3/2}$  and  $2p_{1/2}$  electrons are excited to a Stoner-split  $3d$  valence band (typically a  $3d$  transition metal) by circularly polarized photons. Depending on the photon helicity, spin up or down electrons will be excited. The polarized  $3d$  valence band will act as spin detector. One can equally change the photon helicity or change the sample magnetization direction. On the right: XAS spectra measured for parallel (blue), perpendicular (gray) and anti-parallel (orange) helicity-magnetization alignment. With the sum rules<sup>205</sup>, it is possible to extract magnetic and electronic quantities from the difference of these spectra. Figure taken from Stöhr and Siegmann<sup>205</sup>.

by keeping the helicity constant and changing the sample magnetization. In order for the photon to transfer angular momentum to the electron spin, both helicity and magnetization axis have to be aligned to some extent, the XMCD signal will be maximum for a parallel alignment.

To extract electronic and magnetic information from dichroic XAS measurements one has to carefully analyze the equations governing light-matter interaction. In order to do so, the time dependent perturbation of the electrons by the electromagnetic wave must be considered. This interaction induces transitions of the electron from a ground state to an excited state. The transition probability can be calculated using the fermi golden rule and the electron-photon interaction Hamiltonian within the dipole approximation (i.e. the light electric field is constant within the atomic range), that holds true for soft X-rays<sup>205</sup>. A model can be established for a particular system by appropriate choice of the initial and final states wavefunctions. For example the tight binding model can be used for a final state involving the  $3d$  valence band. Some approximations, also specific to the considered system, have to be made in order to calculate the transition matrix elements. The derived equations (dipole selections rules, sum rules etc...) allow to extract quantitative information from dichroic measurements. The equations are beyond the scope of this

thesis and will not be discussed here.

### 3.3.2 Versatile insert for in situ electrical probing

DEIMOS is equipped with a variable temperature insert allowing temperature variation in the 1.5 K-370 K range. A new versatile variable temperature insert ( $V^2TI$ ) was designed to increase sample environment capabilities by adding electrical wiring. Electrical wiring can be used, among other possibilities, to apply voltage pulses to change the polarization of ferroelectric samples or measure electrical voltages or current. The insert was developed with the stringent requirements of the synchrotron environment but also to be user-efficient and as accessible as possible. The specification of the  $V^2TI$  can be summarized as follows:

- Simple and fast sample transfer in UHV conditions.
- Device temperature below 20 K.
- $0^\circ$  and  $45^\circ$  angles between incident photon flux and the sample surface plane.
- 12 wires connected to the sample(s) for users' requirements.
- Ability to easily electrically connect user devices using wire-bonding.
- Electrically insulated sample to enable TEY measurements.

Figure 3.12 represents the  $V^2TI$  sample environment.

### 3.3.3 Association of XAS and electrical measurements

In order to combine XAS measurements and electrical measurement on magnetic tunnel junctions, we interfaced our *mobile* magnetotransport setup to the synchrotron experiment. The *mobile* setup features the same elements as the regular setup discussed in Section 3.2, that is a multiplexor and the same control program.

In order to combine both techniques we had to: (i) interface the connector of the  $V^2TI$  to the input of the multiplexor and (ii) somehow correlate data points measured by both experiments. Since the synchrotron facility uses shared tools to collect and store data and has a complex network architecture, it is very hard to access data in real time to relate XAS and electrical points. To achieve point (ii), we used another approach. With took advantage of the Network Time Protocol (NTP) used by the synchrotron to synchronize both experiment. The absolute time difference  $\Delta T$  between both setup is within  $\pm 10$  ms. The data were then related during data analysis by interpolating their values to absolute points in time. This approach is valid as long as a 20 ms mesh is sufficient to interpolate XAS and electrical points, i.e. the energy sweep is slower than  $\Delta T$  and the number of electrical measure ( $N_{el}$ ) per energy point ( $N_{en}$ ) is superior or equal to one, or  $N_{el} \geq N_{en}$ .

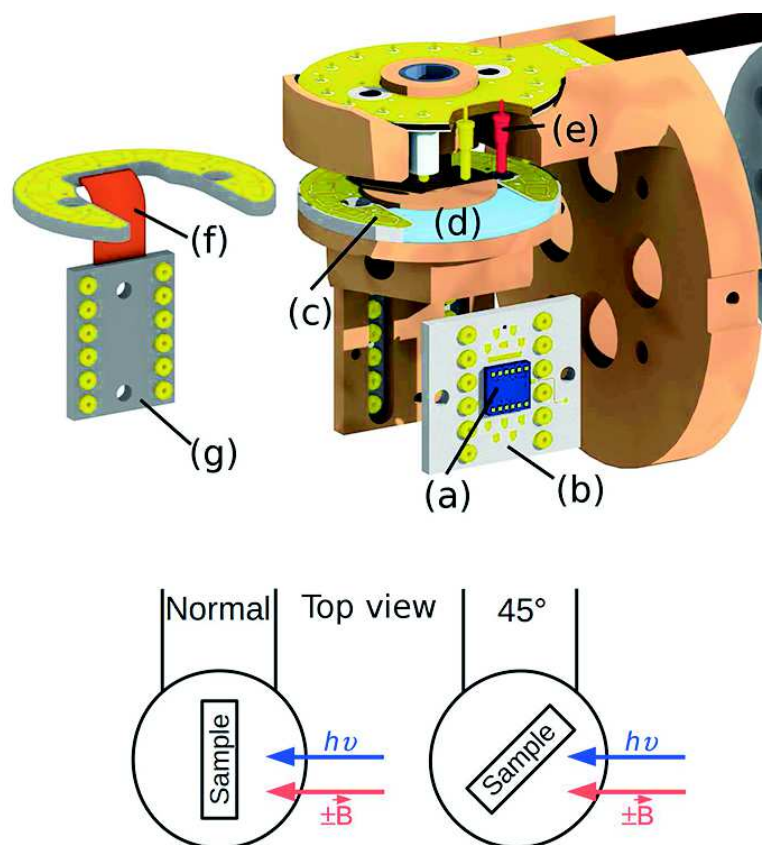


Figure 3.12: **V<sup>2</sup>TI immediate sample environment:** (a) sample (dark blue), (b) sample PCB chip ready to be plugged in (g), (c) 12 electrical contacts, (d) teflon part, (e) spring dot, (f) kapton flex, (g) sample holder PCB. Bottom: top view sketch showing direction of photon and direction of magnetic field for both 0 ° and 45 ° working positions. Figure taken from Joly *et al.*<sup>206</sup>.

# **Part II**

## **Results and discussion**



# Bias and temperature dependent magnetotransport experiments on CoFeB/MgO magnetic tunnel junctions

As it is detailed in the scientific motivations of this thesis (see [Section 2.6](#)), oxides are promising materials to develop multifunctional devices and play a strategic role in current and future applications. Moreover, it is widely accepted that defects have detrimental effects on intrinsic material properties, and in general the presence of structural defects is not desired. Although the presence of oxygen vacancies is often supposed in order to explain the deviation of devices' properties from the expected behavior, detailed studies of the impact of such defects are scarce.

It is well established that removing oxygen atoms from the MgO crystal results in potential wells acting as electron traps (see [Section 2.4.2](#)). The charge state of these point defects may vary, resulting in a variety of different localized states that span the forbidden energy region of the dielectric. Additionally, these defects can be in their ground or excited state or may interact with each other and form double oxygen vacancies. In this chapter we aim to unambiguously identify the impact of specific defect populations induced by oxygen vacancies on the electrical properties of CoFeB/MgO/CoFeB magnetic tunnel junctions. MgO is a comparatively simple oxide, it is investigated for its interesting properties and is one of the most studied oxide. As such, MgO represents a canonical system ideal to investigate the impact of oxygen vacancies.

In order to examine the impact of oxygen vacancies on the electrical properties of our devices, we first measured the photoluminescence (PL) properties of our sputtered MgO thin films and establish the potential landscape, including the energy position of localized states, by confronting our results to several models proposed in the literature and discussed in [Section 2.4.3.1](#).

We then measured the magnetic and electrical properties of our CoFeB/MgO/CoFeB MTJs. In particular, we used an experimental technique in order to determine the effective barrier height felt by tunneling electrons which is free of the deficiencies inherent to fitting techniques based on the WKB approximation. Indeed, semi-classical models based on the WKB approximation such as Brinkman's or Simmons' formula suppose a simple potential step to model the tunneling barrier and do not take into account the electrical band structure of the dielectric nor the presence of localized states.

Results presented in this chapter will be discussed from the point of view of a published paper<sup>190</sup>. In this paper, we propose a scenario in which electrons tunnel with respect to

the energy position of localized states in the band gap of MgO. The signatures of specific localized states on the electrical properties of the device are identified by comparing the electrical and optical measurements and various discrepancies present in the literature are discussed from the perspective of tunneling mediated by localized states.

In parallel to the interpretation of the paper, the discussion will focus on the deficiencies and weaknesses of the aforementioned model. In particular, we'll see that a misconception concerning the optical activity of point defects in crystals lead to the misinterpretation of the photoluminescence spectra, which in turn weakens the model. Finally, some predictions proposed in our paper<sup>190</sup> are discussed from the the point of view of the detailed overview made in [Chapter 2](#).

## 4.1 Optical activity of sputtered MgO thin films

### 4.1.1 Overview of the literature

Before presenting our photoluminescence (PL) experiment, we first summarize PL and models reported in the literature and discussed previously (see [Section 2.4.3.1](#)). [Figure 4.1](#) reviews absorption and emission bands related to  $F$  and  $M$  centers. Energies related to absorption and emission processes are summarized in [Table 4.1](#). Concerning the emission of  $F$  centers, two models discussed in [Section 2.4.3.1](#) are represented in [Figure 4.1](#).

We remind that the  $F/F^+$  bands are characterized by two main features: (i) both  $F$  and  $F^+$  states absorb 5 eV photons and emit 2.3 eV and 3.2 eV photons respectively and (ii) although the optical transition between ground and excited states is allowed, and thus expected to be short lived, emission bands can be detected long times after excitation (several seconds).

In order to explain these experimental observations, [Rosenblatt \*et al.\*](#) suggest the excitation from the ground  $F/F^+$  states to excited states located 5 eV higher in energy. Since electronic transitions are much faster than the motion of atoms in the crystal, electrons are promoted to *unrelaxed* excited states. After the optical transition, neighboring  $Mg^{2+}$  and next neighbors  $O^{2-}$  accommodate for the additional electrons energy and the system evolves towards *relaxed* excited states. Electrons can then radiatively recombine to unrelaxed ground states, after which the system will non-radiatively evolve towards relaxed ground states. This process accounts for the strong Stokes shift of  $F/F^+$  centers, it is further discussed in [Section 2.4.3](#) and summarized in [Figure 2.27\(b\)](#).

In order to explain the long-lived PL signal, [Rosenblatt \*et al.\*](#) propose an additional mechanism occurring during this process. They suppose that unrelaxed excited states are located just below the conduction band minimum (CBM). When electrons are promoted to excited states, they can either recombine to ground states through the aforementioned process or ionize to the conduction band. In the latter case, electrons can be localized on trap centers located near the CBM (not shown) for long times. Trapped electrons can reionize to the conduction band and effectively act as an electron sink available for  $F$  and  $F^+$  emission and explain the long-lived PL that characterizes these bands.

The only deficiency of this model concerns the large Stokes shift of 2.7 eV correspond-

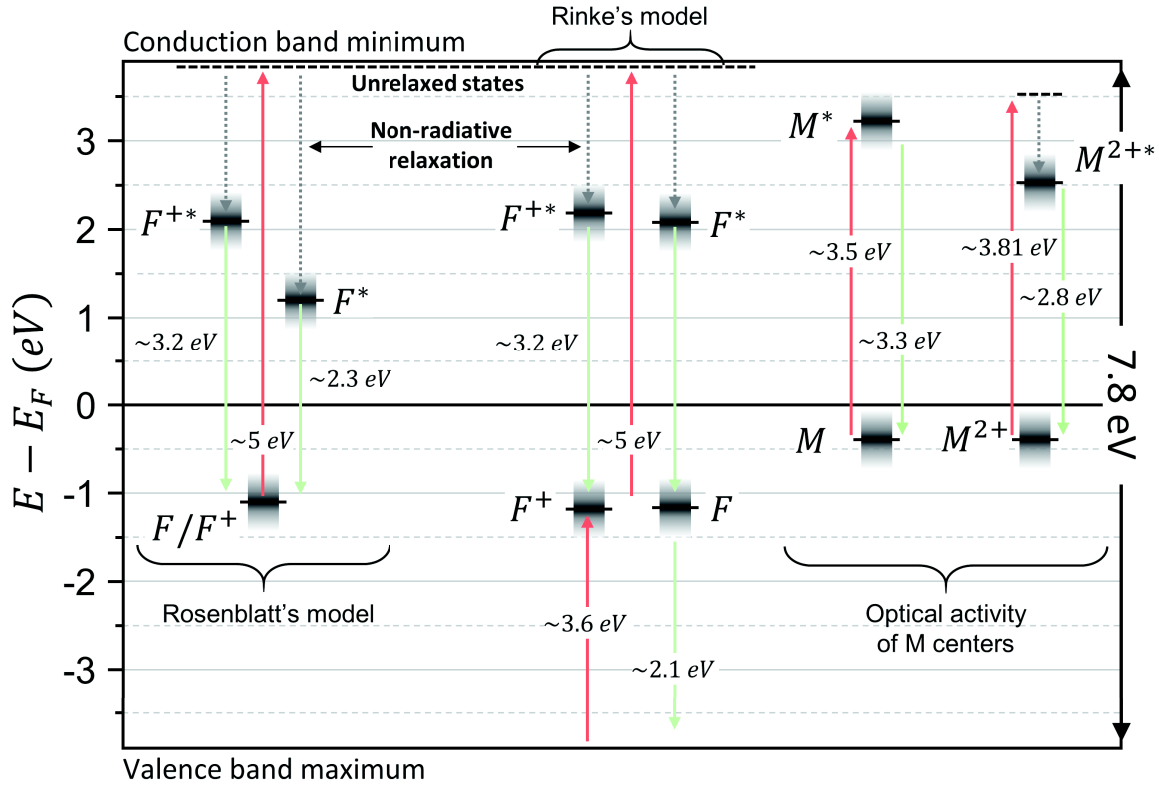


Figure 4.1: **Optical activity of MgO:** This figure summarizes absorption and emission peaks induced by  $F$  and  $M$  center in MgO. Two models for the emission of  $F$  centers, discussed in Section 2.4.3, are represented. Additionally, the photoluminescence of  $M$  and  $M^{2+}$  is also represented. Table 4.1 summarizes the absorption and emission peaks of  $F$  and  $M$  centers.

ing to the  $F$  luminescence band<sup>171</sup>. We emphasize that it is the long lived PL signal and the supposition that unrelaxed excited states are located just below the CBM that allows to pin the  $F/F^+$  ground states 5 eV below the CBM.

Two recent theoretical works<sup>172,173</sup> confirm a possible 1.8 eV Stokes shift related to the reconfiguration energy of neighboring  $Mg^{2+}$  and next neighbors  $O^{2-}$  atoms, but in firm the 2.7 eV Stokes shift. In order to explain experimental observations, Rinke *et al.*<sup>172</sup> propose an alternative scenario also represented in Figure 4.1. In this model, both  $F$  and  $F^+$  centers absorb at 5 eV and luminesce at 3.2 eV. The 2.3 eV emission is related to the excitation of holes in the valence band to the ground  $F$  center. Moreover, an additional absorption band related to the excitation of electrons in the valence band to singly occupied ground states of  $F^+$  centers is predicted. The only shortcoming of this model pertains to the presence of holes in the valence band (VB). Actually no mechanism explaining the creation of holes in the VB with 5 eV photons is proposed.

In addition to  $F$  centers, the hypothetical optical activity of double oxygen vacancies (denoted  $M$  centers) is also represented in Figure 4.1. Although several papers ascribed luminescence peaks to  $M$  centers<sup>169,170,177–184,207,208</sup>, double oxygen vacancies attracted

Center	Absorption	Emission	Th. Absorption	Th. Emission
$F$	5.03 eV <sup>167,169</sup> 248 nm	2.3-2.5 eV <sup>167,169</sup> 500-540 nm	5 eV <sup>172,173</sup> 248 nm	3.45 eV <sup>172,173</sup> 360 nm
$F^+$	4.96 eV <sup>167,169</sup> 250 nm	3.2 eV <sup>167,169</sup> 387 nm	4.96 eV <sup>172,173</sup> 250 nm	3.7 eV <sup>172,173</sup> 335 nm
$M$	3.5 eV <sup>169,177,179,180</sup> 354 nm	3.3 eV <sup>169,179</sup> 375 nm	4.4 eV <sup>181</sup> 282 nm	/
$M^+$	/	2.61 eV <sup>169</sup> 475 nm	1.3 eV and 3.8 eV <sup>181</sup> 954 nm and 326 nm	/
$M^{2+}$	3.81 eV <sup>169,177,178,180</sup> 325 nm	2.8 eV <sup>169,178</sup> 443 nm	/	/

Table 4.1: **Optical activity of MgO:** Absorption and emission peaks related to  $F$  and  $M$  centers found in the literature as well as related references.

less attention than  $F$  centers and their identification is not unambiguous. Conversely to  $F$  centers, there are no experimental evidences (to our knowledge) that allows to locate the ground or excited states of  $M$  centers with respect to the CBM or the VBM. Nevertheless, recent calculations performed in our group suggest that the highest occupied state of  $M$  centers is located approximately 0.3 eV below the gap center in FeCo/Co/MgO(7ML)/Co/FeCo heterostructures.

Additionally, we would like to discuss how the energy levels of the various states were determined and placed in the gap of MgO as represented in Figure 4.1. As it is discussed above, configuration coordinate diagrams allow to qualitatively understand the excitation and relaxation processes of point defects. We stress that PL emission alone cannot be used to locate ground and excited states relative to each other since the proportion of energy lost to the crystal lattice during the excitation and recombination processes is unknown. Some luminescence bands can be accompanied by zero phonon lines (ZPL) that occur due to the direct relaxation between relaxed ground and excited states. The energy position of ZPL allow to directly extract the energy difference between these states. However  $F$  and  $F^+$  bands are not characterized by ZPL.

Nonetheless, in Figure 4.1 and in the rest of this chapter we assume that the relative energy difference between ground and excited states of  $F$  and  $F^+$  states correspond to the energy of their respective luminescence bands. As a qualitative estimate of the error induced by this approximation, we can estimate the energy lost to the crystal lattice during the relaxation process from the computed configuration coordinate diagram of Ertekin *et al.*<sup>173</sup>. Typically, excited states can be  $\sim 0.6$  eV higher in energy compared to their position in Figure 4.1

Finally, another source of incertitude concern the position of the charge neutrality level (CNL) in MgO that will pin the electrodes Fermi energy to the MgO band gap. We choose to pin the electrodes Fermi energy at midgap, which may be a good approximation for per-

fect and isolated MgO. However, when MgO is sandwiched between metallic electrodes, it is established that metal induced gap states (MIGS) might modify the position of the CNL. Besides, the presence of localized states can also influence the position of CNL.

## 4.1.2 Temperature dependent photoluminescence of sputtered MgO thin films

### 4.1.2.1 Photoluminescence spectra

The stack of the samples studied in this chapter are Ta(5)/Co(10)/IrMn(7.5)/FeCoB(4)/MgO(2.5)/FeCoB(4.5)/Ta(5)/Pt(5) (numbers represent layers thickness in nanometer). All layers are sputter deposited, a brief description of the sample growth is given in [Section 3.1.1](#). In order to determine which defect species are present in our MgO thin films we performed photoluminescence experiment on Ta(5)/Co(10)/IrMn(7.5)/FeCoB(4)/MgO(2.5) structures prepared under standard conditions.

A typical PL spectrum acquired at room temperature and using 3.81 eV (325 nm) light is shown in [Figure 4.2\(a\)](#). We can see that excitation with 3.81 eV photons result in two broad luminescence peaks centered around 1.7 eV and 2.8 eV. The broadness and the complex form of the higher energy peak suggest that it is a convolution of several luminescence bands. The experimental spectrum (black line) is tentatively deconvoluted using a multiple gaussian fit and result in four sub peaks located at 2.82, 2.56, 2.18 and 1.68 eV (color lines). The cumulative peak (magenta) overlaps rather well with experimental points.

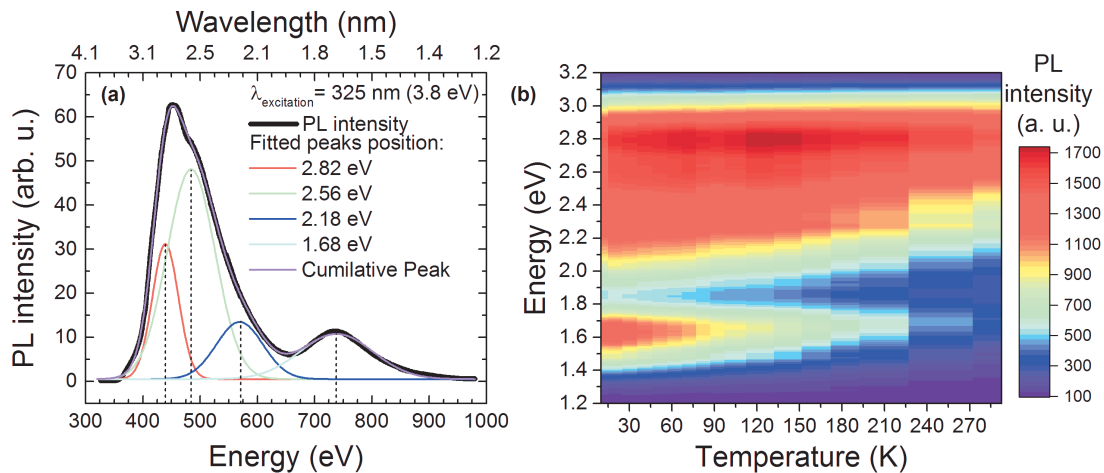


**Figure 4.2: Photoluminescence of rf-sputtered MgO thin films:** A typical PL spectrum acquired at room temperature and using 3.81 eV (325 nm) photons energy is shown in panel (a). The broadness and the complex form of the higher energy peak suggest that it is a convolution of several luminescence bands. The experimental spectrum (black line) is tentatively deconvoluted using a multiple gaussian fit (color lines). The temperature dependence of the PL spectra is plotted in panel (b). See text for more details.

The temperature dependence of the PL spectra is plotted in Figure 4.2(b). The energetic position of all peaks is constant over the whole temperature range (10 K to room temperature). The two peaks at 1.7 eV and 2.2 eV (responsible for the shoulder of the experimental peak) have a strong temperature dependence. Both luminescence bands decrease with increasing temperature and are almost suppressed at room temperature (decrease of 70 % and 80 % compared to low temperature emission). The amplitude of the peak located at 2.6 eV is constant while the magnitude of the peak located at 2.8 eV first increases between 10 K and 140 K (+20 %) and then decreases between 140 K and room temperature (-20 %). In the following section, we'll briefly introduce the potential landscape proposed in our paper<sup>190</sup> in order to explain these PL spectra and discuss the limitations and approximations of the model.

#### 4.1.2.2 Interpretation

Similarly to Figure 4.1, we present another<sup>190</sup> potential landscape in the MgO band gap in Figure 4.3 and discuss our initial interpretation of the PL spectra plotted in Figure 4.2 based on this model. We'll first discuss the energy position of the various levels.

The  $F/F^+$  ground states are located 5 eV below the conduction band (1.2 eV below midgap), in line the literature and Figure 4.1.

$F^*$  centers are located 2.5 eV above  $F/F^+$  ground states, which is also consistent with Rosenblatt's model. However, we note that two possible luminescence bands are ascribed to this state in Figure 4.3. This interpretation suggests that electrons can radiatively recombine between unrelaxed and relaxed excited state (while it is known that this process is non-radiative) but also from the relaxed excited state to the ground state. This is in contradiction with the well-established consecutive steps related to excitation and recombination processes of point defects discussed in Section 2.4.3 and briefly summarized in the beginning of this chapter (Section 4.1.1). We can see that ultimately, this interpretation is consistent with the  $F^*$  emission because it yields two emission bands at the same energy and is compatible with the emission of  $F^*$  states, nevertheless will see that it will be more problematic for the emission of  $F^{+*}$  states.

For similar reasons, we ascribed two emission bands to  $F^{+*}$  states. The first one is supposed to result from the transition between the unrelaxed to the relaxed excited states resulting in a 3.3 eV emission and the second one from the transition between the excited state to the ground state, resulting in a 1.7 eV band. However, all the studies related to  $F^+$  states<sup>165-169,207</sup>, without exception, report a single emission band located at 3.3 eV. Additionally, no emission is reported at 1.7 eV for this state.

Concerning the energy position of  $M$  centers in the band gap of MgO, we refer to the theoretical work of Domínguez-Ariza *et al.*<sup>181</sup> in which the absorption band of  $M$  states is calculated to be 4.4 eV. It is then supposed<sup>190</sup> that the optical activity of  $M$  and  $F$  centers are similar, i.e. we assume that the excited  $M^*$  states are located near the conduction band minimum and the ground state 4.4 eV below. We remind that  $F$  centers can be located in the band gap because of the long lived PL related to these bands, suggesting that unrelaxed excited states are located near the CBM and thus the ground state 5 eV below. However, there is no report of time resolved PL of  $M$  bands to our knowledge, and thus there are

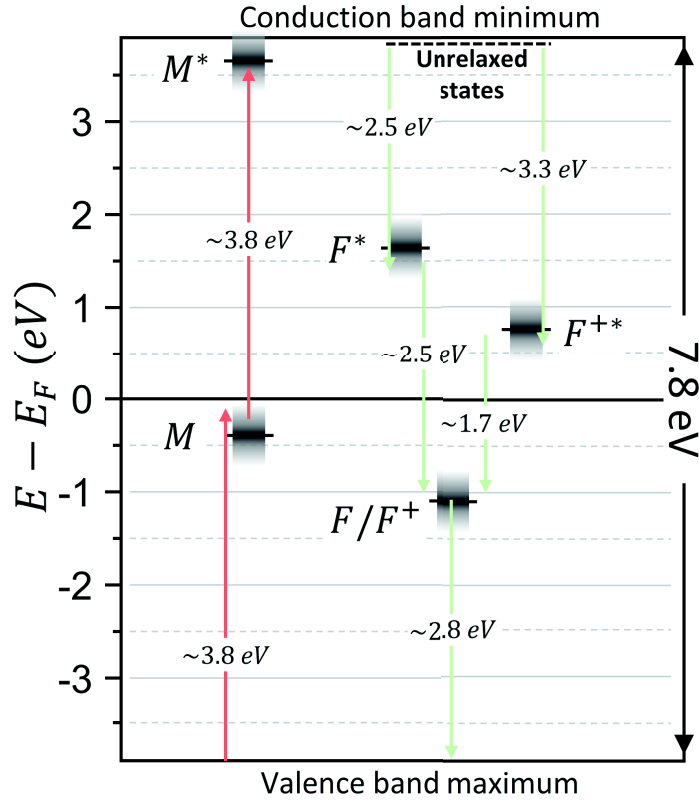


Figure 4.3: **Potential landscape in rf-sputtered MgO thin films:** Potential landscape in rf-sputtered MgO proposed by Schleicher *et al.*<sup>190</sup>. Differences between this diagram and the potential landscape proposed in this thesis (see Figure 4.1) are detailed in the text.

no experimental evidences that allows to locate the ground nor the excited state of these centers with respect to the CBM or VBM. Moreover, Domínguez-Ariza *et al.*<sup>181</sup> emphasize that their calculations are certainly overestimating the absorption energy of  $M$  centers, and thus  $M^*$  states will typically be lower in energy compared to their position in Figure 4.3.

Finally, the PL spectra measured on rf-sputtered MgO thin films and plotted in Figure 4.2 are interpreted using this (questionable) model. It is suggested that 3.8 eV photons are sufficient to overcome the 7.8 eV gap of MgO by promoting electrons from the valence band minimum to  $M$  centers located near midgap and in a second step exciting electrons from  $M$  centers to their excited counterpart located near the CBM. The electrons in the CBM can then successively relax to excited  $F^*$  and  $F^{+*}$  centers, to ground  $F/F$  states and finally to the VBM with the corresponding photon emissions.

Although the picture drawn in our paper<sup>190</sup> allows to explain the measured PL in terms of  $F/F^+$  emission, this interpretation is unrealistic for several reasons. To begin with, we saw that the underlying process related to absorption and emission of point defects were not interpreted correctly. Moreover, it is well established that  $F/F^+$  centers have a single absorption peak centered around 5 eV<sup>165–169,207</sup>. It seems very unlikely that a 3.8 eV excitation would result in  $F$  or  $F^+$  luminescence. In particular, PL excitation spectra of

$F$  and  $F^+$  emission bands measured by Uenaka and Uchino<sup>169</sup> show that these bands are not excited by 3.8 eV photons. Besides, the fact that we suggest two emission bands for  $F^+$  centers located at 3.3 eV and 1.7 eV while only the latter is present in the measured PL spectra is also inconsistent.

Finally, it is interesting to note that absorption peaks in the 3-4 eV range are reported in the literature<sup>169,177-180</sup> but are related to absorption and emission of  $M$  centers. Actually, in Figure 4.2 we can see that the higher energy peak in our PL spectra centered around 2.8 eV is mainly composed of two sub-peaks located at 2.8 eV and 2.6 eV. Interestingly, the absorption at 3.8 eV and these two emission peaks correspond very well to the emission of  $M^{2+}$  and  $M^+$  centers (see Table 4.1). Only the lower energy peak at 1.7 eV is not explained nor reported in the literature.

We'll see that because magnetoresistive properties are interpreted in comparison to optical measurements, the misinterpretation of the latter ones will also weakens the interpretation of the former ones. In the following section, we'll discuss in detail the bias and temperature dependence of magnetotransport properties of our devices.

## 4.2 Magnetotransport experiments

### 4.2.1 Basic magneto-electric properties

Before device fabrication, the magnetic properties of samples are first characterized by SQUID measurements. Figure 4.4 plots the magnetization curve measured at room temperature on Ta(5)/Co(10)/IrMn(7.5)/FeCoB(4)/MgO(2.5)/FeCoB(4.5)/Ta(5)/Pt(5) (numb

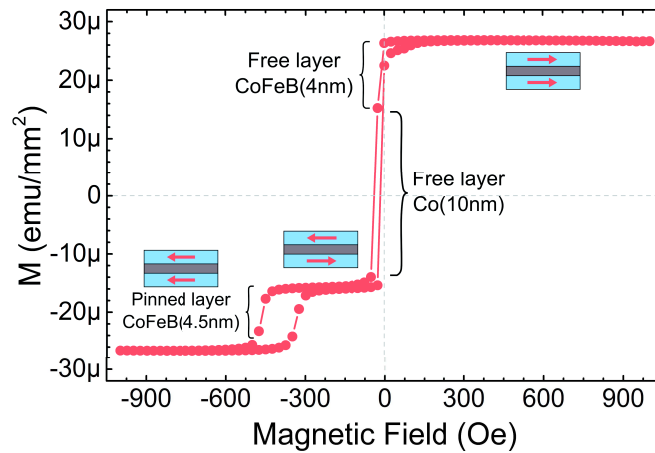


Figure 4.4: **Magnetic properties of samples before optical lithography:** All magnetic layers in our samples have in plane magnetization with the same easy axis direction. We can see that the Co(10 nm) and CoFeB(4 nm) free layers are reversed at small negative applied magnetic fields. The CoFeB(4.5 nm) electrode on top of the IrMn(7.5 nm) antiferromagnetic layer is exchange biased and switches at larger applied magnetic fields.

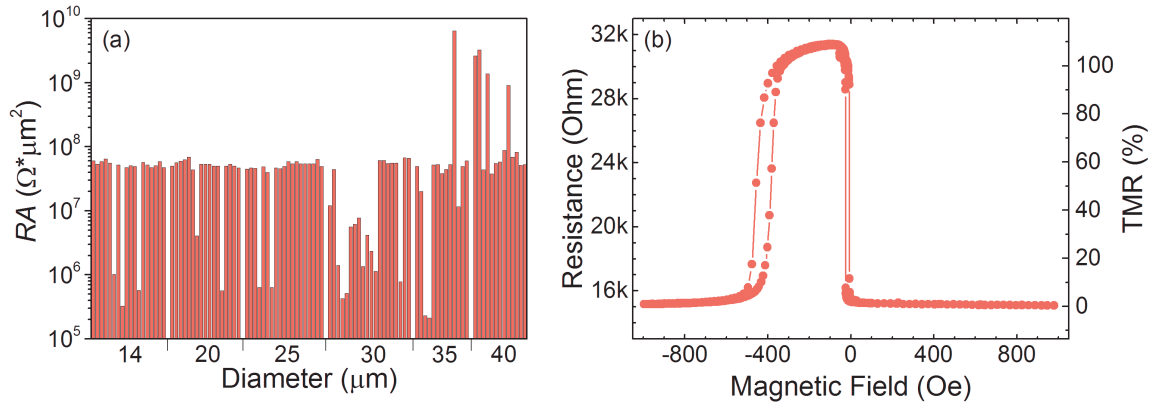


Figure 4.5: **Basic magnetoresistive properties of processed devices:** The resistance area (RA) product of many junctions with diameter ranging from 14 to 40  $\mu\text{m}$  is shown in panel (a). The overall constant RA attests to the uniformity of our samples and the quality of our fabrication process. Panel (b) plots the resistance of a typical device as a function an applied magnetic field measured at room temperature and for an applied bias voltage of  $V = 10$  mV. The typical room temperature TMR of our devices is 110 % at 10 mV.

ers represent layers thickness in nanometer) stacks deposited on Corning 1737 glass substrates.

The reversal of specific layers and the magnetic state of the CoFeB/MgO/CoFeB trilayer are represented for clarity. All the magnetic layers have in plane magnetization with identical easy axis direction. Under a high positive magnetic field, all layers magnetization are aligned in the direction of the applied field. The free Co(10 nm) and CoFeB(4 nm) layers are reversed for very small negative magnetic fields, while the magnetization of the exchange biased CoFeB layer is reversed at larger values. The samples show good magnetic properties required for TMR devices, i.e. well defined parallel (P) and antiparallel (AP) device magnetic states.

Once the magnetic properties of samples are characterized, 144 magnetic tunnel junctions with size varying between 14  $\mu\text{m}$  and 40  $\mu\text{m}$  are fabricated by standard UV lithography. A detailed discussion of the fabrication process can be found in [Section 3.1.3](#). The resistance of each junction is measured using a probe station in 4-points mode and the resistance area (RA) product is computed for each device. By definition, the RA product is a quantity that depends only on the MgO layer thickness and the smoothness of the deposited layers, as such it is useful to control the uniformity of the samples as well as the quality of the fabrication process. [Figure 4.5\(a\)](#) plots the resistance area product (RA) of our sample. We can see that the RA product is uniform, attesting to the good quality of the deposited layers and our fabrication process.

Finally, [Figure 4.5\(b\)](#) plots the resistance of the device as a function of applied magnetic field. As expected from the magnetization curve, we can see that the device shows two resistance states depending on its magnetic configuration and yields a TMR of 110 % at room temperature and 10 mV applied bias voltage.

## 4.2.2 Considerations on the device barrier height

In addition to the basic magnetoresistive properties mentioned before, it is generally desired to extract parameters related to tunneling barriers. These parameters can be obtained by measuring the tunneling current ( $I$ ) of a junction as a function of a bias voltage ( $V$ ) applied across the device. The typical bias dependence of the tunnel current and the TMR of a 25  $\mu\text{m}$  magnetic tunnel junction measured at room temperature are plotted in Figure 4.6(a).

These curves are then fitted to theoretical models in order to extract the effective barrier height of MTJs. The majority of works reported in the literature make use of models based on the WKB approximation, namely Brinkman's<sup>34</sup> and Simmons'<sup>33,209</sup> formulas, that allow to extract the barrier thickness as well as the effective barrier height (see Section 1.2.1.3). However, both formula are derived for perfect potential steps and within the free electron approximation. In Chapter 1, we saw that the tunnel current depends on many parameters such as the density of states in the electrodes and the electrical properties of the tunnel barrier. Moreover, we saw in Chapter 2 that the electrical properties are also very sensitive to many other intrinsic and extrinsic properties such as interfacial resonant states, interfaces quality or localized states induced by impurities or defects in the tunnel barrier. Although these models can yield satisfactory result for AlO (amorphous) based MTJs<sup>210</sup>, they cannot be used to treat epitaxial devices and this is especially true for MgO based MTJs in which the electrical properties of the insulating layer play a crucial role in the transport properties. Actually, Miller *et al.*<sup>193</sup> show that the use of such models in MgO based MTJs yield unphysical parameters.

In this thesis, we decided to take a different approach and based our analysis on a tech-

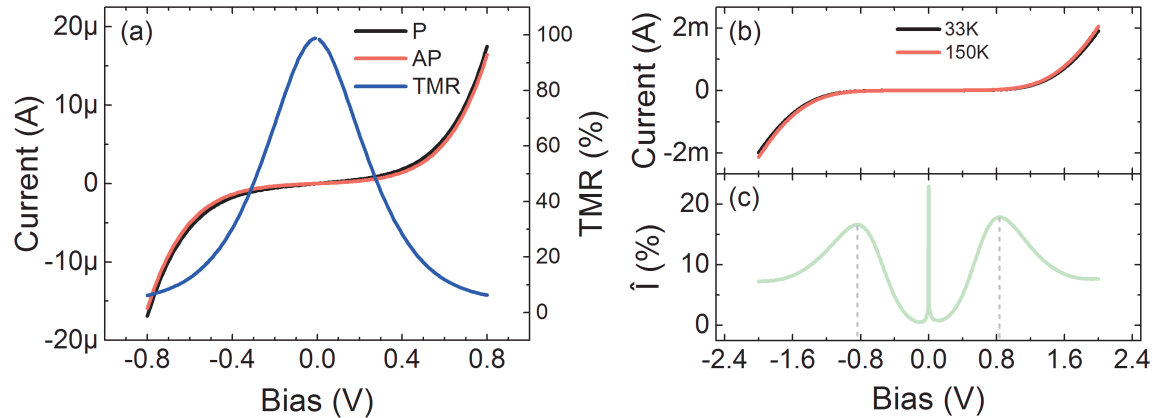


Figure 4.6: **Bias dependence of magnetoresistive properties and experimental method to determine the effective barrier height:** The bias dependence of tunnel current of a MTJ in both P and AP magnetic states is plotted in panel (a). The bias dependence of TMR is also shown (blue curve). Panels (b) and (c) illustrate the  $\hat{I}$  method used in this thesis in order to determine devices' barrier height. This simple method consists in computing the temperature dependence between two I-V curves measured at different temperatures (panel (b)) using 4.1. The resulting peaks are located near the barrier height. See text for more details.

nique proposed by Rottländer *et al.*<sup>211</sup> that allows to extract the effective barrier height experimentally. This technique is free from the aforementioned deficiencies. The working principle is actually very simple and is represented in Figure 4.6 panels (b) and (c). It consists in measuring two current-voltage characteristics at two different temperatures, usually the lowest ( $T_1$ ) and highest ( $T_2$ ) accessible to the system (Figure 4.6(b)) and then compute the temperature dependence with the following formula:

$$\hat{I}(T_1; T_2) = \left( \frac{I(T_2)}{I(T_1)} - 1 \right) \times 100 \quad (4.1)$$

The ensuing  $\hat{I}$  (read *I hat*) curves are characterized by two maxima located at bias voltages 1.2 times larger the barrier height<sup>211</sup> (Figure 4.6(c)).

The presence of peaks in the  $\hat{I}$  curves can be understood by looking at Figure 4.7. As we discussed in Section 2.2.1.1, applying a bias voltage on a MTJ result in a linear potential drop in the insulating layer and a reduction of the average barrier height. As a consequence, the tunnel current is increased. Besides, when the bias voltage becomes larger than the barrier height (represented by grey dashed lines in Figure 4.7(a)), in addition to the reduction of the barrier height the effective barrier thickness is also reduced and the increase rate of  $I$  with increasing bias is further accelerated. It is this change in the tunnel current increase rate that is actually probed by Equation (4.1). When temperature is increased, the additional thermal energy provided to tunneling electrons causes the change

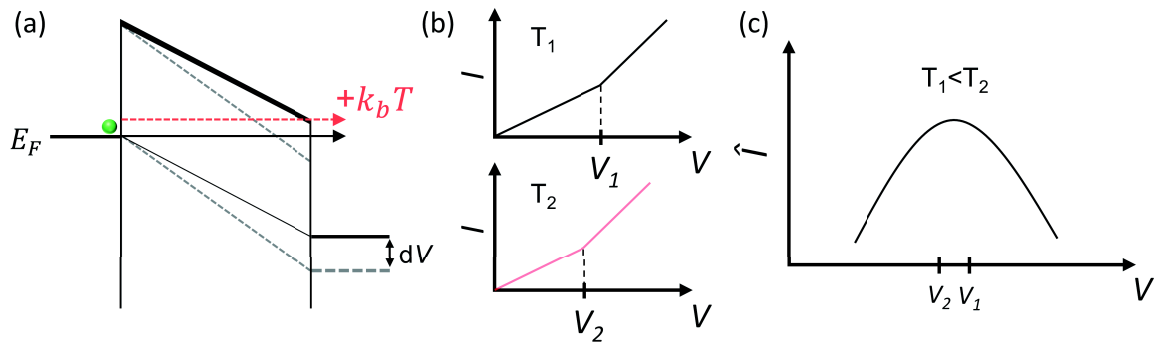


Figure 4.7: **Working principle of Rottländer's method:** Applying a bias voltage across a device cause a linear potential drop in the barrier and reduce the effective barrier height as shown in panel (a). As a consequence, the tunnel current is increased. Besides, when the applied bias becomes larger than the barrier height (dashed grey line in panel (a)), the tunnel current increase rate is further accelerated. This is represented in the upper graph of panel (b) at  $V_1$ . When the temperature is increased (dashed red arrow in panel (a)), the additional thermal energy provided to tunneling electrons causes the change in the increase rate of  $I$  to occur at slightly lower bias voltages. This is represented in the lower graph of panel (b) at  $V_2$ . The resulting temperature dependence computed using Equation (4.1) and schematized in panel (c) is characterized by a peak, the position of which corresponds approximately to the device barrier height. Adapted from Rottländer *et al.*<sup>211</sup>.

in the increase rate of  $I$  to occur at slightly lower bias voltages (see Figure 4.7(b)). As a result, the relative current difference between two I-V characteristics measured at  $T_1$  and  $T_2$  with  $T_1 < T_2$  is characterized by a peak, the position of which correspond approximately to the device barrier height. This is schematized in Figure 4.7(c).

If we take a closer look at  $\hat{I}$ , we can see that it is simply the relative change between two currents measured at the same bias but different temperatures. More generally, the presence of peaks in  $\hat{I}$  can be viewed as the signature of thermally activated processes between  $T_1$  and  $T_2$ . In this sense the interpretation of Rottländer *et al.*<sup>211</sup> is a particular example of such processes. Actually, any process that would increase (or decrease) the current upon temperature change would have an impact on  $\hat{I}$  curves.

In Section 2.4, we discussed in detail the impact of localized states on tunnel current. In particular, we saw that their impact was different depending on whether their energy was close to the electrodes' Fermi energy or not. Briefly, when tunneling electrons have an energy close to that of the localized states, tunneling and localized electrons are resonant and the current is greatly increased. Conversely, when they have distinct energies (nonresonant), localized states act as scattering centers, i.e. the properties of tunneling electrons such as  $k_{\parallel}$  or the spin are not conserved and the symmetry filtering effect is deteriorated.

Put differently, localized states have exactly the same effect on  $\hat{I}$  than the barrier height discussed in Figure 4.7. When the bias voltage applied across devices is swept, tunneling carriers can resonantly tunnel through the interaction with localized states in the band gap of the insulating layer and the change in the tunnel current increase rate should induce a peak in  $\hat{I}$  curves.

In this respect, we decided to use Rottländer's method in a more general way. We actually measured the magnetotransport properties of our devices between 33 K and 250 K with steps of  $\Delta T = 3$  K. Instead of calculating  $\hat{I}$  between the lowest and highest accessible temperature (*absolute I hats* or  $\hat{I}_{abs}$ ), we did so between I-V characteristic measured at  $T$  and  $T + \Delta T$  (*relative I hats* or  $\hat{I}_{rel}$ ). This allows to probe the evolution of thermally activated processes with a resolution of  $\Delta T = 3$  K. Besides, we also applied Equation (4.1) to TMR spectra in order to probe the effect of temperature on TMR. Results are presented in the following section.

### 4.2.3 Bias and temperature dependent measurements

In order to measure the bias and temperature dependence of our devices' magnetoelectric properties and explore the large parameter space involved by these measurements, we used the magnetotransport experiment described in Section 3.2. We measured the bias dependence of tunnel current of a 25  $\mu\text{m}$  MTJ in both parallel (P) and antiparallel (AP) magnetic states from  $T = 33$  K to  $T = 250$  K with steps of  $\Delta T = 3$  K. We then computed the temperature dependence between I-V characteristics measured at  $T$  and  $T + \Delta T$  using Equation (4.1). The resulting  $\hat{I}_{rel}$  are plotted in the form of 2D color maps in the (V,T) parameter space. Results for parallel (P) and antiparallel (AP) magnetic configurations are plotted in Figure 4.8 panels (a) and (b) respectively.

In order not to alter or destroy our MTJs, we have found it necessary to limit measurements up to  $T = 150$  K at  $|V| = 2$  V and up to  $T = 250$  K at  $|V| = 1.3$  V. In both P and

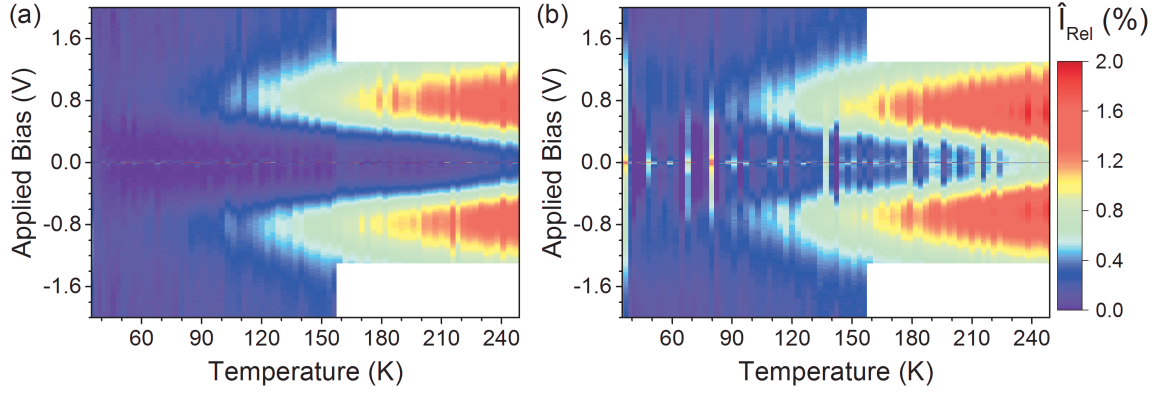


Figure 4.8: **Bias and temperature dependence of the tunnel current in the parallel and antiparallel magnetic configurations:** Following Rottlander’s technique and using Equation (4.1),  $\hat{I}_{rel}$  is computed for both P and AP magnetic states and plotted in panels (a) and (b) respectively. We can see that a dominant peak impacts both P and AP conductance at 0.8 eV. Both the bias position and amplitude of the peak are extracted from these datasets and plotted in Figure 4.10(a).

AP, it is possible to distinguish the impact of a dominant peak centered around 0.8 eV at positive and negative bias voltage. We remind that peaks in  $\hat{I}_{rel}$  reveal thermally activated processes due to an increase of temperature of  $\Delta T = 3$  K. Because the color scale of Figure 4.8 spans the whole temperature range, peaks with low amplitude at low temperatures are not resolved. In order to circumvent this issue and get more quantitative information, we extracted the peak maximum position and amplitude for both P and AP datasets. These quantities are plotted in Figure 4.10(a), but will be discussed later, in parallel to similar data extracted for TMR.

At each temperature, I-V characteristics are measured for both P and AP magnetic configurations and the TMR is computed using Equation (1.12). The resulting  $TMR(V,T)$  dataset is treated with the same approach. The temperature dependence of TMR is computed with both

$$TMR_{abs}(33\text{ K}; T) = \left( \frac{TMR(T)}{TMR(33\text{ K})} - 1 \right) \times 100, \quad (4.2)$$

and

$$TMR_{rel}(T_1; T_2) = \left( \frac{TMR(T_2)}{TMR(T_1)} - 1 \right) \times 100, \quad (4.3)$$

Both  $TMR_{abs}$  and  $TMR_{rel}$  are represented in figure Figure 4.9 panels (a) and (b) respectively. The former dataset represents the TMR drop at a given temperature compared to its value at the lowest temperature (33 K), while the latter corresponds to the TMR thermal drop between  $T$  and  $T + \Delta T$  with  $\Delta T = 9$  K. Note that a  $\Delta T$  of 9 K was chosen because  $\Delta T < 9$  K did not yield exploitable datasets owing to noise issues. Due to the fact that  $\hat{I}_{rel}$  for P and AP are very similar, computing the  $TMR$ ,  $TMR_{abs}$  and  $TMR_{rel}$  is useful because it generates more contrast to the effect of temperature on P and AP. From Figure 4.9(a) and (b), we can broadly distinguish two temperature ranges. Between  $33\text{ K} < T < 140\text{ K}$  the

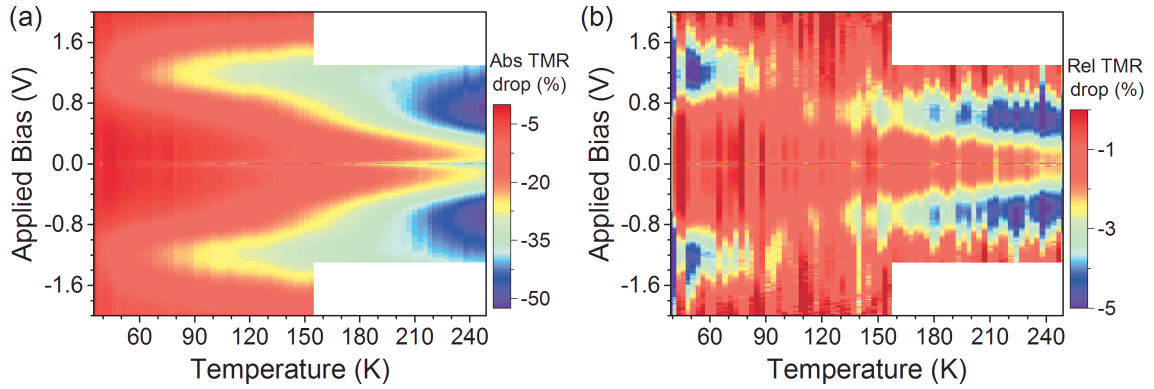


Figure 4.9: **Bias and temperature dependence of TMR:** The temperature dependence of TMR is computed using Equation (4.2) and Equation (4.3). The absolute and relative TMR drops are represented in panels (a) and (b) respectively. We can broadly distinguish two temperature ranges. First, between  $33 \text{ K} < T < 140 \text{ K}$  the maximal TMR drop occurs at 1.2 eV and second, between  $140 \text{ K} < T < 250 \text{ K}$  it occurs at 0.8 eV. Similarly to  $\hat{I}_{rel}$  datasets, the position and amplitude of the peak are extracted and plotted in Figure 4.10(b).

maximal TMR drop occurs at 1.2 eV while between  $140 \text{ K} < T < 250 \text{ K}$  it occurs at 0.8 eV. Similarly to  $\hat{I}_{rel}$  datasets, both the position and amplitude of the peaks in Figure 4.9(b) are extracted and plotted in Figure 4.10(b).

We'll now discuss in more detail the position and amplitude of peaks extracted from  $\hat{I}_{rel}$  and datasets  $TMR_{rel}$  plotted in Figure 4.10 panels (a) and (b) respectively. From Figure 4.10(a), we can see that both P and AP  $\hat{I}_{rel}$  peaks shift rapidly from  $V = 1.1 \text{ V}$  to lower bias voltage values within  $33 \text{ K} < T < 80 \text{ K}$ . In the same temperature range, the corresponding TMR thermal drop is centered at 1.2 V, but its amplitude decreases, Fig-

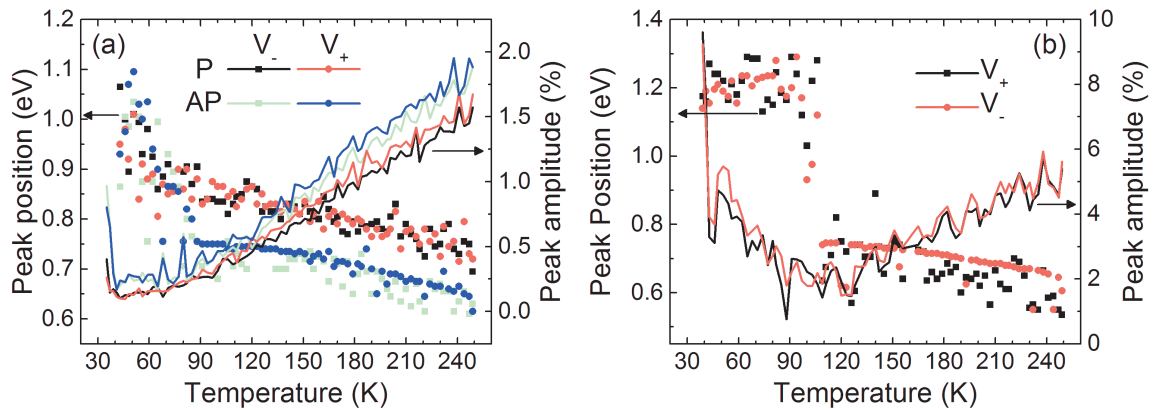


Figure 4.10: **Peak positions and amplitude:** Peak position and amplitude extracted from (a) P and AP  $\hat{I}_{rel}$  datasets and (b) the TMR relative thermal drop. Data for both positive and negative bias voltage are shown. We remind that the position of  $\hat{I}_{rel}$  peaks corresponds to the energy position of a thermally activated process.

ure 4.10(b).

Above 80 K, the decrease in the  $\hat{I}_{rel}$  peak position lessens, while the peak's amplitude start to increase markedly. Interestingly, the decrease of the peak position with increasing temperature is not the same for the P and AP channels for  $T > 80$  K. Concurrent to this change in  $\hat{I}_{rel}$  peaks at  $T = 80$  K is an abrupt change in the bias position of the maximum in relative TMR thermal drop from 1.2 to 0.7 V. Moreover, the amplitude of the TMR thermal drop, which was decreasing within  $33 \text{ K} < T < 80 \text{ K}$ , stabilizes before increasing for  $T > 100$  K. This suggest the gradually increasing impact on magnetotransport of a feature at  $V \sim \pm 0.7$  V. Indeed, above 80 K, this feature becomes more prominent in the TMR thermal drop and at 100 K it totally dominates all other spectral signatures of TMR decrease.

## 4.3 Discussion

In our paper<sup>190</sup>, we interpret the temperature dependent magnetotransport experiment based on the interpretation of PL spectra measured on our rf-sputtered MgO thin films. However, our detailed discussion in Section 4.1.2.2 shows that a misconception concerning the optical activity of point defects in crystals lead to the misinterpretation of the PL spectra.

In this section, we first discuss in details the initial model proposed in the paper and reveal deficiencies induced by the misconception of the optical activity of MgO. Secondly, alternative models are tentatively proposed in order to explain the temperature dependence of the magnetotransport properties.

### 4.3.1 Initial model and limitations

#### 4.3.1.1 Model

**Identification of peaks at 1.2 and 0.7 V:** In our paper<sup>190</sup> we consider that the bias position of  $\hat{I}_{rel}$  peaks corresponds to the effective barrier height felt by tunneling electrons, i.e. the barrier height is not defined by the intrinsic properties of the tunnel barrier, but by the energy position of localized states. Datasets and results presented in Section 4.2.3 are interpreted as follow (see Figure 4.10).

At low temperature, a feature located at 1.2 V dominates the transport properties. As the temperature increases, an additional feature located at 0.7 V starts to impact the tunnel current. This feature causes the shift of the  $\hat{I}_{rel}$  peaks, or equivalently the shift of the effective barrier height, to lower bias voltages within the  $33 \text{ K} < T < 80 \text{ K}$  temperature range. In this temperature range, the feature at 1.2 V still dominates as inferred by the maximum TMR thermal drop at 1.2 V. However, an abrupt change occurs at  $T = 80$  K and the 0.7 V feature start to dominates. This is suggested by (i) the slowing down of the  $\hat{I}_{rel}$  peaks shift that stabilize around 0.7 V with the concurrent increase in peaks' amplitude and (ii) the abrupt change in the bias position of the maximum in relative TMR thermal drop from 1.2 to 0.7 V.

In this model, it is supposed that the aforementioned thermally induced changes are exclusively caused by oxygen vacancies. In order to identify exactly which defect species are involved, we proposed to compare magnetotransport experiments to luminescence bands obtained in PL spectra. According to our interpretation of the PL spectra, discussed in Section 4.1.2.2 and summarized in Figure 4.3, we can identify the 1.2 and 0.7 V features to the ground  $F/F^+$  and excited  $F^{+*}$  located at  $E - E_F = -1.1$  eV and  $E - E_F = 0.7$  eV respectively.

Moreover, we propose that at low temperature, excited  $F^{+*}$  states decay back to ground  $F/F^+$  states leading to little occupancy of these states. Increasing the temperature impedes the decay from the excited to the ground states, leading to an increase in the occupancy of these states. This would in turn explain both the reduction of the luminescence peak related to the  $F^{+*} \rightarrow F^+$  recombination (Figure 4.2) as well as the increasing weight of the  $F^{+*}$  centers on the magnetotransport properties (feature at 0.7 eV in Figure 4.10). We'll discuss later why this picture is not realistic.

**Other defect states:** According to this model and to the potential landscape proposed in Figure 4.3, ground  $M$  centers as well as excited  $F^*$  states located at 0.4 eV below and 1.6 eV above  $E_F$  should also impact devices' magnetotransport properties. We suggest that subtle changes in the presented datasets might imply the presence of these states. According to us, the low temperature spectral width of the TMR thermal drop shown in Figure 4.9 is 0.9-1.6 eV at  $T = 50$  K implies the presence of an additional state at higher energies and could possibly reflect the impact of  $F^*$  centers. Secondly, it can be seen that the bias positions of  $\hat{I}_{rel}$  peaks and relative TMR thermal decrease (Figure 4.10 (a) and (b)) shift to values below 0.7 eV. This might reflect the impact of  $M$  ground state.

**Discussion:** With this model, in which specific defects states are dominant in specific temperature ranges, we proceed to discuss discrepancies reported in the literature<sup>190</sup>.

First, the low barrier height reported in the literature is explained in terms of tunneling with respect to localized states that effectively reduce the band gap of the dielectric.

It is also suggested that the distinct impact of localized states on P and AP could be induced by the electronic character of the localized state. For example, we know that electrons in the  $F/F^+$  have  $s$ -like characters, while electrons in excited states have  $p$ -like orbitals. If localized states interact more efficiently with evanescent states with similar symmetry, it would change the weight of  $F^+$  and  $F^{+*}$  states on the  $\Delta_1$  ( $s$ -like) and  $\Delta_5$  ( $p$ -like) dominated tunnel current in the MTJ's P and AP states respectively, potentially explaining the lower barrier height in AP than in P.

Finally, it is suggested that  $M$  centers play a crucial role in devices with very high TMR. Indeed, in our paper<sup>190</sup> we suggest that these states lower devices' barrier height to  $\sim 0.4$  eV while promoting coherent tunneling<sup>185</sup>, and thus would yield very large TMR values.

#### 4.3.1.2 Limitations

In this section, we would like to discuss the deficiencies of the aforementioned model.

**Identification of localized states:** First, we remind that our initial interpretation of the PL spectra and the potential landscape of MgO proposed in our paper<sup>190</sup> is in contradiction

with elements in the literature. As it was thoroughly discussed in Section 4.1.2.2,  $F$  and  $F^+$  centers PL are characterized by a single absorption peak at 5 eV and two emission bands at 2.3 eV and 3.2 eV respectively. As it is shown in Figure 4.1, this would result in  $F/F^+$  and  $F^*$  centers located 1.2 eV below and  $\sim 1.2$  eV above midgap respectively. However,  $F^{+*}$  centers would be  $\sim 2.1$  eV above midgap and not 0.7 eV as suggested in our initial interpretation<sup>190</sup>. This makes the whole interpretation in term of increasing weight of  $F^{+*}$  on tunnel current irrelevant. In fact, the detailed bibliography made on the optical activity of oxygen vacancies in MgO (see Section 2.4.3) suggests that our PL spectra are characteristic of  $M$  centers, whose energy position in the gap is not known precisely.

Moreover, the fact the peaks in  $\hat{I}_{rel}$  are actually located 1.2 higher in energy than the barrier height<sup>211</sup> is not addressed in our paper<sup>211</sup>. We also discussed the fact that the relative energy position between the ground and excited states cannot be determined with PL absorption and emission bands only. This further impedes the possibility to compare and relate peaks in the magnetotransport dataset to peaks in the PL spectra. In light of these new elements, it is not possible to unambiguously identify the impact of a specific defect population on magnetotransport properties, and the description in terms of tunneling with respect to  $F/F^+$  and  $F^{+*}$  states becomes irrelevant.

**Impact of temperature:** Another inconsistency concerns the effect of temperature on the ground and excited  $F^+$  centers. Indeed, we state that increasing the temperature impedes the  $F^{+*} \rightarrow F^+$  recombination process, and result in a larger occupancy of the  $F^{+*}$  excited state<sup>190</sup>. However it is difficult to conceive that an increase of temperature, that typically increase the energy of electrons by tenth of meV, would result in the change of occupancy between  $F^+$  and  $F^{+*}$  centers that are separated by more than 3.3 eV.

**Other crystal imperfections:** In light of the detailed overview given in Chapter 2, it would be surprising that other effects do not play an important role in the current increase and TMR thermal drop. For instance it is well established that interface disorder, Boron diffusion in the barrier (that most probably occur in our MTJs)<sup>124–126</sup>, misfit dislocations<sup>212</sup>, grain boundaries<sup>213</sup> and other type of defects can result in localized states and might strongly impact devices performance. We remind that our polycrystalline MgO thin films are sputter deposited and most probably contain several of the aforementioned imperfections. In this sense, peaks in  $\hat{I}_{rel}$  might actually be the convolution of many thermally activated processes and do not necessarily yield the energy position of a particular defect population.

**Impact of double oxygen vacancies:** Finally, we would like to discuss the prediction that  $M$  centers actually play a crucial role in MgO based MTJs. Based on a theoretical work of McKenna and Blumberger<sup>185</sup> it is supposed that  $M$  centers would result in a barrier height of  $\sim 0.4$  eV but still promote coherent tunneling and high TMR ratios. In this theoretical paper, discussed in Section 2.4.3.4, McKenna and Blumberger calculate the electrical properties of two adjacent  $F$  and  $F^+$  centers and shows that an electron of the  $F$  center is actually delocalized on both defects site. Now, in order for  $M$  centers to promote coherent tunneling in a CoFeB/MgO/CoFeB MTJ, it would require a very specific arrangements of  $F$  center, i.e. they should be aligned in a specific direction in a straight line across the whole MgO layer, configuration that seem very unlikely.

Moreover, we remind that in MgO based MTJs, TMR is due to the symmetry filtering

effect. In order for this effect to occur, both electrodes and the oxide layer have to be crystalline (to some extent). Any deviations from the perfect crystal should decrease the effectiveness of the effect and reduce TMR. It makes no doubt that the effect of  $F$  centers is detrimental, because they break the symmetry of the crystal and introduce scattering centers. Now, in order to create  $M$  centers, one has to increase the concentration of  $F$  centers. It seems very unlikely, or least very counter-intuitive, that increasing  $F$  centers in order to create  $M$  centers would yield higher TMR.

One possibility to obtain high TMR is that the conduction channel opened by  $M$  centers is strongly spin polarized. This suggest that (i)  $M$  centers actually conserve the spin and the symmetry of tunneling electrons and that (ii)  $M$  centers effectively filter the  $\Delta_5$  electrons that dominate the AP conduction channel, similarly to the symmetry filtering effect. Although it is possible, there are no experimental nor theoretical evidences that support either of these two points.

### 4.3.2 Extended dataset

In this section, we would like to briefly discuss extended dataset measured after the upgrade of our magnetotransport experiment (see [Section 3.2.2.1](#)). After the upgrade, the base temperature accessible to the system dropped from 33 K to 16 K. We measured I-V characteristics for both P and AP magnetic states between  $T = 16$  K and  $T = 300$  K with steps of  $\Delta T = 3$  K. We used the same data treatment that we used in the previous section, i.e. we computed  $\hat{I}_{rel}$  for both P and AP using [Equation \(4.1\)](#). At each temperature, the TMR was computed and the relative TMR drop was calculated using [Equation \(4.3\)](#). Again peaks amplitude and position were extracted and are plotted separately.

Figure [Figure 4.11\(b\)](#) plots  $\hat{I}_{rel}$  peaks position and amplitude for both P and AP magnetic states for positive applied bias voltage. In order to calculate  $\hat{I}_{rel}$  (see [Equation \(4.1\)](#)) we used a  $\Delta T$  of 12 K in order to circumvents noise issues.  $TMR_{rel}$  and related peaks position and amplitude calculated using  $\Delta T = 12$  K are shown in [Figure 4.11](#) panels (a) and (c), respectively. Since we used  $\Delta T = 12$  K, the first temperature plotted in these figure is  $T = 28$  K. This is not much lower that the previous dataset, but allows to get a better signal to noise ratio.

From figure [Figure 4.11\(a\)](#) and (c), we can clearly distinguish a third temperature range that wasn't visible before. In the  $28 \text{ K} < T < 60 \text{ K}$  temperature range, the peak amplitude of the feature located at  $V = 1.2 \text{ V}$  increases with increasing temperature. The TMR thermal drop induced by this feature then decreases in the  $60 \text{ K} < T < 90 \text{ K}$  temperature range. This strongly suggest that the 1.2 V peak has a well defined temperature range, i.e other intrinsic or extrinsic features should be visible at lower temperatures.

Besides, from panel (b) we can also clearly see the onset of the impact of the feature located at  $V = 1.2 \text{ V}$ . But we can also better determine where the TMR decrease comes from. In general, the  $\hat{I}_{rel}$  peak amplitude, i.e. the current increase due to an additional thermal energy, is larger in AP than in P. This effectively reduce the tunnel current asymmetry between the P and AP conduction channels and the ensuing TMR. Additionally, we can see that the TMR decrease around  $V = 1.2 \text{ V}$  seen in [Figure 4.11](#) is due to an increase of current of the AP conduction channel. Indeed, the  $\hat{I}_{rel}$  peak position in AP rapidly in-

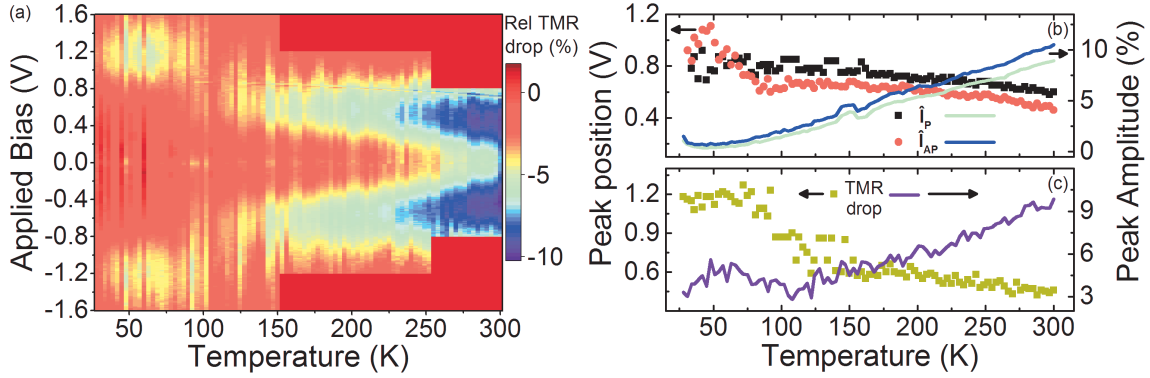


Figure 4.11: **Extended dataset of the magnetoresistive properties in the (V,T) parameter space:** (a) 2D color map of the TMR relative thermal drop in the (V,T) parameter space, (b) peak maximum position and amplitude extracted from  $\hat{I}_{rel}$  for both magnetic states and (c) peak maximum position and amplitude of TMR relative thermal drop. Extended dataset measured between 16 K and 300 K.

creases to values close to 1.2 V in the  $28 \text{ K} < T < 50 \text{ K}$  temperature range, concurrently to the TMR thermal drop amplitude within the same temperature range. The AP  $\hat{I}_{rel}$  peak position then monotonously decreases and falls below the peak position in the P channel. At  $T = 80 \text{ K}$ , the peak position of AP stabilizes and marks the onset of the impact of the feature located at 0.7 V. Conversely, the  $\hat{I}_{rel}$  peak position of the P channel varies more smoothly.

Finally, we can see that both  $\hat{I}_{rel}$  peaks position and the maximum thermal drop peak position decreases with increasing temperature. At 300 K, the TMR thermal drop is maximum at 0.4 eV and the TMR thermal drop amplitude continues to decrease linearly with increasing temperature. Following our initial interpretation<sup>190</sup>, this would be ascribed to  $M$  centers. However, contrary to the prediction that  $M$  centers may promote coherent tunneling and should yield high TMR, the TMR is actually greatly reduced. There are no signs of resilient TMR, i.e. a decrease or a slow down in the decrease rate of the TMR thermal drop.

In summary, this extended dataset suggest that the feature located at 1.2 V has a well defined temperature range. It also stress the need to perform similar measurements at lower temperatures.

### 4.3.3 Alternative interpretations

Given the detailed overview made in Chapter 2, it is interesting to investigate other possible explanations to our interesting magnetotransport results.

**The effective mass of electrons in MgO:** As it was already discussed in this thesis, the low barrier height of MgO thin films extracted from I-V characteristics was puzzling (typically 1 eV). Indeed, independent optical<sup>186</sup> and STM<sup>85,187,188</sup> experiments determined the band gap of MgO to be 7.8 eV in the bulk and in thin films. This discrepancy could

be partially explained by the fact that in MgO, the effective mass of  $\Delta_1$  electrons is 0.37 times that of free electrons<sup>191,192</sup>. Using this value yield a barrier height of about 1.4 eV, that would be compatible with the 1.2 eV peak observed in our magnetotransport dataset.

As we mentioned before,  $\hat{I}_{rel}$  peaks can actually represent the convolution of several thermally activated processes. This is most probably the case because the resolution of  $I(V)$ s and  $\hat{I}_{rel}$  is poor and do not allow to precisely identify the impact of the various localized states (or other thermally activated processes).

Below 80 K, the  $\hat{I}_{rel}$  and TMR thermal drop peaks at 1.2 eV could reflect the impact of this reduced barrier height on tunnel transport. Above 80 K, extrinsic features (e.g. various localized states) start to impact the tunnel current and dominate  $\hat{I}_{rel}$  and TMR thermal drop but cannot be distinguished due to the poor resolution of the  $\hat{I}_{rel}$  method. This explanation is limited in several ways:

1. The effective mass of  $\Delta_1$  states should impact the parallel conduction channel only because the related conduction channel is closed in the AP channel. However, our extended dataset shows that the 1.2 eV feature mostly impacts the AP channel.
2. STM and CT-AFM (contact mode) experiments established that the gap of MgO is close to the optical gap of 7.8 eV<sup>188,214</sup>. Moreover, these studies establish the presence of pinholes where the gap is strongly reduced and ascribe their presence to oxygen vacancies.
3. The barrier height is an intrinsic feature of the MgO barrier, as such its impact on the electrical properties should be visible at low temperatures. However, our extended dataset strongly suggest that the 1.2 eV feature disappears below 28 K.

**Density of states effect:** In Section 2.2.1.2 we discussed in detail the impact of density of states features on tunnel current. In particular, we emphasized that around  $V \sim 1$  V of applied bias the  $\Delta_1$  channel is opened in the AP conduction channel. This result in a strong increase of the tunnel current in the AP magnetic configuration accompanied by a strong reduction of the TMR at this precise bias voltage. Although this explanation is very appealing because it explains why the AP conduction channel is impacted and why P not, it also has some limitations listed hereafter:

1. Similarly to the MgO barrier height, DOS effects are also intrinsic features of the electrodes and their impact is expected to be visible at lower temperatures.
2. Our discussion of DOS features concerned Fe/MgO/Fe MTJs. In our case, after the annealing step, we expect to have an alloy of CoFe at the interface with MgO. More precisely  $\text{Fe}_{0.5}\text{Co}_{0.5}$ . Several works<sup>101,102</sup> suggest that the minority  $\Delta_1^\downarrow$  lies closer to the Fermi energy in  $\text{Fe}_{1-x}\text{Co}_x$  alloys and thus that the opening of the  $\Delta_1$  conduction channel in the AP magnetic state should occur at lower bias voltages. However, the precise composition of the alloy at the interface of our devices is not known.

Here, similar measurements at lower temperatures and a better knowledge of the interface  $\text{Fe}_{1-x}\text{Co}_x$  alloy composition would help to confirm or infirm this model with certainty.

## 4.4 Conclusion and perspectives

In this chapter, we presented photoluminescence spectra as well as bias and temperature dependent experiments measured on CoFeB/MgO/CoFeB MTJs.

We used an experimental technique in order to determine the effective barrier height felt by tunneling electrons in our device. This technique is free of the deficiencies related to fitting techniques but is limited by a poor resolution in both  $V$  and  $T$  parameter space. Our magnetotransport dataset clearly shows that the potential landscape felt by tunneling electrons is modified when the temperature is increased. Our goal was to identify the impact of specific populations of localized state by comparing the magnetoresistive measurements to photoluminescence spectra measured on our rf-sputtered MgO thin films.

However, the excitation wavelength used in our PL experiments was not appropriate to excite the  $F/F^+$  states that were of interest. Instead, double oxygen vacancies, or  $M$  centers, were excited. Unfortunately,  $M$  centers are not investigated as much as  $F$  states, and their absorption and emission peaks are not unambiguously identified. Additionally, we didn't clearly understand the optical activity of localized states in crystals. Although our PL spectra have a strong temperature dependence, both predicaments preclude the possibility to compare or relate optical and electrical dataset and clearly identify the impact of localized in our magnetotransport dataset as initially desired.

We also discussed two alternative explanations as well as their limitations. The Impact of DOS features at low temperature is appealing because it explains why the 1.2 V feature impact the AP conduction channel only.

The initial goal of the project was to unambiguously identify the impact of specific localized states. Obviously, our goal is not achieved. In the following, we would like to discuss several points in our approach that can be improved.

First, both the optical activity of  $F$  and  $M$  centers should be carefully investigated with temperature dependent and time resolved photoluminescence experiments using appropriate photon energies. Both absorption and emission band have to be investigated with attention.

Moreover, we saw that many effects can result in localized states and impact the tunnel current in our junctions. This is especially the case for exchange-biased MTJs with CoFeB electrodes. Indeed, light elements present in the antiferromagnetic layer can easily diffuse across the heterostructure. Similarly, during the post annealing step necessary to pin one of the electrode and crystallize both interfaces, CoFe is created at both interfaces and Boron might diffuse into the MgO barrier. Interface disorder, grain boundaries in polycrystalline MgO, misfit dislocations and other crystal imperfections or impurities can result in localized states. In order to identify the impact of specific defects, systematic studies of the electrical properties of MTJs (using the same approach as we did in this chapter) as a function of some parameter of the system can be considered. In this respect, more detailed characterization of the sample should also be carried.

Finally, more powerful methods than simple  $I(V)$ s should be tried. For instance, time-resolved electrical measurements could be used in order to characterize the dynamic related to localized states, or measurements in the frequency domain.



# Optical excitation of localized states

## 5.1 Introduction

In the preceding chapter, we attempted to describe the transport properties of CoFeB/MgO/CoFeB magnetic tunnel junctions in terms of electrons tunneling with respect to a specific population of localized states. Our approach is based on an experimental technique that allows to directly extract the devices' barrier height from temperature and bias dependent magnetotransport experiments. The detailed investigation of the dataset revealed the peculiar temperature dependence of the effective barrier height. This temperature dependence underscores the impact of localized states at specific bias voltages and in precise temperature ranges.

In order to identify the specific defect population responsible for these changes in the electrical properties of our MTJs, we tried to compare photoluminescence spectra and magnetotransport experiments. However, after a detailed analysis, we revealed a misconception concerning our understanding of the optical activity of point defects in MgO. More precisely, we showed that the photoluminescence of our rf-sputtered MgO thin films was not characteristic of  $F/F^+$  centers and concluded that our initial model<sup>190</sup> was not consistent.

In our initial model, two distinct temperature ranges are distinguished. Within  $33\text{ K} < T < 80\text{ K}$ , the changes induced by thermal energy are maximum at 1.2 V and ascribed to the impact of ground  $F/F^+$  states located  $E - E_F = -1.1\text{ eV}$  below the Fermi energy. With increasing temperature, an additional feature, that is located at 0.7 V, starts to impact the electrical properties and eventually dominates above  $T = 80\text{ K}$ . This mechanism is ascribed to the increasing weight of the excited  $F^{+*}$  states, located  $E - E_F = 0.7\text{ eV}$  above  $E_F$ , on tunnel current. To briefly summarize, we supposed that the temperature dependence of the magnetoresistive properties was caused by the occupancy switchover from the ground  $F/F^+$  to the excited  $F^{+*}$  states.

All the experiments presented in this chapter are based on the erroneous interpretation of PL spectra. Based on our initial model, our aim was to craft the potential landscape of MgO, and in a sense modify the effective barrier height felt by tunneling electrons, by optically modifying the population occupancy of localized states. In order to change the population of defects, we tried to use photons with an energy corresponding to the energy difference between ground and excited states of a specific population. The changes induced by the optical excitation on the barrier properties were simultaneously probed with bias and temperature dependent magnetoresistive experiments. The experiments involved

in this chapter are similar to that of the preceding chapter except that, in addition to the temperature and bias degrees of freedom, the optical degree of freedom was concurrently explored.

In order to promote the ground state of a specific defect population to its excited counterpart, we used photon energies given by peaks in our photoluminescence (PL) spectra. However, from our detailed discussion of the excitation and recombination processes of point defects in MgO (see [Figure 2.27\(b\)](#)) we know that (i) excitation and relaxation processes are always from relaxed to unrelaxed states (Franck-Condon principle) and thus (ii) that the energy of PL emission bands (characteristic of the recombination from excited to ground state) cannot be used to induce the reverse process, i.e. excite electrons from the ground to the excited state. It is thus clear that our attempt to change the defect population occupancy is not achievable.

We didn't clearly understand the optical activity of point defects when these experiments were made and although results presented in this chapter are negative, they will be presented nevertheless. We'll see that our attempts failed not only because of the aforementioned lack of knowledge concerning point defects but also because of other fundamental limitations in our approach. These limitations should be carefully considered in the perspective of future experiments, in which photons with appropriate energy should be used.

Similarly to the previous chapter, we'll first present the results from the point of view of our original ideas. In the first part of this chapter, we'll see that initial measurements could be explained by two models. The first one suggests the excitation of electrons from the ground to the excited state of a defect, but also the interaction between the electric field of linearly polarized photons and the anisotropic charge distribution of Bloch states with specific symmetries. The second one involves the effect of heating due continuous light excitation. While the former effect could result in interesting photonic applications, the second one is trivial.

Secondly, we'll try to discriminate which of these two models is relevant. In order to do so, we performed similar experiments using different photon energies in order to excite different defect populations. These measurements show that all the photons energies used in this thesis (ranging from 0.8 eV to 3.05 eV) have the same effect on magnetoresistive properties and strongly suggest that the first model is irrelevant. Additionally, we solved the Fresnel equations for our heterostructures and showed that laser-induced heat could qualitatively explain our dataset.

## 5.2 Initial results and models

### 5.2.1 Experiment

As it was mentioned earlier, the deficiencies of our model developed in [Chapter 4](#) were not known before the writing of this manuscript. In this model, electrons are not tunneling with respect to the barrier intrinsic properties, but with respect to localized states such that that potential landscape felt by tunneling electrons is defined by the energy po-

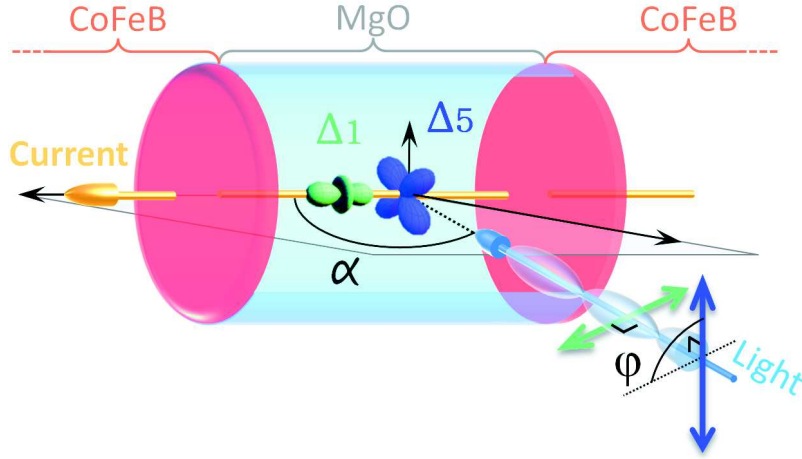


Figure 5.1: **Geometry of optical excitation:** A current with dominant  $\Delta_1$  or  $\Delta_5$  electronic symmetry tunnels between electrodes (red) across MgO (transparent blue). The photon impinges the device at an angle  $\alpha$  relative to the MTJ normal. The angle between the direction of junction current  $I$  and the light's electric field is denoted  $\phi$ .

sition of these localized states. We then suggested that the temperature increase induced a change in the defect population occupancy from the ground  $F/F^+$  to the excited  $F^{++}$  states, effectively modifying the potential landscape felt by tunneling electrons. The aim in this chapter was to induce this population change optically.

Being able to optically modify the population occupancy of defects would allow to tune the barrier height that governs the electrical properties of the device. This could result in interesting applications in photonic or opto-electronic.

In order to optically excite our devices, we used the same experiment as in the previous chapter (see [Chapter 4](#)) which is also described in [Section 3.2](#). The presence of optical windows on the skirt of the cryostat allow optical access on the device. Our optical line consists of various laser sources, a Glan-Taylor polarizer to absolutely define the plane of linear polarization and further enhance the polarization ratio, a zero-order half-wave plate mounted on a motorized rotation stage and a mechanical shutter to obstruct the laser beam as needed. Finally, a plano-convex lens focused the laser beam onto the sample. The waist of each focused laser beam when focused onto the sample was determined along two directions for each laser source by moving a knife-edge along the plane of incidence of the laser beam while monitoring the transmitted power.

The experimental geometry is schematized in [Figure 5.1](#). We consider linearly polarized light impinging at a laser angle  $\alpha$  relative to the MTJ normal and with an azimuthal angle  $\phi$  between the direction of junction current  $I$  and the light's electric field.

In order to ensure optimal optical excitation of the MgO barrier, we proceeded to two modifications compared to devices investigated in the preceding chapter: (i) the top electrode and the capping layers atop the MgO barrier were made as thin as possible. Devices measured in this chapter have the following stack Ta(5)/Co(10)/IrMn(7.5)/FeCoB(4)/

MgO(2.5)/FeCoB(2.5)/Ta(1)/Pt(1) (numbers represent layers thickness in nanometer) and (ii) we modified our technological process in order to define circular openings atop the MTJs in the top technological electrode (see Figure 3.5).

## 5.2.2 Basic magneto-electric properties

Because we modified our technological process, we first made sure that these changes didn't impact the devices' properties. In particular, the inhomogeneous electrical contact to the MTJ pillar could be suspected of generating an inhomogeneous current injection that would alter magnetotransport properties<sup>215,216</sup>. To verify this point, we compared the magnetotransport response of MTJs on the same chip with and without optical opening. Not only were the RA products at  $V = 10$  mV and  $T = 300$  K similar for these two MTJ designs, but essential characteristics such as the bias dependence of TMR remain unchanged (see Figure 5.2 panel (a) and inset of panel (b)). In this sense, we conclude that the optical access provided by the hole in the top technological electrode does not affect the outcome of our magnetotransport study.

To optically address the MTJ, we use the resistance of the junction itself. In a first step, we roughly align the laser beam onto the MTJ thanks to a CCD camera trained onto the zone of interest. Then we use a two-axis motorized displacement stage to align the MTJ onto the laser beam. Figure 5.2 panel (b) presents the example of aligning the 2.6 eV source by following the evolution of resistance for  $V = 10$  mV and  $T = 33$  K during the two-axis displacement sweep. Repeating this process allows us to align the laser spot and the junction with a precision of  $10\ \mu\text{m}$ . Upon changing temperature, the MTJ's absolute coordinates are dynamically corrected through motor control to account for a calibrated thermal dilation of the cryostat (see Section 3.2.2.2).

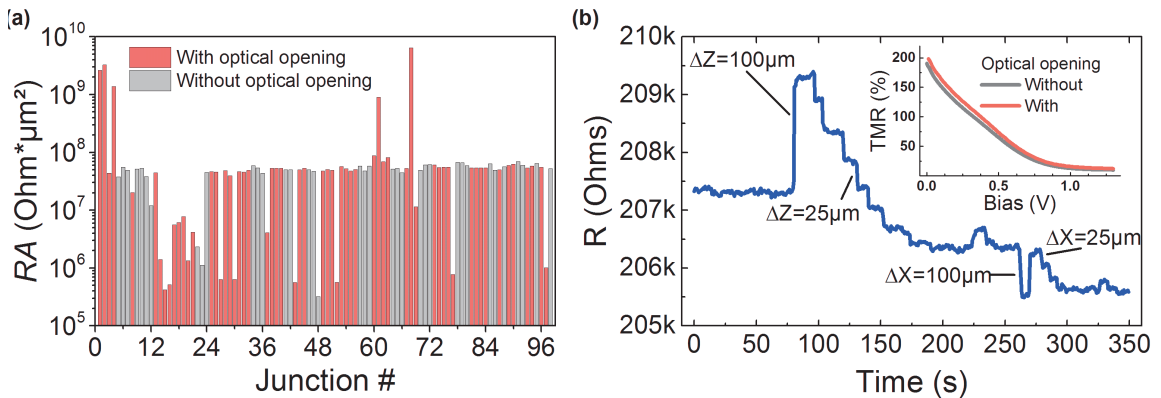


Figure 5.2: **Basic magneto-electric properties and alignment procedure:** (a) RA product of MTJs with and without optical opening on the same chip. (b) Examples of aligning the 2.6 eV source by following the evolution of resistance for  $V = 10$  mV and  $T = 33$  K during the two-axis displacement sweep. The inset of panel (b) plots the bias dependence of TMR for MTJs with and without optical opening.

## 5.2.3 Bias and temperature dependence of optically excited devices

### 5.2.3.1 Impact of 3.05 eV p-polarized light on magnetotransport

We first investigated the impact of shining continuous 3.05 eV linearly polarized light. This energy corresponds to the luminescence band induced by the  $F^* \rightarrow F$  recombination process (see Figure 4.3). Following our initial understanding of the optical activity of point defects, we wanted to use photons with the same energy in order to induce the reverse process, i.e. the  $F \rightarrow F^*$  excitation process.

Figure 5.3 plots the optical absorption of our 2.5 nm thick MgO and confirms that the dielectric layer absorbs photon at 3.05 eV. However, from our discussion on the optical activity of MgO we know that the  $F \rightarrow F^*$  cannot be promoted with 3.05 eV photons and consequently the 3.05 eV absorption has to be ascribed to another excitation process. An important point to note is that there are no absorption band reported at this energy in pristine MgO crystal, this strongly suggests that this particular absorption band is specific to our sputtered thin films.

Our approach is very similar to that of the previous chapter. We measured I-V characteristics from 16 K to 300 K with steps of  $\Delta T = 3$  K for both P and AP magnetic configurations. Additionally, for each temperature, we acquired the same I-V characteristics while exciting our device with linearly polarized light.

In order to probe the impact of optical excitation on the devices' magnetoresistive properties, we use Rottländer's approach except that instead of computing the difference between I-Vs measured at different temperatures, we do so between I-Vs measured with and without light excitation:

$$\Delta I_\sigma(V, T) = \left( \frac{I_{ON}(V, T)}{I_{OFF}(V, T)} - 1 \right) \times 100 \quad (5.1)$$

where  $\sigma$  represents the device magnetic state (P or AP),  $I_{ON}$  and  $I_{OFF}$  are I-Vs measured with and without light excitation, respectively. Moreover, at each temperature the TMR is

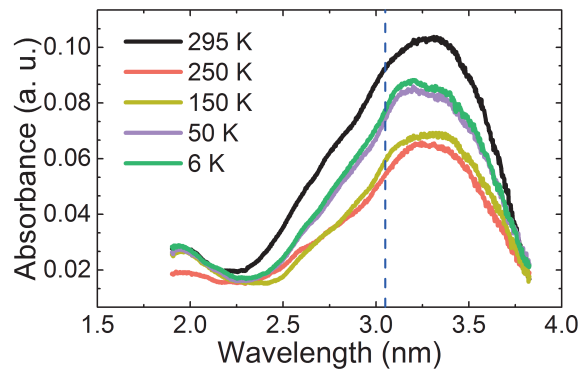


Figure 5.3: **Optical absorption of a 2.5 nm-thick MgO layer:** Energy-dependent absorbance of a 2.5 nm-thick sputtered MgO film.

also computed and the impact of light excitation on TMR is calculated using:

$$\Delta TMR(V, T) = \left( \frac{TMR_{ON}(V, T)}{TMR_{OFF}(V, T)} - 1 \right) \times 100 \quad (5.2)$$

where  $TMR_{ON}$  and  $TMR_{OFF}$  are the TMR of the device with and without light excitation, respectively. Similarly to the impact of temperature,  $\Delta I_{\sigma}(V, T)$  and  $\Delta TMR(V, T)$  are characterized by peaks, the position of which are interpreted as the energy position of optically active localized states relative to  $E_F$ .

We adopt the experimental geometry schematized in Figure 5.1 with light impinging at a laser angle  $\alpha = 45^\circ$  and an azimuthal angle  $\phi = 0^\circ$  (p-polarized light). We plot in Figure 5.4 the impact of shining 3.05 eV photons onto a 25  $\mu\text{m}$  MTJ. Panel (a) plots the 2D color map of the TMR drop induced by light excitation ( $\Delta TMR(V, T)$ ). Panels (b) and (c) plot the peaks position and amplitude of  $\Delta I_{P,AP}(V, T)$  and  $\Delta TMR(V, T)$ .

We immediately note the striking similarities between Figure 5.4 and the dataset presented in the previous chapter that probe the impact of thermal excitation (see Figure 4.11). Indeed, we can see that the  $\Delta I_{P,AP}$  and  $\Delta TMR$  peaks position both follow exactly the same trend as  $\hat{I}_{P,AP}$  and  $TMR_{rel}$  peaks induced by thermal excitation. We can distinguish two feature located at 1.2 V and 0.7 V as well as their well-defined defined temperature ranges. Between  $20 \text{ K} < T < 80 \text{ K}$  the 1.2 V feature dominates. Above 80 K, the second feature, located at 0.7 V, starts to impact the tunnel current. This is supported by the shift of  $\Delta I_{P,AP}$  peaks to lowed bias values (see panel (b)) and the abrupt switchover in the  $\Delta TMR$  peak position from 1.2 V to 0.7 V (see panel (c)). As the temperature increases, the peaks positions monotonously decrease and reach 0.5 eV at room temperature.

The only major difference between the impact of thermal and optical excitation resides in the peaks amplitude in the  $100 \text{ K} < T < 300 \text{ K}$  temperature range. In the case of optical excitation, the peaks amplitude first start to increase between 100 K and 180 K and then decrease up to room temperature (see Figure 5.4). In the same temperature range, the peaks amplitude related to thermal excitation increase monotonously (see Figure 4.11).

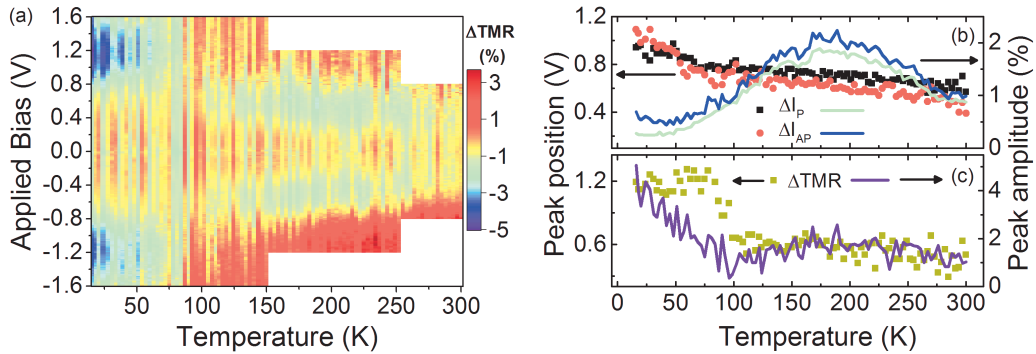


Figure 5.4: **Impact of 3.05 eV linearly polarized light on bias- and temperature-dependent transport properties:** (a) 2D color map of the TMR drop induced by 3.05 eV photons excitation in the  $(V, T)$  parameter space, (b) peaks position and amplitude extracted from  $\Delta I_{\sigma}(V, T)$  for both P and AP device magnetic state and (c) peak position and amplitude of TMR drop extracted from panel (a).

### 5.2.3.2 Impact of varying light's polarization on magnetotransport

We now consider the impact on tunnel transport of varying the polarization of the impinging photons. We use 3.05 eV photons with an angle of incidence  $\alpha = 70^\circ$ . In order to continuously vary the azimuthal angle  $\phi$  between light's electric field and the direction of the current flow in our device (see Figure 5.1), we use a zero-order half waveplate mounted on an automated rotation stage. Given our experimental geometry,  $\phi = 0^\circ$  and  $\phi = 90^\circ$  correspond to p- and s-polarized light, respectively.

For a given temperature, we measure the tunnel current as a function of  $\phi$  for various applied bias voltages. In order to probe the impact of continuously varying  $\phi$  from p to s, we use the same approach as for thermal and optical excitation. In order to probe the current changes upon varying  $\phi$ , we calculate:

$$\Delta I_\sigma^\phi(V) = \left( \frac{I(\phi, V)}{I(\phi = 0^\circ, V)} - 1 \right) \times 100 \quad (5.3)$$

where  $\sigma$  designates the device magnetic state (P or AP). In order to probe changes induced on TMR we compute:

$$\Delta TMR^\phi(V) = \left( \frac{TMR(\phi, V)}{TMR(\phi = 0^\circ, V)} - 1 \right) \times 100 \quad (5.4)$$

In other words, we normalize our dataset to the current of the device when excited by p-polarized photons ( $\phi = 0^\circ$ ).

Figure 5.5 plots the 2D color maps in the  $(\phi, V)$  parameter space of  $\Delta I_P^\phi$ ,  $\Delta I_{AP}^\phi$  and  $\Delta TMR^\phi(V)$  measured at  $T = 33$  K in panels (a), (b) and (c) respectively.

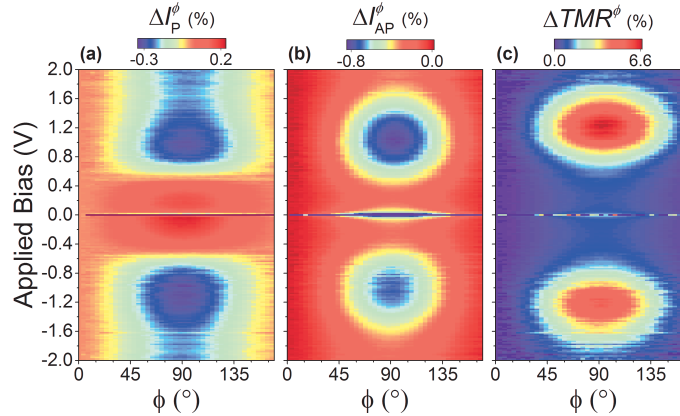


Figure 5.5: **Impact of varying light's polarization on bias- and temperature-dependent transport properties:** 2D color maps in the  $(\phi, V)$  parameter space of the changes induced by continuously varying the polarization of impinging photons ( $\phi$ ) on (a) the tunnel current in the parallel magnetic state, (b) the tunnel current in the antiparallel magnetic state and (c) the TMR. The changes induced on magnetoresistive properties are similar to that induced by thermal excitation, except that the sign are opposite. See text for more details.

In the parallel magnetic configuration (P), we distinguish two bias regions. At low bias, i.e when  $|V| < 0.5$  V, varying photons' polarization from p to s slightly increases the tunnel current of the device. The increase is maximum at  $\phi = 90^\circ$  (+0.23 %). In the high bias region, when  $|V| > 0.5$  V, the current decreases when the polarization is continuously varied from  $0^\circ$  to  $90^\circ$ . The decrease is maximum at  $\phi = 90^\circ$  and  $V = 0.95$  V (−0.34 %).

In the antiparallel magnetic state, the tunnel current decreases in the whole bias range as  $\phi$  is increased from  $0^\circ$  to  $90^\circ$ . The decrease is maximum at  $\phi = 90^\circ$  and  $V = 1.05$  V (−0.8 %).

Finally, varying from p to s-polarized light increases the TMR in the whole bias range. The maximum of TMR increase is located at  $\phi = 90^\circ$  and  $V = 1.22$  V in the  $(\phi, V)$  parameter space.

Although these result look somewhat different from the result presented until now, they are in fact very similar. Indeed, the bias position of the maximal current decrease in P and AP is 0.95 V and 1.05 V, respectively. These values correspond very well with the peaks position of  $\hat{I}$  and  $\Delta I$  induced by thermal (see Figure 4.11) and optical excitation (see Figure 5.4) in the same temperature range. Similarly, the maximum TMR increase is located at a bias  $V = 1.22$  V, precisely the bias position of peaks minimum in  $\Delta TMR_{rel}$  and  $\Delta TMR^\phi$ . The only difference compared to thermal and optical datasets presented previously resides in the sign of the current change induced by light's polarization. While the current is increased when the temperature is increased or when the device is optically excited, it decreases when the polarization is changed from p to s. Similarly, the TMR is decreased when the device is thermally or optically excited while it is increased when the polarization is switched from  $0^\circ$  to  $90^\circ$ .

At first, we didn't have any physical explanation for these differences. That's why we proposed a model based on the interaction between light's electric field and the anisotropic charge distribution of Bloch's states in our device. We then found out the that reflection, transmission and absorption of p- and s-polarized light are not the same when the angle of incidence is not normal to the sample's surface. Both models will be described in the following section.

## 5.3 Discussion

To briefly summarize, the impact of optical excitation on tunnel current is very similar to changes induced by thermal excitation. Only two points could not be explained at first: (i) while peak positions are similar for thermal and optical excitation, the amplitude of the tunnel current increase as well as the amplitude of the TMR decrease don't have the same behavior (see Figure 5.4) and (ii) there was no physical process, to our knowledge, that could explain the current change induced by varying the polarization of impinging photons (see Figure 5.5).

In this section, we'll detail two models that could explain these experimental observations.



nels. When  $\Delta_1$  photo-electron are promoted, it will have little effect on the P conduction channel because the related conduction channel is already opened. However, the impact of  $\Delta_1$  photo-carriers will have more effect on the AP conduction channel because this channel is normally closed. This picture of defect-mediated electron-phonon interaction explains why the tunnel current decreases and TMR increases when the polarization of impinging photons is switched from p ( $\Delta_1$  photo-carriers) to s ( $\Delta_5$  photo-carriers).

The main limitation to this model concerns the optical excitation. We know that the photon energy used in our experiment cannot induce the desired photo-excitation process, i.e. the  $F \rightarrow F^*$  transition. Indeed, we saw that electrons trapped in localized states interact with the crystal structure of MgO (see Section 2.4.3) and that the excitation and recombination process are not symmetric. In other words, it is not possible to use the energy of emission band of PL spectra, that result from the recombination between excited and ground states, in order to induce the reverse process.

Nevertheless, an easy way to test this model is to excite MTJs with photons energy related to another excitation process, or photons for which the MgO barrier is transparent. We carried that kind of experiments, they will be briefly discussed in Section 5.3.4.

We remind that we first proposed this model because we couldn't consistently explain our results otherwise. We soon noticed that a fundamental property of optics could explain our dataset in terms of heat. This interpretation will be detailed below.

### 5.3.2 Model II: Heat

When light encounters an interface between media of differing refractive indices, it can be reflected, refracted or absorbed. The angles between the incident, reflected and refracted rays are given by the well-known Snell–Descartes law. Additionally, the Fresnel equations allow to compute the proportion of light that is reflected and refracted at the interface. Moreover, in multilayer planar stacks (as it is the case for our samples) the light can make multiple reflections between parallel surfaces and induce interferences effects that will depend on impinging light wavelength. It is well established that the reflection, transmission and absorption of p- and s-polarized light is not the same when the angle of incidence is not normal to the surface of the sample.

Our second model is based on the Fresnel equations and on the fact that p- and s-polarized photons are not reflected and transmitted with the same amplitude. If we assume that the optical excitation induces some heat in the device, which is suggested by the similarities between thermal and optical dataset (see Section 5.2.3.1), then the heat induced by p- and s-polarized light will not be the same. As a consequence, switching between p- and s-polarization will impact the tunnel current in the same way that thermal excitation would. In order to solve the Fresnel equations for our thin films heterostructure, we used the *tmm* python package<sup>217</sup>. The *tmm* package is based on the transfer matrix method and allows to compute quantities such as the reflected, transmitted or absorbed light intensity.

Figure 5.7 plots the fraction of transmitted and reflected intensity and the local absorption at a given depth in the heterostructure in panels (a), (b) and (c), respectively. All these quantities are computed as unitless fraction of the total incoming power. From panel (a) and (b), we can see that the fraction of refracted and transmitted light is not the same for the

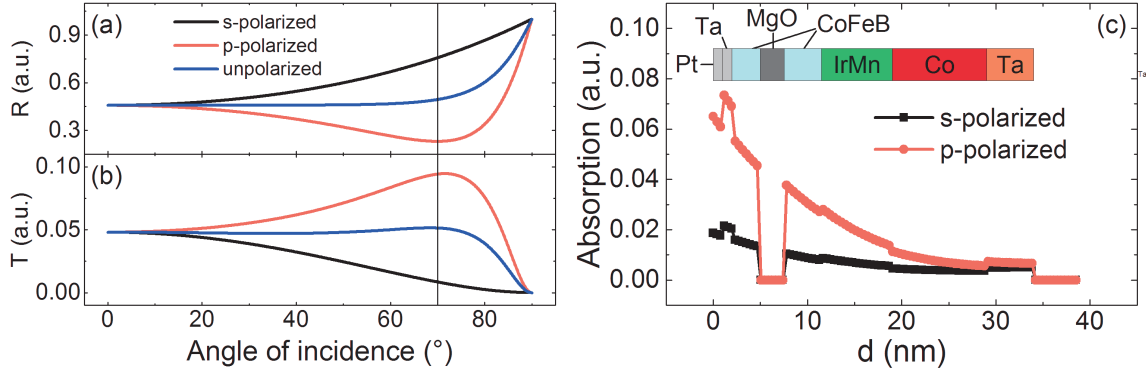


Figure 5.7: **Reflection, transmission and local absorption of 3.05 eV p- and s-polarized light:** The proportion of reflected and transmitted light for both polarization are plotted in panels (a) and (b), respectively. The local absorption as a function of the depth in the multilayer stack is plotted in panel (c). These quantities are computed as unitless fraction of the total incoming power.

two polarizations. More precisely, p-polarized light is less reflected and better transmitted than s-polarized light. We also note that these differences are maximum when the incident angle is close to  $70^\circ$ . This is precisely the experimental geometry we choose when we probed the impact of light's polarization on magnetotransport (see Section 5.2.3.2). Finally, from panel (c) we can see that the p-polarized light is better absorbed than s-polarized light.

In the model considered in this section, we suppose that optical excitation actually heats the sample by a quantity  $\Delta T$ . However, we just discussed the fact that the quantity of p- and s-polarized absorbed by the system is not the same. We can thus argue that the amount of heat induced both polarization is not the same,  $\Delta T_s \neq \Delta T_p$ . More precisely, we saw that p-polarized light was less reflected and better absorbed by the multilayer stack, hence  $\Delta T_s < \Delta T_p$ .

If we now go back to the experiment that probes the impact of light's polarization (Section 5.2.3.2), we can see that switching light's polarization from p to s induces a temperature change  $\Delta T'$ . Since the temperature change induced by p-polarized light is bigger than that of s-polarized photons, switching from p to s actually *decreases* the sample's temperature. We can thus write  $I(\phi = 0^\circ, V) = I(T_s, V)$  and  $I(\phi, V) = I(T', V)$  ( $T' = T_p$  when  $\phi = 90^\circ$ ) and Equation (5.3) used to probe the impact of light's polarization becomes:

$$\Delta I_\sigma^\phi(V) = \left( \frac{I(T', V)}{I(T_s, V)} - 1 \right) \times 100 \quad (5.5)$$

which is exactly the same formula used in order to compute  $\hat{I}$  and probe the impact of thermal excitation (Equation (4.1)). The only difference resides in the fact that  $T_s > T'$  in Equation (5.5), while it is the other way around for  $\hat{I}$ .

Using this model, we can interpret the dataset presented in Section 5.2.3.2 as follows. Switching the impinging photons polarization from p to s actually reduces the heat induced by light's excitation. Normalizing our dataset to the current of the device when excited by

p-polarized light is equivalent to compare I-V characteristics to one measured at *higher* temperature. As a consequence, we expect the impact on tunnel current to be exactly the same that of thermal excitation except that the sign of the induced change on the tunnel current and TMR should be opposite.

From Figure 5.5, we saw that the impact of varying the photons' polarization is maximum at 0.95 V, 1.05 V and 1.22 V for  $\Delta I_P^\phi$ ,  $\Delta I_{AP}^\phi$  and  $\Delta TMR^\phi$  respectively. These values correspond very well to the peak position of  $\hat{I}_P$ ,  $\hat{I}_{AP}$  and the position of the maximum TMR thermal drop located at 0.92 V, 1 V and 1.16 V in the same temperature range (see Figure 4.11). Moreover, we can see that the changes induced on tunnel current and TMR in Figure 5.5 and Figure 4.11 have opposite sign, in agreement with our preceding discussion.

Finally, in order to explain all the changes induced by light excitation, we have to discuss why the amplitude of the peaks maximum induced by light excitation is not the same that of thermal excitation (see Section 5.2.3.1). This point will be detailed in the following section.

### 5.3.3 Estimation of laser-induced heat

In order to get an estimate of the heat induced by optical excitation, we used the the resistance of the technological electrode placed on top of the device (see Figure 3.5). We measured the resistance of the electrode in 4-point mode without optical excitation from  $T = 18$  K to  $T = 300$  K with steps of  $\Delta T = 3$  K. The temperature of the system (Section 3.2.2.1) was then calibrated to the resistance of the top electrode. In order to deduce the heat induced by optical excitation, we monitored the resistance decrease of the top electrode when the laser spot was aligned on the device at each temperature.

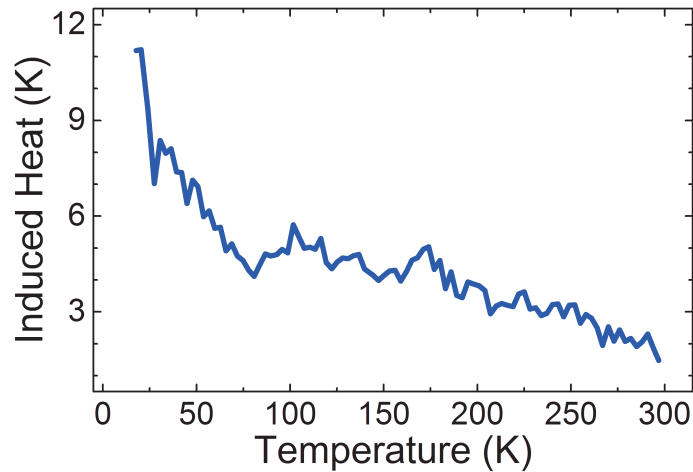


Figure 5.8: **Heat induced by 3.05 eV photons excitation:** Heat induced by laser excitation as a function of the sample's temperature. See text for more details.

From Figure 5.8, we can see that the heat induced by 3 mW 3.05 eV photons excitation is not constant. At  $T = 18$  K, the heat induced by optical excitation is  $\Delta T = 11$  K. As the temperature increases,  $\Delta T$  first decreases rapidly and reaches 4 K at  $T = 75$  K.  $\Delta T$  then

decreases more slowly and monotonously and  $\Delta T = 2$  K at room temperature. Note that we manually verified that this change is not due to the misalignment of the laser spot.

The fact that the laser-induced heat is not linear allows to explain the last discrepancy observed between optical and thermal excitation. The difference between the two dataset resides in that the  $\Delta T$  used in order to probe the impact light is not constant. The fact that  $\Delta T$  decreases with increasing temperature explains the decrease of peaks amplitude in Figure 5.4.

With this last discrepancy between optical and thermal dataset explained, we can consistently explain all the results presented in this chapter in terms of laser-induced heat. In the section below, we'll see that we used various photons energies in an attempt to excite other defect populations.

### 5.3.4 Impact of 0.8 eV photons on magnetotransport properties

In order to definitely affirm the interpretation in terms of optical addressing, we measured similar dataset for various photon energies, that is 0.8 eV, 1.85 eV, 2.33 eV and 2.62 eV. We will first focus on the the impact of 0.8 eV light on the magnetotransport properties of our devices. This photon energy is of particular interest because it doesn't correspond to any optical transition between ground and excited localized states. This is true for both the potential landscape described in this thesis (see Figure 4.1) and the erroneous one initially proposed in our paper<sup>190</sup> (see Figure 4.3).

We plot in figure Figure 5.9 the impact of shining 0.8 eV photons onto a 25  $\mu\text{m}$  MTJ. The quantity plotted are exactly the same that of Section 5.2.3.1 related to the impact of 3.05 eV light. We can see that the impact on TMR as well as the peaks position and amplitude are similar for both wavelength excitation. We can thus conclude with confidence that the impact on tunnel current result from laser induced heat and not optical addressing as

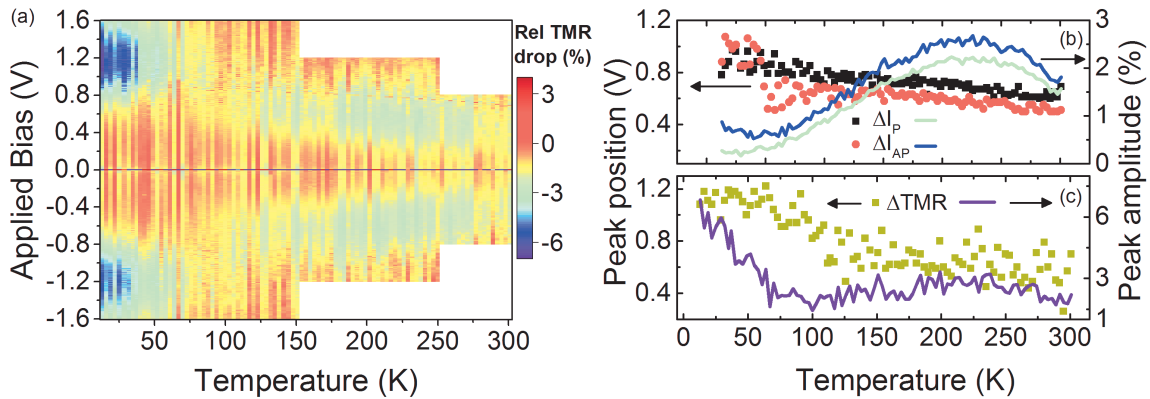


Figure 5.9: **Impact of 0.8 eV linearly polarized light on bias- and temperature-dependent transport properties:** (a) 2D color map of the TMR drop induced by 0.8 eV photons excitation in the  $(V,T)$  parameter space, (b) peaks position and amplitude extracted from  $\Delta I_{\sigma}(V,T)$  for both P and AP device magnetic state and (c) peak position and amplitude of TMR drop extracted from panel (a).

initially proposed.

Finally, we would like to mention that similar datasets that of Figure 5.4 and Figure 5.5 were measured for 1.85 eV, 2.33 eV and 2.62 eV (data not shown). All the results obtained for the various photons energies are characterized by the same features located at 1.2 V and 0.7 V and can be consistently explained by laser-induced heat. Additionally, we tried various experimental configurations. In particular, when the angle  $\alpha$  is reduced to  $0^\circ$  (incident angle normal to the sample's surface) both  $\Delta I_\sigma^\phi$  (V) and  $\Delta TMR^\phi$  (V) are canceled. This is conform to our picture of laser-induced heat because s- and p- polarized light are reflected and transmitted with the same amplitude at this angle (see Figure 5.7), and thus varying the polarization from p to s do not change the sample's temperature.

## 5.4 Conclusion

In this chapter, we attempted to use photons with specific energy in order to promote an electronic transition between ground and excited states of a specific defect population. We first showed that initial results could be explained by two models.

The first model is based on a defect mediated photon-electron interaction. It describes how photo-electrons and Bloch states emerging from the emitting electrode are mixed by the localized state. However, we discussed several limitations of this model, and concluded that it was unrealistic. Moreover, we saw that the thermal and optical dataset were very similar, strongly suggesting that the optical excitation was in fact just increasing the sample's temperature. Two differences in the optical dataset couldn't be explained by the laser-induced heat scenario. More precisely, the peaks amplitude in the case of optical excitation didn't have the same behavior that of thermal excitation. But the main features that couldn't be explained were the changes induced by continuously varying the polarization of light from p to s, and especially the fact that the amplitude of the changes induced on tunnel current and TMR was opposite to that of thermal excitation.

In the second model, we focused on how light propagates in multilayer planar stacks. We solved the Fresnel equations for our thin film heterostructures and showed that p- and s-polarized light are not reflected, refracted and thus absorbed with the same amplitude. Assuming that the optical excitation actually results in heat, we argued that the heat induced by p- and s-polarized light was not the same. Based on this assumption, we resolved the apparent contradiction in the peaks amplitude and showed that the impact of varying the polarization of light is exactly the same that of thermal excitation. Finally, we also estimated the heat induced by optical excitation by calibrating the temperature of the sample to the resistance of the technological electrode atop our devices. We showed that the laser-induced heat was decreasing as the temperature increased. This is expected to effectively reduce the peak amplitude of thermally activated processes in our dataset, and explains why the trend of the peaks amplitude was different in the case of optical excitation.

Our goal in this chapter was to use light as an additional degree of freedom in order change the occupancy of localized states in MgO and to craft the MTJ's potential landscape. Obviously, our attempt failed for two main reasons.

Firstly, we didn't really understand the optical activity of localized states in MgO. For

this reason, we used photons with an energy corresponding to emission bands in the photoluminescence spectra of MgO. However, our detailed discussion of the photoluminescence of  $F$  centers showed that luminescence bands are characteristic of recombination from the excited to the ground states of a specific defect population, and that it was not possible to use photons with the same energy in order to induce the reverse process (see [Section 2.4.3.1](#)). In addition to that, results obtained with the 0.8 eV laser (which is supposed to be transparent to localized states) definitely support the scenario of laser-induced heat.

Secondly, our experimental approach was too naive because we didn't consider basic effects induced by optical excitation (difference between p- and s-polarized light, heat... ). Besides, even if we would have used the appropriate photon energy, we wouldn't have been able to avoid the effect of laser-induced heat. If the experiment is headed toward time resolved pump-probe experiment, with optical excitation as the pump and electrical measurements as the probe, the time resolution of the setup should be lower than the typical timescale of phonon processes. This makes the realization of such experiment challenging because electrically measuring below the nanosecond timescale is very difficult.



# Synchrotron experiments

## 6.1 Introduction

During the timespan of my PhD, I had the chance to work on the newly installed versatile variable temperature insert (V<sup>2</sup>TI) on the DEIMOS beamline at the synchrotron SOLEIL. The V<sup>2</sup>TI was designed to allow electrical access on samples exposed to soft x-rays (see [Section 3.3.2](#)) and offers the possibility to perform *operando* studies. The principle of *operando* studies is to use the capabilities of x-rays to probe some properties of a sample under external stimulus, applied in situ. While usually one has to separate the materials science and device studies, *operando* measurements offer the possibility to probe the devices' properties in real operating conditions.

In this chapter, we'll discuss how we used the capabilities of V<sup>2</sup>TI in order to combine x-ray absorption spectroscopy (XAS) and magnetotransport experiments.

X-ray absorption spectroscopy (XAS) measures the absorption coefficient (or a quantity proportional to the absorption coefficient) of a sample as a function of impinging photon energy. When the energy of photons equals the energy necessary to excite core electrons to available empty states, it results in a sharp increase in the absorption spectra. Because this absorption is related to the excitation of core electrons, XAS is chemically selective, i.e. the energy of impinging photons can be tuned to probe a specific chemical element in the sample. XAS spectra can provide detailed information on the electronic and magnetic properties of a specific atomic species as well as its chemical environment. Moreover, the large brilliance of modern synchrotron facilities makes the technique very sensitive (see [Section 3.3.1](#)).

As it was discussed in [Chapter 1](#), spin dependent tunneling is also extremely sensitive to a subset of atoms in the sample. We saw that the properties of MTJs were very sensitive to the electrode-barrier interfaces. In particular, we discussed the importance of the interface Fe-O bond in Fe/MgO MTJs.

Measuring the magnetoresistive properties of a device (atomic-selectivity) and concurrently probing its material properties with XAS (chemical selectivity) could provide a direct experimental insight on how exactly a subset of atoms influence the device properties.

We'll mainly focus on the experimental realization of the experiment. In particular, we'll see how the magnetotransport bench and the synchrotron control station were interfaced and synchronized. The approach used to process our dataset will also be briefly detailed. In the second part of the chapter, we'll discuss results obtained on our magnetic tunnel junctions. We'll see how interface oxidation impact the performance of our de-

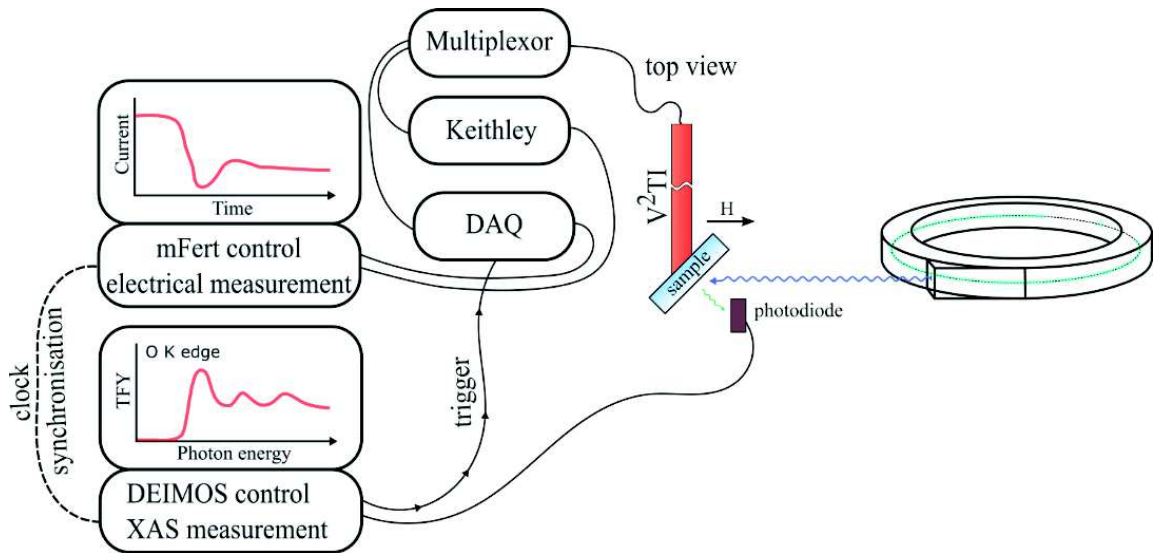


Figure 6.1: **Experimental setup:** X-ray photons interact with an operating device. Simplified schematic of the experimental setup combining the magnetotransport bench and DEIMOS beamline end-station control.

vice, but we'll also discuss changes induced by x-rays on the MgO tunnel barrier from a theoretical point of view.

Results and interpretation discussed in this chapter are presented from the point of view of a recently submitted paper<sup>218</sup>.

## 6.2 Experiment

### 6.2.1 Experimental setup

In order to combine XAS and electrical measurements on magnetic tunnel junctions, we interfaced our *mobile* magnetotransport setup to the DEIMOS beamline control station (see Figure 6.1).

The *mobile* setup (mFert) features the same elements than the regular setup discussed in Section 3.2 and used in the preceding chapters, that is a Keithley 2636 sourcemeter, a multiplexor and an analog/digital input/output board (DAQ). The DAQ is used to control the multiplexor that is designed to protect the sample's devices from the noisy synchrotron environment but also to interface the magnetotransport bench to the DEIMOS beamline.

Due to the complexity of the beamline experimental architecture, we couldn't incorporate the apparatus of the magnetotransport bench directly into the beamline's control program. Instead, the DEIMOS station was programmed to trigger the magnetotransport experiment by sending voltage pulses with specific amplitudes to mFert's DAQ.

In order to relate electrical and XAS measurements, the clock of both experiments were synchronized with the Network Time Protocol (NTP). The electrical and XAS measurements were then related during data analysis by interpolating their values to absolute points

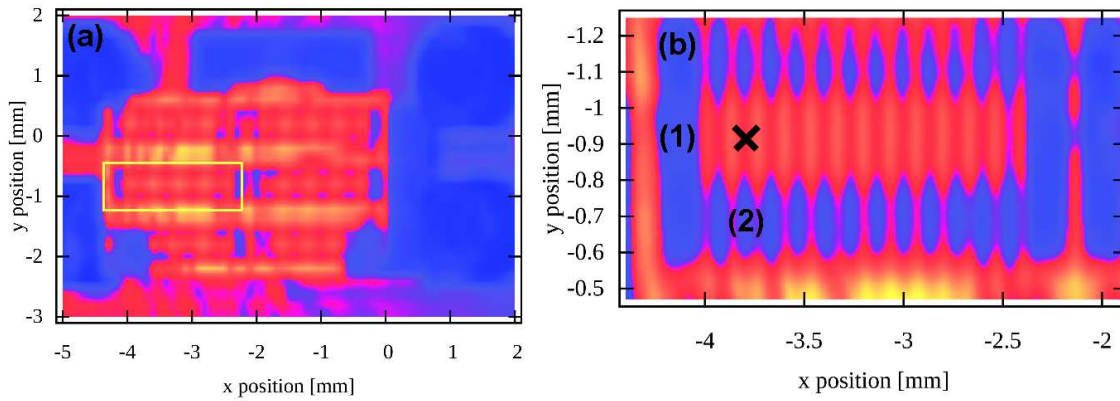


Figure 6.2: **MTJ alignment with the x-ray beam:** Example of mapping a sample containing MTJs using x-ray absorption at 788 eV (Co  $L_3$  edge). (a) Large-scale map of the sample on the chip with the region of interest (containing 20 MTJs) within a yellow rectangle. (b) Fine alignment of the junction with (1) bottom electrode pad, (2) top contact and (black “x”) the exact position of the MTJ of interest. Dark areas represent the regions covered by metal thus with attenuated x-ray absorption.

in time.

The total fluorescence yield (secondary photons emitted by the sample) was measured by a photodiode connected to a NOVELEC MCCE-2 high-sensitivity low-current electrometer. The XAS spectra were systematically normalized to the initial x-ray intensity  $I_0$  measured by a separate electrometer on a gold plated grid located before the end-station.

In order to align the samples under the x-ray beam, the end station is equipped with motors that allow two dimensional displacement in the plane perpendicular to the direction of photons propagation. To precisely align our micrometric size junctions under the x-ray beam, we took advantage of patterned surface of our sample. Indeed, after the last lithography step (Section 3.1.3.4), the surface of our samples present metallic and oxide features. We thus tuned the x-ray energy in order to obtain as much contrast as possible between these two features, and XAS spectra as a function of the sample’s position were measured. Examples of these intensity maps are presented in Figure 6.2. The drawback of this method is the time required to map the entire sample.

We’ll see that similarly to experiments presented in Chapter 5, MTJs can also be aligned by monitoring the device’s resistance change induced by x-ray excitation. This method has the advantage of being much faster than mapping the whole sample. More details about the sample alignment can be found in a separate technical publication on the electrical insert’s capabilities<sup>200</sup>.

## 6.2.2 X-ray absorption reference spectra

Within the sample containing our MTJ devices, oxygen is present not only within the MgO of our MTJ’s tunnel barrier, but also in the form of interfacial Fe oxides, in the

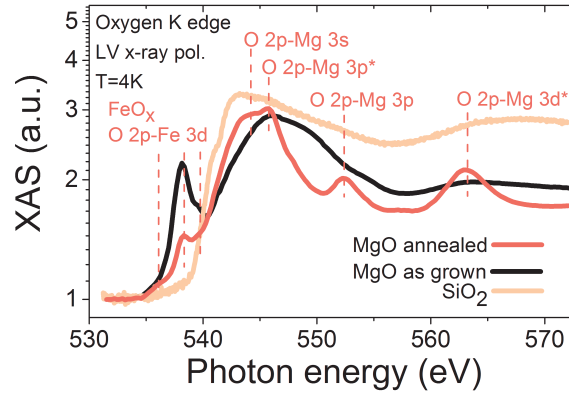


Figure 6.3: **Reference XAS spectra:** XAS O K edge reference spectra of as-grown and annealed MgO, and SiO<sub>2</sub>. The peak identification is based on the literature and reflects the allowed transitions from oxygen 1s core to final states assigned in red<sup>219,220</sup>.

glass substrate and in the dielectric SiO<sub>2</sub> layer that insulates the top and bottom electrodes. Finally, during MTJ technological processing, the MTJ pillar's flanks and lower electrode are exposed to air.

Since we used a larger photon beam to address MTJs than the typical junction diameter of 20  $\mu\text{m}$ , XAS data at the O K edge, which were acquired in fluorescence mode during the transport measurement, reflect all these contributions. Therefore, we separately measured spectra on Glass//Ta(5)/Co(10)/IrMn(7.5)/FeCoB(4)/MgO(2.5) reference samples (with numbers in nanometers) that were either annealed or not, but were not lithographically processed. This allowed us to obtain reference spectra for MgO.

A Glass//SiO<sub>2</sub>(150) sample was measured to obtain a reference for the SiO<sub>2</sub> used to encapsulate our devices. The ensuing reference spectra with the peaks assignment based on available literature are presented in Figure 6.3.

### 6.2.3 Synchronized electronic transport measurement

As it was mentioned previously, the electronic transport measurement across the MTJ was performed while sweeping the photon energy  $E_{ph}$ . This yielded two separate records of current vs. timestamp and photon energy vs. timestamp. Using the timestamp common variable, which was synchronized prior to the measurement using the Network Time Protocol of the synchrotron facility, the records are then merged. We may thus examine the MTJ's current flow as a function of photon energy.

Examples of raw MTJ current while sweeping  $E_{ph}$  across the O K edge are presented in Figure 6.4(a). Additionally, we show in panel (b) how the position of the sample can also be synchronized and used concurrently to the MTJ's resistance to align the sample with precision. The oscillations visible in the normalized XAS spectra arises from equally spaced top electrodes that yield attenuated x-ray absorption (see Figure 6.2).

We find that the MTJ current is directly impacted by the photocurrent generated by x-

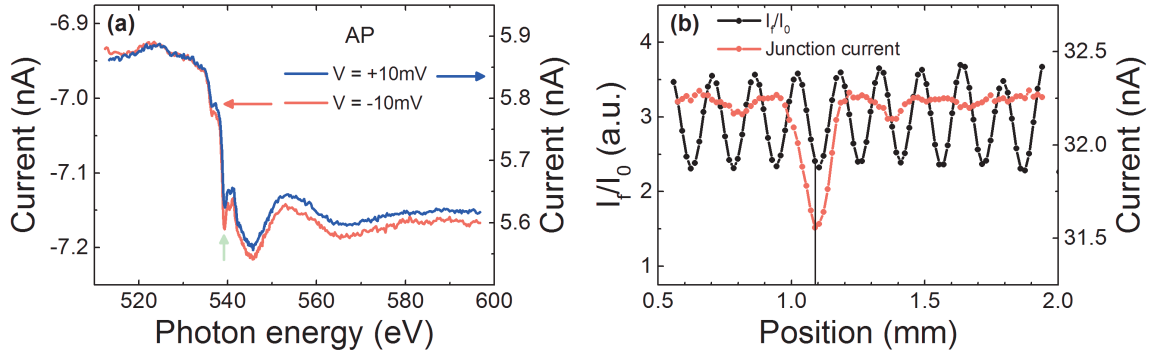


Figure 6.4: **Synchronized measurements:** (a) Raw data of current flowing through the MTJ while sweeping the energy of photons with linear vertical polarization across the O K edge for (left) negative bias voltage  $-10$  mV, and (right) positive bias voltage  $10$  mV. Note a strong variation beginning at  $\sim 545$  eV due to the generated photocurrent, which is of negative sign in both cases. (b) The motors' position and the resistance can also be synchronized and used to align the sample with precision.

ray absorption at the O K edge. To investigate how the device transport is altered, or to investigate pre-edge structures, therefore requires subtracting away the photocurrent. Noting that the photocurrent contributes always in the same direction, we remove its impact by noting that the magnetotransport response of our MTJs is bias-symmetric at low bias (but not perfectly). We acquired two curves for the same bias voltage sign which are then 3pt-smoothed and averaged to reduce the noise level. The acquisition time of a single sweep is 1 h. We repeat the acquisition for the opposite sign of bias voltage and we use the following relation to remove the photocurrent:

$$R(E_{ph}) = \frac{2V}{I_+(E_{ph}) - I_-(E_{ph})} \quad (6.1)$$

where  $V$  is the absolute value of bias voltage and  $I_{+,-}(E_{ph})$  correspond to the photon energy-dependent current flow through MTJ for positive and negative bias voltage. This isolates the effect resulting purely from electronic modifications to the junction's matter while removing the photoelectron contribution to the current across the device. Note that because our MTJ's are not perfectly symmetric to the sign of applied bias voltage, this treatment introduce a systematic error. However, we argue that this introduce at most an offset in the final data, which is not critical to our discussion.

### 6.2.4 Noise management

One of the most challenging experimental aspects of measuring magnetotransport on a beamline is noise management. The complexity of the experimental setup and the electrically noisy synchrotron environment makes studies of such electrostatically sensitive devices as MTJs challenging. We therefore devoted considerable time to reducing electronic noise. First, we improved the cleanliness of the mFert power line using an online

undulator. Care was taken to avoid ground loops, and enhance electromagnetic shielding, between the mFert bench components. These measures resulted in MTJ measurements with  $\sim$  pA noise level. While this can be accomplished within the electrically noisy environment of a synchrotron facility, e.g. when measuring the total electron yield current arising from XAS, doing so for a magnetotransport experiment remains very noteworthy. Future improvements to the DEIMOS beamline may involve improving the shielding of the electrical connections to the samples, and rationalizing the magnetotransport bench implantation onto the beamline so as to reduce cable distances. The error bars of our  $R(E_{ph})$  results are obtained from the smoothed data as the standard deviation at the tail of the scan (593 – 605 eV). The region was selected as it is the least influenced by modifications to magnetotransport due to x-ray absorption by oxygen sites. In other words, we selected a region essentially devoid of features in the XAS spectrum. The resulting error bars are calculated with an exact differential of the form:

$$\Delta R(E_{ph}) = \frac{2V(\Delta I_- + \Delta I_+)}{(I_-(E_{ph}) - I_+(E_{ph}))^2} \quad (6.2)$$

Both  $I_-(E_{ph})$  and  $I_+(E_{ph})$  are calculated as the averages of two contributing errors from consecutive measurements. As a note, the larger error bars within the  $R_{AP}(E_{ph})$  data for linear vertical x-ray polarization reflect the use of fewer raw scans due to measurement artefacts.

### 6.2.5 Principle of concurrent electrical and XAS measurements

In the theoretical part of this thesis, we discussed in detail the mechanism of symmetry filtering effect across Fe/MgO/Fe heterostructures. The relative difference in the device's resistance  $R$  upon switching from a parallel (P) to antiparallel (AP) alignment of electrode magnetization defines the tunneling magnetoresistance (TMR) ratio (a standard metric of device performance). Although the atoms of the ferromagnetic electrodes contribute to define its macroscopic magnetization, the spin- and symmetry-polarized density of electronic states that tunnel across the MTJ is that of the interface between the FM electrode and the tunnel barrier and in particular the interaction between interface Fe and O atoms.

We show in [Figure 6.5](#) how combined electrical and XAS measurements can probe the impact of a particular subset of atoms on devices' magnetoresistive properties. We show in panel (a) how the atoms of a given species can selectively absorb a soft x-ray photon if its energy is tuned to match the energy difference between that atomic species' core state and an unoccupied state. The example of oxygen is shown. The photon energy dependence of x-ray absorption around this energy edge, i.e. XAS, reveals the electronic properties of all the irradiated oxygen atoms.

Panel (b) represents a FM/MgO/FM sample, with Mg (O) atoms in green (red). XAS at the O K absorption edge excites the O atoms (yellow contour). Blue rectangles isolate possible traces of interfacial Fe oxides that would appear in XAS just prior to the edge.

Panel (c) is a schematic of a MTJ encapsulated with a SiO<sub>2</sub> dielectric layer. Within the MgO barrier, defects such as oxygen vacancies form a pinhole that can funnel all the MTJ's current between the interfacial atoms facing the pinhole.

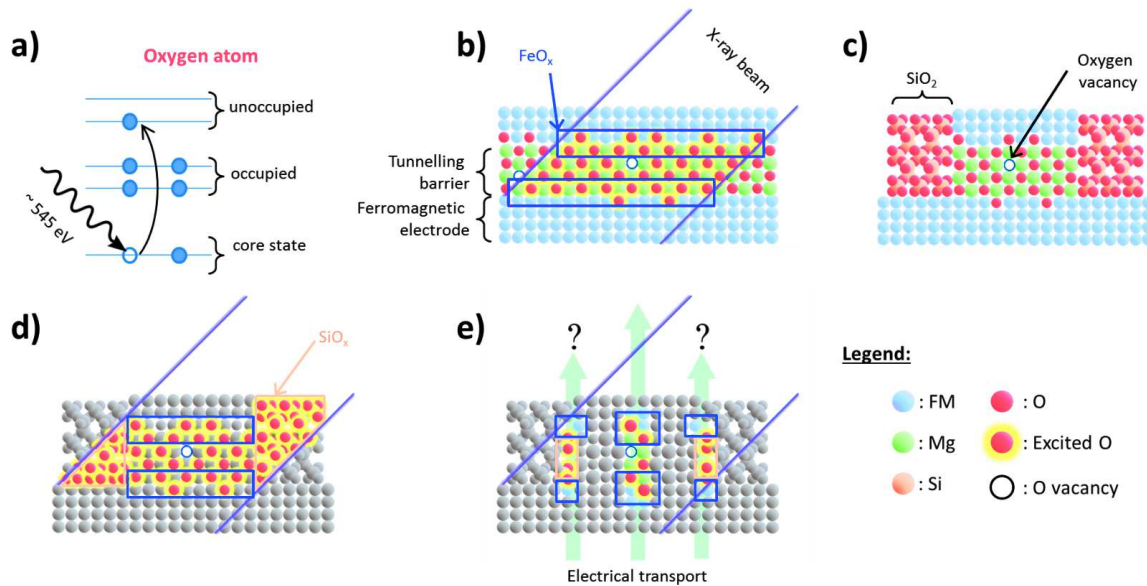


Figure 6.5: **Probing a device's active atoms using x-ray absorption spectroscopy (XAS):**(a) Atoms of a given species can selectively absorb a soft x-ray photon if its energy is tuned to match the energy difference between that atomic species' core state and an unoccupied state. (b) Schematic of the atoms excited by XAS at the O  $K$  in a FM/MgO/FM sample. Blue rectangles isolate possible traces of interfacial Fe oxides. (c) Schematic of a MTJ encapsulated with a  $\text{SiO}_2$  dielectric layer. (d) XAS alone on a MTJ probes all the O atoms within and around the MTJ. (e) The combined magnetotransport/XAS technique probes only those O atoms that contribute to transport.

In panel (d) we show that XAS alone on a MTJ probes all the O atoms within and around the MTJ, including Fe and Si oxides (delimited in salmon). Panel (e) shows that the combined magnetotransport/XAS technique probes only those O atoms that contribute to transport: across pinholes, and potentially around the MTJ pillar periphery. Blue and salmon rectangles delimit those Fe and Si oxides to be probed.

## 6.2.6 Results and discussion

### 6.2.6.1 Combined XAS and magnetotransport measurements

Characterization studies of magnetic tunnel junctions, including XAS, have focused on interfaces in full stacks, either by studying the atoms of ultrathin FM layers<sup>221,222</sup> at these interfaces, or by examining the bonds between these atoms and the barrier's atoms<sup>219,223,224</sup>. In similar fashion, we present in Figure 6.6(a) XAS at the O  $K$  edge of reference stacks for our MTJs with FeCoB FM electrodes and MgO tunnel barrier that are either as-grown (black line) or annealed (red line).

We first focus on the pre-edge region in the  $537 < E(\text{eV}) < 541$  energy range that reveals the oxygen sites' chemical environment. As we can see from Figure 6.6(a), we

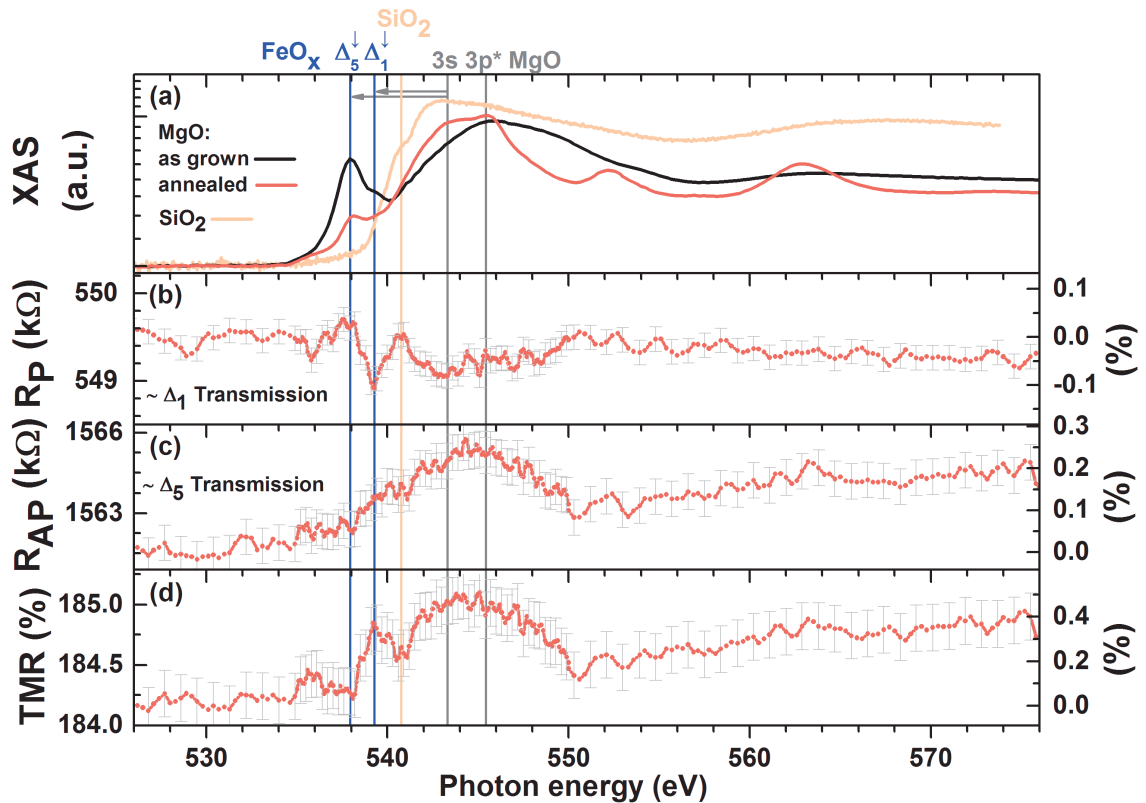


Figure 6.6: **Combined XAS and magnetotransport measurements:** (a) XAS scan of the O K edge acquired atop a reference heterostructure terminated by the MgO barrier that is as-grown (black) or annealed (red). Annealing reduces the spectral weight of pre-edge features, which are associated with Fe oxides (blue lines). A reference spectrum for the SiO<sub>2</sub> that encapsulates our MTJs is shown in salmon. Photon energy dependence of the annealed MTJ resistance  $R$  at 10 mV and  $T = 20$  K in the (b) P, (c) AP magnetization states and (d) of the TMR ratio.

observe pre-peaks in the XAS data on the non-annealed sample (black line) whose energy positions relative to the main 543.5 eV peak are quantitatively identified<sup>219,225,226</sup> as the spin- and symmetry-polarized bands of Fe oxides, with a 1.4 eV crystal field splitting (between  $\Delta_1$  and  $\Delta_5$  states) and a 2.3 eV spin-splitting (between spin up and down states). Annealing the sample results in a strong decrease in the Fe oxide peaks' spectral intensity.

The reduction of these interfacial Fe oxides inferred from XAS studies<sup>219</sup> represent one microscopic explanation as to why annealing increases TMR within separately conducted magnetotransport studies. However, the link between these spectroscopic studies and magnetotransport is indirect.

We propose to focus XAS studies onto only those atoms involved in the annealed MTJ's operation by measuring its magnetotransport properties as it absorbs x-rays (see Figure 6.5). Since x-ray absorption generates the emission of secondary electrons, our raw magnetotransport data upon reaching the O K edge includes a photocurrent. We detail in

Section 6.2.3 how we removed the photocurrent contribution. We plot in Figure 6.6(b) and (c) the resulting photon energy dependence at  $T = 20$  K, upon reaching the O K edge, of the device's resistance for a 10 mV applied voltage in the parallel and anti-parallel configurations ( $R_P$  and  $R_{AP}$ ) of electrode magnetization. We remind that the MTJ's P and AP magnetic states respectively probe the dominant transmission of electrons with  $\Delta_1$  and  $\Delta_5$  symmetries (see Section 1.3.4.3). This dataset, obtained for x-ray photons with linear polarization within the plane of the MTJ's interfaces, is representative of other datasets acquired for other photon polarizations (not shown).

We'll essentially distinguish two energy regions: (i) the pre-edge region in the  $537 < E(\text{eV}) < 541$  energy range and (ii) the main O K edge maximum at 543.5 eV.

### 6.2.6.2 Impact on magnetotransport: Pre-edge region

As discussed previously, in the pre-edge region photons are exciting core electrons of O atoms present in interfacial Fe oxide to empty  $\Delta_1^\downarrow$  and  $\Delta_5^\downarrow$  states (marked by blue lines in Figure 6.6). Upon addressing these states, we note the change induced on the resistance of the device in the parallel magnetic state  $R_P$  (see panel (b)). More precisely, we can see that  $R_P$  exhibit a minimum upon addressing the  $\Delta_1^\downarrow$  state and an extremely weak minimum (actually within the error bars) upon addressing the  $\Delta_5^\downarrow$  state.

This decrease upon exciting a core electron to the  $\Delta_1^\downarrow$  and  $\Delta_5^\downarrow$  can be explained as follows. Recent XAS calculations carried in our group<sup>218</sup>, that reproduce experimental XAS spectra, show that the generated core photo-hole can be neglected (Born-Oppenheimer approximation) and that the excited atomic site could simply be described with an additional photoelectron. We suggest that the extra electrons in this *excited* state promote enhanced electrical transport across the otherwise insulating Fe interfacial oxide. We suppose that both interface are oxidized, and that the tunneling of excited photo-electrons proceed between Fe oxide at both interfaces. The enhanced metallic nature of the MTJ's interface thereby explains why resistance may decrease.

However, because the decay rate of electrons in MgO depends on their orbital character (symmetry filtering effect), the impact of these additional photoelectrons will depend on their symmetries. More particularly, we know that the decay rate of  $\Delta_1$  states is much slower than the decay rate of  $\Delta_5$  states. Within this picture, we expect the impact of  $\Delta_1^\downarrow$  states on  $R_P$  to be larger than that of  $\Delta_5^\downarrow$  photo-electrons. Regarding  $R_{AP}$ , the Fe oxide spin down states have no impact on transport because the corresponding spin up states are fully occupied (no available states in the counter electrode).

This leads to concurrent changes to the MTJ's TMR at 10 mV (see Figure 6.6(d)) within the O K pre-edge due to altering the electronic structure of Fe oxides at the MTJ's interfaces.

Thus, contrary to the qualitative indications provided by XAS-only spectra, which suggest an annealing-induced disappearance of interfacial Fe oxides, our combined magnetotransport/XAS technique reveals how the TMR of our MTJs is unambiguously limited by interfacial Fe oxides. This ability to ascertain the microscopic origin of a device's performance can help detail novel effects at the MTJ's interface.

Also, by comparing the data of see Figure 6.6(b) and (c) with the XAS corresponding to the  $\text{SiO}_2$  that encapsulates the MTJ, we find only a very minor deviation in  $R_P$  and  $R_{AP}$  from their background levels upon charging the Si-O bonds through x-ray absorption that is well within our error bars. This explicitly demonstrates that the chemical environment of our MTJ pillar plays at best a secondary role in the device's operation/performance, as do any other possible short-circuits across  $\text{SiO}_2$ .

**Limitations:** The main limitations to our discussion are the the noise level of our dataset and the very small amplitude of the changes induced by x-rays. As we discussed in Section 6.2.5, future developments on the beamline may involve a better shielding of the electrical connections to the samples and a better environment for the magnetotransport bench. Moreover, due to a failure of the main cryomagnet, we had to carry our experiment far away from the focal point of the x-ray beam. Using a focused x-ray beam should increase the changes induced by x-ray on the electrical properties of MTJs, and greatly improve the signal-to-noise ratio.

We can also note that the large resistance drop in  $R_P$  upon addressing the  $\Delta_1^\downarrow$  states of interface FeO (Figure 6.6) corresponds to a very sharp peak in the  $I(E_{ph})$  spectra used to calculate  $R_{P,AP}$  (see green arrow in Figure 6.4(a)). One could argue that the small systematic errors induced by our data manipulation (e.g. interpolation) should be maximum at this precise energy, and that the peak in  $R_P$  could arise from such errors. On the other hand, if this was the case, there is no reason for this peak to be present in  $R_P$  and not in  $R_{AP}$ .

### 6.2.6.3 Impact on magnetotransport: Oxygen K absorption edge

Turning from this focus on the atoms at the MTJ's interfaces and periphery, we now discuss how a device's operation is impacted by absorbed x-rays. Upon reaching the K absorption edge for all O atoms ( $530 \text{ eV} \rightarrow 545 \text{ eV}$ ),  $R_P$  is mostly unaffected, with a decrease of 0.02-0.1 %. In contrast,  $R_{AP}$  increases by 0.2 %. The ensuing TMR ratio, which reaches  $\sim 180 \%$  in our MTJs at 20 K, thus increases by  $\sim 0.5 \%$ .

In order to understand the impact of x-ray absorption on magnetotransport, we present in Figure 6.7 complex band structure calculations (CBS) for MgO in both its ground state (see Section 1.3.4.2) and in the aforementioned 'excited' state. The additional electron is modeled by replacing all O sites with F atoms according to the so-called  $Z+1$  method<sup>227-229</sup>. We unsurprisingly observe an increase in band gap for the *excited* state, which can in turn artificially increase the complex loop amplitudes. At the energy corresponding to the MTJ's Fermi level, we observe a moderate increase in the rate  $\kappa_1$  of tunneling attenuation for  $\Delta_1$  electrons, which dominate transmission in the MTJ's P state. On the other hand, we witness a considerable increase in the rate  $\kappa_5$  of tunneling attenuation for  $\Delta_5$  electrons, which dominate transmission in the MTJ's AP state.

If we model  $R_0(R)$  as the MTJ resistance without (with) the x-ray photoelectron, such that  $R = R_0 e^{-\kappa d}$  ( $d$  is the barrier thickness), then the absolute changes  $\delta\kappa_1 = -0.05$  and  $\delta\kappa_5 = -0.15$  in the tunneling attenuation (see Figure 6.7) lead to a three times smaller impact on  $R_P$  compared to  $R_{AP}$ , conform to our experimental results (within the experimental noise level of  $R_P$ ). This supports experimental observations of a sizable increase in  $R_{AP}$

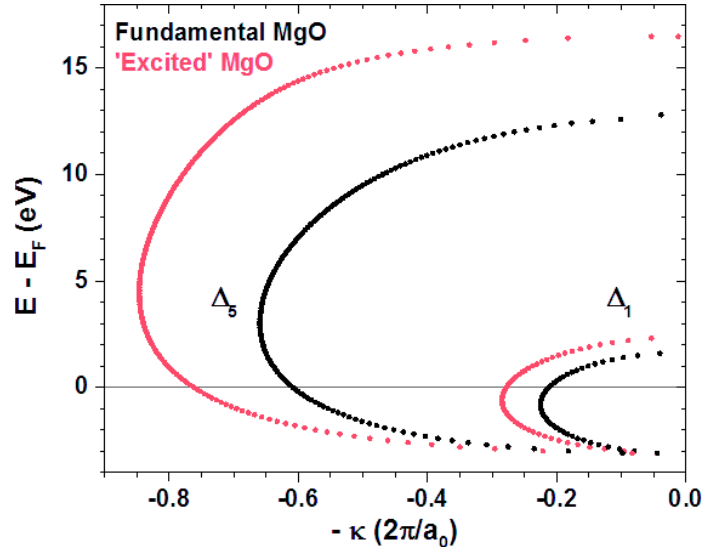


Figure 6.7: **Complex band structure of MgO under x-ray excitation:** Complex band structure of MgO in its fundamental (black) and excited (red) states. Excited MgO is modeled by replacing all the O atoms by F atoms. This could artificially increase the band gap and the complex loop amplitudes, we nevertheless observe an increase in  $\kappa_5$  that is much larger than for  $\kappa_1$ .

and a much lower impact on  $R_P$ .

## 6.3 Conclusion

In this chapter, we discussed how we combined the chemical selectivity of XAS and the atomic selectivity of MTJs electronic properties. We showed that the tunnel current was mainly modified by two mechanism when the device was excited by x-rays at the O K edge.

First, in the pre-edge region, we showed that the electrical changes were related the excitation of core electrons in Fe oxide at the interface. We explained the resistance drop in the parallel magnetic state by the participation to the tunnel current of excited  $\Delta_1^\downarrow$  and  $\Delta_5^\downarrow$  photo-electrons. The fact that the impact is stronger upon exciting  $\Delta_1^\downarrow$  states is explained by the fact that these states have the slowest decay rate in MgO. We suggested that these photoelectron tunnel between Fe oxide sites present at both interfaces. Because the corresponding spin up states are fully occupied, these photo-electrons are not expected to impact the current in the antiparallel magnetic configuration.

Secondly, at the O K absorption edge, we explained the change in device operation induced by x-rays by the modification of the properties of the MgO barrier itself. Our calculations showed that the decay constant of  $\Delta_1$  and  $\Delta_5$  states was increased in the MgO excited state. The calculations suggest that the absolute change induced on the decay constant is three time larger for  $\Delta_5$  than for  $\Delta_1$ , explaining the smaller impact on  $R_P$  (dominated by  $\Delta_1$  electrons) compared to  $R_{AP}$  (dominated by  $\Delta_5$  electrons).

Finally, we saw that our interpretation was not conclusive, at times, due to small signal to noise ratio of our dataset. But improving the samples' environment and using a focused x-ray beam should partially solve this issue.

## Conclusion and perspectives

In this thesis, our first objective was to characterize the impact of localized states induced by oxygen vacancies on the electrical properties of MgO based magnetic tunnel junctions. More precisely, we wanted to unambiguously identify the impact of the specific defect population responsible for the changes induced on the electrical properties of the device. In order to do so, we mainly used two type of probes, that is electrical measurements and optical excitation.

In [Chapter 4](#) the two techniques were used separately and results obtained from both experiments were related indirectly. In [Chapter 5](#) and [Chapter 6](#) our approach was different in that we attempted to combine the two experimental techniques, i.e. probe the changes induced by optical excitation on the devices' properties with electrical measurements.

### 7.1 Bias and temperature dependence of magnetotransport properties

In order to identify the impact of specific localized states responsible for the changes in the devices' properties, we attempted to compare the photoluminescence spectra induced by the optical activity of localized states in the gap of MgO and magnetotransport measurements.

Photoluminescence is a powerful technique that allows to get useful information on the characteristics of localized states. However, the technique also has its limitations. For example, it is not possible to determine the energy position of relaxed excited states with precision. Besides, the optical activity of oxygen vacancies in MgO is particularly complex, and although the literature is consequent, a clear interpretation of the photoluminescence spectra is still not available. In order to determine the electrical properties of our device, we decided to use an experimental technique in order to extract the effective barrier height directly from magnetotransport experiments. This technique consists in probing the current change induced by thermal excitation and is free of the deficiencies inherent to fitting techniques based on semi classical tunneling models.

Our temperature and bias dependent magnetotransport results strongly suggest the impact of two types localized states in specific temperature ranges. At low temperature, the changes in the electrical properties are maximum at 1.2 V. Around  $T = 80$  K an abrupt switchover occurs, and a feature located at 0.7 V dominates the tunnel current.

We then tried to identify these features by comparing their energy positions to the luminescence bands of temperature dependent photoluminescence data measured on our rf-sputtered MgO thin films. However, we showed that our initial interpretation of these PL

spectra was not consistent. The difficulty to interpret our PL spectra stems from the fact that (i) we misconceived the excitation and recombination processes between the ground and excited states of a specific localized state and (ii) the excitation energy used to measure our PL spectra was not appropriate.

As a perspective to this work, it is clear that the optical activity of our MgO thin films has to be better understood. In order to do so, time-resolved and temperature dependent photoluminescence spectra should be acquired, with the appropriate photon energy, i.e. 5 eV photons to excite  $F$  centers and 3-4 eV photons to excite  $M$  centers. Both the excitation and luminescence bands should be investigated carefully. Additionally, the technique used to measure the tunnel current in the device could also be upgraded in order to obtain a better signal to noise ratio and improve the resolution of the measurements.

## 7.2 Optical excitation of localized states

The work carried in this chapter was based on our initial understanding of excitation and recombination processes of localized states in MgO and on our initial interpretation of the results obtained in the preceding chapter. To briefly summarize, we supposed that the temperature dependence of the magnetoresistive properties of our devices was caused by the occupancy switchover from the ground  $F/F^+$  to the excited  $F^{+*}$  states.

Our objective was to induce the change in the population occupancy of defects optically. Being able to optically change the defect population, which in turn drive the devices properties, could have interesting applications in photonics.

We mainly carried two types of experiments. We first investigated the impact of exciting our junctions with 3.05 eV p-polarized light and found that the results were mostly identical to the impact of thermal excitation, suggesting a laser-heating effect.

We then focused on the impact of smoothly varying the polarization of light from p to s. At first, the impact of varying light's polarization couldn't be explained by laser-induced heat. We thus proposed an initial model in which the excited photo-electrons are characterized by orbitals that points mostly along the direction of light's electric field. Because the decay rate of charge carriers in MgO depends their electronic symmetry, we supposed that the impact of excited photo-electrons on the tunnel current was different depending on their orbital character.

However, we then focused on how light propagates in multilayer planar stacks. We found that p- and s-polarized light are not reflected, refracted and thus absorbed with the same amplitude. Assuming that the optical excitation actually results in heat, we showed that our results could consistently be explained in terms of laser-induced heat.

The main difficulty arises from heat induced by the optical excitation. This effect will be difficult to circumvent. Time resolved experiments could help, but will require a major upgrade of the magnetotransport bench. Using a tunable laser source could also help to enter resonant and non-resonant regimes and ease the identification of the excitation energy of specific localized states.

## 7.3 Synchrotron experiments

In the last chapter of this thesis, we briefly introduced our work carried on the DEIMOS beamline at the synchrotron SOLEIL. Our goal was to combine the chemical selectivity of x-ray absorption spectroscopy and magnetotransport experiments in order to probe the devices' properties in real operating conditions.

We found that the current was mainly modified by two mechanisms. First, in the pre-edge region, we showed that the electrical changes were related to the excitation of core electrons in Fe oxide at the interface. We showed that, contrary to the qualitative indications provided by XAS-only spectra, which suggest an annealing-induced disappearance of interfacial Fe oxides, our combined magnetotransport/XAS technique reveals how the TMR of our MTJs is unambiguously limited by interfacial Fe oxides.

Secondly, at the O K absorption edge, we explained the change in device operation induced by x-rays by the modification of the solid-state tunneling properties of the MgO barrier itself. Our calculations showed that the decay constant of  $\Delta_1$  and  $\Delta_5$  states was increased in the MgO excited state. The calculations suggest that the absolute change induced on the decay constant is three times larger for  $\Delta_5$  than for  $\Delta_1$ , explaining the smaller impact on  $R_P$  (dominated by  $\Delta_1$  electrons) compared to  $R_{AP}$  (dominated by  $\Delta_5$  electrons).

Finally, we saw that our interpretation was not conclusive, at times, due to a small signal to noise ratio of our dataset. But improving the samples' environment and using a focused x-ray beam should partially solve this issue.



# Bibliography

1. M. Julliere. Tunneling between ferromagnetic films. *Phys. Lett. A*, 54(3):225–226, 1975. ISSN 03759601. doi: 10.1016/0375-9601(75)90174-7.
2. Patryk Krzysteczko, Gunter Reiss, and Andy Thomas. Memristive switching of MgO based magnetic tunnel junctions. *Appl. Phys. Lett.*, 95(11):112508, 2009. ISSN 00036951. doi: 10.1063/1.3224193. URL <http://link.aip.org/link/APPLAB/v95/i11/p112508/s1{&}Agg=doi>.
3. a. Droghetti, C. D. Pemmaraju, and S. Sanvito. Polaronic distortion and vacancy-induced magnetism in MgO. *Phys. Rev. B*, 81(9):092403, mar 2010. ISSN 1098-0121. doi: 10.1103/PhysRevB.81.092403. URL <http://link.aps.org/doi/10.1103/PhysRevB.81.092403>.
4. C. Martínez-Boubeta, J. I. Beltrán, Ll. Balcells, Z. Konstantinović, S. Valencia, D. Schmitz, J. Arbiol, S. Estrade, J. Cornil, and B. Martínez. Ferromagnetism in transparent thin films of MgO. *Phys. Rev. B*, 82(2):024405, jul 2010. ISSN 1098-0121. doi: 10.1103/PhysRevB.82.024405. URL <http://link.aps.org/doi/10.1103/PhysRevB.82.024405>.
5. Jing Li, Yinzhu Jiang, Yong Li, Deren Yang, Yongbing Xu, and Mi Yan. Origin of room temperature ferromagnetism in MgO films. *Appl. Phys. Lett.*, 102(7):072406, 2013. ISSN 00036951. doi: 10.1063/1.4793308. URL <http://scitation.aip.org/content/aip/journal/apl/102/7/10.1063/1.4793308>.
6. P. P. Freitas, F. a. Cardoso, V. C. Martins, S. a. M. Martins, J. Loureiro, J. Amaral, R. C. Chaves, S. Cardoso, L. P. Fonseca, a. M. Sebastião, M. Pannetier-Lecoeur, and C. Fermon. Spintronic platforms for biomedical applications. *Lab Chip*, 12(3):546, 2012. ISSN 1473-0197. doi: 10.1039/c1lc20791a.
7. Ivar Giaever. Electron tunneling between two superconductors. *Phys. Rev. Lett.*, 5(10):464–466, 1960. ISSN 00319007. doi: 10.1103/PhysRevLett.5.464.
8. M. N. Baibich, J. M. Broto, A. Fert, F. Nguyen Van Dau, F. Petroff, P. Eitenne, G. Creuzet, A. Friederich, and J. Chazelas. Giant magnetoresistance of (001)Fe/(001)Cr magnetic superlattices. *Phys. Rev. Lett.*, 61(21):2472–2475, 1988. ISSN 00319007. doi: 10.1103/PhysRevLett.61.2472.
9. G. Binasch, P. Grünberg, F. Saurenbach, and W. Zinn. Enhanced magnetoresistance in layered magnetic structures with antiferromagnetic interlayer exchange. *Phys. Rev. B*, 39(7):4828–4830, mar 1989. ISSN 0163-1829. doi: 10.1103/PhysRevB.39.4828. URL <http://journals.aps.org/prb/abstract/10.1103/PhysRevB.39.4828>.

## Bibliography

10. J. S. Moodera, Lisa R. Kinder, Tunnel Junctions, Terrilyn M. Wong, and R. Meservey. Large Magnetoresistance at Room Temperature in Ferromagnetic Thin Film Tunnel Junctions. *Phys. Rev. B*, 74(16):3273–3276, 1995.
11. T. Miyazaki and N. Tezuka. Giant magnetic tunneling effect in Fe/Al<sub>2</sub>O<sub>3</sub>/Fe junction. *J. Magn. Magn. Mater.*, 139(3):94–97, 1995. ISSN 03048853. doi: 10.1016/0304-8853(95)90001-2.
12. Johan Akerman. Toward a Universal Memory. *Science (80-. )*, 308, 2005.
13. Sining Mao, Yonghua Chen, Feng Liu, Xingfu Chen, Bin Xu, Puling Lu, Mohammed Patwari, Haiwen Xi, Clif Chang, Brad Miller, Dave Menard, Bharat Pant, Jay Loven, Kristin Duxstad, Shaoping Li, Zhengyong Zhang, Alan Johnston, Robert Lamberton, Mark Gubbins, Tom McLaughlin, Jason Gadbois, Juren Ding, Bill Cross, Song Xue, and Pat Ryan. Commercial TMR heads for hard disk drives: Characterization and extendibility at 300 Gbit/in<sup>2</sup>. *IEEE Trans. Magn.*, 42(2):97–102, 2006. ISSN 00189464. doi: 10.1109/TMAG.2005.861788.
14. Rie Matsumoto, Akio Fukushima, Kay Yakushiji, Satoshi Yakata, Taro Nagahama, Hitoshi Kubota, Toshikazu Katayama, Yoshishige Suzuki, Koji Ando, Shinji Yuasa, Benoit Georges, Vincent Cros, Julie Grollier, and Albert Fert. Spin-torque-induced switching and precession in fully epitaxial Fe/MgO/Fe magnetic tunnel junctions. *Phys. Rev. B - Condens. Matter Mater. Phys.*, 80(17):1–8, 2009. ISSN 10980121. doi: 10.1103/PhysRevB.80.174405.
15. Patryk Krzysteczko, Jana Münchenberger, Markus Schäfers, Günter Reiss, and Andy Thomas. The memristive magnetic tunnel junction as a nanoscopic synapse-neuron system. *Adv. Mater.*, 24(6):762–6, feb 2012. ISSN 1521-4095. doi: 10.1002/adma.201103723. URL <http://www.ncbi.nlm.nih.gov/pubmed/22223304>.
16. Guo-Xing Miao, Markus Münzenberg, and Jagadeesh S Moodera. Tunneling path toward spintronics. *Reports Prog. Phys.*, 74(3):036501, mar 2011. ISSN 0034-4885. doi: 10.1088/0034-4885/74/3/036501. URL <http://stacks.iop.org/0034-4885/74/i=3/a=036501?key=crossref.7b39c4c133cc384896c0ba96a48023e6>.
17. X. G. Zhang and W. H. Butler. Large magnetoresistance in bcc Co/MgO/Co and FeCo/MgO/FeCo tunnel junctions. *Phys. Rev. B - Condens. Matter Mater. Phys.*, 70(17):1–4, 2004. ISSN 01631829. doi: 10.1103/PhysRevB.70.172407.
18. S. Ikeda, J. Hayakawa, Y. Ashizawa, Y. M. Lee, K. Miura, H. Hasegawa, M. Tsunoda, F. Matsukura, and H. Ohno. Tunnel magnetoresistance of 604% at 300 K by suppression of Ta diffusion in CoFeB/MgO/CoFeB pseudo-spin-valves annealed at high temperature. *Appl. Phys. Lett.*, 93(8):082508, 2008. ISSN 00036951. doi: 10.1063/1.2976435. URL <http://scitation.aip.org/content/aip/journal/apl/93/8/10.1063/1.2976435>.

19. J. P. Velev, M. Ye Zhuravlev, K. D. Belashchenko, S. S. Jaswal, E. Y. Tsymbal, T. Katayama, and S. Yuasa. Defect-mediated properties of magnetic tunnel junctions. *IEEE Trans. Magn.*, 43(6):2770–2775, 2007. ISSN 00189464. doi: 10.1109/TMAG.2007.893311.
20. D. C. Ralph and M. D. Stiles. Spin transfer torques. *J. Magn. Magn. Mater.*, 320(7): 1190–1216, 2008. ISSN 03048853. doi: 10.1016/j.jmmm.2007.12.019.
21. Neil W. Ashcroft and N. David Mermin. *Solid State Physics*. Harcourt College Publishers, 1976.
22. N. F. Mott. The Electrical Conductivity of Transition Metals. *Proc. R. Soc. A Math. Phys. Eng. Sci.*, 153(880):699–717, 1936. ISSN 1364-5021. doi: 10.1098/rspa.1936.0031. URL <http://rspa.royalsocietypublishing.org/cgi/doi/10.1098/rspa.1936.0031>.
23. H. A. KRAMERS. Linteraction entre les atomes magnétogène dans un crystal paramagnétique. *Physica*, 1(1-6):182–192, 1934. doi: 10.1016/S0031-8914(34)90023-9.
24. Clarence Zener. Interaction between the d-Shells in the Transition Metals. II. Ferromagnetic Compounds of Manganese with Perovskite Structure. *Phys. Rev.*, 82(3): 403–405, 1951.
25. Toru Moriya and Yoshinori Takahashi. Itinerant Electron Magnetism. *Annu. Rev. Mater. Sci.*, pages 1–25, 1984.
26. S. S. P. Parkin, N. More, and K P Roche. Oscillations in Exchange Coupling and Magnetoresistance in Metallic Superlattice Structures: Co/Ru, Co/Cr and Fe/Cr. *Phys. Rev. Lett.*, 23(2):130, 1990. ISSN 1550-5154. doi: 10.1097/01.QMH.0000446529.07330.f3. URL <http://www.ncbi.nlm.nih.gov/pubmed/24712349>.
27. P. Grunberg, R. Schreiber, Y. Pang, M. B. Brodsky, and H. Sowers. Layered magnetic structures: Evidence for antiferromagnetic coupling of Fe layers across Cr interlayers. *J. Appl. Phys.*, 57(19), 1986. ISSN 00218979. doi: 10.1063/1.338656.
28. Claude Cohen-Tannoudji, Bernard Diu, and Frank Laloë. *Mécanique quantique I*. Hermann, Paris, hermann edition, 1997.
29. J. Bardeen. TUNNELLING FROM A MANY-PARTICLE POINT OF VIEW. *Phys. Rev. Lett.*, 6(2), 1961. doi: 10.1103/PhysRevLett.6.57.
30. Samir Lounis. Theory of Scanning Tunneling Microscopy. In *45th Spring Sch. Comput. Solids Model. Ab-initio Methods Supercomput. Organ. Forschungszentrum J\ulich.*, page 38, apr 2014. URL <http://arxiv.org/abs/1404.0961>.
31. C. Julian Chen. *Introduction to Scanning Tunneling Microscopy*. Oxford University Press, USA, New York, 1993. ISBN 9780195071504.

## Bibliography

32. Walter A. Harrison. Tunneling from an independent-particle point of view. *Phys. Rev.*, 123(1):85–89, 1961. ISSN 0031899X. doi: 10.1103/PhysRev.123.85.
33. John G. Simmons. Generalized Formula for the Electric Tunnel Effect between Similar Electrodes Separated by a Thin Insulating Film. *J. Appl. Phys.*, 34(6):1793–1803, 1963. ISSN 00218979. doi: 10.1063/1.1702682.
34. W. F. Brinkman, R. C. Dynes, and J. M. Rowell. Tunneling conductance of asymmetrical barriers. *J. Appl. Phys.*, 41(5):1915–1921, 1970. ISSN 00218979. doi: 10.1063/1.1659141.
35. Patrick Royce LeClair. *Fundamental Aspects of Spin Polarized Tunneling*. PhD thesis, Eindhoven University of Technology, 2002.
36. R. Meservey, P. M. Tedrow, and Peter Fulde. Magnetic field splitting of the quasiparticle states in superconducting aluminum films. *Phys. Rev. Lett.*, 25(18):1270–1272, 1970. ISSN 00319007. doi: 10.1103/PhysRevLett.25.1270.
37. Dimitris A. Papaconstantopoulos. *Handbook of the Band Structure of Elemental Solids: From Z = 1 To Z = 112*. Springer US, New York, second edition, 1986. ISBN 978-1-4419-8263-6. doi: 10.1007/978-1-4419-8264-3.
38. Mary Beth Stearns. Simple explanation of tunneling spin-polarization of Fe, Co, Ni and its alloys. *J. Magn. Magn. Mater.*, 5(2):167–171, 1977. ISSN 03048853. doi: 10.1016/0304-8853(77)90185-8.
39. Jagadeesh S. Moodera, Joaquim Nassar, and George Mathon. Spin-Tunneling in Ferromagnetic Junctions. *Annu. Rev. Mater. Sci.*, 29:381–432, 1999. ISSN 0084-6600. doi: 10.1146/annurev.matsci.29.1.381.
40. J. M. De Teresa. Role of Metal-Oxide Interface in Determining the Spin Polarization of Magnetic Tunnel Junctions. *Science (80-. )*, 286(5439):507–509, 1999. ISSN 00368075. doi: 10.1126/science.286.5439.507.
41. Evgeny Y. Tsymbal and Igor Zutic. *HANDBOOK OF SPIN TRANSPORT AND MAGNETISM*. CRC Press, 2012.
42. R. C. Whited, Christopher J. Flaten, and W. C. Walker. Exciton thermoreflectance of MgO and CaO. *Solid State Commun.*, 13(11):1903–1905, 1973. ISSN 00381098. doi: 10.1016/0038-1098(73)90754-0.
43. U. Schönberger and F. Aryasetiawan. Bulk and surface electronic structures of MgO. *Phys. Rev. B*, 52(12):8788–8793, 1995. ISSN 01631829. doi: 10.1103/PhysRevB.52.8788.
44. W. Butler, X.-G. Zhang, T. Schulthess, and J. MacLaren. Spin-dependent tunneling conductance of Fe/MgO/Fe sandwiches. *Phys. Rev. B*, 63(5):054416, jan 2001. ISSN 0163-1829. doi: 10.1103/PhysRevB.63.054416. URL <http://link.aps.org/doi/10.1103/PhysRevB.63.054416>.

45. S Yuasa and D D Djayaprawira. Giant tunnel magnetoresistance in magnetic tunnel junctions with a crystalline MgO(001) barrier. *J. Phys. D. Appl. Phys.*, 40(21):R337–R354, nov 2007. ISSN 0022-3727. doi: 10.1088/0022-3727/40/21/R01. URL <http://stacks.iop.org/0022-3727/40/i=21/a=R01?key=crossref.5e4ad43797a155e306a576b1744a6d26>.
46. M. Klaua, D. Ullmann, J. Barthel, W. Wulfhekel, J. Kirschner, R. Urban, T. Monch-  
esky, a. Enders, J. Cochran, and B. Heinrich. Growth, structure, electronic, and mag-  
netic properties of MgO/Fe(001) bilayers and Fe/MgO/Fe(001) trilayers. *Phys. Rev. B*, 64(13):1–8, 2001. ISSN 0163-1829. doi: 10.1103/PhysRevB.64.134411.
47. Toshio Urano and Toru Kanaji. Atomic and electronic structure of ultrathin iron film  
on MgO(001) surface, 1988. ISSN 00319015.
48. Chun Li and A. J. Freeman. Giant monolayer magnetization of Fe on MgO: A nearly  
ideal two-dimensional magnetic system. *Phys. Rev. B*, 43(1):780–787, jan 1991. ISSN  
0163-1829. doi: 10.1103/PhysRevB.43.780. URL [http://journals.aps.org/prb/abstract/  
10.1103/PhysRevB.43.780](http://journals.aps.org/prb/abstract/10.1103/PhysRevB.43.780).
49. X-G Zhang and W.H. Butler. Band structure , evanescent states , and transport in spin  
tunnel junctions. *J. Phys. Condens. Matter*, 15:1603–1639, 2003.
50. J. MacLaren, X.-G. Zhang, W. Butler, and Xindong Wang. Layer KKR approach  
to Bloch-wave transmission and reflection: Application to spin-dependent tunneling.  
*Phys. Rev. B*, 59(8):5470–5478, 1999. ISSN 0163-1829. doi: 10.1103/PhysRevB.59.  
5470.
51. W. H. Butler, X.-G. Zhang, Xindong Wang, Jan van Ek, and J. M. MacLaren.  
Electronic structure of FM|semiconductor|FM spin tunneling structures. *J. Appl.  
Phys.*, 81(8):5518, apr 1997. ISSN 00218979. doi: 10.1063/1.364587. URL  
<http://scitation.aip.org/content/aip/journal/jap/81/8/10.1063/1.364587>.
52. W. Butler, X.-G. Zhang, T. Schulthess, and J. MacLaren. Reduction of electron  
tunneling current due to lateral variation of the wave function. *Phys. Rev. B*, 63  
(9):092402, 2001. ISSN 0163-1829. doi: 10.1103/PhysRevB.63.092402. URL  
<http://link.aps.org/doi/10.1103/PhysRevB.63.092402>.
53. P Mavropoulos, N Papanikolaou, and Ph Dederichs. Complex band structure and  
tunneling through Ferromagnet/Insulator/Ferromagnet junctions. *Phys. Rev. Lett.*, 85  
(5):1088–91, jul 2000. ISSN 1079-7114. URL [http://www.ncbi.nlm.nih.gov/pubmed/  
10991481](http://www.ncbi.nlm.nih.gov/pubmed/10991481).
54. P. H. Dederichs, Ph Mavropoulos, O. Wunnicke, N. Papanikolaou, V. Bellini,  
R. Zeller, V. Drchal, and J. Kudrnovský. Importance of complex band structure and  
resonant states for tunneling. *J. Magn. Magn. Mater.*, 240(1-3):108–113, 2002. ISSN  
03048853. doi: 10.1016/S0304-8853(01)00728-4.

## Bibliography

55. M. Bowen, V. Cros, F. Petroff, A. Fert, C. Martinez Boubeta, J. L. Costa-Kramer, J. V. Anguita, A. Cebollada, F. Briones, J. M. de Teresa, L. Morellon, M. R. Ibarra, F. Guell, F. Peiro, and A. Cornet. Large magnetoresistance in Fe/MgO/FeCo(001) epitaxial tunnel junctions on GaAs(001). *Appl. Phys. Lett.*, 79(11):1655, 2001. ISSN 00036951. doi: 10.1063/1.1404125. URL <http://scitation.aip.org/content/aip/journal/apl/79/11/10.1063/1.1404125>.
56. J. Faure-Vincent, C. Tiusan, E. Jouguelet, F. Canet, M. Sajieddine, C. Bellouard, E. Popova, M. Hehn, F. Montaigne, and A. Schuhl. High tunnel magnetoresistance in epitaxial Fe/MgO/Fe tunnel junctions. *Appl. Phys. Lett.*, 82(25):4507, 2003. ISSN 00036951. doi: 10.1063/1.1586785. URL <http://scitation.aip.org/content/aip/journal/apl/82/25/10.1063/1.1586785>.
57. Shinji Yuasa, Taro Nagahama, Akio Fukushima, Yoshishige Suzuki, and Koji Ando. Giant room-temperature magnetoresistance in single-crystal Fe/MgO/Fe magnetic tunnel junctions. *Nat. Mater.*, 3(12):868–71, dec 2004. ISSN 1476-1122. doi: 10.1038/nmat1257. URL <http://www.ncbi.nlm.nih.gov/pubmed/15516927>.
58. Stuart S P Parkin, Christian Kaiser, Alex Panchula, Philip M Rice, Brian Hughes, Mahesh Samant, and See-Hun Yang. Giant tunnelling magnetoresistance at room temperature with MgO(100) tunnel barriers. *Nat. Mater.*, 3(12):862–7, dec 2004. ISSN 1476-1122. doi: 10.1038/nmat1256. URL <http://dx.doi.org/10.1038/nmat1256>.
59. Shinji Yuasa, Akio Fukushima, Hitoshi Kubota, Yoshishige Suzuki, and Koji Ando. Giant tunneling magnetoresistance up to 410% at room temperature in fully epitaxial Co/MgO/Co magnetic tunnel junctions with bcc Co(001) electrodes. *Appl. Phys. Lett.*, 89(4):042505, jul 2006. ISSN 00036951. doi: 10.1063/1.2236268. URL <http://scitation.aip.org/content/aip/journal/apl/89/4/10.1063/1.2236268>.
60. J. Mathon and A. Umerski. Theory of tunneling magnetoresistance of an epitaxial Fe/MgO/Fe(001) junction. *Phys. Rev. B*, 63(22):220403, may 2001. ISSN 0163-1829. doi: 10.1103/PhysRevB.63.220403. URL <http://link.aps.org/doi/10.1103/PhysRevB.63.220403>.
61. Shinji Yuasa, Akio Fukushima, Taro Nagahama, Koji Ando, and Yoshishige Suzuki. High Tunnel Magnetoresistance at Room Temperature in Fully Epitaxial Fe/MgO/Fe Tunnel Junctions due to Coherent Spin-Polarized Tunneling. *Jpn. J. Appl. Phys.*, 43 (No. 4B):L588–L590, apr 2004. ISSN 0021-4922. doi: 10.1143/JJAP.43.L588. URL <http://iopscience.iop.org/article/10.1143/JJAP.43.L588>.
62. Shinji Yuasa, Taro Nagahama, Akio Fukushima, Yoshishige Suzuki, and Koji Ando. Giant room-temperature magnetoresistance in single-crystal Fe/MgO/Fe magnetic tunnel junctions. *Nat. Mater.*, 3(12):868–71, dec 2004. ISSN 1476-1122. doi: 10.1038/nmat1257. URL <http://dx.doi.org/10.1038/nmat1257>.
63. David D. Djayaprawira, Koji Tsunekawa, Motonobu Nagai, Hiroki Maehara, Shinji Yamagata, Naoki Watanabe, Shinji Yuasa, Yoshishige Suzuki, and Koji Ando. 230%

- room-temperature magnetoresistance in CoFeB/MgO/CoFeB magnetic tunnel junctions. *Appl. Phys. Lett.*, 86(9):092502, feb 2005. ISSN 00036951. doi: 10.1063/1.1871344. URL <http://scitation.aip.org/content/aip/journal/apl/86/9/10.1063/1.1871344>.
64. Shinji Yuasa, Yoshishige Suzuki, Toshikazu Katayama, and Koji Ando. Characterization of growth and crystallization processes in CoFeB/MgO/CoFeB magnetic tunnel junction structure by reflective high-energy electron diffraction. *Appl. Phys. Lett.*, 87(24):242503, dec 2005. ISSN 00036951. doi: 10.1063/1.2140612. URL <http://scitation.aip.org/content/aip/journal/apl/87/24/10.1063/1.2140612>.
  65. J. Hayakawa, S. Ikeda, Y. M. Lee, F. Matsukura, and H. Ohno. Effect of high annealing temperature on giant tunnel magnetoresistance ratio of CoFeB/MgO/CoFeB magnetic tunnel junctions. *Appl. Phys. Lett.*, 89(23):232510, 2006. ISSN 00036951. doi: 10.1063/1.2402904. URL <http://scitation.aip.org/content/aip/journal/apl/89/23/10.1063/1.2402904>.
  66. Y. M. Lee, J. Hayakawa, S. Ikeda, F. Matsukura, and H. Ohno. Effect of electrode composition on the tunnel magnetoresistance of pseudo-spin-valve magnetic tunnel junction with a MgO tunnel barrier. *Appl. Phys. Lett.*, 90(21):212507, may 2007. ISSN 00036951. doi: 10.1063/1.2742576. URL <http://scitation.aip.org/content/aip/journal/apl/90/21/10.1063/1.2742576>.
  67. S. Ikeda, K. Miura, H. Yamamoto, K. Mizunuma, H. D. Gan, M. Endo, S. Kanai, J. Hayakawa, F. Matsukura, and H. Ohno. A perpendicular-anisotropy CoFeB-MgO magnetic tunnel junction. *Nat. Mater.*, 9(9):721–4, sep 2010. ISSN 1476-1122. doi: 10.1038/nmat2804. URL <http://www.ncbi.nlm.nih.gov/pubmed/20622862>.
  68. Joseph A. Stroscio, D. T. Pierce, A. Davies, R. J. Celotta, and M. Weinrt. Tunneling Spectroscopy of bcc (001) Surface States. *Phys. Rev. Lett.*, 75(16):2960–2963, 1995. doi: 10.1103/PhysRevLett.75.2960.
  69. J. P. Velev, K. D. Belashchenko, and E. Y. Tsymlal. Comment on "destructive effect of disorder and bias voltage on interface resonance transmission in symmetric tunnel junctions". *Phys. Rev. Lett.*, 96(11):119601, 2006. ISSN 00319007. doi: 10.1103/PhysRevLett.96.119601.
  70. O. Wunnicke, N. Papanikolaou, R. Zeller, P. Dederichs, V. Drchal, and J. Kudrnovský. Effects of resonant interface states on tunneling magnetoresistance. *Phys. Rev. B*, 65(6):064425, 2002. ISSN 0163-1829. doi: 10.1103/PhysRevB.65.064425. URL <http://link.aps.org/doi/10.1103/PhysRevB.65.064425>.
  71. C. Tiusan, J. Faure-Vincent, C. Bellouard, M. Hehn, E. Jouguelet, and A. Schuhl. Interfacial resonance state probed by spin-polarized tunneling in epitaxial Fe/MgO/Fe tunnel junctions. *Phys. Rev. Lett.*, 93(10):3–6, 2004. ISSN 00319007. doi: 10.1103/PhysRevLett.93.106602.

## Bibliography

72. K D Belashchenko, J Velev, and E Y Tsymbal. Effect of interface states on spin-dependent tunneling in Fe/MgO/Fe tunnel junctions. *Phys. Rev. B*, 72:140404(R), 2005. doi: 10.1103/PhysRevB.72.140404.
73. P.-J. Zermatten, G. Gaudin, G. Maris, M. Miron, A. Schuhl, C. Tiusan, F. Greullet, and M. Hehn. Experimental evidence of interface resonance states in single-crystal magnetic tunnel junctions. *Phys. Rev. B*, 78(3):033301, 2008. ISSN 1098-0121. doi: 10.1103/PhysRevB.78.033301. URL <http://link.aps.org/doi/10.1103/PhysRevB.78.033301>.
74. H L Meyerheim, R Popescu, J Kirschner, N Jedrecy, M Sauvage-Simkin, B Heinrich, and R Pinchaux. Geometrical and compositional structure at metal-oxide interfaces: MgO on Fe(001). *Phys. Rev. Lett.*, 87(7):076102, 2001. ISSN 0031-9007. doi: 10.1103/PhysRevLett.87.076102.
75. S. G. Wang, G. Han, G. H. Yu, Y. Jiang, C. Wang, A. Kohn, and R. C C Ward. Evidence for FeO formation at the Fe/MgO interface in epitaxial TMR structure by X-ray photoelectron spectroscopy. *J. Magn. Magn. Mater.*, 310(2 SUPPL. PART 3): 1935–1936, 2007. ISSN 03048853. doi: 10.1016/j.jmmm.2006.10.767.
76. X.-G. Zhang, W. H. Butler, and Amrit Bandyopadhyay. Effects of the iron-oxide layer in Fe-FeO-MgO-Fe tunneling junctions. *Phys. Rev. B*, 68(9):6–9, 2003. ISSN 0163-1829. doi: 10.1103/PhysRevB.68.092402. URL <http://link.aps.org/doi/10.1103/PhysRevB.68.092402>.
77. F. Bonell, S. Andrieu, a. Bataille, C. Tiusan, and G. Lengaigne. Consequences of interfacial Fe-O bonding and disorder in epitaxial Fe/MgO/Fe(001) magnetic tunnel junctions. *Phys. Rev. B*, 79(22):224405, jun 2009. ISSN 1098-0121. doi: 10.1103/PhysRevB.79.224405. URL <http://link.aps.org/doi/10.1103/PhysRevB.79.224405>.
78. P. Luches, S. Benedetti, M. Liberati, F. Boscherini, I. I. Pronin, and S. Valeri. Absence of oxide formation at the Fe/MgO(0 0 1) interface. *Surf. Sci.*, 583(2-3):191–198, 2005. ISSN 00396028. doi: 10.1016/j.susc.2005.03.038.
79. L. Plucinski, Y. Zhao, B. Sinkovic, and E. Vescovo. MgO Fe (100) interface: A study of the electronic structure. *Phys. Rev. B - Condens. Matter Mater. Phys.*, 75(21):1–8, 2007. ISSN 10980121. doi: 10.1103/PhysRevB.75.214411.
80. M. Sicot, S. Andrieu, C. Tiusan, F. Montaigne, and F. Bertran. On the quality of molecular-beam epitaxy grown FeMgO and CoMgO (001) interfaces. *J. Appl. Phys.*, 99(8):65–68, 2006. ISSN 00218979. doi: 10.1063/1.2165914.
81. C. Tiusan, M. Sicot, M. Hehn, C. Belouard, S. Andrieu, F. Montaigne, and A. Schuhl. Fe/MgO interface engineering for high-output-voltage device applications. *Appl. Phys. Lett.*, 88(6):86–89, 2006. ISSN 00036951. doi: 10.1063/1.2172717.

82. C Tiusan, M Sicot, J Faure-Vincent, M Hehn, C Bellouard, F Montaigne, S Andrieu, and A Schuhl. Static and dynamic aspects of spin tunnelling in crystalline magnetic tunnel junctions. *J. Phys. Condens. Matter*, 18:941–956, 2006. ISSN 0953-8984. doi: 10.1088/0953-8984/18/3/012.
83. C. Zhang, X. G. Zhang, P. S. Krstić, Hai Ping Cheng, W. H. Butler, and J. M. MacLaren. Electronic structure and spin-dependent tunneling conductance under a finite bias. *Phys. Rev. B - Condens. Matter Mater. Phys.*, 69(13):1–12, 2004. ISSN 01631829. doi: 10.1103/PhysRevB.69.134406.
84. T. X. Wang, Y. Li, K. J. Lee, J. U. Cho, D. K. Kim, S. J. Noh, and Y. K. Kim. Influence of interface state in Fe/MgO/Fe magnetic tunnel junction system: C modified interfaces—a first principle study. *J. Appl. Phys.*, 109(8), 2011. ISSN 00218979. doi: 10.1063/1.3575337.
85. M. Klaua, D. Ullmann, J. Barthel, W. Wulfhekkel, J. Kirschner, R. Urban, T. Monchisky, a. Enders, J. Cochran, and B. Heinrich. Growth, structure, electronic, and magnetic properties of MgO/Fe(001) bilayers and Fe/MgO/Fe(001) trilayers. *Phys. Rev. B*, 64(13):1–8, 2001. ISSN 0163-1829. doi: 10.1103/PhysRevB.64.134411.
86. C Tiusan, F Greullet, M Hehn, F Montaigne, S Andrieu, and A Schuhl. Spin tunnelling phenomena in single-crystal magnetic tunnel junction systems. *J. Phys. Condens. Matter*, 19(16):165201, 2007. ISSN 0953-8984. doi: 10.1088/0953-8984/19/16/165201.
87. Frederic Bonell, Stephane Andrieu, Francois Bertran, Patrick Lefevre, Amina Taleb Ibrahim, Etienne Snoeck, Coriolan Viorel Tiusan, and Francois Montaigne. MgO-based epitaxial magnetic tunnel junctions using Fe-V electrodes. *IEEE Trans. Magn.*, 45(10):3467–3471, 2009. ISSN 00189464. doi: 10.1109/TMAG.2009.2022644.
88. Frédéric Bonell. *Analyse du transport dans les jonctions tunnel magnétiques épitaxiées à barrière de MgO(001) par manipulation des interfaces, de la barrière et des électrodes*. PhD thesis, Université Henri Poincaré - Nancy I, 2009. URL <https://tel.archives-ouvertes.fr/tel-00456413>.
89. F. Bonell, S. Andrieu, C. Tiusan, F. Montaigne, E. Snoeck, B. Belhadji, L. Calmels, F. Bertran, P. Le Fèvre, and A. Taleb-Ibrahimi. Influence of misfit dislocations on the magnetoresistance of MgO-based epitaxial magnetic tunnel junctions. *Phys. Rev. B - Condens. Matter Mater. Phys.*, 82(9):1–4, 2010. ISSN 10980121. doi: 10.1103/PhysRevB.82.092405.
90. C. Tusche, H. L. Meyerheim, N. Jedrecy, G. Renaud, A. Ernst, J. Henk, P. Bruno, and J. Kirschner. Oxygen-induced symmetrization and structural coherency in Fe/MgO/Fe(001) magnetic tunnel junctions. *Phys. Rev. Lett.*, 95(17):1–4, 2005. ISSN 00319007. doi: 10.1103/PhysRevLett.95.176101.
91. Hiroyoshi Itoh. Theory of tunnel magnetoresistance and spin filter effect in magnetic tunnel junctions. *J. Phys. D. Appl. Phys.*, 40(5):1228–1233, 2007. ISSN 0022-3727.

## Bibliography

- doi: 10.1088/0022-3727/40/5/S03. URL <http://stacks.iop.org/0022-3727/40/i=5/a=S03?key=crossref.db3d3419f299a57b3d78d45af08c7f92>.
92. P. X. Xu, V. M. Karpan, K. Xia, M. Zwierzycki, I. Marushchenko, and P. J. Kelly. Influence of roughness and disorder on tunneling magnetoresistance. *Phys. Rev. B - Condens. Matter Mater. Phys.*, 73(18):1–4, 2006. ISSN 10980121. doi: 10.1103/PhysRevB.73.180402.
  93. Youqi Ke, Ke Xia, and Hong Guo. Disorder scattering in magnetic tunnel junctions: Theory of nonequilibrium vertex correction. *Phys. Rev. Lett.*, 100(16):1–4, 2008. ISSN 00319007. doi: 10.1103/PhysRevLett.100.166805.
  94. R. Guerrero, D. Herranz, F. G. Aliev, F. Greullet, C. Tiusan, M. Hehn, and F. Montaigne. High bias voltage effect on spin-dependent conductivity and shot noise in carbon-doped Fe (001) MgO (001) Fe (001) magnetic tunnel junctions. *Appl. Phys. Lett.*, 91(13):8–11, 2007. ISSN 00036951. doi: 10.1063/1.2793619.
  95. Christian Heiliger, Peter Zahn, Bogdan Yu Yavorsky, and Ingrid Mertig. Influence of the interface structure on the bias dependence of tunneling magnetoresistance. *Phys. Rev. B*, 72(18):1–4, 2005. ISSN 10980121. doi: 10.1103/PhysRevB.72.180406.
  96. Derek Waldron, Vladimir Timoshevskii, Yibin Hu, Ke Xia, and Hong Guo. First principles modeling of tunnel magnetoresistance of Fe/MgO/Fe trilayers. *Phys. Rev. Lett.*, 97(22):1–4, 2006. ISSN 00319007. doi: 10.1103/PhysRevLett.97.226802.
  97. Ivan Rungger, Oleg Mryasov, and Stefano Sanvito. Resonant electronic states and I-V curves of Fe/MgO/Fe(100) tunnel junctions. *Phys. Rev. B*, 79(9):2–6, 2009. ISSN 10980121. doi: 10.1103/PhysRevB.79.094414.
  98. By R H Fowler and L Nordheim. Electron Emission in Intense Electric Fields. *Phys. Rev. Proc. Nat. Ac. Sci. Roy. Soc. Proc. Z. f. Phys.*, 119(781), 1928. ISSN 1364-5021. doi: 10.1098/rspa.1928.0091.
  99. Bert Voigtländer. *Scanning Probe Microscopy Atomic Force Microscopy and Scanning Tunneling Microscopy*. Springer-Verlag Berlin Heidelberg, Berlin, springer edition, 2015.
  100. S. O. Valenzuela, D. J. Monsma, C. M. Marcus, V. Narayanamurti, and M. Tinkham. Spin polarized tunneling at finite bias. *Phys. Rev. Lett.*, 94(19):1–4, 2005. ISSN 00319007. doi: 10.1103/PhysRevLett.94.196601.
  101. B. Belhadji and L. Calmels. Bulk electron states with Delta symmetry in disordered Fe-based alloys for magnetic tunnel junctions. *Phys. Rev. B*, 83(9):1–4, 2011. ISSN 10980121. doi: 10.1103/PhysRevB.83.092401.
  102. F. Bonell, T. Hauet, S. Andrieu, F. Bertran, P. Le Fèvre, L. Calmels, a. Tejada, F. Montaigne, B. Warot-Fonrose, B. Belhadji, a. Nicolaou, and a. Taleb-Ibrahimi.

- Spin-Polarized Electron Tunneling in bcc FeCo/MgO/FeCo(001) Magnetic Tunnel Junctions. *Phys. Rev. Lett.*, 108(17):176602, apr 2012. ISSN 0031-9007. doi: 10.1103/PhysRevLett.108.176602. URL <http://link.aps.org/doi/10.1103/PhysRevLett.108.176602>.
103. Do Bang, T. Nozaki, D. D. Djayaprawira, M. Shiraishi, Y. Suzuki, A. Fukushima, H. Kubota, T. Nagahama, S. Yuasa, H. Maehara, K. Tsunekawa, Y. Nagamine, N. Watanabe, and H. Itoh. Inelastic tunneling spectra of MgO barrier magnetic tunneling junctions showing large magnon contribution. *J. Appl. Phys.*, 105(7):25–28, 2009. ISSN 00218979. doi: 10.1063/1.3063674.
104. Paul K. Hansma. Inelastic Electron Tunneling. *Phys. Rep.*, 30(2):145–206, 1977.
105. C. J. Adkin. Inelastic electron tunnelling spectroscopy. *J. Phys. C Solid State Phys.*, 18:1313–1346, 1985.
106. D.M. Lewis, J.E.D. Spencer, and B.O. Field. An introduction to Inelastic Electron Tunneling Spectroscopy (IETS) and its chemical applications. *Spectrochim. Acta Part A Mol. Spectrosc.*, 44(3):247–261, 1988. ISSN 05848539. doi: 10.1016/0584-8539(88)80014-X. URL <http://www.sciencedirect.com/science/article/pii/058485398880014X>.
107. Wei He and T. P. Ma. Inelastic electron tunneling spectroscopy study of traps in ultrathin high-k gate dielectrics. *Appl. Phys. Lett.*, 83(26):5461–5463, 2003. ISSN 00036951. doi: 10.1063/1.1636519.
108. Wei He and T P Ma. Inelastic electron tunneling spectroscopy study of ultrathin HfO<sub>2</sub> and HfAlO. *Appl. Phys. Lett.*, 83(13):2605, 2003. ISSN 00036951. doi: 10.1063/1.1614837.
109. Miaomiao Wang, Wei He, and T. P. Ma. Electron tunneling spectroscopy study of traps in high-k gate dielectrics: Determination of physical locations and energy levels of traps. *Appl. Phys. Lett.*, 86(19):192113, 2005. ISSN 00036951. doi: 10.1063/1.1924893. URL <http://link.aip.org/link/APPLAB/v86/i19/p192113/s1{&}Agg=doi>.
110. James W Reiner, Sharon Cui, Zuoguang Liu, Miaomiao Wang, Charles H Ahn, and T P Ma. Inelastic electron tunneling spectroscopy study of thin gate dielectrics. *Adv. Mater.*, 22(26-27):2962–2968, 2010. ISSN 1521-4095. doi: 10.1002/adma.200904311.
111. S. Zhang, P. Levy, a. Marley, and S. Parkin. Quenching of Magnetoresistance by Hot Electrons in Magnetic Tunnel Junctions. *Phys. Rev. Lett.*, 79(19):3744–3747, 1997. ISSN 0031-9007. doi: 10.1103/PhysRevLett.79.3744.
112. Xiu-Feng Han, Andrew C C Yu, Mikihiro Oogane, Junichirou Murai, Tadaomi Dai-bou, and Terunobu Miyazaki. Analyses of intrinsic magnetoelectric properties in spin-valve-type tunnel junctions with high magnetoresistance and low resistance. *Phys. Rev. B*, 63:224404, 2001. ISSN 0163-1829. doi: 10.1103/PhysRevB.63.224404.

## Bibliography

113. V. Drewello, J. Schmalhorst, A. Thomas, and G. Reiss. Evidence for strong magnon contribution to the TMR temperature dependence in MgO based tunnel junctions. *Phys. Rev. B*, 77(1):1–5, 2008. ISSN 10980121. doi: 10.1103/PhysRevB.77.014440.
114. H. X. Wei, Q. H. Qin, Q. L. Ma, X. G. Zhang, and X. F. Han. Inelastic electron tunneling spectrum from surface magnon and magnetic impurity scatterings in magnetic tunnel junctions. *Phys. Rev. B*, 82(13):1–6, 2010. ISSN 10980121. doi: 10.1103/PhysRevB.82.134436.
115. A. M. Bratkovsky. Assisted tunneling in ferromagnetic junctions and half-metallic oxides. *Appl. Phys. Lett.*, 72(18):2334–2336, 1998. ISSN 00036951. doi: 10.1063/1.121342.
116. T. Dimopoulos, Y. Henry, V. Da Costa, C. Tiusan, and K. Ounadjela. Influence of barrier overoxidation and annealing on the inelastic spin-dependent tunneling in AlO<sub>x</sub>-based junctions. *J. Appl. Phys.*, 95(11 II):6936–6938, 2004. ISSN 00218979. doi: 10.1063/1.1667411.
117. G. X. Du, S. G. Wang, Q. L. Ma, Yan Wang, R. C C Ward, X. G. Zhang, C. Wang, A. Kohn, and X. F. Han. Spin-dependent tunneling spectroscopy for interface characterization of epitaxial Fe/MgO/Fe magnetic tunnel junctions. *Phys. Rev. B*, 81(6):3–6, 2010. ISSN 10980121. doi: 10.1103/PhysRevB.81.064438.
118. Y. Ando, T. Miyakoshi, M. Oogane, T. Miyazaki, H. Kubota, K. Ando, and S. Yuasa. Spin-dependent tunneling spectroscopy in single-crystal Fe/MgO/Fe tunnel junctions. *Appl. Phys. Lett.*, 87(14):1–3, 2005. ISSN 00036951. doi: 10.1063/1.2077861.
119. Shingo Nishioka, Rie Matsumoto, Hiroyuki Tomita, Takayuki Nozaki, Yoshishige Suzuki, Hiroyoshi Itoh, and Shinji Yuasa. Spin dependent tunneling spectroscopy in single crystalline bcc-Co/MgO/bcc-Co(001) junctions. *Appl. Phys. Lett.*, 93(12):91–94, 2008. ISSN 00036951. doi: 10.1063/1.2988647.
120. W. G. Wang, C. Ni, A. Rumaiz, Y. Wang, X. Fan, T. Moriyama, R. Cao, Q. Y. Wen, H. W. Zhang, and John Q. Xiao. Real-time evolution of tunneling magnetoresistance during annealing in CoFeBMgOCoFeB magnetic tunnel junctions. *Appl. Phys. Lett.*, 92(15):2006–2009, 2008. ISSN 00036951. doi: 10.1063/1.2903147.
121. Shinji Isogami, Masakiyo Tsunoda, Kojiro Komagaki, Kazuyuki Sunaga, Yuji Uehara, Masashige Sato, Toyoo Miyajima, and Migaku Takahashi. In situ heat treatment of ultrathin MgO layer for giant magnetoresistance ratio with low resistance area product in CoFeB/MgO/CoFeB magnetic tunnel junctions. *Appl. Phys. Lett.*, 93(19):91–94, 2008. ISSN 00036951. doi: 10.1063/1.3021372.
122. Q. L. Ma, S. G. Wang, H. X. Wei, H. F. Liu, X. G. Zhang, and X. F. Han. Evidence for magnon excitation contribution to the magnetoresistance behavior during thermal annealing in CoFeB/MgO/CoFeB magnetic tunnel junctions. *Phys. Rev. B*, 83(22):2–5, 2011. ISSN 10980121. doi: 10.1103/PhysRevB.83.224430.

123. Zhongchang Wang, Mitsuhiro Saito, Keith P. McKenna, Shunsuke Fukami, Hideo Sato, Shoji Ikeda, Hideo Ohno, and Yuichi Ikuhara. Atomic-Scale Structure and Local Chemistry of CoFeB–MgO Magnetic Tunnel Junctions. *Nano Lett.*, 16(3):1530–1536, 2016. ISSN 1530-6984. doi: 10.1021/acs.nanolett.5b03627. URL <http://pubs.acs.org/doi/abs/10.1021/acs.nanolett.5b03627>.
124. J. C. Read, P. G. Mather, and R. A. Buhrman. X-ray photoemission study of CoFeB/MgO thin film bilayers. *Appl. Phys. Lett.*, 90(13), 2007. ISSN 00036951. doi: 10.1063/1.2717091.
125. J. J. Cha, J. C. Read, W. F. Egelhoff, P. Y. Huang, H. W. Tseng, Y. Li, R. A. Buhrman, and D. A. Muller. Atomic-scale spectroscopic imaging of CoFeB/Mg-B-O/CoFeB magnetic tunnel junctions. *Appl. Phys. Lett.*, 95(3):2007–2010, 2009. ISSN 00036951. doi: 10.1063/1.3184766.
126. Zhaoqiang Bai, Lei Shen, Qingyun Wu, Minggang Zeng, Jian Sheng Wang, Guchang Han, and Yuan Ping Feng. Boron diffusion induced symmetry reduction and scattering in CoFeB/MgO/CoFeB magnetic tunnel junctions. *Phys. Rev. B - Condens. Matter Mater. Phys.*, 87(1):1–6, 2013. ISSN 10980121. doi: 10.1103/PhysRevB.87.014114.
127. S. V. Karthik, Y. K. Takahashi, T. Ohkubo, K. Hono, S. Ikeda, and H. Ohno. Transmission electron microscopy investigation of CoFeB/MgO/CoFeB pseudospin valves annealed at different temperatures. *J. Appl. Phys.*, 106(2), 2009. ISSN 00218979. doi: 10.1063/1.3182817.
128. W. G. Wang, J. Jordan-Sweet, G. X. Miao, C. Ni, A. K. Rumaiz, L. R. Shah, X. Fan, P. Parsons, R. Stearrett, E. R. Nowak, J. S. Moodera, and J. Q. Xiao. In-situ characterization of rapid crystallization of amorphous CoFeB electrodes in CoFeB/MgO/CoFeB junctions during thermal annealing. *Appl. Phys. Lett.*, 95(24):93–96, 2009. ISSN 00036951. doi: 10.1063/1.3273397.
129. W. G. Wang, C. Ni, G. X. Miao, C. Weiland, L. R. Shah, X. Fan, P. Parson, J. Jordan-sweet, X. M. Kou, Y. P. Zhang, R. Stearrett, E. R. Nowak, R. Opila, J. S. Moodera, and J. Q. Xiao. Understanding tunneling magnetoresistance during thermal annealing in MgO-based junctions with CoFeB electrodes. *Phys. Rev. B*, 81(14):144406, apr 2010. ISSN 1098-0121. doi: 10.1103/PhysRevB.81.144406. URL <http://link.aps.org/doi/10.1103/PhysRevB.81.144406>.
130. Volker Drewello, Markus Schäfers, Oliver Schebaum, Ayaz Arif Khan, Jana Münchenberger, Jan Schmalhorst, Günter Reiss, and Andy Thomas. Inelastic electron tunneling spectra of MgO-based magnetic tunnel junctions with different electrode designs. *Phys. Rev. B*, 79(17):1–6, 2009. ISSN 10980121. doi: 10.1103/PhysRevB.79.174417.
131. P. A. Thiry, M. Liehr, J. J. Pireaux, and R. Caudano. Infrared optical constants of insulators determined by high-resolution electron-energy-loss spectroscopy. *Phys. Rev. B*, 29(8), 1984. ISSN 1098-6596.

## Bibliography

132. Rie Matsumoto, Yusuke Hamada, Masaki Mizuguchi, Masashi Shiraishi, Hiroki Maehara, Koji Tsunekawa, David D. Djayaprawira, Naoki Watanabe, Yoshinari Kurosaki, Taro Nagahama, Akio Fukushima, Hitoshi Kubota, Shinji Yuasa, and Yoshishige Suzuki. Tunneling spectra of sputter-deposited CoFeB/MgO/CoFeB magnetic tunnel junctions showing giant tunneling magnetoresistance effect. *Solid State Commun.*, 136(11-12):611–615, 2005. ISSN 00381098. doi: 10.1016/j.ssc.2005.08.032.
133. Guo Xing Miao, Krishna B. Chetry, Arunava Gupta, William H. Butler, Koji Tsunekawa, David Djayaprawira, and Gang Xiao. Inelastic tunneling spectroscopy of magnetic tunnel junctions based on CoFeB/MgO/CoFeB with Mg insertion layer. *J. Appl. Phys.*, 99(8):1–4, 2006. ISSN 00218979. doi: 10.1063/1.2162047.
134. J. Bernos, M. Hehn, F. Montaigne, C. Tiusan, D. Lacour, M. Alnot, B. Negulescu, G. Lengaigne, E. Snoeck, and F. G. Aliev. Impact of electron-electron interactions induced by disorder at interfaces on spin-dependent tunneling in CoFeB MgO CoFeB magnetic tunnel junctions. *Phys. Rev. B*, 82(6):060405, 2010. ISSN 1098-0121. doi: 10.1103/PhysRevB.82.060405.
135. J. M. Teixeira, J. Ventura, M. P. Fernandez-Garcia, J. P. Araujo, J. B. Sousa, P. Wisniowski, and P. P. Freitas. Electrode band structure effects in thin MgO magnetic tunnel junctions. *Appl. Phys. Lett.*, 100(7):072406, 2012. ISSN 00036951. doi: 10.1063/1.3687200. URL <http://link.aip.org/link/APPLAB/v100/i7/p072406/s1?Agg=doi>.
136. S. Ringer, M. Vieth, L. B??r, M. R??hrig, and G. Bayreuther. Conductance anomalies of CoFeB/MgO/CoFeB magnetic tunnel junctions. *Phys. Rev. B*, 90(17):1–9, 2014. ISSN 1550235X. doi: 10.1103/PhysRevB.90.174401.
137. J. M. Teixeira, J. D. Costa, J. Ventura, J. B. Sousa, P. Wisniowski, and P. P. Freitas. Observation of spin-dependent quantum well resonant tunneling in textured CoFeB layers. *Appl. Phys. Lett.*, 104(11):0–4, 2014. ISSN 00036951. doi: 10.1063/1.4869484.
138. J. M. Teixeira, J. Ventura, J. P. Araujo, J. B. Sousa, P. Wisniowski, S. Cardoso, and P. P. Freitas. Resonant Tunneling through Electronic Trapping States in Thin MgO Magnetic Junctions. *Phys. Rev. Lett.*, 106(19):196601, may 2011. ISSN 0031-9007. doi: 10.1103/PhysRevLett.106.196601. URL <http://link.aps.org/doi/10.1103/PhysRevLett.106.196601>.
139. Chang Shang, Janusz Nowak, Ronnie Jansen, and Jagadeesh Moodera. Temperature dependence of magnetoresistance and surface magnetization in ferromagnetic tunnel junctions. *Phys. Rev. B*, 58(6):R2917–R2920, aug 1998. ISSN 0163-1829. doi: 10.1103/PhysRevB.58.R2917. URL <http://link.aps.org/doi/10.1103/PhysRevB.58.R2917>.

140. R. Stratton. Volt-current characteristics for tunneling through insulating films. *J. Phys. Chem. Solids*, 23(9):1177–1190, 1962. ISSN 00223697. doi: 10.1016/0022-3697(62)90165-8.
141. John G. Simmons. Generalized thermal J-V characteristic for the electric tunnel effect. *J. Appl. Phys.*, 35(9):2655–2658, 1964. ISSN 00218979. doi: 10.1063/1.1713820.
142. X. Kou, J. Schmalhorst, A. Thomas, and G. Reiss. Temperature dependence of the resistance of magnetic tunnel junctions with MgO barrier. *Appl. Phys. Lett.*, 88(21):1–4, 2006. ISSN 00036951. doi: 10.1063/1.2206680.
143. S. G. Wang, R. C C Ward, G. X. Du, X. F. Han, C. Wang, and A. Kohn. Temperature dependence of giant tunnel magnetoresistance in epitaxial Fe/MgO/Fe magnetic tunnel junctions. *Phys. Rev. B - Condens. Matter Mater. Phys.*, 78(18):2–5, 2008. ISSN 10980121. doi: 10.1103/PhysRevB.78.180411.
144. Q. L. Ma, S. G. Wang, J. Zhang, Yan Wang, R. C C Ward, C. Wang, A. Kohn, X. G. Zhang, and X. F. Han. Temperature dependence of resistance in epitaxial Fe/MgO/Fe magnetic tunnel junctions. *Appl. Phys. Lett.*, 95(5):1–4, 2009. ISSN 00036951. doi: 10.1063/1.3194150.
145. J. M. Teixeira, J. Ventura, J. P. Araujo, J. B. Sousa, P. Wisniowski, and P. P. Freitas. Tunneling processes in thin MgO magnetic junctions. *Appl. Phys. Lett.*, 96(26):2008–2011, 2010. ISSN 00036951. doi: 10.1063/1.3458701.
146. Sir Nevill Mott. Electrons in glass. *Nobel Lect.*, 1977.
147. A. I. Larkin and K. A. Matveev. Current-voltage characteristics of mesoscopic semiconductor contacts. *Zh. Eksp. Teor. Fiz.*, 93(January 1987):1030–1038, 1987. URL [http://www.jetp.ac.ru/cgi-bin/dn/e/{\\_}066{\\_-}03{\\_-}0580.pdf](http://www.jetp.ac.ru/cgi-bin/dn/e/{_}066{_-}03{_-}0580.pdf).
148. Yizi Xu, D. Ephron, and M. R. Beasley. Directed inelastic hopping of electrons through metal-insulator-metal tunnel junctions. *Phys. Rev. B*, 52(4):2843–2859, 1995. ISSN 01631829. doi: 10.1103/PhysRevB.52.2843.
149. L. I. Glazman and R. I. Shekhter. Inelastic resonant tunneling of electrons through a potential barrier. *J. Exp. Theor. Phys.*, 67(1):163–170, 1988. URL <http://www.jetp.ac.ru/cgi-bin/e/index/e/67/1/p163?a=list>.
150. N. S. Wingreen, K. W. Jacobsen, and J. W. Wilkins. Resonant Tunneling with Electron-Phonon Interaction: An Exactly Solvable Model. *Phys. Rev. Lett.*, 61(12), 1988.
151. L I Glazman and K A Matveev. Inelastic tunneling across thin amorphous films. *Sov. Phys. JETP*, 67(6):1276–1282, 1988.

## Bibliography

152. A. M. Bratkovsky. Tunneling of electrons in conventional and half-metallic systems: Towards very large magnetoresistance. *Phys. Rev. B*, 56(5):2344–2347, 1997. ISSN 0163-1829. doi: 10.1103/PhysRevB.56.2344.
153. F. Guinea. Spin-flip scattering in magnetic junctions. *Phys. Rev. B*, 58(14):9212, 1998. ISSN 0163-1829. doi: 10.1103/PhysRevB.58.9212. URL <http://link.aps.org/doi/10.1103/PhysRevB.58.9212>~~delimiter"026E30F\$nh~~[http://prb.aps.org/abstract/PRB/v58/i14/p9212{ }1](http://prb.aps.org/abstract/PRB/v58/i14/p9212{ }1$delimiter)~~delimiter"026E30F\$nh~~<http://prb.aps.org/pdf/PRB/v58/i14/p9212{ }1>.
154. A Vedyayev, D Bagrets, A Bagrets, and B Dieny. Resonant spin-dependent tunneling in spin-valve junctions in the presence of paramagnetic impurities. *Phys. Rev.*, 63, 2001. ISSN 0163-1829. doi: 10.1103/PhysRevB.63.064429.
155. R. Jansen and J. Moodera. Magnetoresistance in doped magnetic tunnel junctions: Effect of spin scattering and impurity-assisted transport. *Phys. Rev. B*, 61(13):9047–9050, 2000. ISSN 0163-1829. doi: 10.1103/PhysRevB.61.9047.
156. Y. Lu, M. Tran, H. Jaffrès, P. Seneor, C. Deranlot, F. Petroff, J-M. George, B. Lépine, S. Ababou, and G. Jézéquel. Spin-Polarized Inelastic Tunneling through Insulating Barriers. *Phys. Rev. Lett.*, 102(17):176801, apr 2009. ISSN 0031-9007. doi: 10.1103/PhysRevLett.102.176801. URL <http://link.aps.org/doi/10.1103/PhysRevLett.102.176801>.
157. Gianfranco Pacchioni and Hajo Freund. Electron transfer at oxide surfaces. the MgO paradigm: From defects to ultrathin films. *Chem. Rev.*, 113(6):4035–4072, 2013. ISSN 00092665. doi: 10.1021/cr3002017.
158. J. P. Velev, K. D. Belashchenko, S. S. Jaswal, and E. Y. Tsympal. Effect of oxygen vacancies on spin-dependent tunneling in Fe/MgO/Fe magnetic tunnel junctions. *Appl. Phys. Lett.*, 90(7):072502, 2007. ISSN 00036951. doi: 10.1063/1.2643027. URL <http://link.aip.org/link/APPLAB/v90/i7/p072502/s1{&}Agg=doi>.
159. Youqi Ke, Ke Xia, and Hong Guo. Oxygen-Vacancy-Induced Diffusive Scattering in Fe/MgO/Fe Magnetic Tunnel Junctions. *Phys. Rev. Lett.*, 105(23):236801, nov 2010. ISSN 0031-9007. doi: 10.1103/PhysRevLett.105.236801. URL <http://link.aps.org/doi/10.1103/PhysRevLett.105.236801>.
160. J. Mathon and A. Umerski. Theory of tunneling magnetoresistance in a disordered Fe/MgO/Fe(001) junction. *Phys. Rev. B*, 74(14):140404, oct 2006. ISSN 1098-0121. doi: 10.1103/PhysRevB.74.140404. URL <http://link.aps.org/doi/10.1103/PhysRevB.74.140404>.
161. P Bruno. Theory of interlayer magnetic coupling. *Phys. Rev. B*, 52(1), 1995.
162. J Faure-Vincent, C Tiusan C Bellouard, E Popova, M Hehn, F Montaigne, and a Schuhl. Interlayer magnetic coupling interactions of two ferromagnetic layers by

- spin polarized tunneling. *Phys. Rev. Lett.*, 89(10):107206, 2002. ISSN 0031-9007. doi: 10.1103/PhysRevLett.89.189902.
163. M. Ye Zhuravlev, E. Y. Tsymbal, and A. V. Vedyayev. Impurity-assisted interlayer exchange coupling across a tunnel barrier. *Phys. Rev. Lett.*, 94(2):1–4, 2005. ISSN 00319007. doi: 10.1103/PhysRevLett.94.026806.
164. T Katayama, S Yuasa, J Velez, M Ye Zhuravlev, S S Jaswal, and E Y Tsymbal. Interlayer exchange coupling in Fe/MgO/Fe magnetic tunnel junctions. *Appl. Phys. Lett.*, 89(11):112503, 2006. doi: 10.1063/1.2349321. URL <http://link.aip.org/link/?APL/89/112503/1>.
165. A. Lawrence Kappers, Roger L. Kroes, and Eugene B. Hensley. F<sup>+</sup> and F<sup>'</sup> Centers in Magnesium Oxide\*. *Phys. Rev. B*, 863(1968), 1970.
166. G.P Summers, T. M. Wilson, B. T. Jeffries, H.T Thover, Y. Chen, and M. M. Abraham. Luminescence from oxygen vacancies in MgO crystals thermochemically reduced at high temperatures. *Phys. Rev. B*, 27(2):1283–1291, 1983.
167. G. H. Rosenblatt, M. W. Rowe, G. P. Williams Jr., R. T. Williams, and Y. Chen. Luminescence of F and F<sup>+</sup> centers in magnesium oxide. *Phys. Rev. B*, 39(14), 1989.
168. R. Gonzalez, M. A. Monge, J. E. Munoz Santiuste, R. Pareja, Y. Chen, E. Kotomin, M. M. Kukla, and A. I. Popov. Photoconversion of F<sup>-</sup> type centers in thermochemically reduced MgO single crystals. *Phys. Rev. B*, 59(7):4786–4790, 1999.
169. Y. Uenaka and T. Uchino. Photoexcitation, trapping, and recombination processes of the F-type centers in lasing MgO microcrystals. *Phys. Rev. B*, 83(19):195108, may 2011. ISSN 1098-0121. doi: 10.1103/PhysRevB.83.195108. URL <http://link.aps.org/doi/10.1103/PhysRevB.83.195108>.
170. A. E. Hughes and B. Henderson. Color Centers in Simple Oxides. In J. H. Crawford and L. M. Slifkin, editors, *Point Defects in Solids*, chapter 7, pages 381–484. Plenum Press, New York, 1972.
171. Andrew Gibson, Roger Haydock, and John P Lapemina. Stability of vacancy defects in Mgo: The role of charge neutrality. *Phys. Rev. B*, 50(4):2582–2592, 1994.
172. Patrick Rinke, André Schleife, Emmanouil Kioupakis, Anderson Janotti, Claudia Rödl, Friedhelm Bechstedt, Matthias Scheffler, and Chris G. Van de Walle. First-Principles Optical Spectra for F Centers in MgO. *Phys. Rev. Lett.*, 108(12):126404, mar 2012. ISSN 0031-9007. doi: 10.1103/PhysRevLett.108.126404. URL <http://link.aps.org/doi/10.1103/PhysRevLett.108.126404>.
173. Elif Ertekin, Lucas K. Wagner, and Jeffrey C. Grossman. Point-defect optical transitions and thermal ionization energies from quantum Monte Carlo methods: Application to the F-center defect in MgO. *Phys. Rev. B - Condens. Matter Mater. Phys.*, 87(15):1–7, 2013. ISSN 10980121. doi: 10.1103/PhysRevB.87.155210.

## Bibliography

174. Barry M Klein, Warren E Pickett, Larry L Boyer, and R Zeller. Theory of F centers in the alkaline-earth oxides MgO and CaO. *Phys. Rev. B*, 35(11), 1987.
175. Q. S. Wang and N. A W Holzwarth. Electronic structure of vacancy defects in MgO crystals. *Phys. Rev. B*, 41(5):3211–3225, 1990. ISSN 01631829. doi: 10.1103/PhysRevB.41.3211.
176. R. W. Grimes, C. R. A. Catlow, and A. M. Stoneham. A comparison of defect energies in MgO using Mott-Littleton and quantum mechanical procedures. *J. Phys. Condens. Matter*, 1(40):7367–7384, 1989. ISSN 0953-8984. doi: 10.1088/0953-8984/1/40/011. URL <http://www.iop.org/EJ/abstract/0953-8984/1/40/011>  $\backslash$ delimiter"026E30F\$nh<http://www.iop.org/EJ/article/0953-8984/1/40/011/cmv1i40p7367.pdf?request-id=89a58592-0574-43a4-bb1b-49adf9a47dc6>.
177. Y. Chen, R. T. Williams, and W. A. Sibley. Defect Cluster Centers in MgO. *Phys. Rev.*, 182(3), 1969.
178. J.D. Bolton, B. Henderson, and D.O. O’Connell. Photoluminescence of F2 2+ centres in additively coloured magnesium oxide. *Solid State Commun.*, 38:287–290, 1980.
179. D. O. O’Connell, B. Henderson, and J. M. Bolton. Uniaxial stress and polarisation studies of F2 centre luminescence in MgO. *Solid State Commun.*, 38(4):283–285, 1981. ISSN 00381098. doi: 10.1016/0038-1098(81)90462-2.
180. M. A. Monge, A. I. Popov, C. Ballesteros, R. González, Y. Chen, and E. A. Kotomin. Formation of anion-vacancy clusters and nanocavities in thermochemically reduced MgO single crystals. *Phys. Rev. B - Condens. Matter Mater. Phys.*, 62(14):9299–9304, 2000. ISSN 01631829. doi: 10.1103/PhysRevB.62.9299.
181. David Domínguez-Ariza, Carmen Sousa, Francesc Illas, Davide Ricci, and Gianfranco Pacchioni. Ground- and excited-state properties of M-center oxygen vacancy aggregates in the bulk and surface of MgO. *Phys. Rev. B*, 68(5):054101, aug 2003. ISSN 0163-1829. doi: 10.1103/PhysRevB.68.054101. URL <http://link.aps.org/doi/10.1103/PhysRevB.68.054101>.
182. C. Martínez-Boubeta, A. Martínez, S. Hernández, P. Pellegrino, A. Antony, J. Bertomeu, Ll. Balcells, Z. Konstantinović, and B. Martínez. Blue luminescence at room temperature in defective MgO films. *Solid State Commun.*, 151(10):751–753, may 2011. ISSN 00381098. doi: 10.1016/j.ssc.2011.03.007. URL <http://www.sciencedirect.com/science/article/pii/S003810981100127X>.
183. Biswajit Choudhury and Amarjyoti Choudhury. Microstructural, optical and magnetic properties study of nanocrystalline MgO. *Mater. Res. Express*, 1(2):025026, 2014. ISSN 2053-1591. doi: 10.1088/2053-1591/1/2/025026. URL <http://stacks.iop.org/2053-1591/1/i=2/a=025026?key=crossref.1862c93640d4f4c78dd92ef7230cf804>.

184. Biswajit Choudhury, Priyanka Basyach, and Amarjyoti Choudhury. Monitoring F, F<sup>+</sup> and F<sup>2+</sup> related intense defect emissions from nanocrystalline MgO. *J. Lumin.*, 149:280–286, 2014. ISSN 00222313. doi: 10.1016/j.jlumin.2014.01.041. URL <http://dx.doi.org/10.1016/j.jlumin.2014.01.041>.
185. Keith P. McKenna and Jochen Blumberger. Crossover from incoherent to coherent electron tunneling between defects in MgO. *Phys. Rev. B*, 86(24):245110, dec 2012. ISSN 1098-0121. doi: 10.1103/PhysRevB.86.245110. URL <http://link.aps.org/doi/10.1103/PhysRevB.86.245110>.
186. D. M. Roessler and W. C. Walker. Electronic spectrum and ultraviolet optical properties of crystalline MgO. *Phys. Rev.*, 159(3):733–738, 1967. ISSN 0031899X. doi: 10.1103/PhysRev.159.733.
187. Martin Sterrer, Markus Heyde, Marek Novicki, Niklas Nilius, Thomas Risse, Hans Peter Rust, Gianfranco Pacchioni, and Hans Joachim Freund. Identification of color centers on MgO(001) thin films with scanning tunneling microscopy. *J. Phys. Chem. B*, 110(1):46–49, 2006. ISSN 15206106. doi: 10.1021/jp056306f.
188. P. G. Mather, J. C. Read, and R. A. Buhrman. Disorder, defects, and band gaps in ultrathin (001) MgO tunnel barrier layers. *Phys. Rev. B*, 73(20):1–5, 2006. ISSN 10980121. doi: 10.1103/PhysRevB.73.205412.
189. Filip Schleicher. *Institut de Physique et Chimie des Matériaux de Strasbourg Impact of structural defects on spin-polarized transport across magnetic tunnel junctions Dreyse François Montaigne Frédéric Petroff*. PhD thesis, Université de Strasbourg, 2012.
190. F Schleicher, U Halisdemir, D Lacour, M Gallart, S Boukari, G Schmerber, V Davesne, P Panissod, D Halley, H Majjad, Y Henry, B Leconte, a Boulard, D Spor, N Beyer, C Kieber, E Sternitzky, O Cregut, M Ziegler, F Montaigne, E Beaurepaire, P Gilliot, M Hehn, and M Bowen. Localized states in advanced dielectrics from the vantage of spin- and symmetry-polarized tunnelling across MgO. *Nat. Commun.*, 5:4547, jan 2014. ISSN 2041-1723. doi: 10.1038/ncomms5547. URL <http://www.ncbi.nlm.nih.gov/pubmed/25088937>.
191. W. H. Butler, X. G. Zhang, S. Vutukuri, M. Chshievand, and T. G. Schulthess. Theory of tunneling magnetoresistance for epitaxial systems. *IEEE Trans. Magn.*, 41(10):2645–2648, 2005. ISSN 00189464. doi: 10.1109/TMAG.2005.854763.
192. G. Miao, Y. Park, J. Moodera, M. Seibt, G. Eilers, and M. Münzenberg. Disturbance of Tunneling Coherence by Oxygen Vacancy in Epitaxial Fe/MgO/Fe Magnetic Tunnel Junctions. *Phys. Rev. Lett.*, 100(24):246803, jun 2008. ISSN 0031-9007. doi: 10.1103/PhysRevLett.100.246803. URL <http://link.aps.org/doi/10.1103/PhysRevLett.100.246803>.

## Bibliography

193. Casey W. Miller, Zhi Pan Li, Ivan K. Schuller, R. W. Dave, J. M. Slaughter, and Johan Åkerman. Origin of the breakdown of Wentzel-Kramers-Brillouin-based tunneling models. *Phys. Rev. B - Condens. Matter Mater. Phys.*, 74(21):1–4, 2006. ISSN 10980121. doi: 10.1103/PhysRevB.74.212404.
194. Tomasz Dietl. A ten-year perspective on dilute magnetic semiconductors and oxides. *Nat. Mater.*, 9(12):965–74, dec 2010. ISSN 1476-1122. doi: 10.1038/nmat2898. URL [http://www.nature.com/nmat/journal/v9/n12/fig\\_{ }tab/nmat2898\\_{ }F1.html](http://www.nature.com/nmat/journal/v9/n12/fig_{ }tab/nmat2898_{ }F1.html).
195. John L. Vossen and Werner Kern. *Thin film processes II*. Academic Press, Inc, Boston, 1991.
196. P.J Kelly and R.D Arnell. Magnetron sputtering: a review of recent developments and applications. *Vacuum*, 56(3):159–172, 2000. ISSN 0042207X. doi: 10.1016/S0042-207X(99)00189-X.
197. Julien Bernos. *Elaboration de jonctions tunnel magnétiques et de jonctions metal oxyde semi-conducteur pour l'étude du transport et de la precession du spin d'électrons chauds*. PhD thesis, Université Henri Poincaré, 2010.
198. Filip Schleicher. *The Impact of structural defects on spin-polarized transport across magnetic tunnel junctions par*. PhD thesis, Université de Strasbourg, Strasbourg, 2012. URL <http://www.theses.fr/2012STRAE036>.
199. Vincent Davesne. *Organic Spintronics : an Investigation on Spin-Crossover Complexes From Isolated Molecules To the Device*. PhD thesis, Université de Strasbourg, 2013. URL <http://www.theses.fr/2013STRAE005>.
200. L Joly, B Muller, E Sternitzky, J.-G. Faullumel, A Boulard, E Otero, F Choueikani, J.-P. Kappler, M Studniarek, M Bowen, and P Ohresser. Versatile variable temperature insert at the DEIMOS beamline for in situ electrical transport measurements. *J. Synchrotron Radiat.*, 23(3):652–657, 2016. ISSN 1600-5775. doi: 10.1107/S1600577516002551. URL <http://scripts.iucr.org/cgi-bin/paper?S1600577516002551>.
201. P Ohresser, E Otero, F Choueikani, S Stanescu, F Deschamps, L Ibis, T Moreno, F Polack, B Lagarde, F Marteau, F Scheurer, L Joly, J.-P. Kappler, B Muller, and Ph Saintavit. Polarization characterization on the DEIMOS beamline using dichroism measurements. *J. Phys. Conf. Ser.*, 425(21):212007, 2013. ISSN 1742-6596. doi: 10.1088/1742-6596/425/21/212007. URL <http://iopscience.iop.org/1742-6596/425/21/212007>.
202. P. Ohresser, E. Otero, F. Choueikani, K. Chen, S. Stanescu, F. Deschamps, T. Moreno, F. Polack, B. Lagarde, J. P. Daguerrre, F. Marteau, F. Scheurer, L. Joly, J. P. Kappler, B. Muller, O. Bunau, and Ph Saintavit. DEIMOS: A beamline dedicated to dichroism measurements in the 350-2500 eV energy range. *Rev. Sci. Instrum.*, 85(1), 2014. ISSN 00346748. doi: 10.1063/1.4861191.

203. L Joly, E Otero, F Choueikani, F Marteau, L Chapuis, and P Ohresser. Fast continuous energy scan with dynamic coupling of the monochromator and undulator at the DEIMOS beamline. *J. Synchrotron Radiat.*, 21(Pt 3):502–6, may 2014. ISSN 1600-5775. doi: 10.1107/S1600577514003671. URL <http://www.ncbi.nlm.nih.gov/pubmed/24763639>.
204. Christian Felix. *X-ray absorption studies of metal-loporphyrin molecules on surfaces : Electronic interactions , magnetic coupling , and chemical switches*. PhD thesis, Frei Universität Berlin, 2013. URL [http://www.diss.fu-berlin.de/diss/receive/FUDISS{}\\_thesis{}\\_000000095352](http://www.diss.fu-berlin.de/diss/receive/FUDISS{}_thesis{}_000000095352).
205. Joachim Stöhr and Hans Christoph Siegmann. *Magnetism: From Fundamentals to Nanoscale Dynamics*. Springer, Berlin, springer s edition, 2006. ISBN 9783642312311.
206. L Joly, B Muller, E Sternitzky, A Boulard, E Otero, F Choueikani, M Studniarek, M Bowen, and P Ohresser. Versatile variable temperature insert at the DEIMOS beamline for in situ electrical transport measurements. *J. Synchrotron Radiat.*, Accepted,, 2016.
207. Y Chen, D L Trueblood, O E Schow, and H T Tohver. Colour centres in electron irradiated MgO. *J. Phys. C Solid State Phys.*, 3(12):2501, 1970. ISSN 03701972. doi: 10.1002/pssb.2220450156. URL <http://stacks.iop.org/0022-3719/3/i=12/a=016>.
208. P Edel, B Henderson, and R Romestain. Photoluminescence of additively coloured magnesium oxide : Transient features in circular polarisation and optically detected magnetic resonance. *J. Phys. C Solid State Phys.*, 15:1569–1580, 1981. ISSN 00223719. doi: 10.1088/0022-3719/15/7/022.
209. John G. Simmons. Electric Tunnel Effect between Dissimilar Electrodes Separated by a Thin Insulating Film. *J. Appl. Phys.*, 34(9):2581, 1963. ISSN 00218979. doi: 10.1063/1.1729774. URL <http://scitation.aip.org/content/aip/journal/jap/34/9/10.1063/1.1729774>.
210. L. S. Dorneles, D. M. Schaefer, M. Carara, and L. F. Schelp. The use of Simmons' equation to quantify the insulating barrier parameters in Al/AlO<sub>x</sub>/Al tunnel junctions. *Appl. Phys. Lett.*, 82(17):2832–2834, 2003. ISSN 00036951. doi: 10.1063/1.1569986.
211. P. Rottländer, M. Hehn, and a. Schuhl. Determining the interfacial barrier height and its relation to tunnel magnetoresistance. *Phys. Rev. B*, 65(5):054422, jan 2002. ISSN 0163-1829. doi: 10.1103/PhysRevB.65.054422. URL <http://link.aps.org/doi/10.1103/PhysRevB.65.054422>.
212. Hadj-Mohamed Benia, Philipp Myrach, Anastasia Gonchar, Thomas Risse, Niklas Nilius, and Hans-Joachim Freund. Electron trapping in misfit dislocations of MgO thin films. *Phys. Rev. B*, 81(24):1–4, 2010. ISSN 1098-0121. doi: 10.1103/PhysRevB.81.241415.

## Bibliography

213. K. P. McKenna and A. L. Shluger. First-principles calculations of defects near a grain boundary in MgO. *Phys. Rev. B - Condens. Matter Mater. Phys.*, 79(22):1–11, 2009. ISSN 10980121. doi: 10.1103/PhysRevB.79.224116.
214. D. J. Kim, W. S. Choi, F. Schleicher, R. H. Shin, S. Boukari, V. Davesne, C. Kieber, J. Arabski, G. Schmerber, E. Beaurepaire, W. Jo, and M. Bowen. Control of defect-mediated tunneling barrier heights in ultrathin MgO films. *Appl. Phys. Lett.*, 97(26):263502, 2010. ISSN 00036951. doi: 10.1063/1.3531652. URL <http://scitation.aip.org/content/aip/journal/apl/97/26/10.1063/1.3531652>.
215. F Montaigne, F Nguyen Van Dau, and A Schuhl. Current distribution effects in patterned non-linear magnetoresistive tunnel junctions. *J. Magn. Magn. Mater.*, 217:231–235, 2000.
216. R. J. M. van de Veerdonk, J. Nowak, R. Meservey, J. S. Moodera, and W. J. M. de Jonge. Current distribution effects in patterned non-linear magnetoresistive tunnel junctions. *Appl. Phys. Lett.*, 71(19):2839, 1997. doi: 10.1063/1.120149.
217. Steven J. Byrnes. Multilayer optical calculations. *arXiv:1603.02720*, 2016. URL <http://arxiv.org/abs/1603.02720>.
218. M Studniarek, U Halisdemir, F Schleicher, B Taudul, E Urbain, M Herve, A Hamadeh, O Zill, D Lacour, S Boukari, L Joly, F Scheurer, G Schmerber, A Dixit, M Acosta, F Leduc, F Chouekani, E Otero, W Wulfhchel, F Montaigne, E Montebianco, J Arabski, E Beaurepaire, W Weber, M Alouani, M Hehn, and M Bowen. Probing a device’s active atoms. *Submitted*, 2016.
219. D. Telesca, B. Sinkovic, See Hun Yang, and S. S P Parkin. X-ray studies of interface Fe-oxide in annealed MgO based magnetic tunneling junctions. *J. Electron Spectros. Relat. Phenomena*, 185(5-7):133–139, 2012. ISSN 03682048. doi: 10.1016/j.elspec.2012.04.002. URL <http://dx.doi.org/10.1016/j.elspec.2012.04.002>.
220. Mukes Kapilashrami, Hui Zhang, Mei Fang, Xin Li, Xuhui Sun, K. V. Rao, Lyubov Belova, Yi Luo, and Jinghua Guo. Electronic structure of room-temperature ferromagnetic Mg<sub>1-x</sub>Fe<sub>x</sub>O<sub>y</sub> thin films. *Appl. Phys. Lett.*, 101(8):082411, 2012. ISSN 00036951. doi: 10.1063/1.4747445. URL <http://link.aip.org/link/APPLAB/v101/i8/p082411/s1{&}Agg=doi>.
221. Abdul K. Rumaiz, J. C. Woicik, W. G. Wang, Jean Jordan-Sweet, G. H. Jaffari, C. Ni, John Q. Xiao, and C. L. Chien. Effects of annealing on the local structure of Fe and Co in CoFeB/MgO/CoFeB tunnel junctions: An extended x-ray-absorption fine structure study. *Appl. Phys. Lett.*, 96(11), 2010. ISSN 00036951. doi: 10.1063/1.3364137.
222. Ezana Negusse, A. Lussier, J. Dvorak, Y. U. Idzerda, S. R. Shinde, Y. Nagamine, S. Furukawa, K. Tsunekawa, and D. D. Djayaprawira. Magnetic characterization of CoFeB/MgO and CoFe/MgO interfaces. *Appl. Phys. Lett.*, 90(9):65–68, 2007. ISSN 00036951. doi: 10.1063/1.2709619.

223. V. Serin, S. Andrieu, R. Serra, F. Bonell, C. Tiusan, L. Calmels, M. Varela, S. J. Pennycook, E. Snoeck, M. Walls, and C. Colliex. TEM and EELS measurements of interface roughness in epitaxial Fe/MgO/Fe magnetic tunnel junctions. *Phys. Rev. B - Condens. Matter Mater. Phys.*, 79(14):1–7, 2009. ISSN 10980121. doi: 10.1103/PhysRevB.79.144413.
224. a. T. Hindmarch, K. J. Dempsey, D. Ciudad, E. Negusse, D. a. Arena, and C. H. Marrows. Fe diffusion, oxidation, and reduction at the CoFeB/MgO interface studied by soft x-ray absorption spectroscopy and magnetic circular dichroism. *Appl. Phys. Lett.*, 96(9):092501, 2010. ISSN 00036951. doi: 10.1063/1.3332576. URL <http://link.aip.org/link/APPLAB/v96/i9/p092501/s1{&}Agg=doi>.
225. F. M F De Groot, M. Grioni, J. C. Fuggle, J. Ghijsen, G. A. Sawatzky, and H. Petersen. Oxygen 1s X-ray-absorption edges of transition-metal oxides. *Phys. Rev. B*, 40(8):5715–5723, 1989. ISSN 01631829. doi: 10.1103/PhysRevB.40.5715.
226. Carlos Martinez-Boubeta, Lluís Balcells, and Benjam??n Mart??nez. On the changes at the Fe/MgO interface upon annealing. *J. Appl. Phys.*, 113(12), 2013. ISSN 00218979. doi: 10.1063/1.4798242.
227. Boon-Keng Teo and P A Lee. Ab Initio Calculations of Amplitude and Phase Functions for Extended X-ray Absorption Fine Structure Spectroscopy. *Journal Am. Chem. Soc.*, 101(11):2815–2832, 1979. ISSN 0002-7863. doi: 10.1021/ja00505a003. URL <http://dx.doi.org/10.1021/ja00505a003>\delimeter"026E30F\$nhhttp://pubs.acs.org/doi/abs/10.1021/ja00505a003.
228. P Lee and G Beni. New method for the calculation of atomic phase shifts: Application to extended x-ray absorption fine structure (EXAFS) in molecules and crystals. *Phys. Rev. B*, 15(6):2862–2883, 1977. ISSN 0556-2805. doi: 10.1103/PhysRevB.15.2862. URL <http://link.aps.org/doi/10.1103/PhysRevB.15.2862>\delimeter"026E30F\$npapers3://publication/doi/10.1103/PhysRevB.15.2862.
229. J. Mustre De Leon, J. J. Rehr, S. I. Zabinsky, and R. C. Albers. Ab initio curved-wave x-ray-absorption fine structure. *Phys. Rev. B*, 44(9):4146–4156, 1991. ISSN 01631829. doi: 10.1103/PhysRevB.44.4146.





**HALISDEMIR Ufuk**  
**Probing the impact of structural  
defects on spin dependent  
tunneling using photons**



## Résumé

L'étude de l'impact des défauts sur les propriétés électriques des semi-conducteurs a joué un rôle crucial dans la révolution des technologies de l'information dans le milieu du 20ème siècle. Jusqu'ici, la course à la miniaturisation a permis de répondre à la demande croissante en termes de puissance de calcul. Cependant, cette stratégie est vouée à rencontrer des limites physiques qu'il ne sera pas possible de surpasser, c'est pourquoi de nouvelles approches sont nécessaires. Dans ce nouveau paradigme de recherche, les dispositifs électroniques à base d'oxydes sont des candidats prometteurs afin de réaliser de nouveaux dispositifs multifonctionnels. L'importance des défauts sur les propriétés nominale des oxydes n'est pas autant reconnue que dans le domaine des semi-conducteurs. Notre projet de recherche tourne autour de deux objectifs principaux, le premier a pour but d'identifier explicitement l'impact de défauts spécifiques sur les propriétés électrique de dispositifs à base d'oxydes. Le second a pour but de tirer avantage des propriétés induites pour les défauts pour des applications optoélectroniques.

**Mots clés :** spintronique, TMR, jonctions tunnels magnétiques, défauts, états localisés, photoluminescence

## Abstract

The study of the impact of defects on the electrical properties of semiconductors played a crucial role in the revolution of information technologies in the middle of the 20th century. Up to now, the race to miniaturization allowed to meet the increasing demand in terms of processing power. However, this strategy is predicted to encounter physical limits impossible to overcome and new approaches are necessary. Within this new research paradigm, oxide based electronic devices are promising candidates to fabricate new multifunctional devices. The importance of defects on the nominal properties of oxides is not acknowledged as much as it is in the field of semiconductors. Our research project revolved around two primary objectives, the first one aimed to explicitly identify the impact of specific defects on the properties of oxide-based electronic devices. The second one aimed to actually take advantage of properties induced by defects for optoelectronic applications.

**Keywords:** spintronic, TMR, magnetic tunnel junctions, oxide, defects, localized states, photoluminescence